TECHNISCHE UNIVERSITÄT MÜNCHEN

Friedrich Schiedel-Institut für Neurowissenschaften

Analysis of neuronal network function in the mouse visual cortex *in vivo*

Christine Maria Grienberger

Vollständiger Abdruck der von der Fakultät für Medizin der Technischen Universität München zur Erlangung des akademischen Grades eines

Doctor of Philosophy (Ph.D.).

genehmigten Dissertation.

Vorsitzender: Univ.-Prof. Dr. Claus Zimmer

Prüfer der Dissertation:

1. Univ.-Prof. Dr. Thomas Misgeld
2. apl. Prof. Dr. Helmuth K. H. Adelsberger
3. Univ.-Prof. Dr. Martin Kerschensteiner,
   Ludwig-Maximilians-Universität München

Die Dissertation wurde am 10.12.2012 bei der Fakultät für Medizin der Technischen Universität München eingereicht und durch die Fakultät für Medizin am 18.03.2013 angenommen.

Abstract

In the studies presented in this thesis, *in vivo* two-photon calcium imaging was used to obtain new insights into the physiological development of orientation and direction preference of mouse primary visual cortex neurons and into the disruption of these properties in an animal model of Alzheimer's disease (AD).

First, visual cortex neurons responding selectively to the orientation of drifting gratings were detected just after eye opening, and approximately all of them were also highly tuned for the direction of stimulus motion. This formation of direction selectivity was not dependent on previous visual experience. Thus, the conclusion can be drawn that the early establishment of these properties depends on intrinsic factors that are present within visual cortex.

Second, the effect of the amyloid-beta peptide (Aβ) on cortical circuit function was assessed through comparing wild mice and APP23xPS45 mice at an age of 2 – 10 months. These results established a relation between the increase of Aβ load, progressive cortical dysfunction and behavioral deficits in the AD mice. In detail, both orientation and direction selectivity declined as the animals accumulated more Aβ in the brain. This was mediated by an increasing number of hyperactive neurons that had impaired responsiveness, whereas neurons with a normal range of activity had similar sensitivities to neurons in wild type animals. Moreover, a significant fraction of hypoactive neurons was characterized by a complete lack of responsiveness to any visual stimulation. Together, these results demonstrate that the presence of Aβ causes disturbances that have consequences at the level of entire neuronal networks that finally lead to an impairment of behavioral performance.

Table of contents

Abbreviation

Aβ	Amyloid-β peptide, toxic cleavage product of the amyloid precursor protein, major variants consists of 40 amino acids (Aβ40) or 42 amino acids (Aβ42)
AD	Alzheimer's disease
APP	Gene encoding the amyloid precursor protein
APP	Amyloid precursor protein
LGN	Lateral geniculate nucleus of the thalamus
p	postnatal day
PS	Presenilin
PSEN1	Gene encoding presenilin 1
PSEN2	Gene encoding presenilin 2
SC	Superior colliculus
V1	Primary visual cortex

1 Introduction

The focus of the work presented in this thesis is the function of neuronal networks in primary visual cortex of wild type and APP23xPS45 mice, an animal model of Alzheimer's disease. Using *in vivo* two-photon calcium imaging in combination with behavioral and biochemical analyses, the following questions were addressed:

- How do the functional properties of visual cortex neurons develop initially at the onset of vision in juvenile mice (from the age of 10 days to 2 months)?
- How does a neurodegenerative disorder, such as Alzheimer's disease, affect the functionality of visual cortex in aged mice (from the age of 2 months to 10 months)?

1.1 The mouse sensory systems

How do we experience our environment? Sensory systems, which consist of peripheral sensory receptors, afferent and efferent pathways as well as areas within the central nervous system, mediate the interactions with our surroundings. Hence, their function is to detect environmental stimuli and transmit this perception to specialized regions of the cerebral cortex. There are different sensory modalities in mammals, such as vision, hearing, taste, smell and touch, which are each represented in different cortical areas (O'Leary et al., 2007). The processing of sensory information within the cortical neuronal networks involves integration with past experiences and recent incoming information from other sensory modalities in order to form a coherent picture of the environment (Hudspeth and Logothetis, 2000). Neurons, which represent the basic units of these cortical circuits, can be specifically activated by a sensory stimulus or by a particular feature of this stimulus. For example, neurons in the primary visual cortex of mammals are characterized by specific responses to the direction and orientation of a moving visual stimulus (Hubel

and Wiesel, 1959; Niell and Stryker, 2008; Ohki et al., 2005). In addition, sensory systems are topographically organized at their different anatomical levels. This can be strikingly illustrated by the vibrissae-receptive primary somatosensory cortex, or the ‘barrel cortex’. The thalamic inputs to the layer 4 of this cortical area are organized in a columnar fashion, with each column corresponding to an individual rodent vibrissa (Durham and Woolsey, 1977). Notably, the vibrissae maps are preserved throughout the stages of the whisker-related sensory system, including the trigeminal nuclei, the thalamus, and the neocortex (Petersen, 2007). Similarly, for instance, in the mouse visual system, the retinotopic map is present in the retina, the LGN and the superior colliculus and finally also in the primary visual cortex (Huberman and Niell, 2011).

It is widely accepted that the processing of sensory information is performed in neuronal networks (Harris et al., 2011; Kwan, 2008). The activity of neuronal ensembles as a whole mediates the perception of a particular stimulus, initiates learning and memory formation and triggers an adequate behavioral response (Averbeck et al., 2006; Ohl and Scheich, 2005). The underlying mechanisms on the level of neuronal networks are at the moment not entirely understood. To address the question of how the brain performs sensory processing, it is therefore very important to investigate, in addition to the single-cell analysis, activity patterns on the level of population of neurons. One fundamental challenge for understanding the basic principles of sensory information processing in the mammalian brain is to dissect the participating neural circuits (Kerr and Denk, 2008). This requires the systematic characterization of the participating cell types, their connections, and their activity during sensory processing. The understanding of these processes helps to identify pathological states associated with disorders of the nervous system, such as Alzheimer’s disease or ischemia-induced network dysfunction (Palop et al., 2006).

1.2 The mouse visual cortex

The experimental part of this thesis was performed in the mouse primary visual cortex (V1). This area has increasingly attracted attention in the recent years. Mice allow examining defined categories of cells and circuits (Luo et al., 2008).

Genetic tools provide the opportunity to investigate the effect of a specific transgene on neuronal activity (such as the impact of Alzheimer's disease-related mutations), see the structure of a defined cell type, record its activity in response to sensory stimulation and finally selectively manipulate molecularly-defined cell types in a reversible manner. In addition, mouse V1 neurons possess most of the important hallmarks of cortical visual processing found in higher mammals, including spatial frequency tuning, orientation and direction selectivity, contrast gain control, contrast-invariant tuning and specific receptive fields (Niell and Stryker, 2008). These findings suggest that the visual cortex in mice is performing similar computations as the cortices in other well-studied species, such as cats, ferrets and non-human primates. In addition, the smaller total size of the mouse nervous system makes it possible to collect data over a large spatial scale; for instance, the entire area of the mouse primary and higher associative visual cortices extends over only several millimeters, potentially allowing the entire system to be visualized at once (Wang and Burkhalter, 2007).

For these reasons, the mouse visual system is a valuable and suitable model to investigate the mechanisms underlying sensory processing under physiological and pathophysiological conditions. Thus, mice have been used for investigating visual system development (Cang et al., 2005; Fagiolini et al., 2003), the mechanisms of synaptic plasticity (Fagiolini et al., 2004; Syken et al., 2006), and the function of distinct cellular subtypes, such as inhibitory interneurons, in the visual cortex (Kerlin et al., 2010; Runyan et al., 2010; Sohya et al., 2007).

1.2.1 The architecture of the mouse visual system

Visual information is transmitted from the retina to the lateral geniculate nucleus (LGN) of the thalamus and further to V1, which is located in the occipital part of the brain. Moving further up the cortical hierarchy, there exist a set of associative visually responsive regions, which are involved in more complex sensory processing.

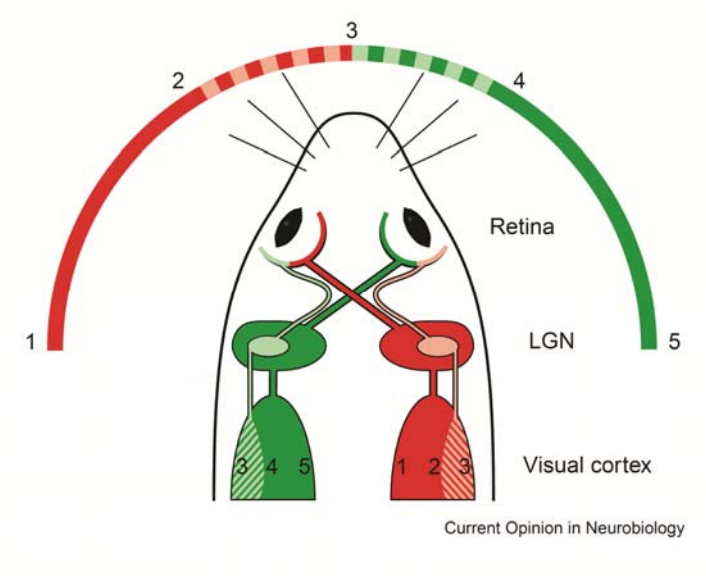

Figure 1: The mouse visual system.

The schematic diagram of the main mouse visual pathway shows retinal projections to the lateral geniculate nucleus (LGN) as well as the thalamo-cortical pathway from LGN to visual cortex. The binocular field of vision (striped portion of the visual field) is relatively small. In the visual cortex, binocular responses are found in the lateral third of this area (striped area).
(Modified from Hübener, 2003)

Figure 1 schematically illustrates the structure of the mouse visual system and its relation to the visual field of a mouse. At the beginning of the visual pathway, the mouse retina contains photoreceptors, which translate the incoming photons into electrical signals. The mouse retina is rod-dominated and therefore specialized for vision under low light conditions (Jeon et al., 1998). Notably, mice do not have a fovea, and, as a consequence, have low visual acuity. After the photoreceptors have converted photons into electrical activity the information is mainly filtered by three classes of retinal neurons, namely the horizontal, bipolar and amacrine cells, and transferred to the retinal ganglion cells (Masland, 2001). These act as retinal output cells and project to more than 20 subcortical target regions (Ling et al., 1998). Thus, the axons of the retinal ganglion cells leave the retina and form both optic nerves that are linked at the optic chiasm. At this location about 90% of the ganglion cells axons cross the midline in mice and get to the contralateral side whereas the remainder of the axons continues on the ipsilateral side (Valverde, 1968). As part of the main visual pathway, retinal ganglion cells from both eyes project into distinct

eye-specific regions in the LGN (Fig. 1). These eye-specific regions are formed during development through retraction of the initially diffuse retinal projections, a process that is finalized by the time of natural eye opening at postnatal day 12-14 (p 12-14) (Jaubert-Miazza et al., 2005). From the LGN the fibers enter the internal capsule and continue their way in the white matter to end predominantly in the thalamorecipient layer 4 of mouse V1 (Valverde, 1968). V1 contains a complete and continuous map of the visual field. Thalamocortical axons carrying information from one eye project to the monocular region while those that carry information from both eyes converge in the binocular region of V1. This binocular region is located in the lateral one third of V1 (Fig. 1) (Metin et al., 1988). In this part of the visual cortex, the majority of neurons (around 70%) usually respond to inputs from the two eyes, however overall there is a strong dominance of the contralateral eye, only 5% of the cells being exclusively driven by the ipsilateral eye (Gordon and Stryker, 1996).

Beside the above described retino-thalamo-cortical pathway there exists an important projection from the retina to the superior colliculus (SC). This midbrain structure receives direct retinal input to its superficial layers and integrates other sensory modalities throughout its complete depth (May, 2006). Neurons that are located in the superficial layers respond to moving spots within a rather extended region of the visual space. Furthermore, orientation- and direction-selective responses that are independent of cortical input have been found in these SC neurons (Wang et al., 2010). Activity in the deep layers of this area, however, is known to have an important role in controlling eye movements (McHaffie and Stein, 1982). This functional diversity of collicular neurons suggests that SC and cortex play a combined role in visual processing. Interestingly, mice can still perform simple target detection tasks even after lesioning V1, suggesting that some of the functions classically ascribed to mouse visual cortex are in fact mediated by the superior colliculus (Huberman and Niell, 2011).

1.2.2 The functional properties of mouse visual cortex neurons

Functional analyses of the neurons in mouse V1 have revealed that these neurons possess nearly all the functional properties that have been previously described in higher mammals such as cats (Hubel and Wiesel, 1959) or monkeys (Hubel and Wiesel, 1968). Mouse V1 has the typical six-layered structure, retinotopic organization, and is characterized by various excitatory and inhibitory neuronal cell types. Prominently, V1 neurons respond most strongly to a particular orientation or direction of the visual stimulus, a property known as orientation or direction selectivity (Dräger, 1975; Metin et al., 1988; Niell and Stryker, 2008). Similarly, other aspects of cortical processing, including tuning to the temporal and spatial frequency of the stimulus as well as the contrast-invariant tuning of visually-evoked responses, are found equally in this cortical area in mice. Furthermore, it was shown that the mouse brain is also able to undergo plastic changes similar to those of higher mammals (for review, see Espinosa and Stryker, 2012). However, there are also clear differences between the visual cortices of rodents and higher mammals. For example, the average receptive field diameter for the mouse is around 14° (Metin et al., 1988), in contrast to around 1° in cats and below 1° in macaques (Hübener, 2003). Most importantly, the large-scale organization of the neurons in radial columns, which is a characteristic of the functional architecture of the visual cortex of carnivores and most primates (Hubel and Wiesel, 1962; Hubel et al., 1977), has not been detected in rodent V1 (Girman et al., 1999; Ohki et al., 2005; Van Hooser et al., 2005). These cortical columns are based on the functional response properties of the cells. For example, using imaging of intrinsic optical signals isoorientation columns, organized in ‘pinwheel’ structures, were identified in cat V1 (Bonhoeffer and Grinvald, 1991).

1.2.3 Orientation and direction selectivity of mouse visual cortex neurons

In this work I studied specifically the fundamental property of mouse V1 neurons to respond preferentially to a specific orientation or direction of movement of a visual stimulus (see e.g. Dräger, 1975; Wagor et al., 1980). As mentioned above,

mouse visual cortex does not contain feature maps and as such lacks for example orientation columns (Hübener, 2003). Nevertheless, highly tuned orientation- and direction-selective neurons are present in mouse V1 and scattered throughout this cortical region in a salt-and-pepper fashion (Ohki et al., 2005). Thus, orientation maps are apparently dispensable for generating strict orientation tuning in individual cells. In fact, the level of orientation selectivity in mouse, in terms of the range of orientations that a given cell will respond to, is similar to that seen in the cat or monkey (Niell and Stryker, 2008). This is despite the fact that visual acuity varies tremendously across these species (Van Hooser, 2007).

Several studies, performed in cats, ferrets and non-human primates, have focused on the mechanisms underlying the development of response properties of visual cortical neurons. It has been shown that orientation and direction selectivity are established through distinct mechanisms. While the formation of orientation-selective response features in cortical neurons is not dependent on visual experience in these animal models (for review, see White and Fitzpatrick, 2007), the emergence of direction selectivity rigorously requires visual experience. This was shown in the ferret visual cortex, in which direction-preference maps cannot be found at eye opening as well as in animals reared in darkness (Li et al., 2006).

In the mouse primary visual cortex, the development of orientation selectivity has been examined in detail (Fagiolini et al., 2003; Fagiolini et al., 1994). After topographic maps have been organized V1 neurons acquire inputs in a specific arrangement such that they are endowed with the capability to respond in an orientation-selective manner (Priebe and Ferster, 2012). However, the establishment of direction selectivity has so far not been studied in rodents. The exceptions are recent studies that investigated the emergence of direction selectivity in the mouse retina. In mice, retinal ganglion cells exhibit direction selectivity (Elstrott et al., 2008; Yonehara et al., 2009). Remarkably, this strong direction-selectivity is already present at the time point of opening of the eyes. Moreover, this direction selectivity has been detected also in mice lacking any visual experience, as they were brought up in complete darkness (Elstrott et al., 2008). Taken together, these evidences suggest that visual experience is not mandatory for direction selectivity in the retina. At present, it remains an open question how direction selectivity emerges in the mouse visual cortex and how direction selectivity in the retina, so at the starting point of the visual pathway, is related to the motion sensitivity of cortical neurons.

1.3 Alzheimer's Disease

Alzheimer's disease (AD) is a devastating progressive neurodegenerative disorder and considered to be the most frequent cause of dementia in aged persons (Querfurth and LaFerla, 2010). Worldwide, there are currently more than 35 million AD patients and, notably, due to the demographic change it is expected that in 2050 about 115 million people will suffer from this disease (Ashe and Zahs, 2010). Clinical symptoms include memory loss, in initial phases of the disease in particular of recent events, as well as deficits in other cognitive fields, such as language, mood, reason and judgment (McKhann et al., 1984). Eventually, the patient becomes completely socially dependent and is even not able to perform routine tasks. Moreover, patients progressively experience problems with processing of sensory information, particularly at later stages of their disease. Different sensory modalities can be affected, including processing of information in the olfactory or the visual system (Bublak et al., 2011; Cronin-Golomb et al., 1991; Devanand et al., 2000; Djordjevic et al., 2008; Fernandez et al., 2007; Mesholam et al., 1998; Trick and Silverman, 1991). At the moment, there is no disease-modifying treatment available (Roberson and Mucke, 2006).

AD is in most cases sporadic and usually of later onset (age > 60 years) (Tanzi and Bertram, 2005). Nonetheless a small fraction of patients (1-2%) suffer from early-onset autosomal-dominant familial forms of AD, which affect mostly younger individuals, usually before the age of 60. However, the clinical appearances of early-onset and late-onset AD are undistinguishable. It should be however emphasized that also up to 60-80% of sporadic late-onset AD cases are genetically determined (Gatz et al., 2006). For example, the $\varepsilon 4$ allele of apolipoprotein E remains the most important variant modulating risk of late-onset AD (Strittmatter et al., 1993). Histopathologically, AD is characterized by the presence of amyloid-β (Aβ) plaques, the presence of intracellular neurofibrillary tangles consisting of hyperphosphorylated forms of the tau protein and the progressive loss of neurons resulting in brain atrophy (Duyckaerts et al., 2008). There exists a plethora of different hypotheses, each emphasizing a different cascade of events that may finally cause AD. These include Aβ toxicity, impaired presenilin function, dysregulation of intracellular calcium homeostasis, autophagy dysfunction and hyperphosphorylation of the tau protein (Sheng et al., 2012). However, the exact

underlying pathomechanisms remain unknown, most likely because multiple factors (genetic, epigenetic, age-dependent and environmental) and different sequence of events combine to determine disease susceptibility and the course of the disease.

1.3.1 The role of amyloid-β in the pathogenesis of Alzheimer's disease

Research on the rare early-onset familial AD subtypes revealed that mutations in three different genes are sufficient to cause AD (Bertram et al., 2010). All three genes, namely the genes encoding the amyloid precursor protein (*APP*), encoding presenilin 1 (*PSEN1*) and encoding presenilin 2 (*PSEN2*), act mainly through increasing the production and aggregation of a toxic cleavage product of the amyloid precursor protein (APP), the Aβ peptide (Selkoe, 2004). The increase in accumulation is thereby caused by a shift of the Aβ42/Aβ40 ratio towards more Aβ42 generation, with Aβ42 being more prone to aggregation (Tanzi and Bertram, 2005). Hence, Aβ has been identified as an essential factor in disease pathogenesis and the amyloid hypothesis states that, in AD, the aggregation of Aβ, as either plaques or other forms, underlies a sequence leading to synaptic dysfunction and synapse loss (“synaptic dismantling”) as well as to tau hyperphosphorylation and to neuronal degeneration (Haass and Selkoe, 2007; Hardy and Selkoe, 2002; Krafft and Klein, 2010; Selkoe, 2002).

The Aβ peptide is present in different forms in AD brains, including soluble oligomeric species and insoluble Aβ plaques (Glabe, 2008). *In vitro* studies have proposed various mechanisms of Aβ-mediated pathological changes , including modifications of ion channel properties and impairments of synaptic transmission and plasticity (Chapman et al., 1999; Kamenetz et al., 2003; Li et al., 2009; Shankar et al., 2008; Wei et al., 2010). Furthermore, histological studies have revealed *in vivo* neuritic path disruption and dendritic spine loss in the brains of multiple AD mouse models (D'Amore et al., 2003; Hsieh et al., 2006; Knowles et al., 1999; Kuchibhotla et al., 2008; Meyer-Luehmann et al., 2008). The spine loss occurred prominently near plaques (Spires et al., 2005; Tsai et al., 2004) and might be associated with different processes, including altered glutamate receptor trafficking (Lacor et al.,

2007) or a pathologically increased level of synaptic activation, which would lead to spine loss due to homeostatic mechanisms (Swann et al., 2000). These morphological changes suggest that the aggregation of Aβ could mediate impairment of connectivity and consequently to disruption of neuronal signal integration, a process that would certainly severely disrupt neuronal circuit function.

Effects of Aβ on the network level have equally been investigated *in vivo* in various mouse models of AD (Palop and Mucke, 2010). Recordings of electrical stimulation-evoked activity showed that synaptic response reliability is reduced in the Aβ plaques-bearing cortex (Stern et al., 2004). In addition, generalized spontaneous pathological epileptiform activity was recorded in the cortex and the hippocampus of another AD mouse model by electroencephalography (Palop et al., 2007). In the olfactory system, local field potential recordings revealed pathologically altered spontaneous and evoked oscillations in the Tg2576 mouse model of AD (Wesson et al., 2011). Using two-photon calcium imaging a study in frontal cortex identified two distinct subsets of nerve cells according to the pathological modification of their spontaneous activities (Busche et al., 2008). In addition to a noticeable decrease of activity in a fraction of neurons, a second subset of neurons was found to be highly active in the Aβ peptide containing cortex. Nevertheless it remains an open question how the Aβ peptide affects the functionality of individual neurons as part of cortical circuits *in vivo* and how this relates to the behavioral performance.

1.3.2 Mouse models of Alzheimer's disease

For studying the role of Aβ in AD pathogenesis, animal models of the disease have become indispensable. Thus, the identification of mutations associated with the genetic form of the disease, which allowed the development of various mouse models of AD, has represented a crucial step for investigating the pathomechanisms associated with this disorder (Götz and Ittner, 2008). Meanwhile, a large variety of transgenic mouse models has been established using mostly disease-associated forms of the human *APP*, the *PSEN1* or *PSEN2* genes (Janus and Westaway, 2001). These models produce to varying degrees, at different ages and in different combinations cognitive behavioral deficits, Aβ plaques, tau pathology, gliosis,

synapse loss and axonopathy (Hall and Roberson, 2012). They exhibit, however, either minimal or modest degrees of neuronal loss, even at advances disease stages.

Such a transgenic mouse model was used for the investigation of the Aβ-related cortical dysfunction in one of the studies presented in this thesis. The double-transgenic APP23xPS45 mice express mutant forms of the human *APP* and *PSEN1* genes under the Thy-1 promoter (Busche et al., 2012; Busche et al., 2008; Grienberger et al., 2012; Herzig et al., 2004; Sturchler-Pierrat et al., 1997). These mice develop Aβ plaques and other AD-relevant pathologies, such as gliosis and inflammatory processes, in an age-dependent manner. For example, plaques develop initially at the age of about three months in the deeper cortical layers and then cover increasingly more brain area (Fig. 2). In parallel, an age-dependent increase in the concentration of soluble Aβ species can be found in the brain. Therefore, these mice represent a suitable animal model to study Aβ-related neuronal dysfunction.

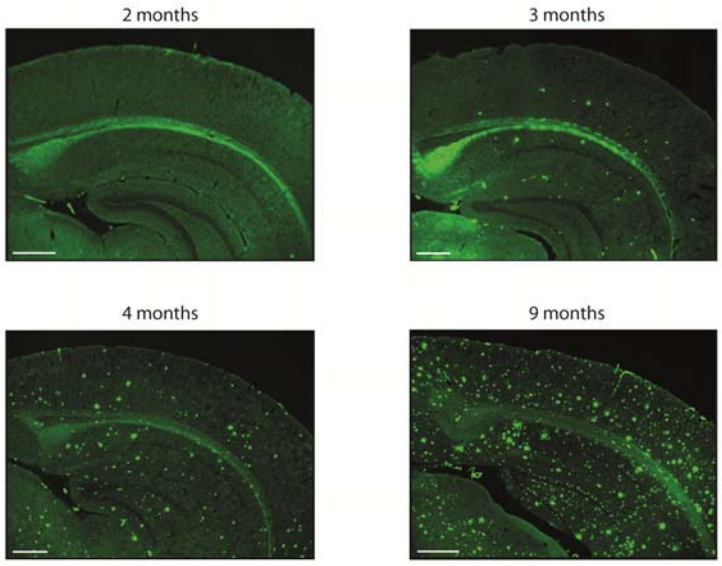

Figure 2: Aβ plaque deposition in the primary visual cortex of APP23xPS45 mice.
Thioflavin-S labeled Aβ plaques in coronal brain slices of 2 month-, 3 month-, 4 month- and 9 month-old APP23xPS45 mice. (Modified from Grienberger et al., 2012)

2 Aim

The aim of the work presented in this thesis was to analyze neuronal network activity with single-cell resolution during regular development and in an animal model of Alzheimer's disease. Hence, experiments in the primary visual cortex (V1) of juvenile wild type mice (from the age of 12 days to 2 months) as well as in older APP23xPS45 and wild type mice (from the age of 2 months to 10 months) were performed.

In order to probe network functionality, orientation and direction tuning of V1 neurons provided a direct read-out of cortical function. These tuning properties could be directly evaluated in anesthetized mice through drifting grating stimulation and analysis of the pattern of evoked activity. Thus, for these studies, the visual cortex provided an excellent model system to investigate for the first time cortical function in the context of sensory processing during development as well as cortical circuit functionality in the presence of amyloid-β (Aβ) in a mouse model of Alzheimer's disease (AD).

Responses to visual stimulation have previously been assessed using extra- and intracellular electrical recordings (see e.g. Hubel and Wiesel, 1959, 1968; Jia et al., 2010; Niell and Stryker, 2008). In recent years, however, *in vivo* two-photon calcium imaging has become an important tool to study functional properties of visual cortex neurons (see e.g. Ohki et al., 2005; Rochefort et al., 2009; Smith and Häusser, 2010; Sohya et al., 2007) as it has been shown that the recorded somatic calcium transients directly reflect the suprathreshold action potential firing of the individual neurons in the field of view (Kerr et al., 2005).

This approach was chosen for investigating the neuronal network function in mouse visual cortex because it allowed (1) recording simultaneously the sensory-evoked activity of many neurons with single-cell resolution *in vivo*, (2) studying the function of visual cortical networks in anesthetized animals in the intact brain, thus with all incoming sensory inputs, connections with other brain regions and output signals preserved, (3) sampling neuronal activity without bias towards more active neurons, (4) collecting information about the spatial distribution of neurons within the neuronal network and (5) examining the relative position of the neurons and Aβ plaques in the APP23xPS45 mouse model of AD.

The following questions were addressed in this thesis:

Project I

- What are the advantages and limitations of imaging neuronal calcium signaling?
- What are the possible applications of calcium imaging in neurons?

Project II

- How is direction selectivity in mouse primary visual cortex neurons established during development (from eye opening until adulthood)?
- Does the formation of direction selectivity require visual experience?

Project III

- Does amyloid-beta affect the function of the mouse primary visual cortex, assessed by the orientation/direction tuning of the visual cortex neurons, in the APP23xPS45 mouse model of Alzheimer disease?
- How does this dysfunction manifest at different stages of the disease?
- How does this cortical dysfunction relate to the behavioral phenotype?

Each of the three studies was published in peer-reviewed journals: Grienberger & Konnerth, Neuron, 2012 (Project I), Rochefort et al., Neuron, 2011 (Project II), Grienberger et al., Nature Communications, 2012 (Project III).

.

3 Project I - Imaging calcium in neurons

Published in **Neuron**, 2012, 73(5): 862-85

The purpose of this article was to provide a comprehensive assessment of calcium imaging in neurons to a scientific audience. It was divided in three main parts: first, we introduced the neuronal calcium signaling, then we discussed technical aspects of the method and finally, we presented important applications of calcium imaging. It should be mentioned that neuronal calcium signaling is highly interesting as calcium ions underlie a variety of intracellular signals that determine a large variety of functions in nearly every cell type in biological organisms. In the nervous system, calcium influx initiates exocytosis of neurotransmitter-containing synaptic vesicles and mediates induction of activity-dependent synaptic plasticity at the postsynaptic site. In the cell nucleus, calcium signals regulate gene transcription. Thus, after presenting the importance of calcium signaling in neurons we evaluated the different types of calcium indicators and discussed their advantages and limitations. This was followed by a section on the various loading techniques of calcium indicators and a description of the calcium imaging instrumentation, including confocal and two-photon microscopy as well as miniaturized head-fixed devices that can be applied in freely-moving animals. Using application examples, we put emphasis on new and exciting methodological developments, such as calcium imaging in behaving animals.

Together with Prof. Dr. Arthur Konnerth, I designed all the figures, collected the literature and wrote the draft of the manuscript.

4 Project II – Development of direction selectivity in mouse cortical neurons

Published in **Neuron**, 2011, 71(3): 425-432

In this article, the formation of orientation and direction selectivity of layer 2/3 neurons of the mouse visual cortex was studied during early development. These phenomena have been investigated before in higher mammals. For example, a study in the ferret visual cortex indicated that, in contrast to orientation selectivity, the establishment of direction selectivity requires visual experience. Here, we used *in vivo* two-photon calcium imaging in anesthetized mice in order to record the spiking activity of many neurons simultaneously. By combining this approach with visual stimulation with drifting gratings it was found that right after eye opening already nearly all orientation-selective neurons were as well direction-selective. Later, the number of neurons showing response to drifting gratings increased together with the fraction of neurons that were selective for orientation, but not direction. We found a normal development of direction selectivity in the absence of any visual experience when comparing normally- and dark-reared mice. Striking parallels could be identified when relating the development of cortical direction selectivity and the previously reported direction selectivity formation in the mouse retina. Together, these experiments demonstrate that orientation and direction selectivity in the mouse visual cortex is shaped through distinct mechanisms which differ, for example, substantially from those in ferret visual cortex.

For this study, I executed a significant part of the *in vivo* two-photon calcium imaging experiments in mice at different stages of early development (from an age of 13 days to 2 months). In these experiments, I independently conducted all experimental steps, including the surgical preparation of the animal, the loading of the calcium indicator, the recording of calcium signals and finally the post-hoc histological analysis. In addition, I performed the analysis for these experiments involving image processing as well as analysis of the visually-evoked calcium signals.

5 Project III – Staged decline of neuronal function *in vivo* in an animal model of Alzheimer's disease

Published in **Nature Communications**, 2012, 3: 774

The impact of amyloid-β peptide (Aβ) aggregation on neuronal dysfunction on the single cell level *in vivo* is not well understood. In this paper, we achieved direct insights into the relationship between the age-dependent increase of Aβ load, the specific changes in the function of cortical neurons and the behavioral alterations in the APP23xPS45 mouse model of AD. Using *in vivo* two-photon calcium imaging in anesthetized mice we studied how the presence of Aβ affects the ability of visual cortex neurons to distinguish the orientation and direction of moving grating patterns. We found that both sensitivities decline as the animals accumulate more Aβ with age. This is caused by an increasing number of hyperactive neurons that have impaired responsiveness, whereas neurons with a normal range of activity have similar sensitivities to neurons found in wild type animals. In addition, a significant fraction of hypoactive neurons was characterized by a complete lack of responsiveness to any visual stimulation. Thus, these results demonstrate that the presence of Aβ causes disturbances that have consequences at the level of whole neuronal networks. Moreover, we found that the staged impairment of neuronal circuit function was paralleled by a reduced behavioral performance in the visual discrimination test. Together, the results establish that there is a parallel progression in the increase of Aβ load, cortical dysfunction and sensory information processing deficits in the APP23×PS45 mouse model of AD.

For this study, I performed all the *in vivo* two-photon calcium imaging experiments as well as the subsequent analysis of the acquired data. In these experiments, I conducted all experimental steps, including the surgical preparation of the animal, the calcium indicator loading, the recording of calcium signals and finally the post-hoc histological analysis. In addition, I participated in the Thioflavin-S and antibody staining of Aβ plaques and, contributed to the analysis of the visual discrimination test. Finally I designed, together with Dr. Nathalie Rochefort and Prof. Dr. Arthur Konnerth, the figures and wrote the manuscript.

6 Discussion

In the studies that are part of this thesis, *in vivo* two-photon calcium imaging (Grienberger and Konnerth, 2012) was used to obtain new insights into the physiological development of orientation and direction preference of mouse primary visual cortex (V1) neurons (Rochefort et al., 2011) and into the disruption of these properties under pathological conditions (Grienberger et al., 2012).

First, neurons selective for the orientation of drifting gratings were detected right after eye opening, and nearly all of them were also highly tuned for the direction of stimulus motion. At later developmental stages, the number of neurons responding to drifting gratings increased together with the proportion of nerve cells that were orientation- and not direction-selective. This formation of orientation- and direction-preference was independent of visual experience. Thus, the conclusion can be drawn that the early establishment of these properties depends on intrinsic factors that are present within visual cortex.

Second, the effect of the amyloid-beta (Aβ) peptide on cortical circuit function was assessed by comparing wild mice and APP23xPS45 mice at an age of 2 – 10 months. To address this issue the mouse visual cortex was used as a model system. An advantage of this model was that the assessment of orientation and direction preference provided an unbiased read-out of network functionality and could be directly assessed in anesthetized mice using drifting grating stimulation (Niell and Stryker, 2008). In this study, biochemical, behavioral and functional analyses at different stages of the disease were combined and established a firm relation between the increase of Aβ load, progressive cortical dysfunction and behavioral deficits in the APP23xPS45 mouse model of AD. In detail, both orientation and direction selectivity declined as the animals accumulated more Aβ in the brain. This was caused by an increasing number of hyperactive neurons that had impaired responsiveness, whereas neurons with a normal range of activity had similar sensitivities to neurons in wild type animals. Moreover, a significant fraction of hypoactive neurons was characterized by a complete lack of responsiveness to any visual stimulation. Together, these results demonstrate that the presence of Aβ causes disturbances that have consequences at the level of whole neuronal networks that finally lead to an impairment of the behavioral performance.

6.1 Development of direction selectivity in mouse cortical neurons

Before eye opening, which occurs at around postnatal day 13, cortical neurons in some species can respond to visual stimuli through the eyelids. For example, in ferrets, visual cortex neurons' activity is modified by drifting gratings presented through eyelids (Krug et al., 2001). These results, however, contrast with those obtained in the study now performed in mice, where drifting grating stimuli evoked specific neuronal responses only after eye opening. Before, only strong changes in luminance, for instance bright light flashes, were able to elicit cortical activity that was characterized by highly correlated calcium transients in most of the layer 2/3 neurons. Our present results indicate that, similarly to spontaneous activity (Rochefort et al., 2009), a transition from a dense activity to a stimulus-specific one occurred for sensory-evoked neuronal responses around the time point of eye opening. It has been suggested in the literature that this switch has an important role in preparing the developing cortex for processing of visual patterns (Colonnese et al., 2010). Then, immediately after eye opening, neurons responding to the orientation and direction of drifting gratings were observed in the mouse V1. These results are in contrast to those obtained in the ferret visual cortex, where only orientation-selective neurons are present at eye opening. These cells, subsequently, acquire direction selectivity in the first two weeks following eye opening (Li et al., 2006). Importantly, in ferrets, visual experience is mandatory for the formation of direction-selective maps (Li et al., 2006). In the mouse visual cortex, however, visual experience is not required for the development of direction selectivity.

Interestingly, in the mouse retina, direction-selective ganglion cells are also, independent of visual experience, already present at eye opening (Elstrott and Feller, 2009). It was shown that at this developmental stage the direction-selective ganglion cells exhibit a strong preference for motion toward the temporal or the ventral end of the retina. In adult retinas, the asymmetry disappears. Notably, the results obtained in the study presented here demonstrate a strikingly similar temporal pattern of direction selectivity in mouse V1. As in the retina, direction selectivity was present at eye opening and developed independently of visual experience. Furthermore, these cortical direction-selective neurons showed a preference for a specific motion direction of the visual stimulus that was strikingly

similar to the one found in retinal neurons. Thus, in the mouse visual system, direction selectivity could be transmitted from the retina to the visual cortex. The visual pathway from the retina to the cortex comprises the lateral geniculate nucleus (LGN) of the thalamus, which acts as a relay for sensory information. Indeed, anatomical studies have identified direction-selective territories within spatially distinct layers of mouse LGN (Huberman et al., 2009; Kay et al., 2011; Rivlin-Etzion et al., 2011). A recent study using *in vivo* two-photon calcium imaging, which provides single-cell resolution, now demonstrated direction-selective neurons in the superficial layers of LGN (Marshel et al., 2012). The finding that LGN neurons are tuned for stimulus motion supports the hypothesis that direction selectivity could propagate from the retina to the visual cortex. This may be even not specific to the mouse visual system as direction-selective receptive fields have also been described in the rabbit LGN (Levick et al., 1969), and both orientation- and direction-selective neurons are present in the cat LGN (Thompson et al., 1994).

In conclusion, the study presented here suggests that the organizational difference between the primary visual cortices of higher mammals (ferrets, cats or primates) and rodents, columnar vs. scattered organization, is paralleled by functional differences during development. These differences include for instance the time course of the development of fundamental functional properties and the relative contributions of visual experience and intrinsic factors.

Future studies will have to address the role of the inhibitory interneurons in the establishment of direction selectivity. Several studies using a combination of *in vivo* recording techniques and molecular tools to enable the identification of specific inhibitory cell subtypes investigated differences in visual response properties between inhibitory and excitatory neurons in V1 of adult mice (Kerlin et al., 2010; Ma et al., 2010; Runyan et al., 2010; Zariwala et al., 2011). Two recent studies using optogenetics demonstrated that interneurons are actively involved in the orientation and direction tuning of adult mouse V1 pyramidal neurons (Lee et al., 2012; Wilson et al., 2012). Furthermore, it has been shown in younger mice that parvalbumin-positive interneurons change their response preference during development. Their orientation tuning is well defined at eye opening and subsequently broadens with increasing amount of visual experience (Kuhlman et al., 2011). To investigate a possible causal role of the different subclasses of interneurons in the establishment of direction selectivity, optogenetic inactivation of the different subclasses of

interneurons could be combined with *in vivo* recordings of sensory-evoked responses in mice around eye opening. It would be interesting to see whether manipulating the activity pattern of interneurons, acutely or chronically over several days, has any effect on the formation of direction selectivity. The potential role of structural rearrangements at this developmental stage could be, for example, studied through the use of fluorescently tagged synaptic proteins, including those that may indicate the strength of synaptic connections (Lin et al., 2008). The application of transsynaptic tracing would allow probing the properties of the neurons that provide input to a cell of interest and could help identify changes in the synaptic connectivity (Wickersham et al., 2007).

6.2 Staged decline of neuronal function in an animal model of Alzheimer's disease *in vivo*

In vivo two-photon imaging using animal models has helped extending substantially the knowledge on the pathomechanisms underlying AD (Koffie et al., 2009; Kuchibhotla et al., 2008; Meyer-Luehmann et al., 2008; Spires et al., 2005). Several studies have revealed pathology-associated neuronal changes, including neuritic dystrophies and dendritic spine loss (Meyer-Luehmann et al., 2008; Spires et al., 2005), a disrupted dendritic calcium signaling (Kuchibhotla et al., 2008), aberrant spontaneous activity and absolute resting calcium concentration in glial cells (Kuchibhotla et al., 2009) as well as an increase in highly active and silent neurons (Busche et al., 2012; Busche et al., 2008).

In the study that is part of this thesis *in vivo* two-photon calcium imaging was used to analyze sensory-evoked neuronal signals in the APP23xPS45 mouse model. An age-dependent increase of Aβ in the visual cortex was found in these mice and, in parallel with this increase in Aβ, orientation and direction tuning of many neurons was substantially disrupted. Importantly, no tuning impairment of the visual cortex neurons was detected in transgenic mice that carry only a mutation in the *PSEN1*

gene, the PS45 mice. Thus, these results establish for the first time an Aβ-related cortical circuit dysfunction in a mouse model of AD.

The disruption in cortical functionality can be associated with distinct stages (Bublak et al., 2011), from stage I that is characterized by a normal behavioral performance, normal neuronal tuning properties, no plaque deposition and moderately increased levels of soluble Aβ to stage III, that is characterized by substantial behavioral impairment, disruption of visual cortex tuning and high levels of soluble Aβ and Aβ plaques. Stage II represents an intermediate stage. It is important to note that, while only 50% of the neurons in the primary visual cortex showed normal response sensitivities, the transgenic mice were still able to distinguish some forms of visual cues, in our case the drifting gratings differing by 45°. This indicates that even a diminished circuit of 'normal' neurons is in principal capable of sustaining normal behavioral performance, perhaps with the help of compensating mechanisms (Palop et al., 2006; Palop and Mucke, 2010). It should be furthermore mentioned that neuronal dysfunction in the visual thalamus may contribute to the impaired behavioral phenotype that was revealed through the visual discrimination test. The inconspicuous optomotor test, however, suggests that at least retina and superior colliculus exhibited rather regular function.

Interestingly, long-term functional impairments by traumatic and ischemic cortical lesions share likenesses with those observed in the Aβ containing cortical regions. For example, a strong enhancement in neuronal excitability has been observed in the vicinity of injuries in the cat visual cortex (Eysel and Schmidt-Kastner, 1991). This hyperexcitability was shown to cause both a rise in spontaneous and in visually-evoked activity. Moreover, in rodent models of stroke, hyperexcitability was found in the somatosensory cortex after the ischemic event (Murphy and Corbett, 2009). *In vivo* two-photon post-stroke calcium imaging of individual neurons showed that their limb selectivity was modified. Thus, neurons that were previously responding to stimulation of a single contralateral limb began to process incoming signals from multiple limbs (Winship and Murphy, 2008). Thus, Aβ plaques might be seen as multiple small cortical lesions, causing hyperexcitability and loss of functional selectivity.

Taken the presented results together, it becomes evident that Aβ-associated alterations in neuronal circuit function represent an important pathological process in

AD. Thus, as Aβ is produced by neurons in an activity-dependent manner (Cirrito et al., 2005), accumulation of Aβ and pathological neuronal activity may aggravate each other leading into a circle (Palop and Mucke, 2010). It is certainly worth mentioning that spontaneous and sensory-evoked aberrant neuronal activity has not only been found in different animal models of AD (Busche et al., 2012; Busche et al., 2008; Grienberger et al., 2012; Palop et al., 2007; Rudinskiy et al., 2012), but also in older non-demented persons with amyloid deposition (Sperling et al., 2009), making the assumption very tempting that disrupted neuronal activity due to the presence of Aβ is in fact a feature that can be generally found in AD patients. However, recent clinical trials targeting specifically Aβ provided rather disappointing results challenging the hypothesis that Aβ is the primary trigger for a cascade of events leading to AD (Hyman, 2011). In fact, many other parameters, such as tau-related pathology, vascular alterations, glial responses, inflammatory changes, oxidative stress, epigenetic determinants and finally environmental factors, may all have important co-pathogenic roles.

These evidences together lead to some important questions including: what are the actual molecular processes underlying the pathological activity patterns, what comes first, Aβ or neuronal dysfunction or are other factors playing a critical role in causing this dysfunction, and, finally, at what point are the alterations actually reversible? The answers to these questions will be certainly critical for future research on treatment approaches in Alzheimer's disease. Possible experiments could include the recording of neuronal activity over a long period of time using genetically-encoded calcium indicators (for review, see Looger and Griesbeck, 2011) as well as the examination of the electrophysiological and morphological properties of the hyperactive vs. hypoactive vs. normal neurons. Furthermore, it will be interesting to apply our assay of Aβ-related dysfunction for evaluating different forms of therapeutic approaches, such as active and passive vaccination (Huang and Mucke, 2012).

7 References

Ashe, K.H., Zahs, K.R. (2010) Probing the biology of Alzheimer's disease in mice. Neuron. 66, 631-645.

Averbeck, B.B., Latham, P.E., Pouget, A. (2006) Neural correlations, population coding and computation. Nat Rev Neurosci. 7, 358-366.

Bertram, L., Lill, C.M., Tanzi, R.E. (2010) The genetics of Alzheimer disease: back to the future. Neuron. 68, 270-281.

Bonhoeffer, T., Grinvald, A. (1991) Iso-orientation domains in cat visual cortex are arranged in pinwheel-like patterns. Nature. 353, 429-431.

Bublak, P., Redel, P., Sorg, C., Kurz, A., Förstl, H., Müller, H.J., Schneider, W.X., Finke, K. (2011) Staged decline of visual processing capacity in mild cognitive impairment and Alzheimer's disease. Neurobiol Aging. 32, 1219-1230.

Busche, M.A., Chen, X., Henning, H.A., Reichwald, J., Staufenbiel, M., Sakmann, B., Konnerth, A. (2012) Critical role of soluble amyloid-beta for early hippocampal hyperactivity in a mouse model of Alzheimer's disease. Proc Natl Acad Sci U S A. 109, 8740-8745.

Busche, M.A., Eichhoff, G., Adelsberger, H., Abramowski, D., Wiederhold, K.H., Haass, C., Staufenbiel, M., Konnerth, A., Garaschuk, O. (2008) Clusters of hyperactive neurons near amyloid plaques in a mouse model of Alzheimer's disease. Science. 321, 1686-1689.

Cang, J., Renteria, R.C., Kaneko, M., Liu, X., Copenhagen, D.R., Stryker, M.P. (2005) Development of precise maps in visual cortex requires patterned spontaneous activity in the retina. Neuron. 48, 797-809.

Chapman, P.F., White, G.L., Jones, M.W., Cooper-Blacketer, D., Marshall, V.J., Irizarry, M., Younkin, L., Good, M.A., Bliss, T.V., Hyman, B.T., Younkin, S.G., Hsiao, K.K. (1999) Impaired synaptic plasticity and learning in aged amyloid precursor protein transgenic mice. Nat Neurosci. 2, 271-276.

Cirrito, J.R., Yamada, K.A., Finn, M.B., Sloviter, R.S., Bales, K.R., May, P.C., Schoepp, D.D., Paul, S.M., Mennerick, S., Holtzman, D.M. (2005) Synaptic activity regulates interstitial fluid amyloid-beta levels in vivo. Neuron. 48, 913-922.

Colonnese, M.T., Kaminska, A., Minlebaev, M., Milh, M., Bloem, B., Lescure, S., Moriette, G., Chiron, C., Ben-Ari, Y., Khazipov, R. (2010) A conserved switch in sensory processing prepares developing neocortex for vision. Neuron. 67, 480-498.

Cronin-Golomb, A., Corkin, S., Rizzo, J.F., Cohen, J., Growdon, J.H., Banks, K.S. (1991) Visual dysfunction in Alzheimer's disease: relation to normal aging. Ann Neurol. 29, 41-52.

D'Amore, J.D., Kajdasz, S.T., McLellan, M.E., Bacskai, B.J., Stern, E.A., Hyman, B.T. (2003) In vivo multiphoton imaging of a transgenic mouse model of Alzheimer disease reveals marked thioflavine-S-associated alterations in neurite trajectories. J Neuropathol Exp Neurol. 62, 137-145.

Devanand, D.P., Michaels-Marston, K.S., Liu, X., Pelton, G.H., Padilla, M., Marder, K., Bell, K., Stern, Y., Mayeux, R. (2000) Olfactory deficits in patients with mild cognitive impairment predict Alzheimer's disease at follow-up. Am J Psychiatry. 157, 1399-1405.

Djordjevic, J., Jones-Gotman, M., De Sousa, K., Chertkow, H. (2008) Olfaction in patients with mild cognitive impairment and Alzheimer's disease. Neurobiol Aging. 29, 693-706.

Dräger, U.C. (1975) Receptive fields of single cells and topography in mouse visual cortex. J Comp Neurol. 160, 269-290.

Durham, D., Woolsey, T.A. (1977) Barrels and columnar cortical organization: evidence from 2-deoxyglucose (2-DG) experiments. Brain Res. 137, 169-174.

Duyckaerts, C., Potier, M.C., Delatour, B. (2008) Alzheimer disease models and human neuropathology: similarities and differences. Acta Neuropathol. 115, 5-38.

Elstrott, J., Anishchenko, A., Greschner, M., Sher, A., Litke, A.M., Chichilnisky, E.J., Feller, M.B. (2008) Direction selectivity in the retina is established independent of visual experience and cholinergic retinal waves. Neuron. 58, 499-506.

Elstrott, J., Feller, M.B. (2009) Vision and the establishment of direction-selectivity: a tale of two circuits. Curr Opin Neurobiol. 19, 293-297.

Espinosa, J.S., Stryker, M.P. (2012) Development and plasticity of the primary visual cortex. Neuron. 75, 230-249.

Eysel, U.T., Schmidt-Kastner, R. (1991) Neuronal dysfunction at the border of focal lesions in cat visual cortex. Neurosci Lett. 131, 45-48.

Fagiolini, M., Fritschy, J.M., Low, K., Mohler, H., Rudolph, U., Hensch, T.K. (2004) Specific GABAA circuits for visual cortical plasticity. Science. 303, 1681-1683.

Fagiolini, M., Katagiri, H., Miyamoto, H., Mori, H., Grant, S.G., Mishina, M., Hensch, T.K. (2003) Separable features of visual cortical plasticity revealed by N-methyl-D-aspartate receptor 2A signaling. Proc Natl Acad Sci U S A. 100, 2854-2859.

Fagiolini, M., Pizzorusso, T., Berardi, N., Domenici, L., Maffei, L. (1994) Functional postnatal development of the rat primary visual cortex and the role of visual experience: dark rearing and monocular deprivation. Vision Res. 34, 709-720.

Fernandez, R., Kavcic, V., Duffy, C.J. (2007) Neurophysiologic analyses of low- and high-level visual processing in Alzheimer disease. Neurology. 68, 2066-2076.

Gatz, M., Reynolds, C.A., Fratiglioni, L., Johansson, B., Mortimer, J.A., Berg, S., Fiske, A., Pedersen, N.L. (2006) Role of genes and environments for explaining Alzheimer disease. Arch Gen Psychiatry. 63, 168-174.

Girman, S.V., Sauve, Y., Lund, R.D. (1999) Receptive field properties of single neurons in rat primary visual cortex. J Neurophysiol. 82, 301-311.

Glabe, C.G. (2008) Structural classification of toxic amyloid oligomers. J Biol Chem. 283, 29639-29643.

Gordon, J.A., Stryker, M.P. (1996) Experience-dependent plasticity of binocular responses in the primary visual cortex of the mouse. J Neurosci. 16, 3274-3286.

Götz, J., Ittner, L.M. (2008) Animal models of Alzheimer's disease and frontotemporal dementia. Nat Rev Neurosci. 9, 532-544.

Grienberger, C., Konnerth, A. (2012) Imaging calcium in neurons. Neuron. 73, 862-885.

Grienberger, C., Rochefort, N.L., Adelsberger, H., Henning, H.A., Hill, D.N., Reichwald, J., Staufenbiel, M., Konnerth, A. (2012) Staged decline of neuronal function in vivo in an animal model of Alzheimer's disease. Nat Commun. 3, 774.

Haass, C., Selkoe, D.J. (2007) Soluble protein oligomers in neurodegeneration: lessons from the Alzheimer's amyloid beta-peptide. Nat Rev Mol Cell Biol. 8, 101-112.

Hall, A.M., Roberson, E.D. (2012) Mouse models of Alzheimer's disease. Brain Res Bull. 88, 3-12.

Hardy, J., Selkoe, D.J. (2002) The amyloid hypothesis of Alzheimer's disease: progress and problems on the road to therapeutics. Science. 297, 353-356.

Harris, K.D., Bartho, P., Chadderton, P., Curto, C., de la Rocha, J., Hollender, L., Itskov, V., Luczak, A., Marguet, S.L., Renart, A., Sakata, S. (2011) How do neurons work together? Lessons from auditory cortex. Hear Res. 271, 37-53.

Herzig, M.C., Winkler, D.T., Burgermeister, P., Pfeifer, M., Kohler, E., Schmidt, S.D., Danner, S., Abramowski, D., Sturchler-Pierrat, C., Burki, K., van Duinen, S.G., Maat-Schieman, M.L., Staufenbiel, M., Mathews, P.M., Jucker, M. (2004) Abeta is targeted to the vasculature in a mouse model of hereditary cerebral hemorrhage with amyloidosis. Nat Neurosci. 7, 954-960.

Hsieh, H., Boehm, J., Sato, C., Iwatsubo, T., Tomita, T., Sisodia, S., Malinow, R. (2006) AMPAR removal underlies Abeta-induced synaptic depression and dendritic spine loss. Neuron. 52, 831-843.

Huang, Y., Mucke, L. (2012) Alzheimer mechanisms and therapeutic strategies. Cell. 148, 1204-1222.

Hubel, D.H., Wiesel, T.N. (1959) Receptive fields of single neurones in the cat's striate cortex. J Physiol. 148, 574-591.

Hubel, D.H., Wiesel, T.N. (1962) Receptive fields, binocular interaction and functional architecture in the cat's visual cortex. J Physiol. 160, 106-154.

Hubel, D.H., Wiesel, T.N. (1968) Receptive fields and functional architecture of monkey striate cortex. J Physiol. 195, 215-243.

Hubel, D.H., Wiesel, T.N., Stryker, M.P. (1977) Orientation columns in macaque monkey visual cortex demonstrated by the 2-deoxyglucose autoradiographic technique. Nature. 269, 328-330.

Hübener, M. (2003) Mouse visual cortex. Curr Opin Neurobiol. 13, 413-420.

Huberman, A.D., Niell, C.M. (2011) What can mice tell us about how vision works? Trends Neurosci. 34, 464-473.

Huberman, A.D., Wei, W., Elstrott, J., Stafford, B.K., Feller, M.B., Barres, B.A. (2009) Genetic identification of an On-Off direction-selective retinal ganglion cell subtype reveals a layer-specific subcortical map of posterior motion. Neuron. 62, 327-334.

Hudspeth, A.J., Logothetis, N.K. (2000) Sensory systems. Curr Opin Neurobiol. 10, 631-641.

Hyman, B.T. (2011) Amyloid-dependent and amyloid-independent stages of Alzheimer disease. Arch Neurol. 68, 1062-1064.

Janus, C., Westaway, D. (2001) Transgenic mouse models of Alzheimer's disease. Physiol Behav. 73, 873-886.

Jaubert-Miazza, L., Green, E., Lo, F.S., Bui, K., Mills, J., Guido, W. (2005) Structural and functional composition of the developing retinogeniculate pathway in the mouse. Vis Neurosci. 22, 661-676.

Jeon, C.J., Strettoi, E., Masland, R.H. (1998) The major cell populations of the mouse retina. J Neurosci. 18, 8936-8946.

Jia, H., Rochefort, N.L., Chen, X., Konnerth, A. (2010) Dendritic organization of sensory input to cortical neurons in vivo. Nature. 464, 1307-1312.

Kamenetz, F., Tomita, T., Hsieh, H., Seabrook, G., Borchelt, D., Iwatsubo, T., Sisodia, S., Malinow, R. (2003) APP processing and synaptic function. Neuron. 37, 925-937.

Kay, J.N., De la Huerta, I., Kim, I.J., Zhang, Y., Yamagata, M., Chu, M.W., Meister, M., Sanes, J.R. (2011) Retinal ganglion cells with distinct directional preferences differ in molecular identity, structure, and central projections. J Neurosci. 31, 7753-7762.

Kerlin, A.M., Andermann, M.L., Berezovskii, V.K., Reid, R.C. (2010) Broadly tuned response properties of diverse inhibitory neuron subtypes in mouse visual cortex. Neuron. 67, 858-871.

Kerr, J.N., Denk, W. (2008) Imaging in vivo: watching the brain in action. Nat Rev Neurosci. 9, 195-205.

Kerr, J.N., Greenberg, D., Helmchen, F. (2005) Imaging input and output of neocortical networks in vivo. Proc Natl Acad Sci U S A. 102, 14063-14068.

Knowles, R.B., Wyart, C., Buldyrev, S.V., Cruz, L., Urbanc, B., Hasselmo, M.E., Stanley, H.E., Hyman, B.T. (1999) Plaque-induced neurite abnormalities: implications for disruption of neural networks in Alzheimer's disease. Proc Natl Acad Sci U S A. 96, 5274-5279.

Koffie, R.M., Meyer-Luehmann, M., Hashimoto, T., Adams, K.W., Mielke, M.L., Garcia-Alloza, M., Micheva, K.D., Smith, S.J., Kim, M.L., Lee, V.M., Hyman, B.T., Spires-Jones, T.L. (2009) Oligomeric amyloid beta associates with postsynaptic densities and correlates with excitatory synapse loss near senile plaques. Proc Natl Acad Sci U S A. 106, 4012-4017.

Krafft, G.A., Klein, W.L. (2010) ADDLs and the signaling web that leads to Alzheimer's disease. Neuropharmacology. 59, 230-242.

Krug, K., Akerman, C.J., Thompson, I.D. (2001) Responses of neurons in neonatal cortex and thalamus to patterned visual stimulation through the naturally closed lids. J Neurophysiol. 85, 1436-1443.

Kuchibhotla, K.V., Goldman, S.T., Lattarulo, C.R., Wu, H.Y., Hyman, B.T., Bacskai, B.J. (2008) Abeta plaques lead to aberrant regulation of calcium homeostasis in vivo resulting in structural and functional disruption of neuronal networks. Neuron. 59, 214-225.

Kuchibhotla, K.V., Lattarulo, C.R., Hyman, B.T., Bacskai, B.J. (2009) Synchronous hyperactivity and intercellular calcium waves in astrocytes in Alzheimer mice. Science. 323, 1211-1215.

Kuhlman, S.J., Tring, E., Trachtenberg, J.T. (2011) Fast-spiking interneurons have an initial orientation bias that is lost with vision. Nat Neurosci. 14, 1121-1123.

Kwan, A.C. (2008) What can population calcium imaging tell us about neural circuits? J Neurophysiol. 100, 2977-2980.

Lacor, P.N., Buniel, M.C., Furlow, P.W., Clemente, A.S., Velasco, P.T., Wood, M., Viola, K.L., Klein, W.L. (2007) Abeta oligomer-induced aberrations in synapse composition, shape, and density provide a molecular basis for loss of connectivity in Alzheimer's disease. J Neurosci. 27, 796-807.

Lee, S.H., Kwan, A.C., Zhang, S., Phoumthipphavong, V., Flannery, J.G., Masmanidis, S.C., Taniguchi, H., Huang, Z.J., Zhang, F., Boyden, E.S., Deisseroth, K., Dan, Y. (2012) Activation of specific interneurons improves V1 feature selectivity and visual perception. Nature. 488, 379-383.

Levick, W.R., Oyster, C.W., Takahashi, E. (1969) Rabbit lateral geniculate nucleus: sharpener of directional information. Science. 165, 712-714.

Li, S., Hong, S., Shepardson, N.E., Walsh, D.M., Shankar, G.M., Selkoe, D. (2009) Soluble oligomers of amyloid Beta protein facilitate hippocampal long-term depression by disrupting neuronal glutamate uptake. Neuron. 62, 788-801.

Li, Y., Fitzpatrick, D., White, L.E. (2006) The development of direction selectivity in ferret visual cortex requires early visual experience. Nat Neurosci. 9, 676-681.

Lin, M.Z., Glenn, J.S., Tsien, R.Y. (2008) A drug-controllable tag for visualizing newly synthesized proteins in cells and whole animals. Proc Natl Acad Sci U S A. 105, 7744-7749.

Ling, C., Schneider, G.E., Jhaveri, S. (1998) Target-specific morphology of retinal axon arbors in the adult hamster. Vis Neurosci. 15, 559-579.

Looger, L.L., Griesbeck, O. (2011) Genetically encoded neural activity indicators. Curr Opin Neurobiol. 22, 18-23.

Luo, L., Callaway, E.M., Svoboda, K. (2008) Genetic dissection of neural circuits. Neuron. 57, 634-660.

Ma, W.P., Liu, B.H., Li, Y.T., Huang, Z.J., Zhang, L.I., Tao, H.W. (2010) Visual representations by cortical somatostatin inhibitory neurons--selective but with weak and delayed responses. J Neurosci. 30, 14371-14379.

Marshel, J.H., Kaye, A.P., Nauhaus, I., Callaway, E.M. (2012) Anterior-Posterior Direction Opponency in the Superficial Mouse Lateral Geniculate Nucleus. Neuron. 76, 713-720.

Masland, R.H. (2001) The fundamental plan of the retina. Nat Neurosci. 4, 877-886.

May, P.J. (2006) The mammalian superior colliculus: laminar structure and connections. Prog Brain Res. 151, 321-378.

McHaffie, J.G., Stein, B.E. (1982) Eye movements evoked by electrical stimulation in the superior colliculus of rats and hamsters. Brain Res. 247, 243-253.

McKhann, G., Drachman, D., Folstein, M., Katzman, R., Price, D., Stadlan, E.M. (1984) Clinical diagnosis of Alzheimer's disease: report of the NINCDS-ADRDA Work Group under the auspices of Department of Health and Human Services Task Force on Alzheimer's Disease. Neurology. 34, 939-944.

Mesholam, R.I., Moberg, P.J., Mahr, R.N., Doty, R.L. (1998) Olfaction in neurodegenerative disease: a meta-analysis of olfactory functioning in Alzheimer's and Parkinson's diseases. Arch Neurol. 55, 84-90.

Metin, C., Godement, P., Imbert, M. (1988) The primary visual cortex in the mouse: receptive field properties and functional organization. Exp Brain Res. 69, 594-612.

Meyer-Luehmann, M., Spires-Jones, T.L., Prada, C., Garcia-Alloza, M., de Calignon, A., Rozkalne, A., Koenigsknecht-Talboo, J., Holtzman, D.M., Bacskai, B.J., Hyman, B.T. (2008) Rapid appearance and local toxicity of amyloid-beta plaques in a mouse model of Alzheimer's disease. Nature. 451, 720-724.

Murphy, T.H., Corbett, D. (2009) Plasticity during stroke recovery: from synapse to behaviour. Nat Rev Neurosci. 10, 861-872.

Niell, C.M., Stryker, M.P. (2008) Highly selective receptive fields in mouse visual cortex. J Neurosci. 28, 7520-7536.

O'Leary, D.D., Chou, S.J., Sahara, S. (2007) Area patterning of the mammalian cortex. Neuron. 56, 252-269.

Ohki, K., Chung, S., Ch'ng, Y.H., Kara, P., Reid, R.C. (2005) Functional imaging with cellular resolution reveals precise micro-architecture in visual cortex. Nature. 433, 597-603.

Ohl, F.W., Scheich, H. (2005) Learning-induced plasticity in animal and human auditory cortex. Curr Opin Neurobiol. 15, 470-477.

Palop, J.J., Chin, J., Mucke, L. (2006) A network dysfunction perspective on neurodegenerative diseases. Nature. 443, 768-773.

Palop, J.J., Chin, J., Roberson, E.D., Wang, J., Thwin, M.T., Bien-Ly, N., Yoo, J., Ho, K.O., Yu, G.Q., Kreitzer, A., Finkbeiner, S., Noebels, J.L., Mucke, L. (2007) Aberrant excitatory neuronal activity and compensatory remodeling of inhibitory hippocampal circuits in mouse models of Alzheimer's disease. Neuron. 55, 697-711.

Palop, J.J., Mucke, L. (2010) Amyloid-beta-induced neuronal dysfunction in Alzheimer's disease: from synapses toward neural networks. Nat Neurosci. 13, 812-818.

Petersen, C.C. (2007) The functional organization of the barrel cortex. Neuron. 56, 339-355.

Priebe, N.J., Ferster, D. (2012) Mechanisms of neuronal computation in mammalian visual cortex. Neuron. 75, 194-208.

Querfurth, H.W., LaFerla, F.M. (2010) Alzheimer's disease. N Engl J Med. 362, 329-344.

Rivlin-Etzion, M., Zhou, K., Wei, W., Elstrott, J., Nguyen, P.L., Barres, B.A., Huberman, A.D., Feller, M.B. (2011) Transgenic mice reveal unexpected diversity of on-off direction-selective retinal ganglion cell subtypes and brain structures involved in motion processing. J Neurosci. 31, 8760-8769.

Roberson, E.D., Mucke, L. (2006) 100 years and counting: prospects for defeating Alzheimer's disease. Science. 314, 781-784.

Rochefort, N.L., Garaschuk, O., Milos, R.I., Narushima, M., Marandi, N., Pichler, B., Kovalchuk, Y., Konnerth, A. (2009) Sparsification of neuronal activity in the visual cortex at eye-opening. Proc Natl Acad Sci U S A. 106, 15049-15054.

Rochefort, N.L., Narushima, M., Grienberger, C., Marandi, N., Hill, D.N., Konnerth, A. (2011) Development of direction selectivity in mouse cortical neurons. Neuron. 71, 425-432.

Rudinskiy, N., Hawkes, J.M., Betensky, R.A., Eguchi, M., Yamaguchi, S., Spires-Jones, T.L., Hyman, B.T. (2012) Orchestrated experience-driven Arc responses are disrupted in a mouse model of Alzheimer's disease. Nat Neurosci. 15, 1422-1429.

Runyan, C.A., Schummers, J., Van Wart, A., Kuhlman, S.J., Wilson, N.R., Huang, Z.J., Sur, M. (2010) Response features of parvalbumin-expressing interneurons suggest precise roles for subtypes of inhibition in visual cortex. Neuron. 67, 847-857.

Selkoe, D.J. (2002) Alzheimer's disease is a synaptic failure. Science. 298, 789-791.

Selkoe, D.J. (2004) Cell biology of protein misfolding: the examples of Alzheimer's and Parkinson's diseases. Nat Cell Biol. 6, 1054-1061.

Shankar, G.M., Li, S., Mehta, T.H., Garcia-Munoz, A., Shepardson, N.E., Smith, I., Brett, F.M., Farrell, M.A., Rowan, M.J., Lemere, C.A., Regan, C.M., Walsh, D.M., Sabatini, B.L., Selkoe, D.J. (2008) Amyloid-beta protein dimers isolated directly from Alzheimer's brains impair synaptic plasticity and memory. Nat Med. 14, 837-842.

Sheng, M., Sabatini, B.L., Südhof, T.C. (2012) Synapses and Alzheimer's disease. Cold Spring Harb Perspect Biol. 4.

Smith, S.L., Häusser, M. (2010) Parallel processing of visual space by neighboring neurons in mouse visual cortex. Nat Neurosci. 13, 1144-1149.

Sohya, K., Kameyama, K., Yanagawa, Y., Obata, K., Tsumoto, T. (2007) GABAergic neurons are less selective to stimulus orientation than excitatory neurons in layer II/III of visual cortex, as revealed by in vivo functional Ca^{2+} imaging in transgenic mice. J Neurosci. 27, 2145-2149.

Sperling, R.A., Laviolette, P.S., O'Keefe, K., O'Brien, J., Rentz, D.M., Pihlajamaki, M., Marshall, G., Hyman, B.T., Selkoe, D.J., Hedden, T., Buckner, R.L., Becker, J.A., Johnson, K.A. (2009) Amyloid deposition is associated with impaired default network function in older persons without dementia. Neuron. 63, 178-188.

Spires, T.L., Meyer-Luehmann, M., Stern, E.A., McLean, P.J., Skoch, J., Nguyen, P.T., Bacskai, B.J., Hyman, B.T. (2005) Dendritic spine abnormalities in amyloid precursor protein transgenic mice demonstrated by gene transfer and intravital multiphoton microscopy. J Neurosci. 25, 7278-7287.

Stern, E.A., Bacskai, B.J., Hickey, G.A., Attenello, F.J., Lombardo, J.A., Hyman, B.T. (2004) Cortical synaptic integration in vivo is disrupted by amyloid-beta plaques. J Neurosci. 24, 4535-4540.

Strittmatter, W.J., Saunders, A.M., Schmechel, D., Pericak-Vance, M., Enghild, J., Salvesen, G.S., Roses, A.D. (1993) Apolipoprotein E: high-avidity binding to beta-amyloid and increased frequency of type 4 allele in late-onset familial Alzheimer disease. Proc Natl Acad Sci U S A. 90, 1977-1981.

Sturchler-Pierrat, C., Abramowski, D., Duke, M., Wiederhold, K.H., Mistl, C., Rothacher, S., Ledermann, B., Burki, K., Frey, P., Paganetti, P.A., Waridel, C., Calhoun, M.E., Jucker, M., Probst, A., Staufenbiel, M., Sommer, B. (1997) Two amyloid precursor protein

transgenic mouse models with Alzheimer disease-like pathology. Proc Natl Acad Sci U S A. 94, 13287-13292.

Swann, J.W., Al-Noori, S., Jiang, M., Lee, C.L. (2000) Spine loss and other dendritic abnormalities in epilepsy. Hippocampus. 10, 617-625.

Syken, J., Grandpre, T., Kanold, P.O., Shatz, C.J. (2006) PirB restricts ocular-dominance plasticity in visual cortex. Science. 313, 1795-1800.

Tanzi, R.E., Bertram, L. (2005) Twenty years of the Alzheimer's disease amyloid hypothesis: a genetic perspective. Cell. 120, 545-555.

Thompson, K.G., Leventhal, A.G., Zhou, Y., Liu, D. (1994) Stimulus dependence of orientation and direction sensitivity of cat LGNd relay cells without cortical inputs: a comparison with area 17 cells. Vis Neurosci. 11, 939-951.

Trick, G.L., Silverman, S.E. (1991) Visual sensitivity to motion: age-related changes and deficits in senile dementia of the Alzheimer type. Neurology. 41, 1437-1440.

Tsai, J., Grutzendler, J., Duff, K., Gan, W.B. (2004) Fibrillar amyloid deposition leads to local synaptic abnormalities and breakage of neuronal branches. Nat Neurosci. 7, 1181-1183.

Valverde, F. (1968) Structural changes in the area striata of the mouse after enucleation. Exp Brain Res. 5, 274-292.

Van Hooser, S.D. (2007) Similarity and diversity in visual cortex: is there a unifying theory of cortical computation? Neuroscientist. 13, 639-656.

Van Hooser, S.D., Heimel, J.A., Chung, S., Nelson, S.B., Toth, L.J. (2005) Orientation selectivity without orientation maps in visual cortex of a highly visual mammal. J Neurosci. 25, 19-28.

Wagor, E., Mangini, N.J., Pearlman, A.L. (1980) Retinotopic organization of striate and extrastriate visual cortex in the mouse. J Comp Neurol. 193, 187-202.

Wang, L., Sarnaik, R., Rangarajan, K., Liu, X., Cang, J. (2010) Visual receptive field properties of neurons in the superficial superior colliculus of the mouse. J Neurosci. 30, 16573-16584.

Wang, Q., Burkhalter, A. (2007) Area map of mouse visual cortex. J Comp Neurol. 502, 339-357.

Wei, W., Nguyen, L.N., Kessels, H.W., Hagiwara, H., Sisodia, S., Malinow, R. (2010) Amyloid beta from axons and dendrites reduces local spine number and plasticity. Nat Neurosci. 13, 190-196.

Wesson, D.W., Borkowski, A.H., Landreth, G.E., Nixon, R.A., Levy, E., Wilson, D.A. (2011) Sensory network dysfunction, behavioral impairments, and their reversibility in an Alzheimer's beta-amyloidosis mouse model. J Neurosci. 31, 15962-15971.

White, L.E., Fitzpatrick, D. (2007) Vision and cortical map development. Neuron. 56, 327-338.

Wickersham, I.R., Lyon, D.C., Barnard, R.J., Mori, T., Finke, S., Conzelmann, K.K., Young, J.A., Callaway, E.M. (2007) Monosynaptic restriction of transsynaptic tracing from single, genetically targeted neurons. Neuron. 53, 639-647.

Wilson, N.R., Runyan, C.A., Wang, F.L., Sur, M. (2012) Division and subtraction by distinct cortical inhibitory networks in vivo. Nature. 488, 343-348.

Winship, I.R., Murphy, T.H. (2008) In vivo calcium imaging reveals functional rewiring of single somatosensory neurons after stroke. J Neurosci. 28, 6592-6606.

Yonehara, K., Ishikane, H., Sakuta, H., Shintani, T., Nakamura-Yonehara, K., Kamiji, N.L., Usui, S., Noda, M. (2009) Identification of retinal ganglion cells and their projections involved in central transmission of information about upward and downward image motion. PLoS One. 4, e4320.

Zariwala, H.A., Madisen, L., Ahrens, K.F., Bernard, A., Lein, E.S., Jones, A.R., Zeng, H. (2011) Visual tuning properties of genetically identified layer 2/3 neuronal types in the primary visual cortex of cre-transgenic mice. Front Syst Neurosci. 4, 162.

8 List of publications

8.1 Publications that are part of this thesis (see attachment)

Rochefort N.L., **Grienberger C.**, Konnerth A., *In vivo* two-photon calcium imaging using multicell bolus loading of fluorescent indicators, *Imaging in Neuroscience: A Laboratory Manual*, F. Helmchen and A. Konnerth, editors, Cold Spring Harbor Laboratory Press, NY, 2011.

Rochefort N.L.*, Narushima M.*, **Grienberger C.**, Marandi N., Hill D.N. and Konnerth A. (2011) Development of direction-selectivity in mouse cortical neurons, *Neuron* 71(3):425-432

Grienberger C., Konnerth A. (2012) Imaging calcium in neurons. *Neuron* 73(5):862-885.

Grienberger C.*, Rochefort N.L.*, Adelsberger H., Henning H.A., Hill D.N., Reichwald J., Staufenbiel M. and Konnerth A. (2012) Staged decline of neuronal function *in vivo* in an animal model of Alzheimer's Disease. *Nature Communications* 3: 774.

* Equal contribution

8.2 Other publications

Garaschuk O., Milos R.I., **Grienberger C.**, Marandi N., Adelsberger H., Konnerth A. (2006) Optical monitoring of brain function in vivo: from neurons to networks. Pflügers Arch 453:385-396

Adelsberger H., **Grienberger C.**, Stroh A., Konnerth A. In Vivo Calcium Recordings and Channelrhodopsin-2 Activation through an Optical Fiber, Imaging in Neuroscience: A Laboratory Manual, F. Helmchen and A. Konnerth, editors, Cold Spring Harbor Laboratory Press, NY, 2011.

Grienberger C.*, Adelsberger H.*, Stroh A., Milos R.I., Garaschuk O., Schierloh A., Nelken I., Konnerth A. (2012) Sound-evoked network calcium transients in mouse auditory cortex in vivo. J Physiol 590(Pt 4):899-918

* Equal contribution

8.3 Participation in scientific conferences

Invited Talk - 4th Neurowind Scientific Symposium, November 2nd-4th, 2012, Motzen, Germany. Staged decline of cortical circuit function in an animal model of Alzheimer's disease in vivo.

Annual meeting of the Society for Neuroscience, October 13th-17th, 2012, New Orleans, USA. Grienberger C., Chen X., Konnerth A. Complex spike bursts in CA1 hippocampal neurons in vivo require NMDA-R activation. Program No. 435.10/C53. 2012. Neuroscience Meeting Planner.

Annual meeting of the Society for Neuroscience, November 12th-16th, 2011, Washington, USA. Rochefort N.L., Narushima M., Grienberger C., Hill D.N., Konnerth A. Development of direction selectivity in mouse cortical neurons. Program No. 377.12/NN33. 2011 Neuroscience Meeting Planner.

Annual meeting of the Society for Neuroscience, November 13th-17th, 2010, San Diego, USA. Grienberger C., Rochefort N.L., Adelsberger H., Henning H.A., Staufenbiel M. and Konnerth A., Impaired orientation-tuning of visual cortical neurons in an animal model of Alzheimer's Disease Program No. 748.6/G9. 2010 Neuroscience Meeting Planner.

Conférence Jacques Monod, Imaging brain circuits in health and disease, June 30th-July 4th, 2010, Roscoff, France. Poster: Impaired orientation-tuning of visual cortical neurons in an animal model of Alzheimer's disease. Grienberger C., Rochefort NL., Adelsberger H., Henning HA., Staufenbiel M., Konnerth A.

9 Acknowledgment

I would like to warmly thank Prof. Arthur Konnerth for his exceptional mentorship and outstanding generosity, for giving me the fantastic chance to obtain top research training in neuroscience, for his encouragement to learn innovative techniques and for the numerous discussions that taught me how to assess critically scientific results. I would like to thank him for an atmosphere of ‘support and challenge’ (‘Fördern und Fordern’), which helped me learning the discipline and accuracy that is required for producing valuable and interesting scientific results.

I would like to thank Dr. Nathalie Rochefort for her excellent support, for teaching me the technique of two-photon microscopy, for her advices and help in solving difficult practical and theoretical problems, as well as for her great personal commitment.

I am profoundly grateful to Prof. Helmuth Adelsberger, who introduced me, at the beginning of my training, to the basics of neuroscience and calcium recordings. He has accompanied my work for my entire time in the lab and offered his great personal support, advice and encouragement.

I would also like to express my gratitude to Prof. Thomas Misgeld who is a wonderful role model. He is a great teacher and his excellent course on light microscopy has provided the indispensable basis for my understanding of imaging techniques.

I am also very thankful to all the colleagues at the Institute of Neuroscience for the exceptional atmosphere and the great team spirit.

Personal thanks go to my family, my parents and my siblings. They offered me their unconditional affection and support. This work has not been possible without them.

Project I - Imaging calcium in neurons

Published in **Neuron**, 2012, 73(5): 862-85

Neuron
Primer

Imaging Calcium in Neurons

Christine Grienberger[1] and Arthur Konnerth[1,*]
[1]Institute of Neuroscience, Technical University Munich, Biedersteinerstr. 29, 80802 Munich, Germany
*Correspondence: arthur.konnerth@lrz.tum.de
DOI 10.1016/j.neuron.2012.02.011

Calcium ions generate versatile intracellular signals that control key functions in all types of neurons. Imaging calcium in neurons is particularly important because calcium signals exert their highly specific functions in well-defined cellular subcompartments. In this Primer, we briefly review the general mechanisms of neuronal calcium signaling. We then introduce the calcium imaging devices, including confocal and two-photon microscopy as well as miniaturized devices that are used in freely moving animals. We provide an overview of the classical chemical fluorescent calcium indicators and of the protein-based genetically encoded calcium indicators. Using application examples, we introduce new developments in the field, such as calcium imaging in awake, behaving animals and the use of calcium imaging for mapping single spine sensory inputs in cortical neurons in vivo. We conclude by providing an outlook on the prospects of calcium imaging for the analysis of neuronal signaling and plasticity in various animal models.

Introduction

Calcium ions generate versatile intracellular signals that determine a large variety of functions in virtually every cell type in biological organisms (Berridge et al., 2000), including the control of heart muscle cell contraction (e.g., Dulhunty, 2006) as well as the regulation of vital aspects of the entire cell cycle, from cell proliferation to cell death (Lu and Means, 1993; Orrenius et al., 2003). In the nervous system, calcium ions preserve and, perhaps, even extend their high degree of versatility because of the complex morphology of neurons. In presynaptic terminals, calcium influx triggers exocytosis of neurotransmitter-containing synaptic vesicles (for review, see Neher and Sakaba, 2008). Postsynaptically, a transient rise of the calcium level in dendritic spines is essential for the induction of activity-dependent synaptic plasticity (Zucker, 1999). In another cellular subcompartment, the nucleus, calcium signals can regulate gene transcription (Lyons and West, 2011). Importantly, intracellular calcium signals regulate processes that operate over a wide time range, from neurotransmitter release at the microsecond scale to gene transcription, which lasts for minutes and hours (Berridge et al., 2003). Thus, the time course, the amplitude, and, most notably, the local action site in well-defined cellular subcompartments are essential determinants for the function of intracellular calcium signals. Therefore, not surprisingly, the direct investigation of the plethora of diverse neuronal calcium functions benefited enormously from the development of techniques allowing the visualization and quantitative estimation of the intracellular calcium signals.

Historically, the development of calcium imaging involved two parallel processes: the development and the continuous improvement of calcium sensors, and the development and the implementation of the appropriate instrumentation. Among the first calcium indicators used for monitoring the dynamics of cellular calcium signaling were bioluminescent calcium-binding photoproteins, such as aequorin (Ashley and Ridgway, 1968; Shimomura et al., 1962). A next class of calcium indicators is represented by the synthetic compound arsenazo III, an absorbance dye that changes its absorption spectrum as a function of bound calcium (Brown et al., 1975). While aequorin and arsenazo III provided important early insights into the calcium-dependent regulation of neuronal processes (Hallett and Carbone, 1972; Llinás and Nicholson, 1975; Stinnakre and Tauc, 1973), their implementation and use was often tedious, mostly because of problems with dye delivery. A true breakthrough was then the development of more sensitive and versatile fluorescent calcium indicators and buffers by Roger Tsien and colleagues (Tsien, 1980). These indicators were the result of the hybridization of highly calcium-selective chelators like EGTA or BAPTA with a fluorescent chromophore. The first generation of fluorescent calcium indicators consisted of quin-2, fura-2, indo-1, and fluo-3. Quin-2 is excited by ultraviolet light (339 nm) and was the first dye of this group to be used in biological experiments (Pozzan et al., 1982; Tsien et al., 1982). Quin-2, however, is not particularly bright and needs to be used at high intracellular concentrations to overcome cellular autofluorescence (Tsien, 1989). Instead, another dye of that family, namely fura-2 (Grynkiewicz et al., 1985), is in many ways superior to quin-2 and became very popular among neuroscientists. Fura-2 is usually excited at 350 and/or 380 nm and shows calcium-dependent fluorescence changes that are significantly larger than the ones produced by quin-2. Furthermore, fura-2 is particularly useful because it allows more quantitative calcium measurements involving the ratioing of the signals obtained with alternating the excitation wavelengths (Neher, 1995). Over the years, many more calcium indicators with a wide range of excitation spectra and affinities for calcium have been introduced. These include, among others, the Oregon Green BAPTA and fluo-4 dye families (Paredes et al., 2008). These dyes are widely used in neuroscience because they are relatively easy to implement and provide large signal-to-noise ratios. An important next breakthrough, again from the laboratory of Roger Tsien (Miyawaki et al., 1997), was the introduction of protein-based genetically encoded calcium indicators (GECIs). While the early types of GECIs had somewhat limited areas of application because of their slow response kinetics and low signal-to-noise ratios,

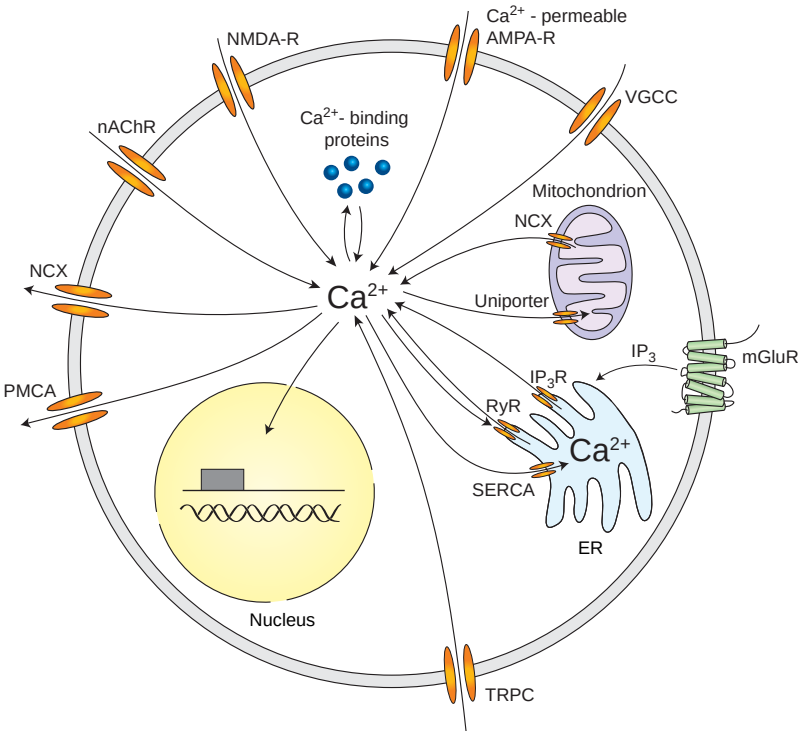

Figure 1. Neuronal Calcium Signaling
Sources of calcium influx are calcium-permeable α-amino-3-hydroxy-5-methyl-4-isoxazolepropionic acid (AMPA) and N-methyl-D-aspartate (NMDA) glutamate-type receptors, voltage-gated calcium channels (VGCC), nicotinic acetylcholine receptors (nAChR), and transient receptor potential type C (TRPC) channels. Calcium release from internal stores is mediated by inositol trisphosphate receptors (IP_3R) and ryanodine receptors (RyR). Inositol trisphosphate can be generated by metabotropic glutamate receptors (mGluR). Calcium efflux is mediated by the plasma membrane calcium ATPase (PMCA), the sodium-calcium exchanger (NCX), and the sarco-/endoplasmic reticulum calcium ATPase (SERCA). Also the mitochondria are important for neuronal calcium homeostasis

there had been tremendous progress in recent years (for review, see Looger and Griesbeck, 2011; Rochefort et al., 2008).

The development of the fluorescent indicators was paralleled by the development of new imaging instrumentation. This included the implementation of video imaging (Smith and Augustine, 1988; Swandulla et al., 1991), of CCD cameras (Connor, 1986; Lasser-Ross et al., 1991), and of high-speed confocal microscopy (Eilers et al., 1995) for calcium imaging. The high signal strength of the fluorescent probes in combination with these emerging technologies allowed for real-time fluorescence observations of biological processes at the single-cell level. A major advance was in the early 1990s the introduction of two-photon microscopy by Winfried Denk and colleagues (Denk et al., 1990) and its use for calcium imaging in the nervous system (Yuste and Denk, 1995). Two-photon imaging has revolutionized the field of calcium imaging (Helmchen and Denk, 2005; Svoboda and Yasuda, 2006) and is now used worldwide in many laboratories. In this Primer, after providing an introduction to neuronal calcium signaling, we describe what we believe to be the most important features for the application of calcium imaging in the nervous system. This includes the selection of the appropriate calcium indicator, the different dye-loading techniques, and the most popular imaging devices used for in vitro and in vivo calcium imaging. We focus on experiments performed in rodents as animal models, mostly because of their widespread use in the calcium imaging community.

Neuronal Calcium Signaling

Calcium is an essential intracellular messenger in mammalian neurons. At rest, most neurons have an intracellular calcium concentration of about 50–100 nM that can rise transiently during electrical activity to levels that are ten to 100 times higher (Berridge et al., 2000). Figure 1 summarizes some of the most important sources of neuronal calcium signaling, without taking into account their spatial organization into the different cellular subcompartments, such as dendritic arbor, cell body, or presynaptic terminal. At any given moment, the cytosolic calcium concentration is determined by the balance between calcium influx and efflux as well as by the exchange of calcium with internal stores. In addition, calcium-binding proteins such as parvalbumin, calbindin-D28k, or calretinin, acting as calcium buffers, determine the dynamics of free calcium inside neurons (Schwaller, 2010). Importantly, only free calcium ions are biologically active. There are multiple mechanisms underlying the calcium influx from the extracellular space, including voltage-gated calcium channels, ionotropic glutamate receptors, nicotinic acetylcholine receptors (nAChR), and transient receptor potential type C (TRPC) channels (Fucile, 2004; Higley and Sabatini, 2008; Ramsey et al., 2006). Calcium ions are removed from the cytosol by the plasma membrane calcium ATPase (PMCA) and the sodium-calcium exchanger (NCX) (Berridge et al., 2003). Calcium release from internal stores, mostly the endoplasmic reticulum (ER), is mediated by inositol trisphosphate receptors and ryanodine receptors (Berridge, 1998). Inositol trisphosphate can be generated in neurons, for example, by the activation of metabotropic glutamate receptors (Niswender and Conn, 2010). The high calcium level inside the ER is maintained by the sarco-/endoplasmic reticulum calcium ATPase (SERCA) that transports calcium ions from the cytosol to the lumen of the ER. In addition to the ER, mitochondria are also important for neuronal calcium homeostasis. Mitochondria can act as calcium buffers by taking calcium up during cytosolic calcium elevations through the calcium uniporter and then releasing it back to the cytosol slowly through sodium-calcium exchange (Duchen, 1999). In the following we describe in more detail some of the main contributors to neuronal calcium signaling.

Voltage-Gated Calcium Channels

VGCCs comprise a broad class of channels with a high selectivity for calcium ions and a wide variety of voltage-dependent

activation and inactivation features. Based on their threshold of voltage-dependent activation they are generally categorized into high- (HVA) and low-voltage-activated (LVA) channels (Catterall, 2000). HVA channels can be further subdivided based on their biophysical, pharmacological, and molecular features. They are traditionally classified as L-, P/Q-, N-, and R-type calcium channels. Which class of VGCC is present in a given neuron depends on the cell type and also on the cellular subcompartment. For example, T-type LVA channels are highly expressed in thalamic neurons (Coulter et al., 1989), while P-type channels are highly abundant in cerebellar Purkinje neurons (Usowicz et al., 1992). L-type and predominantly R-type VGCCs are abundant in dendritic spines of pyramidal neurons (Bloodgood and Sabatini, 2007b; Hoogland and Saggau, 2004; Yasuda et al., 2003), while P/Q- and N-type channels are found in many nerve terminals (Catterall, 2000; Plant et al., 1998). In the dendrites and spines of most central neurons, VGCCs are effectively activated by backpropagation of action potentials (Spruston et al., 1995; Waters et al., 2005) and by synaptically mediated depolarization of dendritic spines (Bloodgood and Sabatini, 2007b; Reid et al., 2001). As the recording of somatic calcium signals is widely used for the monitoring of action potential activity in vitro (Mao et al., 2001) and in vivo (Stosiek et al., 2003), it is important to note that here VGCCs are the main determinant of these signals. An important functional role of somatic calcium signals is the induction of gene transcription (Lyons and West, 2011).

N-Methyl-D-Aspartate Receptors

NMDA receptors are ionotropic glutamate receptors and mediate a major part of the postsynaptic calcium influx in the dendritic spines of various neuronal cell types, such as pyramidal neurons of the hippocampus (Bloodgood and Sabatini, 2007b; Kovalchuk et al., 2000; Sabatini et al., 2002; Yuste et al., 1999) and cortex (Koester and Sakmann, 1998; Nevian and Sakmann, 2006). This rise in spine calcium concentration is particularly important for the long-term modification of synaptic strength (Zucker, 1999). NMDA receptor channels are nonspecific cation channels that are permeable for sodium, potassium, and calcium ions. The fraction of calcium ions contributing to the total cation current through NMDA receptor channels is about 6%–12% (Burnashev et al., 1995; Garaschuk et al., 1996; Rogers and Dani, 1995; Schneggenburger et al., 1993). The specific properties of NMDA receptors are determined by the subunit composition, the phosphorylation status of the receptor, and, importantly, the membrane potential of the neuron. NMDA receptors are heteromers of the subunit NR1 in combination with NR2 subunits, like NR2A or NR2B (Bloodgood and Sabatini, 2007a). In CA1 hippocampal neurons, dendritic spines express preferentially either the NR2A or the NR2B subunits and, in a given neuron, the contribution of NR2A- or NR2B-mediated calcium influx to the spine calcium signal is variable among the different dendritic spines (Sobczyk et al., 2005). Another factor that determines the permeability for calcium ions is the phosphorylation status of the NMDA receptors. Thus, the permeability is enhanced by increased phosphorylation whereas dephosphorylation decreases calcium permeability (Skeberdis et al., 2006; Sobczyk and Svoboda, 2007). Finally, a critical modulator of NMDA receptor function is the membrane potential as it determines the efficacy of the voltage-dependent block of NMDA receptors by magnesium (Mayer et al., 1984; Nowak et al., 1984). The NMDA receptor-dependent ionic current increases as a function of increasing neuronal depolarization from the resting membrane potential.

Calcium-Permeable α-Amino-3-Hydroxy-5-Methyl-4-Isoxazolepropionic Acid Receptors

Calcium-permeable AMPA receptors are another class of ionotropic glutamate receptors. They are found in many forms of aspiny GABAergic neurons and characterized by the relative lack of the GluR2 receptor subunit (Jonas et al., 1994). GluR2-lacking AMPA receptors are permeable for sodium, calcium, potassium, but also zinc ions (Liu and Zukin, 2007). They exhibit fast gating kinetics (Geiger et al., 1995) and their inwardly rectifying I-V relationship arises from a voltage-dependent block due to intramolecular polyamines (Bowie and Mayer, 1995; Koh et al., 1995). The subunit composition varies in a synapse-specific manner within individual neurons (Tóth and McBain, 1998). This feature enables individual neurons to produce different types of responses to distinct synaptic inputs. Importantly, the presence of GluR2-containing and GluR2-lacking AMPA receptors is not static, but is highly regulated, particularly in response to neuronal activity (Liu and Cull-Candy, 2000). Thus, permeability of AMPA receptors to calcium is dynamic within a given neuron and can therefore contribute to synaptic plasticity mechanisms in aspiny neurons. For example, tetanic stimulation of synaptic inputs from excitatory neurons onto amygdala interneurons produces long-term potentiation (LTP) of the excitatory postsynaptic currents, a form of plasticity thought to be an important cellular mechanism for fear conditioning (Mahanty and Sah, 1998). This potentiation was independent of NMDA receptors and thus, in these aspiny neurons, calcium-permeable AMPA receptors probably mediate a major component of calcium signaling during LTP induction. In another type of aspiny neurons, namely, neocortical GABAergic cells, Goldberg et al. (2003) used two-photon calcium imaging to demonstrate that activation of single synapses creates highly localized dendritic calcium signals. The characteristics of this calcium signal are determined by the fast kinetics of calcium-permeable AMPA receptors, the fast local extrusion through the sodium-calcium-exchanger, and the buffering by calcium-binding proteins, such as parvalbumin (Goldberg et al., 2003). Thus, the authors concluded that the expression of calcium-permeable AMPA receptors in spine-lacking neurons might enable calcium signal compartmentalization in response to single synapse activation, somewhat similarly to synapses located on dendritic spines in excitatory neurons, a feature that may have important consequences for neuronal processing in aspiny neurons. In pyramidal neurons, calcium-permeable AMPA receptors have also been shown to be involved in some forms of synaptic calcium signaling. For example, sensory activation can promote an increase in calcium that is mediated by GluR2-lacking AMPA receptors at neocortical layer 4-layer 2/3 excitatory synapses. This calcium signal may represent an alternate source for activity-dependent calcium entry, facilitating the initiation of synaptic plasticity (Clem and Barth, 2006).

Metabotropic Glutamate Receptors

mGluRs are 7-transmembrane G protein-coupled receptors that are broadly distributed within the nervous system (Ferraguti and

Shigemoto, 2006). They are classified in group I, II, and III mGluRs, are expressed in a cell-type-specific fashion, and exert diverse physiological roles (Lüscher and Huber, 2010). The receptor classes differ in their downstream signaling mechanisms; for example, group I mGluRs are coupled to the G_q protein (Wettschureck and Offermanns, 2005). In cerebellar Purkinje neurons, the mGluR1 subtype of this group mediates both an increase in intracellular calcium as well as a TRPC3-dependent inward current (Hartmann et al., 2008). Upon activation of mGluR1, phospholipase C mediates the generation of IP_3, which binds to receptors in the ER and induces calcium release (Niswender and Conn, 2010).

Calcium Release from Internal Stores

Calcium release from internal stores is best known to occur from the ER through inositol trisphosphate receptors (IP_3Rs) and ryanodine receptors (RyRs) but may involve also other intracellular organelles (Rizzuto and Pozzan, 2006). Calcium signals resulting from calcium release from internal stores have been found in various types of neurons at different developmental stages (e.g., Llano et al., 2000; Lohmann et al., 2005; Manita and Ross, 2009). While IP_3-mediated calcium release is mostly triggered by neurotransmitters such as glutamate (see above), RyRs can be activated by elevations of the cytosolic calcium concentration. This RyR-mediated process of calcium-induced calcium release can contribute, for example, to the amplification of the calcium influx generated by action potential firing in neurons (Kano et al., 1995; Tsien and Tsien, 1990). Both IP_3Rs and RyRs are regulated by various intracellular factors, perhaps most importantly by calcium itself (Berridge, 1993). The regulatory action through calcium applies from both the lumenal or cytosolic side of the channels. This calcium dependence establishes a feedback loop coordinating calcium influx from the internal stores into the cytosol and plays, in the case of IP_3Rs, an essential role for synaptically evoked dendritic calcium waves in neocortical and other types of neurons (Larkum et al., 2003; Nakamura et al., 1999).

A major challenge in the analysis of the various sources of neuronal calcium signaling is that they are generally not active one at a time, but have overlapping activities with strong interactions. For example, during strong synaptic activity calcium influx through both NMDA receptors and VGCCs in the dendrites and spines of CA1 hippocampal neurons sum up nonlinearly and their combined signals acts as a coincidence detector between pre- and postsynaptic activity (Yuste and Denk, 1995). Similarly, in cerebellar Purkinje cells, the pairing of climbing fiber activity with parallel fiber bursts triggers dendritic calcium signals that are largest when activation of parallel fibers precedes the climbing fiber activation by a certain time window (Wang et al., 2000). In view of these complexities, calcium imaging is often indispensable for the dissection of the specific signaling mechanisms in neurons.

Calcium Indicators

Figure 2A describes the mode of action of the bioluminescent calcium indicator *aequorin*, derived from marine organisms, such as the luminescent jellyfish aequorea victoria (Shimomura et al., 1962). It is composed of the apoprotein apoaequorin and a noncovalently bound chromophore, a combination of coelenterazine and molecular oxygen (Ohmiya and Hirano, 1996). It contains three calcium-binding sites (Head et al., 2000). Upon binding of calcium ions, the protein undergoes a conformational change resulting in the oxidation of coelenterazine to coelenteramide and in the emission of a photon (about 470 nm wavelength) due to the decay of coelenteramide from the excited to the ground state (Ohmiya and Hirano, 1996). The rate of this reaction depends on the cytosolic calcium concentration (Cobbold and Rink, 1987). Importantly, aequorin is characterized by a high signal-to-noise ratio and a wide dynamic range being able to monitor changes in the cytosolic calcium concentration from 10^{-7} to 10^{-3} M (Bakayan et al., 2011; Brini, 2008). Bioluminescent recordings of calcium signals using aequorin do not require external illumination, thus avoiding problems such as phototoxicity, photobleaching, autofluorescence, and undesirable stimulation of photobiological processes (Xu et al., 2007). However, each molecule performs only one emission cycle and, unfortunately, the recharging process with the coelenterazine is relatively slow (Shimomura et al., 1993). Moreover, as the extracted form of aequorin cannot penetrate the plasma membrane of intact cells, it needs to be loaded into single cells by means of a micropipette (Chiesa et al., 2001). The cloning and sequence analysis of the aequorin cDNA has partially overcome this problem by enabling apoaequorin expression in a wide variety of cell types and from defined intracellular compartments (Inouye et al., 1985; Rizzuto et al., 1992). However, all these applications using expression of the apoprotein require exogenous supplementation of coelenterazine (Shimomura, 1997). In general, aequorin-based recording of calcium signals suffers from low quantum yield and low protein stability (Brini, 2008). In an attempt to increase the quantum yield, aequorin has been combined with different fluorescent proteins (Bakayan et al., 2011; Baubet et al., 2000; Martin et al., 2007; Rogers et al., 2005).

Figure 2B shows the structure of *fura-2*, a representative example for the fluorescent chemical (or synthetic) calcium indicators (Grynkiewicz et al., 1985). As already mentioned, fura-2 is a combination of calcium chelator and fluorophore. It is excitable by ultraviolet light (e.g., 350/380 nm) and its emission peak is between 505 and 520 nm (Tsien, 1989). The binding of calcium ions causes intramolecular conformational changes that lead to a change in the emitted fluorescence. With one-photon excitation, fura-2 has the advantage that it can be used with dual wavelength excitation, allowing the quantitative determination of the calcium concentration in a neuron of interest independently of the intracellular dye concentration (Tsien et al., 1985). Another advantage of fura-2 is that it has a good cross-section for two-photon calcium imaging (Wokosin et al., 2004; Xu et al., 1996). However, because of the broad absorption spectrum in conditions of two-photon excitation, ratiometric recording is not feasible. Instead, fura-2 and GFP labeling can be readily combined because of their well-separated absorption peaks. For example, fura-2 has been successfully used for two-photon calcium imaging in GFP-labeled interneurons (Sohya et al., 2007). While fura-2 emitted fluorescence decreases upon calcium elevations in conditions of two-photon imaging, the fluorescence of other indicators, like Oregon Green BAPTA and fluo, increases with calcium elevations inside cells. Perhaps

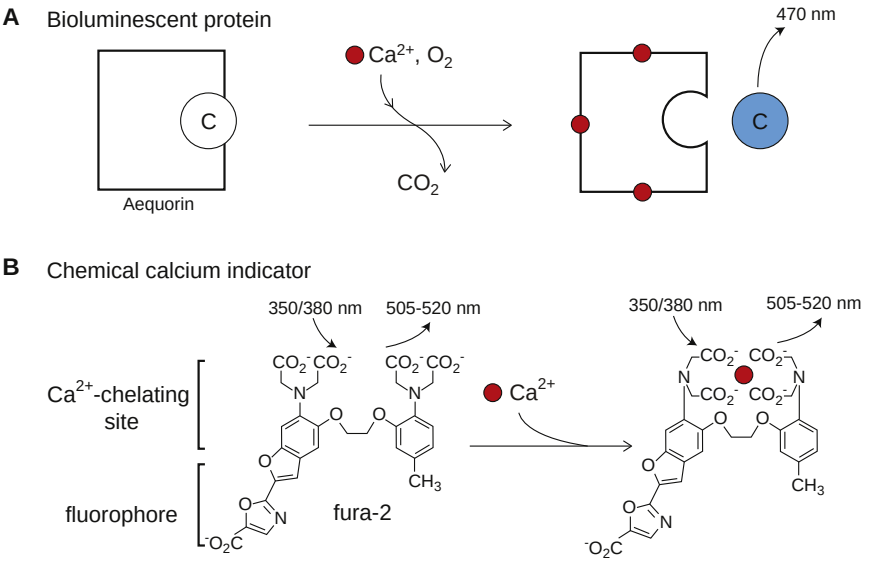

Figure 2. Calcium Indicators

(A) Bioluminescent protein. Binding of calcium ions to aequorin leads to the oxidation of the prosthetic group coelenterazine (C, left side) to colenteramide (C, right side). Colenteramide relaxes to the ground state while emitting a photon of 470 nm.

(B) Chemical calcium indicator. Fura-2 is excitable by ultraviolet light (e.g., 350/380 nm) and its emission peak is between 505 and 520 nm. The binding of calcium ions by fura-2 leads to changes in the emitted fluorescence.

(C) FRET-based genetically encoded calcium indicator (GECI). After binding of calcium ions to yellow cameleon 3.60 the two fluorescent proteins, ECFP (donor) and Venus (acceptor), approach. This enables Förster resonance energy transfer (FRET) and thus, the blue fluorescence of 480 nm decreases, whereas the fluorescence of 530 nm increases.

(D) Single-fluorophore genetically encoded calcium indicator (GECI). After binding of calcium to GCaMP conformational intramolecular changes lead to an increase in the emitted fluorescence of 515 nm.

these indicators became therefore quite popular for more noisy recording conditions like those present in vivo (e.g., Sato et al., 2007; Stosiek et al., 2003). Another major advantage of the chemical calcium indicators is that they exist in a membrane-permeable as well as in a membrane-impermeable form enabling their use in combination with a variety of different loading techniques (see section on dye-loading approaches) (Helmchen and Waters, 2002). Finally, these indicators are available at different calcium affinities and different spectral properties, allowing their simultaneous use (for overview of dye properties, see Johnson and Spence, 2010).

Genetically encoded calcium indicators (GECIs) come in two flavors, namely, those involving Förster resonance energy transfer (FRET) (Figure 2C) and the single-fluorophore ones (Figure 2D). For the illustration of the FRET-based GECIs we selected as a representative *Yellow Cameleon (YC) 3.60* (Nagai et al., 2004) (Figure 2C). FRET refers to a form of nonradiative energy transfer between an excited donor fluorophore and an acceptor fluorophore (Jares-Erijman and Jovin, 2003). Their distance has to be less than 10 nm in order to enable FRET. YC 3.60 consists of two fluorescent proteins and is part of the cameleon family of GECIs (Miyawaki et al., 1999; Miyawaki et al., 1997). It is composed of the enhanced cyan fluorescent protein (ECFP) as donor and the circularly permuted Venus protein as acceptor. These two proteins are connected by a linker sequence that consists of the calcium-binding protein calmodulin and the calmodulin-binding peptide M13 (Nagai et al., 2004). In the absence of calcium ions, the emission is dominated by the blue ECFP fluorescence (480 nm). Upon calcium binding, intramolecular conformational changes lead to reduction of the spatial distance between the two fluorescent proteins. Thus, the Venus protein is excited due to the occurrence of FRET and emits photons of about 530 nm. In practice, the blue fluorescence decreases, whereas the yellow fluorescence increases. The calcium signal is expressed as a ratio between the Venus and the ECFP fluorescence. To avoid possible interactions of calmodulin with endogenous binding partners, two different approaches were taken. In D3cpV-type GECIs, the calmodulin-M13-binding interfaces were mutated to strongly reduce the interactions with cellular targets (Palmer et al., 2006; Wallace et al., 2008). In another type of FRET-based calcium indicators, calmodulin is replaced by troponin C variants (Heim et al., 2007; Heim and Griesbeck, 2004; Mank et al., 2006; Mank et al., 2008). Troponin C is the calcium-binding protein in the cardiac and skeletal muscle cells and as such it does not have endogenous binding partners in neurons.

A prime representative of the single-fluorophore GECIs is the *GCaMP* family (Figure 2D) that is increasingly used for calcium

Table 1. Frequently Used Fluorometric Calcium Indicators

Name	Kd (nM)	Examples of In Vivo Applications	Representative References
Chemical Calcium Indicators			
Oregon Green BAPTA-1	170	Mouse neocortex, mouse hippocampus, mouse olfactory bulb, rat neocortex, rat cerebellum, ferret neocortex, cat neocortex, zebrafish	Dombeck et al., 2010; Sullivan et al., 2005; Ohki et al., 2005; Li et al., 2008; Greenberg et al., 2008; Rochefort et al., 2011; Sumbre et al., 2008; Wachowiak et al., 2004
Calcium Green-1	190	Mouse neocortex, mouse olfactory bulb, honeybee, turtle, zebrafish, rat neocortex	Dombeck et al., 2009; Oka et al., 2006; Galizia et al., 1999; Wachowiak et al., 2002; Brustein et al., 2003; Svoboda et al., 1997
Fura-2	140	Mouse neocortex	Sohya et al., 2007
Indo-1	230	Mouse neocortex	Stosiek et al., 2003
Fluo-4	345	Mouse neocortex, Xenopus larvae	Sato et al., 2007; Demarque and Spitzer, 2010
Rhod-2	570	Mouse neocortex, Zebrafish	Takano et al., 2006; Yaksi et al., 2009
X-rhod-1	700	Mouse neocortex	Nagayama et al., 2007
Genetically Encoded Calcium Indicators			
Camgaroo 1		Drosophila	Yu et al., 2003
Camgaroo 2		Drosophila, mouse olfactory bulb	Yu et al., 2003; Hasan et al., 2004
Inverse pericam	200	Zebrafish, mouse olfactory bulb	Hasan et al., 2004; Li et al., 2005
GCaMP 2	840	Mouse olfactory bulb, mouse cerebellum	Fletcher et al., 2009; Díez-García et al., 2005
GCaMP 3	660	Mouse neocortex, mouse hippocampus, Drosophila, C. elegans	Tian et al., 2009; Dombeck et al., 2010; Seelig et al., 2010; Tian et al., 2009
Yellow Cameleon 3.6	250	Mouse neocortex	Lütcke et al., 2010
Yellow Cameleon Nano	15–50	Zebrafish	Horikawa et al., 2010
D3cpV	600	Mouse neocortex	Wallace et al., 2008
TN-XL	2200	Drosophila, macaque	Mank et al., 2006; Heider et al., 2010
TN-L15	710	Mouse neocortex	Heim et al., 2007
TN-XXL	800	Drosophila, mouse neocortex	Mank et al., 2008; Mank et al., 2008

K_d dissociation constant in nM. K_d values taken from The Molecular Probes Handbook (chemical calcium indicators), Nagai et al., 2001 (Pericam), Tian et al., 2009 (GCaMP), Nagai et al., 2004 (YC 3.6), Horikawa et al., 2010 (YC-Nano), Palmer et al., 2006 (D3cpv), and Mank et al., 2008 (TN-based).

imaging in in vivo conditions (Chalasani et al., 2007; Dombeck et al., 2010; Fletcher et al., 2009; Wang et al., 2003). GCaMPs consist of a circularly permuted enhanced green fluorescent protein (EGFP), which is flanked on one side by the calcium-binding protein calmodulin and on the other side by the calmodulin-binding peptide M13 (Nakai et al., 2001). In the presence of calcium, calmodulin-M13 interactions elicit conformational changes in the fluorophore environment that lead to an increase in the emitted fluorescence (Nakai et al., 2001; Tian et al., 2009). Recently, after elucidating the structure of the GCaMP2, GCaMP3 was developed by protein engineering. It is improved concerning its signal-to-noise ratio, dynamic range, and response kinetics but it does not show reliable single action-potential-associated calcium signals (Tian et al., 2009; Yamada et al., 2011).

Table 1 gives an overview of the most widely used calcium indicators, including some representative references and examples of applications. As a final note, it is important to remain aware of the fact that calcium indicators measure changes in the cytosolic free calcium concentration. Free calcium ions are in equilibrium with the calcium ions that are bound to endogenous calcium buffers, such as parvalbumin, calbindin-D28k, and calretinin (Baimbridge et al., 1992). In calcium imaging experiments, the calcium indicators, except for aequorin, act as exogenous calcium buffer and thereby contribute to the total amount of cellular calcium buffer molecules (Helmchen et al., 1996). Therefore, adding calcium indicator will change the intracellular calcium dynamics (Neher and Augustine, 1992). In its simplest case, this perturbation is described by the "single-compartment model," which takes into account the endogenous calcium-binding proteins and the exogenous calcium indicator (Helmchen et al., 1996; Regehr and Tank, 1994). It is useful because it allows the estimation of the unperturbed calcium dynamics within the cytosol. For example, it has been successfully used for describing calcium dynamics in dendrites (Regehr and Tank, 1994). Notably, calcium indicators differ in their affinities for calcium (Mank and Griesbeck, 2008; Paredes et al., 2008) (Table 1). This is reflected in the dissociation constant (K_d) that describes the likelihood that a complex of indicator and calcium ion will separate. The K_d has a molar unit and corresponds to the calcium concentration at which half of the indicator molecules are bound to calcium. There are low- (e.g., fluo-5N) and high-affinity (e.g., Oregon Green BAPTA-1) calcium indicators. The measured K_d value is dependent on many parameters, including pH, temperature, and the presence of magnesium (Oliver et al., 2000). Consequently, it might vary between in vitro and in vivo condition. When designing an experiment, choosing the appropriate indicator in the appropriate

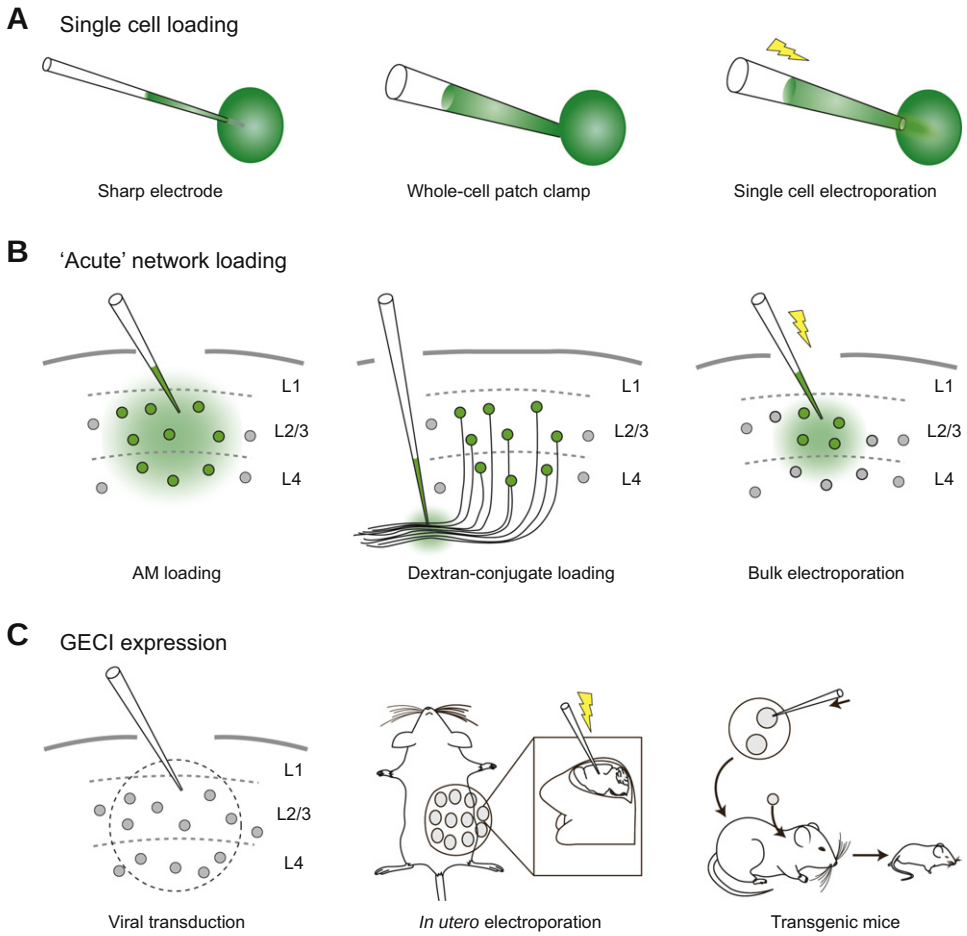

Figure 3. Dye-Loading Approaches

(A) Single-cell loading by sharp electode impalement (left panel), whole-cell patch-clamp configuration (middle panel), and single-cell electroporation (right panel). Note that these approaches can be used for loading of chemical and genetically encoded calcium indicators.

(B) "Acute" network loading. Many neurons are labeled simultaneously by acetoxymethyl ester (AM) loading (left panel), by loading with dextran-conjugated dye (middle panel), and by bulk electroporation (left panel).

(C) Expression of genetically encoded calcium indicators (GECI) by viral transduction (left panel), in utero electroporation (middle panel), and generation of transgenic mouse lines (right panel).

concentration is essential for the interpretation of the results. This decision should be guided by the scientific goals of the measurement and by the cells of interest. For example, fluorescent signals recorded with low-affinity indicators, which add little buffer capacity to the cell, reflect more accurately the change in the free cytosolic calcium concentration. These calcium signals will have faster rise and decay times than those recorded with high-affinity indicators (Helmchen et al., 1997). However, the use of low-affinity calcium indicators is limited by the need for sufficient sensitivity. This problem becomes increasingly significant when imaging in the noisy in vivo condition and when imaging small structures, such as dendritic spines. In these conditions, high-affinity calcium dyes remain, with all their limitations, the indicators of choice. Fortunately, calcium indicators with different properties can often be easily used complementarily in an experimental series. The new developments will certainly add up to our ability of deciphering the highly complex mechanisms of neuronal signaling in the intact nervous system.

Dye-Loading Approaches

The loading of calcium indicators into neurons depends on the type of calcium indicator, the biological preparation, and the specific scientific question. Figure 3A illustrates the three most widely used approaches for dye loading of individual neurons. In the early imaging experiments, chemical calcium dyes were delivered through sharp microelectrodes both in vitro (Jaffe et al., 1992) and in vivo (Svoboda et al., 1997) (Figure 3A, left panel). In more recent years, dye delivery through whole-cell patch-clamp micropipettes became the standard procedure for single-cell dye loading for many applications (Figure 3A, middle panel) (Eilers and Konnerth, 2009; Margrie et al., 2002). A particularly useful variant of this method involves in vivo whole-cell recordings that are performed under visual guidance using two-photon imaging by applying the "shadow patching" technique (Jia et al., 2011; Kitamura et al., 2008). This approach can be combined with the targeting of genetically identified cells expressing a fluorescent marker protein (Margrie et al., 2003).

Other attractive and relatively easy-to-use single-cell approaches are the targeted electroporation (Judkewitz et al., 2009; Kitamura et al., 2008; Nevian and Helmchen, 2007) or single-cell bolus loading (Helmchen et al., 1996). After approaching the soma of the target neuron with a micropipette in the electroporation experiments (Figure 3A, right panel), a few current pulses of appropriate polarity mediate dye delivery to the cell. This approach relies on two distinct mechanisms (for review, see De Vry et al., 2010). First, the electrical current disrupts the integrity of the cellular plasma membrane for a short period of time causing the transient formation of pores through which the dye molecules diffuse into the cell. Second, the current "pushes" the charged indicator molecules out of the pipette into the cell of interest. Importantly, this approach can be used for chemical calcium indicators as well as for DNA encoding for GECIs. A limitation of this method is that, because of the absence of the recording whole-cell microelectrode, the functional status of the neurons is not entirely clear. This can be overcome by combining electroporation of single cells with the cell-attached recordings involving the use of a second, fresh micropipette (Chen et al., 2010).

Single-cell calcium imaging is widely used for the analysis of basic mechanisms of calcium signaling in neurons and for the functional analysis of dendrites and spines and calcium signaling in terminals (for specific examples and application protocols see Helmchen and Konnerth, 2011). However, calcium imaging is also widely used for the monitoring of activity in local populations of interconnected neurons. Early application examples include the analyses of the circuitry of the cortex (Garaschuk et al., 2000; Yuste and Katz, 1991; Yuste et al., 1992), the hippocampus (Garaschuk et al., 1998), and the retina (Feller et al., 1996). This technique has also been successfully applied to identify synaptically connected neurons (Aaron and Yuste, 2006; Bonifazi et al., 2009; Kozloski et al., 2001). Furthermore, it has been used to analyze pathological forms of network activity, such as epileptiform events (Badea et al., 2001; Trevelyan et al., 2006). Here we focus on three widely used approaches for dye loading of neuronal populations in intact tissues. Figure 3B (left panel) illustrates an approach for the targeted bulk dye loading of membrane-permeable acetoxymethyl (AM) ester calcium dyes (Grynkiewicz et al., 1985) involving multicell bolus loading (MCBL) (Stosiek et al., 2003). This simple method consists of the injection of an AM calcium dye, for example Oregon Green BAPTA-1 AM, by means of an air pressure pulse to brain tissue, resulting in a stained area with a diameter of 300–500 μm (Connor et al., 1999; Garaschuk et al., 2006; Stosiek et al., 2003). The method involves the trapping of AM calcium dye molecules into cells, neurons and glia (Kerr et al., 2005; Stosiek et al., 2003), owing to the removal of the hydrophobic ester residue by intracellular esterases (Tsien, 1981). In neurons, the somatic calcium signals are mediated by calcium entry through voltage-gated calcium channels due to action potential activity. In the absence of effective voltage imaging approaches in vivo, imaging of calcium as surrogate marker for the spiking activity is widely used for the analysis of local neuronal circuits in vitro and in vivo (Kerr et al., 2005; Mao et al., 2001; Ohki et al., 2005; Stosiek et al., 2003). An unambiguous identification of astrocytes can be achieved by either morphological analysis (astrocytes appear much brighter and their processes can be well distinguished) or coloading with the glial marker sulforhodamine 101 (Nimmerjahn et al., 2004). Moreover, AM loading is combinable with transgenic mouse lines or virally transduced animals that have fluorescent labeling of specific cell types, for example interneurons (Runyan et al., 2010; Sohya et al., 2007; Tamamaki et al., 2003). It is important to note that Hirase et al. (2004) developed a method that allows the exclusive labeling of astrocytes with fluorescent calcium indicators in vivo and the accurate analysis of glia-specific mechanisms of calcium signaling (Takano et al., 2006; Wang et al., 2006).

Besides AM calcium dyes, dextran-conjugated chemical calcium indicators can also be employed for network loading, mostly by pressure injection to axonal pathways where the dye molecules are taken up and transported antero- and retrogradely to the axon terminals and the cell bodies, respectively (Figure 3B, middle panel) (Gelperin and Flores, 1997). This approach is suitable for the labeling of populations of neurons and has been successfully used to record calcium signals from axonal terminals in the mouse cerebellum and olfactory bulb (Kreitzer et al., 2000; Oka et al., 2006; Wachowiak and Cohen, 2001) as well as calcium signals in spinal cord neurons (O'Donovan et al., 2005). Finally, electroporation is used not only for the labeling of single cells (see above), but also for the dye loading of local neuronal networks (Figure 3B, right panel) (Nagayama et al., 2007). This is achieved by inserting a micropipette containing the dye in salt-form or as dextran-conjugate into the brain or spinal cord area of interest and by applying trains of electrical current pulses. As a result, the dye is taken up by nearby cell bodies and cellular processes, presumably mostly the dendrites. This approach has been successfully utilized in vivo in mouse neocortex, olfactory bulb, and cerebellum (Nagayama et al., 2010, 2007). Variants of this method were used for calcium imaging recordings in whole-mounted adult mouse retina (Briggman and Euler, 2011) and in the antennal lobe of the silkmoth (Fujiwara et al., 2009).

In recent years, GECIs have become a widely used tool in neuroscience (Looger and Griesbeck, 2011). There are different possibilities of expressing GECIs in neurons, of which viral transduction is probably at present the most popular one (Figure 3C, left panel). The viral construct with the GECI can be targeted to specific brain areas by means of stereotaxic injection (Cetin et al., 2006). In principal, lenti- (LV) (Dittgen et al., 2004), adeno- (Soudais et al., 2004), adeno-associated (AAV) (Monahan and Samulski, 2000), herpes-simplex (Lilley et al., 2001), and recently ΔG rabies (Osakada et al., 2011) viral vectors are used to introduce GECIs into the cells of interest. One of the practically relevant differences between the various viral vectors is the size of the genome carried by the virus. For example, LV can contain up to 9 kb whereas AAV-based vectors are restricted to a size of only 4.7 kb (Dong et al., 1996; Kumar et al., 2001). At present, LV- and AAV-based vectors are probably most widely used (Zhang et al., 2007). Both vectors are characterized by a high "multiplicity-of-infection" (many copy numbers of the viral genome per cell) and thus provide high expression levels over long periods of time with only little reported adverse effects (Davidson and Breakefield, 2003). Importantly, there are multiple approaches how to obtain target specificity to specific cell types.

Besides viral tropisms for definite cell types (Nathanson et al., 2009b), specificity for defined cell populations can arise from the use of cell-type-specific promoters (Chhatwal et al., 2007; Nathanson et al., 2009a; Shevtsova et al., 2005) or from the combination of transgenic cell-type-specific Cre recombinase driver mouse and rat lines (Gong et al., 2007; Witten et al., 2011) with a recombinase-dependent viral vector (Wirth et al., 2007). The latter restricts the research to rat and mouse as animal models whereas the other approaches are applicable also in other species. Second, in utero electroporation of DNA plasmids encoding for the GECI can be used and results, in contrast to viral delivery, in a relatively sparser labeling (Figure 3C, middle panel) (Mank et al., 2008). Since the early reports several years ago (e.g., Tabata and Nakajima, 2001), in utero electroporation has emerged as an efficient method to deliver DNA into cerebral precursor cells and, as consequence, neurons (Shimogori and Ogawa, 2008). Similar to single-cell and bulk electroporation techniques (see above), in utero electroporation uses an electrical field to drive negatively charged DNA molecules into the cells (De Vry et al., 2010). The sizes of the transfected area as well as the neuronal specificity depend on the embryo's age and the electrode configuration (Borrell et al., 2005; Langevin et al., 2007). It is important to stress that in utero electroporation has the advantage that there are no limitations concerning the size of the transfected gene of interest and that it can be applied in species where transgenic technology is not easily implemented. Finally, generating transgenic mice expressing GECIs has been a challenge and initial attempts failed (Figure 3C, right panel) (Heim and Griesbeck, 2004; Nagai et al., 2004; Pologruto et al., 2004; Tsai et al., 2003). The precise reason for these failures is not entirely understood, but one problem seemed to be that a substantial fraction of the indicator protein was not functional when expressed in a transgenic mouse line (Hasan et al., 2004). Nevertheless, mice expressing GECIs would tremendously facilitate many experiments and a few transgenic lines are meanwhile available (Kotlikoff, 2007). For example, Hasan et al. (2004) reported the generation of two transgenic mouse lines expressing under a tetracycline-inducible promoter either camgaroo-2 or inverse pericam that was used for calcium imaging in the mouse olfactory bulb in vivo. Fletcher et al. (2009) show odor-evoked calcium responses in a transgenic mouse line expressing GCamp2 and finally Heim et al. (2007) report the presence of glutamate-induced calcium transients in the soma and dendrites of CerTN-L15-expressing neurons.

Chemical and genetically encoded calcium indicators have specific advantages and limitations that need to be taken into account when designing a new experiment. For example, chemical calcium indicators are characterized by a very good signal-to-noise ratio and rapid kinetics (e.g., Helmchen et al., 1997; Hendel et al., 2008). In addition, the methods for targeted dye loading to single cells or small groups of cells are well established (Figures 3A and 3B) and these methods are similar in various mammalian species. One limitation is that it is difficult to specifically label genetically defined classes of neurons—for example, a particular class of interneurons. Another serious limitation is the difficulty to perform chronic recordings over several days (Andermann et al., 2010). For such applications, GECIs are superior as they are functional in neurons over long time periods (Andermann et al., 2010; Mank et al., 2008; Tian et al., 2009). For chronic imaging over weeks and months they can be combined with the chronic window (Holtmaat et al., 2009) or thinned skull preparations (Yang et al., 2010). Unlike chemical indicators, GECIs allow, in conjunction with cell-type-specific promoters (Bozza et al., 2004), targeting sequences (Mao et al., 2008; Shigetomi et al., 2010), and the use of the Cre-loxP system (Luo et al., 2008), recordings from molecularly defined cell types or even subcellular compartments. Moreover, the FRET-based GECIs are rather insensitive to brain pulsation and motion artifacts, a feature that is particularly beneficial for measurements in awake, behaving animals (Lütcke et al., 2010). However, the delivery of GECIs through pipette-based viral transduction or through in utero electroporation can sometimes lead to heterogeneous cellular labeling and/or to tissue damage. Another not yet fully solved problem is the slow kinetics of most GECIs due to their rather slow on and off rates (e.g., Hendel et al., 2008). Furthermore, there is the potential problem of cytotoxicity, which is observed after long-term expression of various GECIs (e.g., GCaMP3, D3cpV, and TN-XXL) through in utero electroporation or viral transduction (Tian et al., 2009). In addition, expression of GECIs in transgenic animals may reduce their calcium sensing performance (Hasan et al., 2004). Currently, there are intense ongoing research efforts that lead to rapid improvements and a continuously growing range of applications of the various GECIs (Looger and Griesbeck, 2011; Zhao et al., 2011).

Common Calcium Imaging Devices

The main types of instrumentation that are used for calcium imaging are summarized in Figure 4. The light-sensing device is usually attached to a microscope and combined, depending on the specific application, with an appropriate light source for the excitation of the calcium indicator dyes. Figures 4A and 4B illustrate schematically two calcium imaging approaches involving wide-field microscopy (for review, see Homma et al., 2009). In these cases, the light source is usually a mercury or xenon lamp, allowing an easy change of the excitation wavelengths. Switching between two excitation wavelengths, as used in excitation ratiometric measurements, can be performed rapidly by using, for example, a filter wheel or a regulated monochromatic light source. Excitation and emission light is usually separated by a dichroic mirror that is located within the microscope. Calcium imaging can be performed by using photodiode arrays (Figure 4A) (Ross and Werman, 1987), devices that are not very common anymore, as well as by intensified video cameras (Smith and Augustine, 1988), by charged coupled detector (CCD)-based cameras (Figure 4B), and increasingly by complementary metal-oxide-semiconductor (CMOS)-based cameras (Baker et al., 2005; Carlson and Coulter, 2008). The classical photodiode arrays consist of a set of photodiodes (typically 124–1020 elements) (Grinvald et al., 1981). Each photodiode represents one pixel. Photodiode arrays are characterized by very high dynamic range and high speed but have a rather poor spatial resolution. CCD-based cameras consist of an array of photodiodes that are densely packed on a chip. In contrast to the traditional photodiode arrays, however, CCD-based cameras involve a serial read-out of the signals. Modern

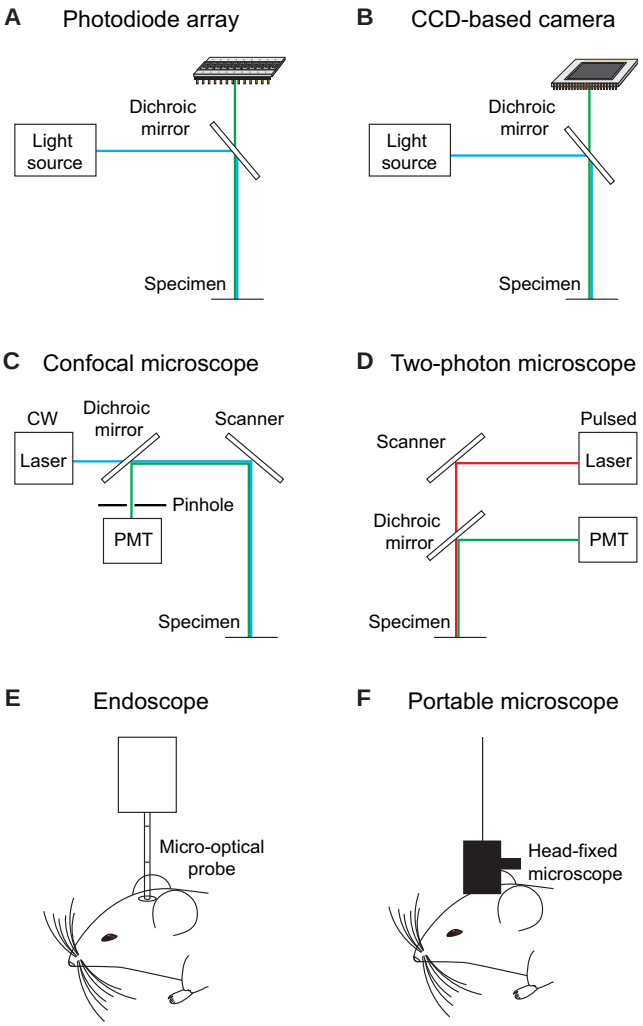

Figure 4. Common Imaging Devices

(A and B) Wide-field microcopy using a photodiode array (A) or a charged coupled device (CCD)-based (B) detection unit. In both cases the light source can be a mercury or xenon lamp. Excitation and emission light is separated by a dichroic mirror.

(C and D) Laser scanning microscopy. (C) Confocal microscopy using a continuous wave (CW) laser as light source. The excitation spot is steered across the specimen by a scanner. The emission light is descanned and reaches the photomultiplier tube (PMT) after passing a pinhole which is blocking out-of-focus fluorescence. Excitation and emission light is separated by a dichroic mirror. (D) Two-photon microscopy using a pulsed near-IR laser suitable for two-photon microscopy. The excitation spot is steered across the specimen by a scanner. The emitted fluorescence is detected by a photomultiplier tube (PMT).

(E and F) Imaging devices used for calcium imaging in non-head-fixed behaving animals. (E) Endoscopic approaches. (F) Portable head-mounted microscopes.

CCD-based cameras have an exquisitely high spatial and temporal resolution, but the noise level per pixel is high in some types of cameras. The contrast and resolution of wide-field microscopy based calcium imaging is limited by light scattering, especially when attempting to image neurons that are located deeper in the brain tissue (e.g., Denk and Svoboda, 1997). Therefore, these techniques are usually more appropriate for in vitro applications, like calcium imaging in neuronal cell cultures (Segal, 1995). In the in vivo situation, CCD-/CMOS-based cameras have found interesting applications in the imaging of large-scale calcium dynamics from the superficial cortical layers (e.g., Berger et al., 2007; Minderer et al., 2012).

Imaging calcium in neurons at deeper locations in the brain or spinal cord is usually performed by using confocal (Figure 4C) or two-photon microscopy (Figure 4D). Laser scanning microscopy generates the image by scanning a laser beam over the specimen (Lichtman and Conchello, 2005). The image is then created from the fluorescence values acquired for each pixel. Confocal microscopy usually involves one-photon excitation and, thus, the specimen is illuminated above and below the focal plane, which may cause photodamage in nonimaged regions. Figure 4C shows a schematic representation of a microscope design, in which optical sectioning is achieved by the implementation of a confocal aperture, a pinhole or slit, in an image-conjugated plane that blocks the out-of-focus fluorescence from reaching the detector unit (Conchello and Lichtman, 2005). Therefore, only photons that have been generated in the focal plane reach the photomultiplier tube (PMT). Unfortunately, the confocal aperture also blocks photons that are in fact generated in the focal plane, but are scattered on the way back through the optical pathway. This waste of photons becomes more and more critical when scattering increases when imaging deeper within the tissue. To compensate for the loss of ballistic photons due to scattering, excitation light power can be initially increased. This comes at the expense of increased tissue photodamage (in focus and out-of-focus), which can be high in confocal microscopy. Therefore, confocal microscopy, like wide-field microscopy, is mostly restricted to in vitro preparations, such as cultured neurons or brain slices. Finally, some applications benefit from the use of spinning disk-based confocal imaging involving the use of a rotating disk with a large number of fine pinholes, each of which acts each as an individual confocal aperture ("Nipkow disk") (Stephens and Allan, 2003; Takahara et al., 2011; Wilson, 2010). During imaging, many focal spots are illuminated simultaneously and the holes are arranged such that rotation of the disk causes the entire sample to be illuminated successively. A CCD-based camera can be used for image detection. Because of the simultaneous sampling from many focal points, this system can achieve higher image acquisition rates than laser scanning confocal microscopes.

The establishment of two-photon microscopy (Denk et al., 1990) that allows high-resolution and high-sensitivity fluorescence microscopy in highly scattering brain tissue in vivo was therefore an important step forward in the field of neuroscience (for review, see Svoboda and Yasuda, 2006) (Figure 4D). In two-photon microscopy, two low-energy near-IR photons cooperate to produce a transition from the ground to the excited state in a fluorescent molecule. This two-photon effect must occur within a femtosecond time window. Importantly, the process of two-photon absorption is nonlinear such that its rate depends on the second power of the light intensity. As a consequence, fluorophores are almost exclusively excited in a diffraction-limited focal volume ("localization of excitation") (Svoboda and Yasuda, 2006). Out-of-focus excitation and bleaching are strongly reduced. Only the development of pulsed

lasers suitable for two-photon microscopy, which are characterized by short pulses of about 100 fs duration containing a high photon density, allowed this process to be exploited for fluorescence microscopy in biological samples. Since excitation is bound to occur only in the focal spot, all fluorescence photons, ballistic or scattered, caught by the microscope and transmitted to the detecting photomultiplier (PMT) at a given time point can be used to generate the image (e.g., Denk et al., 1994). Another advantage is that the usual excitation wavelengths are within the near-IR spectrum, with a better tissue penetration than the visible light used in one-photon microscopy. This is due to the fact that these wavelengths are less scattered and less absorbed by natural chromophores present in the brain (e.g., Oheim et al., 2001). Importantly, the background fluorescence level is very low. For all those reasons, two-photon calcium imaging became the method of choice for recordings in deeper brain regions (for review, see Helmchen and Denk, 2005; Svoboda and Yasuda, 2006). Thus, cortical circuits can be examined in vivo with connections well preserved. Common two-photon lasers are tunable from 700 nm to 1000 nm or more and are suitable for the excitation of most commercially available fluorophores.

There are promising new approaches to extend the quality and versatility of two-photon microscopy and thereby two-photon calcium imaging. Inspired by imaging work that is performed in astronomy the use of adaptive optics in neurobiology aims at correcting in advance (before the illumination light is entering the optical pathway) for spherical aberrations that may distort the laser pulse and, therefore, may decrease the efficiency of two-photon imaging. These aberrations become increasingly more relevant with increasing depth (Girkin et al., 2009). The purpose of this correction is to obtain the optimal duration and shape of the laser pulse at the focal spot (Ji et al., 2010; Rueckel et al., 2006; Sherman et al., 2002). An interesting approach to increase depth penetration in two-photon microscopy is the use of regenerative laser amplifiers, which yields laser pulses with higher photon density, but at lower repetition rate. Because of the increased photon density, the probability for the two-photon effect is elevated, allowing, for example, the recording of sensory-evoked calcium signals from layer 5 pyramidal neuron somata in vivo (Mittmann et al., 2011). Present limitations of this technique are the lack of wavelength tunability and the decreased speed of imaging. Finally, the development of optical parametric oscillators (OPOs) pushes two-photon microscopy toward excitation wavelengths in the infrared spectrum (>1080 nm) and enables the efficient excitation of red-shifted fluorophores. As a result, it can increase imaging depth because of the reduced absorption and scattering at longer wavelengths (Andresen et al., 2009; Kobat et al., 2009). The speed of calcium imaging can be increased by the use of resonant galvo-scanners (Fan et al., 1999; Nguyen et al., 2001; Rochefort et al., 2009) or the use of acousto-optic deflectors (AOD) (Chen et al., 2011; Grewe et al., 2010; Iyer et al., 2006; Lechleiter et al., 2002; Otsu et al., 2008), especially when implementing the random-access imaging mode (Iyer et al., 2006; Kirkby et al., 2010; Otsu et al., 2008). Alternatively, multibeam confocal excitation also allows high imaging speed, but is restricted to superficial layers of nervous tissue and is so far only used in ex vivo preparations (Crépel et al., 2007). Next, there are increasing efforts for 3D imaging, involving various approaches (Cheng et al., 2011; Göbel and Helmchen, 2007; Göbel et al., 2007).

Even when using two-photon microscopy combined with improved depth penetration, imaging depth is ultimately limited (Andresen et al., 2009; Theer et al., 2003). A major limiting factor is the fluorescence generated by off-focus excitation light at the surface of the sample (Helmchen and Denk, 2005). Off-focus excitation increases necessarily because, in order to image deeper in the tissue, the laser intensity needs to be increased. This reduces dramatically the imaging quality. A not too elegant, but obvious approach for the recording from deeper brain regions is the mechanical removal of the covering tissue—for example the removal of cortical tissue located on top of the hippocampus (Dombeck et al., 2010; Mizrahi et al., 2004). Another way for the detection of calcium signals in deep brain structures involves microendoscopic approaches (Figure 4E). These include the insertion of optical fibers and fiber-like GRIN lenses alone or in conjunction with microprisms (Adelsberger et al., 2005; Chia and Levene, 2009; Flusberg et al., 2005; Grienberger et al., 2012; Jung et al., 2004; Levene et al., 2004; Murayama et al., 2007). GRIN-based microendoscopes, usually 350–1000 μm in diameter, comprise typically 1–3 gradient refractive index (GRIN) lenses that use internal variations in their refractive index to guide light to and back from the site of recording. Microendoscopes can, if coupled to an objective, project the scanning pattern into the focal plane, which lies inside the tissue and can also allow for changes in the axial position of the focal plane (Wilt et al., 2009). Their features, such as field-of-view size, numerical aperture, working distance, and physical length can be freely chosen. Complementary to these techniques, a dual-core microprobe that combines an optical core to locally excite and collect fluorescence with an electrolyte-filled core to record electrical signals has been developed (LeChasseur et al., 2011).

Finally, there are increasing efforts directed toward recordings in freely moving animals, involving the development of miniaturized head-mounted imaging devices (Engelbrecht et al., 2008; Flusberg et al., 2008; Helmchen et al., 2001; Sawinski et al., 2009). These imaging devices generally consist of two components (Figure 4F). A mobile component is fixed on the skull of the moving animal and contains the optical components. The other component is connected with the mobile one through an optical fiber and is usually immobile, containing the hard- and software for image recordings. The individual designs of these devices vary substantially. For example, whereas Helmchen et al. (2001) places nearly all components of a traditional microscope in the head-mounted mobile device (including objective, dichroic mirror, PMT, and scanner), Sawinski et al. (2009) included into the head-fixed component only the objective and the dichroic mirror. Recently, Ghosh et al. (2011) reported the development of a one photon-based and completely autochthone head-fixed camera-based device, usable for functional calcium measurements in freely moving animals.

Application Examples of Calcium Imaging

In the following we highlight several applications of calcium imaging obtained in mammalian neurons. It is needless to say that calcium imaging can be successfully performed in many

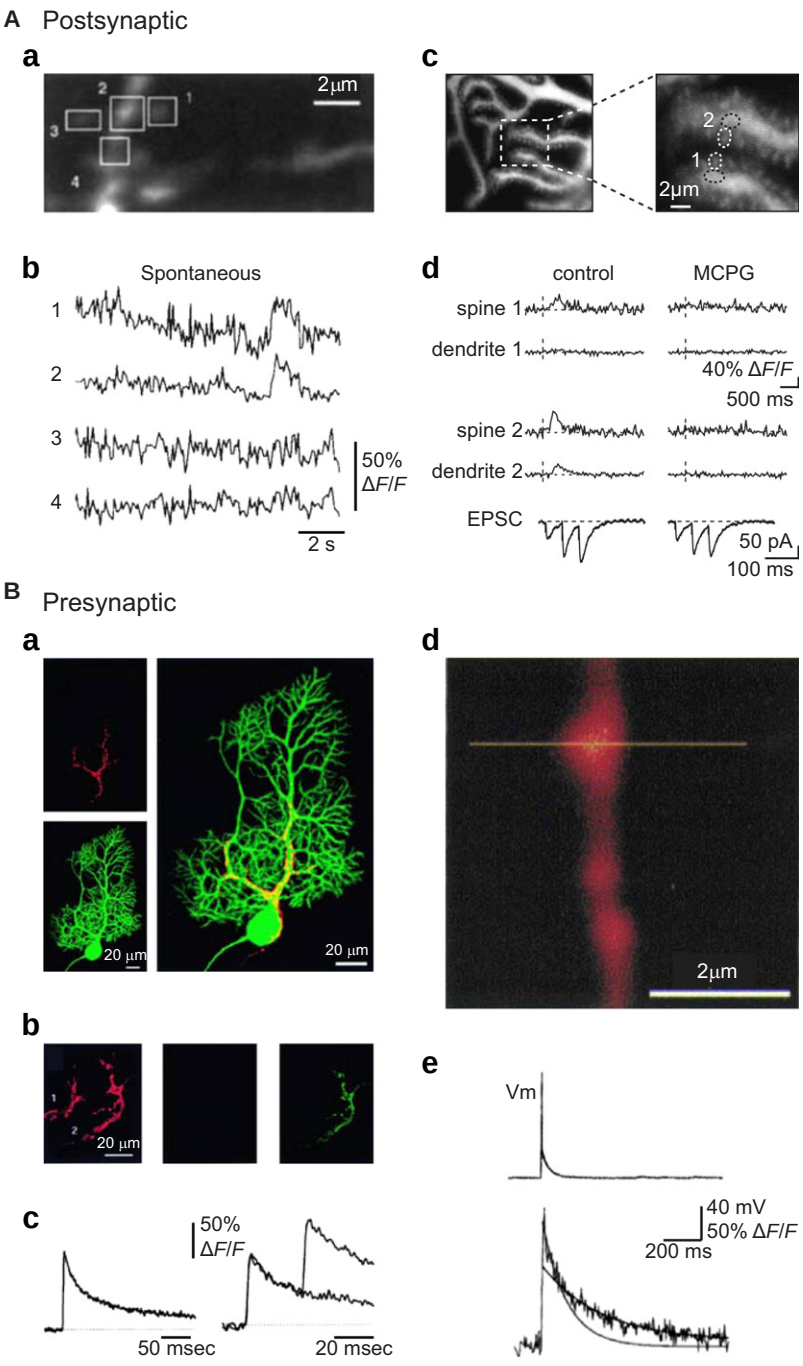

Figure 5. Calcium Imaging at the Synapse In Vitro

(A) Calcium imaging at the postsynaptic site. (Aa and Ab) Spine calcium signals recorded from a CA1 pyramidal neuron in a rat hippocampal slice preparation. (Aa) Image of a dendritic segment covered with many dendritic spines taken in a rat hippocampal slice. The CA1 pyramidal neuron was filled with Calcium Green-1 using the whole-cell patch-clamp configuration. The regions of interest (ROI) 1 and 3 contain dendritic spines whereas ROI 2 and ROI 4 are located on the dendritic shaft. (Ab) Calcium transients caused by spontaneous synaptic activity. Note that there are calcium transients only in ROI 1 and 2. Panels (Aa) and (Ab) adapted by permission from Yuste and Denk (1995). (Ac and Ad) Spine calcium signals recorded from a Purkinje cell in a cerebellar slice preparation. (Ac) Images of a Purkinje cell dendrite (left) with many dendritic spines (right). Dashed squares indicate ROIs (white dashed line: dendritic spine; black dashed line: dendritic shaft). (Ad) Fluorescence measurements taken from the ROIs shown in (Ac). In spine 1, the synaptic calcium transient was restricted to an individual spine. A large synaptic calcium transient was detected in spine 2 and a smaller signal occurred in the adjacent dendritic region. Note that MCPG (1mM), an antagonist of metabotropic glutamate receptors, completely blocked all observed calcium transients. The bottom traces illustrate the corresponding EPSCs evoked by a train of three stimuli (20 Hz). Panels (c) and (d) adapted by permission from Takechi et al. (1998).

(B) Calcium imaging at the presynaptic site. (Ba–Bc) Climbing fiber presynaptic terminals colabeled with the calcium indicator fluo-4 dextran and Texas red Dextran. (Ba) Confocal image stack of a Texas red dextran-labeled climbing fiber (left-upper panel) and the Purkinje cell onto which the climbing fiber synapses (left-lower panel). The Purkinje cell is labeled with the fluorescent marker Alexa Fluor 488. The overlay (right panel) shows the characteristic morphology of this synapse (the overlapping structures are shown in yellow). (Bb) Single section of a confocal image stack. Two climbing fibers are labeled with Texas red dextran (left). Image of these fibers at rest (middle) and during 20 Hz stimulation of fiber 2 (right) showing the fluo-4 channel. (Bc) Stimulus-evoked calcium transients for one (left) and two (right) stimuli. Panels (a)–(c) adapted with permission from Kreitzer et al. (2000). (Bd and Be) Calcium transients in a single bouton of a cortical layer 2/3 pyramidal neuron. (Bd) Presynaptic bouton of a cortical layer 2/3 pyramidal neuron loaded with Oregon Green BAPTA-1. Horizontal line indicates position of the line scan for the fluorescence measurements. (Be) The action potential evoked by somatic current injection is shown in the upper trace. Lower trace shows corresponding calcium transient recorded in the single bouton. Panels (d) and (e) adapted by permission from Koester and Sakmann (2000). Calcium signal amplitudes in all figures and throughout the text are given as the ratio of the relative fluorescence change and the baseline fluorescence (ΔF/F).

other species, including zebrafish (e.g., Brustein et al., 2003; Sumbre et al., 2008; Yaksi et al., 2009), *Aplysia* (e.g., Gitler and Spira, 1998), crayfish (e.g., Ravin et al., 1997), developing *Xenopus* (e.g., Demarque and Spitzer, 2010; Hiramoto and Cline, 2009; Tao et al., 2001), frog (e.g., Delaney et al., 2001), squid (e.g., Smith et al., 1993), turtle (e.g., Wachowiak et al., 2002), *Drosophila* (e.g., Seelig et al., 2010; Wang et al., 2003; Yu et al., 2003), blowfly (e.g., Elyada et al., 2009), and honey bee (e.g., Galizia et al., 1999).

Imaging Post- and Presynaptic Function In Vitro

Imaging dendritic spines, the postsynaptic site of excitatory connections in many neurons, was one of the first biological applications of two-photon calcium imaging. Combining two-photon microscopy with calcium imaging in hippocampal brain slices demonstrated that calcium signals can be restricted to dendritic spines (Figures 5Aa and 5Ab) (Yuste and Denk, 1995). The authors showed additionally that spine calcium signals were abolished by the application of the blockers of

glutamatergic transmission. Subsequently, synaptically evoked spine calcium signaling was found to be caused by a variety of other mechanisms, depending on the type of neuron (Denk et al., 1995; Finch and Augustine, 1998; Kovalchuk et al., 2000; Raymond and Redman, 2006; Wang et al., 2000). For example, Figures 5Ac and 5Ad show results obtained with confocal calcium imaging from mouse cerebellar parallel fiber-Purkinje cell synapses. The authors identified the calcium signaling mechanism of metabotropic glutamate receptor type 1-mediated transmission, involving calcium release from internal stores in dendrites and spines (Takechi et al., 1998). It has been shown that such a localized dendritic calcium signaling is essential for the induction of long-term synaptic depression (Konnerth et al., 1992; Wang et al., 2000), a possible cellular mechanism underlying motor learning in the cerebellum (Aiba et al., 1994; Bender et al., 2006).

Similarly, the calcium dynamics at presynaptic terminals are also accessible to calcium imaging (Delaney et al., 1989; Regehr and Tank, 1991a, 1991b; Rusakov et al., 2004; Smith et al., 1993). For this purpose, presynaptic terminals are loaded with an appropriate calcium indicator dye. A nice example is illustrated in Figures 5Ba–5Bc. To image climbing fibers in the cerebellar cortex, the authors injected the calcium indicator fluo-4 together with the morphological marker Texas red dextran upstream into the inferior olive of neonatal rats in vivo (Kreitzer et al., 2000). The dextran-conjugated calcium dye and Texas red were taken up by the inferior olive neurons and diffused within a few days through the climbing fibers to the cerebellar cortex. Thus, climbing fibers could be identified in subsequently prepared cerebellar slices. Purkinje cells were then counterlabeled with Alexa Fluor 488 (Figure 5Ba). This approach enabled the recording of stimulus-induced calcium signals in the presynaptic climbing fibers (Figures 5Bb and 5Bc). Another example involves calcium imaging of presynaptic boutons of cortical pyramidal neurons by Koester and Sakmann (2000), who combined two-photon microscopy and loading of the presynaptic terminals with Oregon Green BAPTA-1 via whole-cell recordings of the presynaptic neurons (Figure 5Bd and 5Be). Thus, they were able to record action-potential-evoked calcium signals in axonal boutons of cortical layer 2/3 pyramidal neurons of juvenile rats (Figure 5Be). These presynaptic calcium signals were found to be reliably inducible by only a single action potential. Interestingly, the large action-potential-evoked calcium signals were mostly localized to the boutons, but not the surrounding axonal segments.

Dendritic and Spine Calcium Signals In Vivo

In recent years, it has become possible to use two-photon microscopy for imaging dendritic and spine calcium signals in mammalian neurons in vivo (Chen et al., 2011; Helmchen et al., 1999; Jia et al., 2010; Svoboda et al., 1997; Svoboda et al., 1999; Takahashi et al., 2012; Waters and Helmchen, 2004). Svoboda et al. reported in 1997 for the first time dendritic calcium signals in vivo that were obtained from layer 2/3 rat pyramidal neurons (Figure 6A). They were able to record stimulus-associated dendritic calcium signals in barrel cortical neurons (Figures 6Ab–6Ad). The amplitude of these calcium signals was correlated to the number of action potentials and was largest in the proximal dendrite, suggesting that the signals were due to action

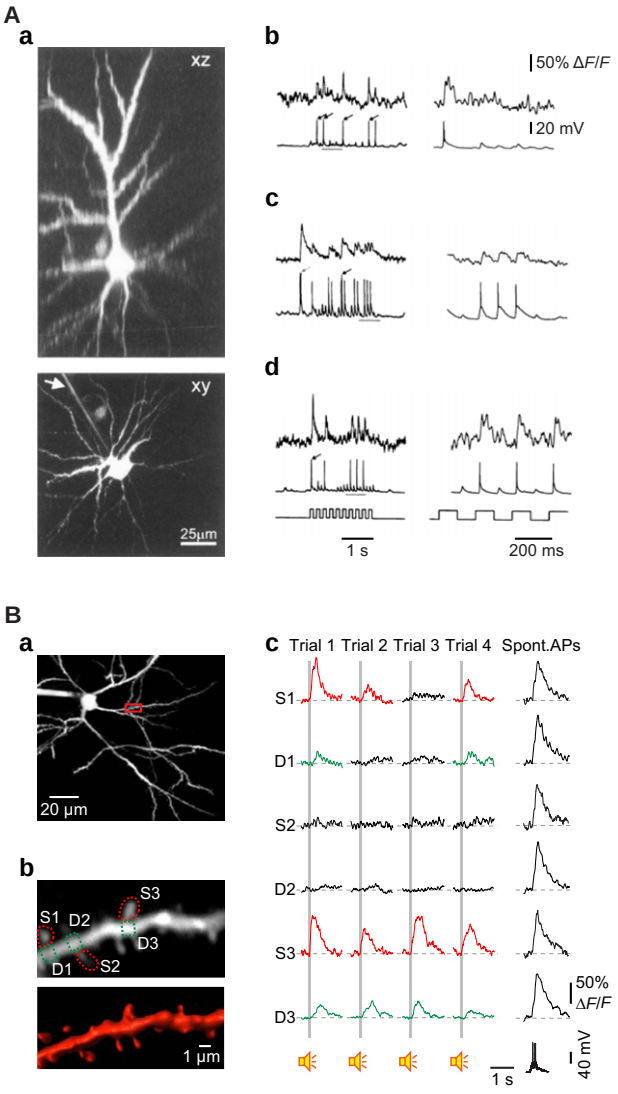

Figure 6. Dendritic and Spine Calcium Signals In Vivo

(A) Recording of dendritic calcium signals from a layer 2/3 pyramidal neuron of rat primary vibrissa cortex in vivo. (Aa) 3D reconstruction of a layer 2/3 pyramidal neuron labeled with calcium green-1. Upper panel: x-z projection. Lower panel: x-y projection. (Ab–Ad) Response of three representative cells to whisker stimulation. Left column: responses to an entire stimulus train (5 Hz, 2 s). Right column: expanded view showing only part of the entire stimulus period. Besides the recording of the membrane potential, recorded by a sharp microelectrode (lower trace), the dendritic calcium recording is shown (upper trace). The time course of the whisker stimulation is shown at the bottom. Recordings of dendritic calcium signals were performed at different positions in the apical dendrite for the three different cells. Adapted by permission from Svoboda et al. (1997).

(B) Recordings of spine calcium signals from a layer 2/3 pyramidal neuron of mouse primary auditory cortex in vivo. (Ba) Z-projection of a layer 2/3 neuron labeled with Oregon Green BAPTA-1. The red rectangle indicates the area magnified in (Bb). (Bb) Upper panel: image at high magnification of the dendritic segment indicated in (Ba). Three spines of interest (S1–S3) and the adjacent dendritic regions (D1–D3) are indicated by dashed lines. Lower panel: 3D image reconstruction of the dendritic segment. (Bc) Calcium transients evoked by auditory stimulation in spines (red) and corresponding dendritic shaft regions (green), as indicated in (Bb). Four consecutive trials of stimulation and a calcium transient evoked by backpropagation of action potentials (Spont. APs, spontaneous action potentials) are shown. Adapted by permission from Chen et al. (2011).

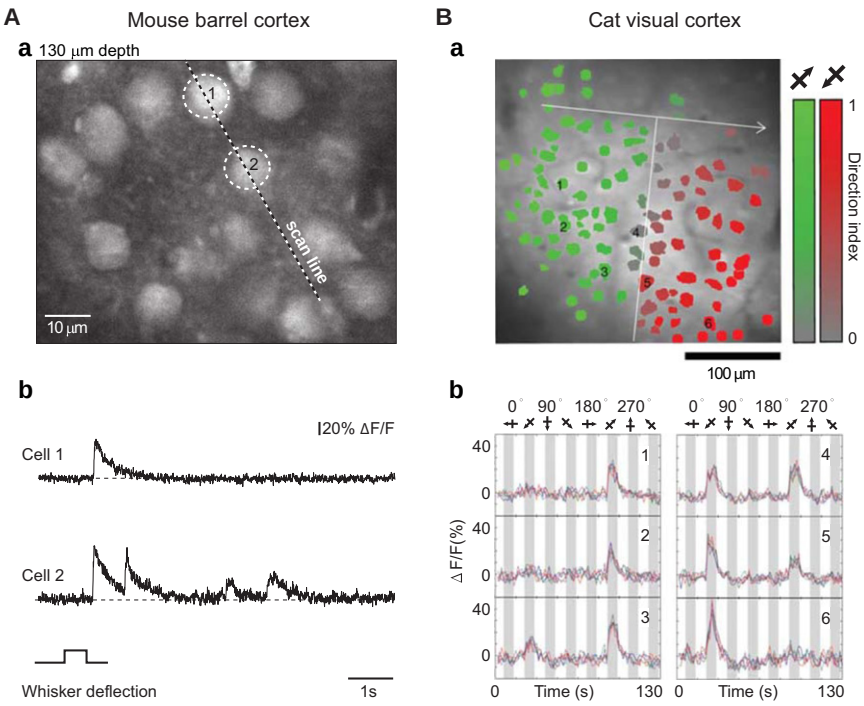

Figure 7. Circuit Analysis in Different Animal Models In Vivo

(A) In vivo recordings of calcium transients evoked by whisker deflection in mouse barrel cortex. (Aa) Image of layer 2/3 neurons in mouse barrel cortex in vivo. The calcium indicator Oregon Green BAPTA-1 AM was used for cell loading. (Ab) Line-scan recordings of calcium transients evoked in two neurons by a deflection of the majority of whiskers on the contralateral side of the mouse's snout. The position of the scanned line and the neurons analyzed are indicated in (a). Adapted by permission from Stosiek et al. (2003).

(B) In vivo recordings of calcium transients evoked by visual stimulation (drifting square-wave gratings of eight different directions separated each by 45°) in cat primary visual cortex. (Ba) Cell-based direction map; the color specifies the preferred direction for each cell according to its individual direction index (see color scale on right; green, 225°; red, 45°). The cells responding to both 45° and 225° are displayed as gray. The vertical white line below the arrow indicates approximate position of the direction discontinuity. (Bb) Single-trial time courses of six individual cells in response to drifting grating stimulation (indicated as 1–6 in Ba). Adapted by permission from Ohki et al. (2005).

potential back-propagation into the dendritic arbor. One role of these dendritic signals may be the amplification of calcium signals that are evoked by synaptic activity (Helmchen et al., 1999; Svoboda et al., 1997; Svoboda et al., 1999; Waters and Helmchen, 2004; Waters et al., 2003).

Besides the study of such backpropagation-evoked calcium signals, it became recently feasible to use calcium imaging for the investigation of the spatial and temporal distribution of synaptic inputs to cortical neurons in vivo (Chen et al., 2011; Jia et al., 2010; Varga et al., 2011). In these studies, the membrane potential of the neurons was slightly hyperpolarized to prevent action potential firing. Thus, it became possible to isolate local dendritic or even single spine calcium signals in response to sensory stimulation. The local calcium signals reflected specific sensory-evoked synaptic input sites on the dendrites of the respective neurons. Figure 6B shows, for example, the sensory-evoked calcium signals recorded by Chen et al. (2011) in the spines and dendrites of mouse layer 2/3 auditory cortex neurons (Figures 6Ba and 6Bb). The stable recording of such single spine calcium signals in vivo required the development of a new method named low-power temporal oversampling (LOTOS). LOTOS helps to increase the yield in fluorescence signal and to reduce phototoxic damage (Chen et al., 2011). The sound-evoked spine calcium signals were found to be, in agreement with previous in vitro studies (e.g., Yuste and Denk, 1995), mostly compartmentalized in dendritic spines (Figure 6Bc). Importantly, calcium imaging enabled the recording of many synaptic sites at the same time and, therefore, to map functionally the synaptic input sites of a specific neuron. While these studies relied on the use of chemical calcium indicators (Jia et al., 2011), we expect that in the future GECIs will be widely used to investigate dendritic calcium signals. A proof-of-principle study demonstrated already a few years ago that, using a transgenic mouse line expressing the Troponin-C-based calcium indicator CerTN-L15, it was possible to record glutamate-induced calcium signals from dendrites in vivo (Heim et al., 2007). Another approach for recording dendritic calcium signals in vivo involves the use of a so called "fiberoptic periscope" (Murayama and Larkum, 2009; Murayama et al., 2007). The periscope is composed of a GRIN lens and a micro-prism angled at 90°, which is inserted in the cortex. The method combines targeted AM loading of apical dendrites of cortical layer 5 pyramidal neurons with a chemical calcium indicator with horizontal fluorescence collection from the top cortical layers (Murayama et al., 2009). It uses one-photon excitation and, strictly speaking, it is not a conventional imaging method as it collects the average fluorescence from many layer 5 dendrites without generating an image. However, it is applicable in anesthetized as well as in awake behaving mice, and there are attempts to combine the periscope approach with two-photon imaging (Chia and Levene, 2009).

Circuit Analysis in Different Animal Models In Vivo

Combining two-photon microscopy with AM calcium dye loading allows the functional analysis of local cortical circuits (Greenberg et al., 2008; Ohki et al., 2005; Stosiek et al., 2003). This approach has been applied in many different animal models, including mouse, rat, cat, and ferret (Kerr et al., 2007; Li et al., 2008; Ohki et al., 2006; Rochefort et al., 2011). Figure 7A shows the first example of such an in vivo two-photon imaging experiment. The authors investigated the responsiveness of mouse barrel cortical neurons to whisker stimulation and demonstrated the feasibility of calcium imaging for the

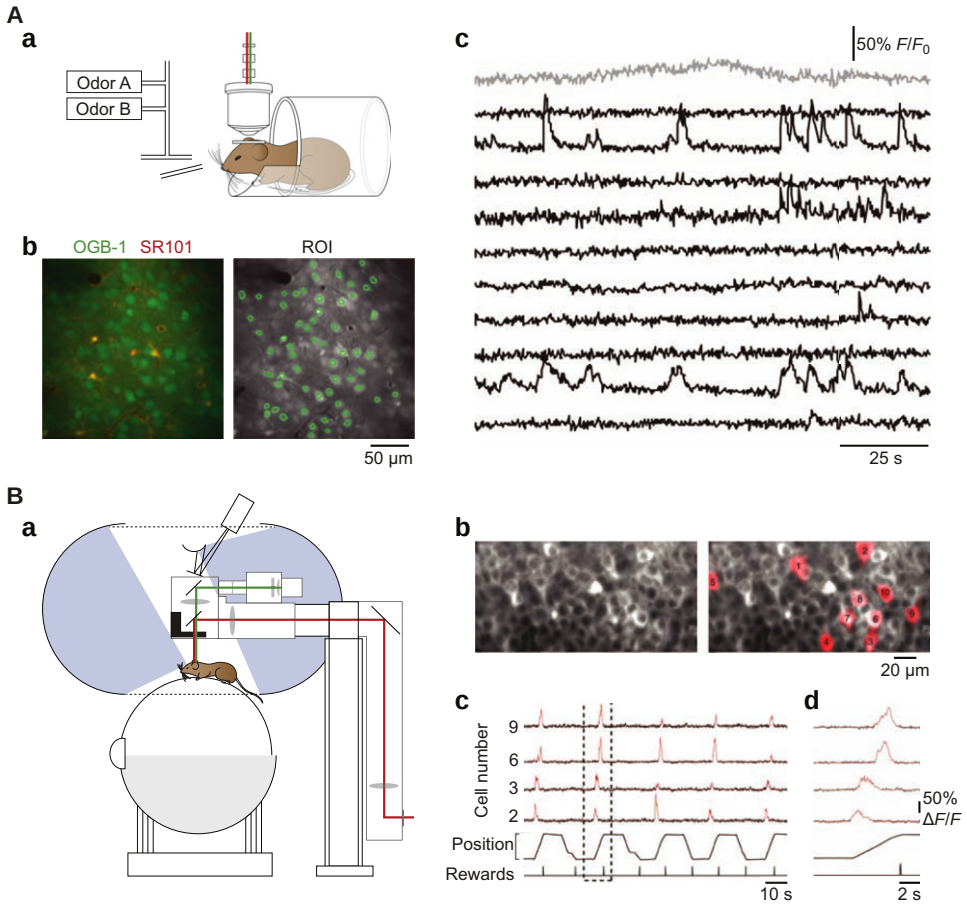

Figure 8. Calcium Imaging in the Behaving Animal

(A) Calcium imaging in the motor cortex of head-fixed mice engaged in an olfactory-related choice behavior with lick/no lick response. (Aa) Scheme of the experimental set-up showing a head-fixed mouse under a two-photon microscope while performing the task. The task consists of the differentiation between odor A and B. The mouse is trained to lick only in response to one of the two odors. (Ab) Two-photon image of layer 2/3 cells. Left, overlay of sulforhodamine 101 (SR101, red) and Oregon Green BAPTA-1 AM (green). Astrocytes are labeled by both dyes and thus appear yellow, whereas neurons are green. Right, regions of interest (ROI, green) overlaid on the Oregon Green BAPTA-1 channel. (Ac) Example of spontaneous calcium traces from ten neurons (black) and one astrocyte (gray). Panels (Ab) and (Ac) adapted by permission from Komiyama et al. (2010).

(B) Calcium imaging of place cells in the CA1 hippocampal region of mice which are placed on a spherical treadmill. (Ba) Experimental set-up: it consists of a spherical treadmill, a virtual reality apparatus (with projector and surrounding screens) and a custom-made two-photon microscope. (Bb) Two-photon images of neuron cell bodies in stratum pyramidale of CA1 labeled with the genetically encoded calcium indicator GCaMP3 (left). (Bc) Imaging CA1 place cells while the mouse is running along a virtual linear track. Calcium traces are shown in black. The respective regions of interest are shown in (Bb), right panel. Red traces indicate significant calcium transients. In parallel, the position of the mouse along the virtual linear track is recorded. Reward times are shown at the bottom. (Bd) Expanded view of the period indicated by the dashed box in (c). Panels (b)–(d) adapted by permission from Dombeck et al. (2010).

recording of action-potential-evoked activity with single-cell resolution (Stosiek et al., 2003). The AM loading approach has also been used in the cat to investigate the orientation preference of visual cortex neurons (Ohki et al., 2005) (Figure 7B). This study showed that orientation columns in the cat visual cortex are segregated with an extremely high spatial precision so that, even at the single cell level, areas of neurons with different orientation preference can be precisely distinguished. Examples of further studies using two-photon calcium imaging include recordings from mouse barrel (Sato et al., 2007), visual (Smith and Häusser, 2010), and auditory cortices (Bandyopadhyay et al., 2010; Rothschild et al., 2010) as well as from the mouse olfactory bulb (Wachowiak et al., 2004) and rat cerebellum (Sullivan et al., 2005). Various approaches can be used for extracting the action potential activity underlying such somatic calcium transients (Holekamp et al., 2008; Kerr et al., 2005; Sasaki et al., 2008; Vogelstein et al., 2010, 2009; Yaksi and Friedrich, 2006). For example, an effective approach is the "peeling algorithm" (Grewe et al., 2010), which is based on subtracting single action-potential-evoked calcium transients from the fluorescent trace until no additional event is present in the residual trace. Again, GECIs can be adapted as well for such studies of neuronal network function in different animal models (see also Table 1). Meanwhile, they have been used in rodents, *Drosophila*, *C. elegans*, zebrafish, and even primates (Díez-García et al., 2005; Heider et al., 2010; Higashijima et al., 2003; Horikawa et al., 2010; Li et al., 2005; Lütcke et al., 2010; Tian et al., 2009; Wallace et al., 2008; Wang et al., 2003).

A promising application of in vivo two-photon calcium imaging is the investigation of neuronal network plasticity. For example, experimental paradigms of visual deprivation (e.g., stripe rearing to influence orientation selectivity or unilateral eyelid closure to influence ocular dominance plasticity) have been shown to impact significantly the functional properties of mouse visual cortex neurons (Kreile et al., 2011; Mrsic-Flogel et al., 2007). Similarly, calcium imaging has been used to study the plasticity of neuronal networks in mouse models of disease, for example after ischemic damage of the somatosensory cortex (Winship and Murphy, 2008).

Calcium Imaging in Behaving Animals

There is a wide interest to examine brain circuits in relation to defined behaviors in awake animals. To achieve this, there are at present two major strategies involving calcium imaging as the central method for cellular functional analysis. One approach involves the use of head-mounted portable minimicroscopes (see section on imaging devices); the other concentrates on the study of head-fixed animals involving the use of standard two-photon microscopes. Figure 8A illustrates an experiment that was performed in the motor cortex of head-fixed mice that were engaged in an olfactory discrimination test (Komiyama et al., 2010). The animals were trained to lick in response to odor A and to stop licking in response to odor B (Figure 8Aa). The somatic calcium transients that were recorded in motor cortical neurons of the behaving mice had an excellent signal-to-noise ratio (Figures 8Ab–8Ac). Such experiments involving head fixation are possible because the mice have been gradually adapted to the experimental set-up, which includes the training in a tube-like construction which provides protection to the animal (in that particular study training lasted for 5 days on average). Another study examined the function of hippocampal neurons during a complex behavior. In this case, the mice were placed on a spherical treadmill on which they could run (Figure 8Ba) (Dombeck et al., 2009, 2007). The authors used two-photon calcium imaging of GCaMP3-labeled pyramidal neurons in the CA1 region of the hippocampus to study the spatial distribution of place cells (Figure 8Bb) (Dombeck et al., 2010). For this purpose, they removed a few days before the experiment some of the cortex tissue covering the hippocampus. In their experiments, they were able to map CA1 place cells by combining the positioning data from the spherical treadmill with the neuronal calcium signals (Figures 8Bb–8Bd). A remaining challenge of such studies is that it is very difficult to obtain calcium imaging and electrophysiological recordings from the same cell. Therefore, the relation between calcium transients and the underlying action potential activity is not yet entirely clear under these recording conditions. Furthermore, motion artifacts are often unavoidable, requiring the use of various motion correction algorithms (Dombeck et al., 2010, 2007; Komiyama et al., 2010). However, such experiments involving the use of GECIs can be repeated during consecutive days and weeks again and again, allowing an in-depth analysis of the mechanisms of neuronal plasticity in vivo (Andermann et al., 2010; Mank et al., 2008).

Outlook

What are the upcoming major challenges in neuronal calcium imaging? On the single-cell level, calcium imaging will remain an important tool for the analysis of the mechanisms associated with synaptic function and synaptic plasticity in specific types of neurons. The in vitro studies in combination with targeted mutations of neuronal signaling proteins can provide highly quantitative information on the intracellular mechanisms involving calcium signaling in specific neuronal subdomains, like spines and nerve terminals. The in vivo studies are likely to extend rapidly beyond the currently used layer 2/3 analysis, to neurons in deeper cortical layers, especially dendrites and somata in layer 4 and layer 5 of the mouse cortex. In combination with optogenetics, the combination of optics and genetics to achieve control over the activity of the target cells (Yizhar et al., 2011), such studies will contribute to a better understanding of local network function in the context of defined simple behaviors. Another important area that is likely to strongly expand in the coming years is calcium imaging in defined types of neurons in awake, behaving animals. These studies will not be restricted to mice and rats, but are likely to be increasingly extended also to other models, like ferrets, cats, and especially primates. An area of application with growing impact will be the use of calcium imaging in molecular medicine for a detailed analysis of signaling mechanisms in the explosively increasing number of disease models (Rochefort et al., 2008). We also expect further developments in calcium imaging technology, especially concerning devices capable of 3D imaging and miniaturized devices to be used in freely moving animals. Finally, calcium imaging may greatly benefit from the development of improved GECIs with higher signal sensitivity and better temporal response characteristics.

ACKNOWLEDGMENTS

We thank Jia Lou for excellent technical assistance. This work was supported by the Deutsche Forschungsgemeinschaft (IRTG 1373), the ERA-Net Program, the CIPSM cluster, and the Schiedel Foundation. A.K. is a Carl-von-Linde Senior Fellow of the Institute for Advanced Study of the TUM.

REFERENCES

Aaron, G., and Yuste, R. (2006). Reverse optical probing (ROPING) of neocortical circuits. Synapse *60*, 437–440.

Adelsberger, H., Garaschuk, O., and Konnerth, A. (2005). Cortical calcium waves in resting newborn mice. Nat. Neurosci. *8*, 988–990.

Aiba, A., Kano, M., Chen, C., Stanton, M.E., Fox, G.D., Herrup, K., Zwingman, T.A., and Tonegawa, S. (1994). Deficient cerebellar long-term depression and impaired motor learning in mGluR1 mutant mice. Cell *79*, 377–388.

Andermann, M.L., Kerlin, A.M., and Reid, R.C. (2010). Chronic cellular imaging of mouse visual cortex during operant behavior and passive viewing. Front Cell Neurosci *4*, 3.

Andresen, V., Alexander, S., Heupel, W.M., Hirschberg, M., Hoffman, R.M., and Friedl, P. (2009). Infrared multiphoton microscopy: subcellular-resolved deep tissue imaging. Curr. Opin. Biotechnol. *20*, 54–62.

Ashley, C.C., and Ridgway, E.B. (1968). Simultaneous recording of membrane potential, calcium transient and tension in single muscle fibers. Nature *219*, 1168–1169.

Badea, T., Goldberg, J., Mao, B., and Yuste, R. (2001). Calcium imaging of epileptiform events with single-cell resolution. J. Neurobiol. *48*, 215–227.

Baimbridge, K.G., Celio, M.R., and Rogers, J.H. (1992). Calcium-binding proteins in the nervous system. Trends Neurosci. *15*, 303–308.

Bakayan, A., Vaquero, C.F., Picazo, F., and Llopis, J. (2011). Red fluorescent protein-aequorin fusions as improved bioluminescent Ca^{2+} reporters in single cells and mice. PLoS ONE *6*, e19520.

Baker, B.J., Kosmidis, E.K., Vucinic, D., Falk, C.X., Cohen, L.B., Djurisic, M., and Zecevic, D. (2005). Imaging brain activity with voltage- and calcium-sensitive dyes. Cell. Mol. Neurobiol. *25*, 245–282.

Bandyopadhyay, S., Shamma, S.A., and Kanold, P.O. (2010). Dichotomy of functional organization in the mouse auditory cortex. Nat. Neurosci. *13*, 361–368.

Baubet, V., Le Mouellic, H., Campbell, A.K., Lucas-Meunier, E., Fossier, P., and Brúlet, P. (2000). Chimeric green fluorescent protein-aequorin as bioluminescent Ca^{2+} reporters at the single-cell level. Proc. Natl. Acad. Sci. USA *97*, 7260–7265.

Bender, V.A., Bender, K.J., Brasier, D.J., and Feldman, D.E. (2006). Two coincidence detectors for spike timing-dependent plasticity in somatosensory cortex. J. Neurosci. *26*, 4166–4177.

Berger, T., Borgdorff, A., Crochet, S., Neubauer, F.B., Lefort, S., Fauvet, B., Ferezou, I., Carleton, A., Lüscher, H.R., and Petersen, C.C. (2007). Combined voltage and calcium epifluorescence imaging in vitro and in vivo reveals subthreshold and suprathreshold dynamics of mouse barrel cortex. J. Neurophysiol. *97*, 3751–3762.

Berridge, M.J. (1993). Inositol trisphosphate and calcium signalling. Nature *361*, 315–325.

Berridge, M.J. (1998). Neuronal calcium signaling. Neuron *21*, 13–26.

Berridge, M.J., Bootman, M.D., and Roderick, H.L. (2003). Calcium signalling: dynamics, homeostasis and remodelling. Nat. Rev. Mol. Cell Biol. *4*, 517–529.

Berridge, M.J., Lipp, P., and Bootman, M.D. (2000). The versatility and universality of calcium signalling. Nat. Rev. Mol. Cell Biol. *1*, 11–21.

Bloodgood, B.L., and Sabatini, B.L. (2007a). $Ca^{(2+)}$ signaling in dendritic spines. Curr. Opin. Neurobiol. *17*, 345–351.

Bloodgood, B.L., and Sabatini, B.L. (2007b). Nonlinear regulation of unitary synaptic signals by $Ca_V(2.3)$ voltage-sensitive calcium channels located in dendritic spines. Neuron *53*, 249–260.

Bonifazi, P., Goldin, M., Picardo, M.A., Jorquera, I., Cattani, A., Bianconi, G., Represa, A., Ben-Ari, Y., and Cossart, R. (2009). GABAergic hub neurons orchestrate synchrony in developing hippocampal networks. Science *326*, 1419–1424.

Borrell, V., Yoshimura, Y., and Callaway, E.M. (2005). Targeted gene delivery to telencephalic inhibitory neurons by directional in utero electroporation. J. Neurosci. Methods *143*, 151–158.

Bowie, D., and Mayer, M.L. (1995). Inward rectification of both AMPA and kainate subtype glutamate receptors generated by polyamine-mediated ion channel block. Neuron *15*, 453–462.

Bozza, T., McGann, J.P., Mombaerts, P., and Wachowiak, M. (2004). In vivo imaging of neuronal activity by targeted expression of a genetically encoded probe in the mouse. Neuron *42*, 9–21.

Briggman, K.L., and Euler, T. (2011). Bulk electroporation and population calcium imaging in the adult mammalian retina. J. Neurophysiol. *105*, 2601–2609.

Brini, M. (2008). Calcium-sensitive photoproteins. Methods *46*, 160–166.

Brown, J.E., Cohen, L.B., De Weer, P., Pinto, L.H., Ross, W.N., and Salzberg, B.M. (1975). Rapid changes in intracellular free calcium concentration. Detection by metallochromic indicator dyes in squid giant axon. Biophys. J. *15*, 1155–1160.

Brustein, E., Marandi, N., Kovalchuk, Y., Drapeau, P., and Konnerth, A. (2003). "In vivo" monitoring of neuronal network activity in zebrafish by two-photon $Ca^{(2+)}$ imaging. Pflugers Arch. *446*, 766–773.

Burnashev, N., Zhou, Z., Neher, E., and Sakmann, B. (1995). Fractional calcium currents through recombinant GluR channels of the NMDA, AMPA and kainate receptor subtypes. J. Physiol. *485*, 403–418.

Carlson, G.C., and Coulter, D.A. (2008). In vitro functional imaging in brain slices using fast voltage-sensitive dye imaging combined with whole-cell patch recording. Nat. Protoc. *3*, 249–255.

Catterall, W.A. (2000). Structure and regulation of voltage-gated Ca^{2+} channels. Annu. Rev. Cell Dev. Biol. *16*, 521–555.

Cetin, A., Komai, S., Eliava, M., Seeburg, P.H., and Osten, P. (2006). Stereotaxic gene delivery in the rodent brain. Nat. Protoc. *1*, 3166–3173.

Chalasani, S.H., Chronis, N., Tsunozaki, M., Gray, J.M., Ramot, D., Goodman, M.B., and Bargmann, C.I. (2007). Dissecting a circuit for olfactory behaviour in Caenorhabditis elegans. Nature *450*, 63–70.

Chen, X., Kovalchuk, Y., Adelsberger, H., Henning, H.A., Sausbier, M., Wietzorrek, G., Ruth, P., Yarom, Y., and Konnerth, A. (2010). Disruption of the olivo-cerebellar circuit by Purkinje neuron-specific ablation of BK channels. Proc. Natl. Acad. Sci. USA *107*, 12323–12328.

Chen, X., Leischner, U., Rochefort, N.L., Nelken, I., and Konnerth, A. (2011). Functional mapping of single spines in cortical neurons in vivo. Nature *475*, 501–505.

Cheng, A., Gonçalves, J.T., Golshani, P., Arisaka, K., and Portera-Cailliau, C. (2011). Simultaneous two-photon calcium imaging at different depths with spatiotemporal multiplexing. Nat. Methods *8*, 139–142.

Chhatwal, J.P., Hammack, S.E., Jasnow, A.M., Rainnie, D.G., and Ressler, K.J. (2007). Identification of cell-type-specific promoters within the brain using lentiviral vectors. Gene Ther. *14*, 575–583.

Chia, T.H., and Levene, M.J. (2009). Microprisms for in vivo multilayer cortical imaging. J. Neurophysiol. *102*, 1310–1314.

Chiesa, A., Rapizzi, E., Tosello, V., Pinton, P., de Virgilio, M., Fogarty, K.E., and Rizzuto, R. (2001). Recombinant aequorin and green fluorescent protein as valuable tools in the study of cell signalling. Biochem. J. *355*, 1–12.

Clem, R.L., and Barth, A. (2006). Pathway-specific trafficking of native AMPARs by in vivo experience. Neuron *49*, 663–670.

Cobbold, P.H., and Rink, T.J. (1987). Fluorescence and bioluminescence measurement of cytoplasmic free calcium. Biochem. J. *248*, 313–328.

Conchello, J.A., and Lichtman, J.W. (2005). Optical sectioning microscopy. Nat. Methods *2*, 920–931.

Connor, J.A. (1986). Digital imaging of free calcium changes and of spatial gradients in growing processes in single, mammalian central nervous system cells. Proc. Natl. Acad. Sci. USA *83*, 6179–6183.

Connor, J.A., Razani-Boroujerdi, S., Greenwood, A.C., Cormier, R.J., Petrozzino, J.J., and Lin, R.C. (1999). Reduced voltage-dependent Ca^{2+} signaling in CA1 neurons after brief ischemia in gerbils. J. Neurophysiol. *81*, 299–306.

Coulter, D.A., Huguenard, J.R., and Prince, D.A. (1989). Calcium currents in rat thalamocortical relay neurones: kinetic properties of the transient, low-threshold current. J. Physiol. *414*, 587–604.

Crépel, V., Aronov, D., Jorquera, I., Represa, A., Ben-Ari, Y., and Cossart, R. (2007). A parturition-associated nonsynaptic coherent activity pattern in the developing hippocampus. Neuron *54*, 105–120.

Davidson, B.L., and Breakefield, X.O. (2003). Viral vectors for gene delivery to the nervous system. Nat. Rev. Neurosci. *4*, 353–364.

De Vry, J., Martínez-Martínez, P., Losen, M., Temel, Y., Steckler, T., Steinbusch, H.W., De Baets, M.H., and Prickaerts, J. (2010). In vivo electroporation of the central nervous system: a non-viral approach for targeted gene delivery. Prog. Neurobiol. *92*, 227–244.

Delaney, K., Davison, I., and Denk, W. (2001). Odour-evoked $[Ca^{2+}]$ transients in mitral cell dendrites of frog olfactory glomeruli. Eur. J. Neurosci. *13*, 1658–1672.

Delaney, K.R., Zucker, R.S., and Tank, D.W. (1989). Calcium in motor nerve terminals associated with posttetanic potentiation. J. Neurosci. *9*, 3558–3567.

Demarque, M., and Spitzer, N.C. (2010). Activity-dependent expression of Lmx1b regulates specification of serotonergic neurons modulating swimming behavior. Neuron *67*, 321–334.

Denk, W., Delaney, K.R., Gelperin, A., Kleinfeld, D., Strowbridge, B.W., Tank, D.W., and Yuste, R. (1994). Anatomical and functional imaging of neurons using 2-photon laser scanning microscopy. J. Neurosci. Methods *54*, 151–162.

Denk, W., Strickler, J.H., and Webb, W.W. (1990). Two-photon laser scanning fluorescence microscopy. Science *248*, 73–76.

Denk, W., Sugimori, M., and Llinás, R. (1995). Two types of calcium response limited to single spines in cerebellar Purkinje cells. Proc. Natl. Acad. Sci. USA *92*, 8279–8282.

Denk, W., and Svoboda, K. (1997). Photon upmanship: why multiphoton imaging is more than a gimmick. Neuron *18*, 351–357.

Díez-García, J., Matsushita, S., Mutoh, H., Nakai, J., Ohkura, M., Yokoyama, J., Dimitrov, D., and Knöpfel, T. (2005). Activation of cerebellar parallel fibers monitored in transgenic mice expressing a fluorescent Ca^{2+} indicator protein. Eur. J. Neurosci. *22*, 627–635.

Dittgen, T., Nimmerjahn, A., Komai, S., Licznerski, P., Waters, J., Margrie, T.W., Helmchen, F., Denk, W., Brecht, M., and Osten, P. (2004). Lentivirus-based genetic manipulations of cortical neurons and their optical and electrophysiological monitoring in vivo. Proc. Natl. Acad. Sci. USA *101*, 18206–18211.

Dombeck, D.A., Graziano, M.S., and Tank, D.W. (2009). Functional clustering of neurons in motor cortex determined by cellular resolution imaging in awake behaving mice. J. Neurosci. *29*, 13751–13760.

Dombeck, D.A., Harvey, C.D., Tian, L., Looger, L.L., and Tank, D.W. (2010). Functional imaging of hippocampal place cells at cellular resolution during virtual navigation. Nat. Neurosci. *13*, 1433–1440.

Dombeck, D.A., Khabbaz, A.N., Collman, F., Adelman, T.L., and Tank, D.W. (2007). Imaging large-scale neural activity with cellular resolution in awake, mobile mice. Neuron *56*, 43–57.

Dong, J.Y., Fan, P.D., and Frizzell, R.A. (1996). Quantitative analysis of the packaging capacity of recombinant adeno-associated virus. Hum. Gene Ther. *7*, 2101–2112.

Duchen, M.R. (1999). Contributions of mitochondria to animal physiology: from homeostatic sensor to calcium signalling and cell death. J. Physiol. *516*, 1–17.

Dulhunty, A.F. (2006). Excitation-contraction coupling from the 1950s into the new millennium. Clin. Exp. Pharmacol. Physiol. *33*, 763–772.

Eilers, J., Augustine, G.J., and Konnerth, A. (1995). Subthreshold synaptic Ca^{2+} signalling in fine dendrites and spines of cerebellar Purkinje neurons. Nature *373*, 155–158.

Eilers, J., and Konnerth, A. (2009). Dye loading with patch pipettes. Cold Spring Harb Protoc *2009*, pdb.prot5201.

Elyada, Y.M., Haag, J., and Borst, A. (2009). Different receptive fields in axons and dendrites underlie robust coding in motion-sensitive neurons. Nat. Neurosci. *12*, 327–332.

Engelbrecht, C.J., Johnston, R.S., Seibel, E.J., and Helmchen, F. (2008). Ultra-compact fiber-optic two-photon microscope for functional fluorescence imaging in vivo. Opt. Express *16*, 5556–5564.

Fan, G.Y., Fujisaki, H., Miyawaki, A., Tsay, R.K., Tsien, R.Y., and Ellisman, M.H. (1999). Video-rate scanning two-photon excitation fluorescence microscopy and ratio imaging with cameleons. Biophys. J. *76*, 2412–2420.

Feller, M.B., Wellis, D.P., Stellwagen, D., Werblin, F.S., and Shatz, C.J. (1996). Requirement for cholinergic synaptic transmission in the propagation of spontaneous retinal waves. Science *272*, 1182–1187.

Ferraguti, F., and Shigemoto, R. (2006). Metabotropic glutamate receptors. Cell Tissue Res. *326*, 483–504.

Finch, E.A., and Augustine, G.J. (1998). Local calcium signalling by inositol-1,4,5-trisphosphate in Purkinje cell dendrites. Nature *396*, 753–756.

Fletcher, M.L., Masurkar, A.V., Xing, J., Imamura, F., Xiong, W., Nagayama, S., Mutoh, H., Greer, C.A., Knöpfel, T., and Chen, W.R. (2009). Optical imaging of postsynaptic odor representation in the glomerular layer of the mouse olfactory bulb. J. Neurophysiol. *102*, 817–830.

Flusberg, B.A., Cocker, E.D., Piyawattanametha, W., Jung, J.C., Cheung, E.L., and Schnitzer, M.J. (2005). Fiber-optic fluorescence imaging. Nat. Methods *2*, 941–950.

Flusberg, B.A., Nimmerjahn, A., Cocker, E.D., Mukamel, E.A., Barretto, R.P., Ko, T.H., Burns, L.D., Jung, J.C., and Schnitzer, M.J. (2008). High-speed, miniaturized fluorescence microscopy in freely moving mice. Nat. Methods *5*, 935–938.

Fucile, S. (2004). Ca^{2+} permeability of nicotinic acetylcholine receptors. Cell Calcium *35*, 1–8.

Fujiwara, T., Kazawa, T., Haupt, S.S., and Kanzaki, R. (2009). Ca^{2+} imaging of identifiable neurons labeled by electroporation in insect brains. Neuroreport *20*, 1061–1065.

Galizia, C.G., Sachse, S., Rappert, A., and Menzel, R. (1999). The glomerular code for odor representation is species specific in the honeybee Apis mellifera. Nat. Neurosci. *2*, 473–478.

Garaschuk, O., Hanse, E., and Konnerth, A. (1998). Developmental profile and synaptic origin of early network oscillations in the CA1 region of rat neonatal hippocampus. J. Physiol. *507*, 219–236.

Garaschuk, O., Linn, J., Eilers, J., and Konnerth, A. (2000). Large-scale oscillatory calcium waves in the immature cortex. Nat. Neurosci. *3*, 452–459.

Garaschuk, O., Milos, R.I., and Konnerth, A. (2006). Targeted bulk-loading of fluorescent indicators for two-photon brain imaging in vivo. Nat. Protoc. *1*, 380–386.

Garaschuk, O., Schneggenburger, R., Schirra, C., Tempia, F., and Konnerth, A. (1996). Fractional Ca^{2+} currents through somatic and dendritic glutamate receptor channels of rat hippocampal CA1 pyramidal neurones. J. Physiol. *491*, 757–772.

Geiger, J.R., Melcher, T., Koh, D.S., Sakmann, B., Seeburg, P.H., Jonas, P., and Monyer, H. (1995). Relative abundance of subunit mRNAs determines gating and Ca^{2+} permeability of AMPA receptors in principal neurons and interneurons in rat CNS. Neuron *15*, 193–204.

Gelperin, A., and Flores, J. (1997). Vital staining from dye-coated microprobes identifies new olfactory interneurons for optical and electrical recording. J. Neurosci. Methods *72*, 97–108.

Ghosh, K.K., Burns, L.D., Cocker, E.D., Nimmerjahn, A., Ziv, Y., Gamal, A.E., and Schnitzer, M.J. (2011). Miniaturized integration of a fluorescence microscope. Nat. Methods *8*, 871–878.

Girkin, J.M., Poland, S., and Wright, A.J. (2009). Adaptive optics for deeper imaging of biological samples. Curr. Opin. Biotechnol. *20*, 106–110.

Gitler, D., and Spira, M.E. (1998). Real time imaging of calcium-induced localized proteolytic activity after axotomy and its relation to growth cone formation. Neuron *20*, 1123–1135.

Göbel, W., and Helmchen, F. (2007). New angles on neuronal dendrites in vivo. J. Neurophysiol. *98*, 3770–3779.

Göbel, W., Kampa, B.M., and Helmchen, F. (2007). Imaging cellular network dynamics in three dimensions using fast 3D laser scanning. Nat. Methods *4*, 73–79.

Goldberg, J.H., Tamas, G., Aronov, D., and Yuste, R. (2003). Calcium microdomains in aspiny dendrites. Neuron *40*, 807–821.

Gong, S., Doughty, M., Harbaugh, C.R., Cummins, A., Hatten, M.E., Heintz, N., and Gerfen, C.R. (2007). Targeting Cre recombinase to specific neuron populations with bacterial artificial chromosome constructs. J. Neurosci. *27*, 9817–9823.

Greenberg, D.S., Houweling, A.R., and Kerr, J.N. (2008). Population imaging of ongoing neuronal activity in the visual cortex of awake rats. Nat. Neurosci. *11*, 749–751.

Grewe, B.F., Langer, D., Kasper, H., Kampa, B.M., and Helmchen, F. (2010). High-speed in vivo calcium imaging reveals neuronal network activity with near-millisecond precision. Nat. Methods *7*, 399–405.

Grienberger, C., Adelsberger, H., Stroh, A., Milos, R.I., Garaschuk, O., Schierloh, A., Nelken, I., and Konnerth, A. (2012). Sound-evoked network calcium transients in mouse auditory cortex in vivo. J. Physiol. *590*, 899–918.

Grinvald, A., Cohen, L.B., Lesher, S., and Boyle, M.B. (1981). Simultaneous optical monitoring of activity of many neurons in invertebrate ganglia using a 124-element photodiode array. J. Neurophysiol. *45*, 829–840.

Grynkiewicz, G., Poenie, M., and Tsien, R.Y. (1985). A new generation of Ca^{2+} indicators with greatly improved fluorescence properties. J. Biol. Chem. *260*, 3440–3450.

Hallett, M., and Carbone, E. (1972). Studies of calcium influx into squid giant axons with aequorin. J. Cell. Physiol. *80*, 219–226.

Hartmann, J., Dragicevic, E., Adelsberger, H., Henning, H.A., Sumser, M., Abramowitz, J., Blum, R., Dietrich, A., Freichel, M., Flockerzi, V., et al. (2008). TRPC3 channels are required for synaptic transmission and motor coordination. Neuron *59*, 392–398.

Hasan, M.T., Friedrich, R.W., Euler, T., Larkum, M.E., Giese, G., Both, M., Duebel, J., Waters, J., Bujard, H., Griesbeck, O., et al. (2004). Functional fluorescent Ca^{2+} indicator proteins in transgenic mice under TET control. PLoS Biol. *2*, e163.

Head, J.F., Inouye, S., Teranishi, K., and Shimomura, O. (2000). The crystal structure of the photoprotein aequorin at 2.3 A resolution. Nature *405*, 372–376.

Heider, B., Nathanson, J.L., Isacoff, E.Y., Callaway, E.M., and Siegel, R.M. (2010). Two-photon imaging of calcium in virally transfected striate cortical neurons of behaving monkey. PLoS ONE *5*, e13829.

Heim, N., Garaschuk, O., Friedrich, M.W., Mank, M., Milos, R.I., Kovalchuk, Y., Konnerth, A., and Griesbeck, O. (2007). Improved calcium imaging in transgenic mice expressing a troponin C-based biosensor. Nat. Methods *4*, 127–129.

Heim, N., and Griesbeck, O. (2004). Genetically encoded indicators of cellular calcium dynamics based on troponin C and green fluorescent protein. J. Biol. Chem. *279*, 14280–14286.

Helmchen, F., Borst, J.G., and Sakmann, B. (1997). Calcium dynamics associated with a single action potential in a CNS presynaptic terminal. Biophys. J. *72*, 1458–1471.

Helmchen, F., and Denk, W. (2005). Deep tissue two-photon microscopy. Nat. Methods *2*, 932–940.

Helmchen, F., Fee, M.S., Tank, D.W., and Denk, W. (2001). A miniature head-mounted two-photon microscope. high-resolution brain imaging in freely moving animals. Neuron *31*, 903–912.

Helmchen, F., Imoto, K., and Sakmann, B. (1996). Ca^{2+} buffering and action potential-evoked Ca^{2+} signaling in dendrites of pyramidal neurons. Biophys. J. *70*, 1069–1081.

Helmchen, F., and Konnerth, A. (2011). Imaging in neuroscience: a laboratory manual (Cold Spring Harbor, N.Y: Cold Spring Harbor Laboratory Press).

Helmchen, F., Svoboda, K., Denk, W., and Tank, D.W. (1999). In vivo dendritic calcium dynamics in deep-layer cortical pyramidal neurons. Nat. Neurosci. *2*, 989–996.

Helmchen, F., and Waters, J. (2002). Ca^{2+} imaging in the mammalian brain in vivo. Eur. J. Pharmacol. *447*, 119–129.

Hendel, T., Mank, M., Schnell, B., Griesbeck, O., Borst, A., and Reiff, D.F. (2008). Fluorescence changes of genetic calcium indicators and OGB-1 correlated with neural activity and calcium in vivo and in vitro. J. Neurosci. *28*, 7399–7411.

Higashijima, S., Masino, M.A., Mandel, G., and Fetcho, J.R. (2003). Imaging neuronal activity during zebrafish behavior with a genetically encoded calcium indicator. J. Neurophysiol. *90*, 3986–3997.

Higley, M.J., and Sabatini, B.L. (2008). Calcium signaling in dendrites and spines: practical and functional considerations. Neuron *59*, 902–913.

Hiramoto, M., and Cline, H.T. (2009). Convergence of multisensory inputs in Xenopus tadpole tectum. Dev. Neurobiol. *69*, 959–971.

Hirase, H., Qian, L., Barthó, P., and Buzsáki, G. (2004). Calcium dynamics of cortical astrocytic networks in vivo. PLoS Biol. *2*, E96.

Holekamp, T.F., Turaga, D., and Holy, T.E. (2008). Fast three-dimensional fluorescence imaging of activity in neural populations by objective-coupled planar illumination microscopy. Neuron *57*, 661–672.

Holtmaat, A., Bonhoeffer, T., Chow, D.K., Chuckowree, J., De Paola, V., Hofer, S.B., Hübener, M., Keck, T., Knott, G., Lee, W.C., et al. (2009). Long-term, high-resolution imaging in the mouse neocortex through a chronic cranial window. Nat. Protoc. *4*, 1128–1144.

Homma, R., Baker, B.J., Jin, L., Garaschuk, O., Konnerth, A., Cohen, L.B., and Zecevic, D. (2009). Wide-field and two-photon imaging of brain activity with voltage- and calcium-sensitive dyes. Philos. Trans. R. Soc. Lond. B Biol. Sci. *364*, 2453–2467.

Hoogland, T.M., and Saggau, P. (2004). Facilitation of L-type Ca^{2+} channels in dendritic spines by activation of β_2 adrenergic receptors. J. Neurosci. *24*, 8416–8427.

Horikawa, K., Yamada, Y., Matsuda, T., Kobayashi, K., Hashimoto, M., Matsuura, T., Miyawaki, A., Michikawa, T., Mikoshiba, K., and Nagai, T. (2010). Spontaneous network activity visualized by ultrasensitive $Ca^{(2+)}$ indicators, yellow Cameleon-Nano. Nat. Methods *7*, 729–732.

Inouye, S., Noguchi, M., Sakaki, Y., Takagi, Y., Miyata, T., Iwanaga, S., Miyata, T., and Tsuji, F.I. (1985). Cloning and sequence analysis of cDNA for the luminescent protein aequorin. Proc. Natl. Acad. Sci. USA *82*, 3154–3158.

Iyer, V., Hoogland, T.M., and Saggau, P. (2006). Fast functional imaging of single neurons using random-access multiphoton (RAMP) microscopy. J. Neurophysiol. *95*, 535–545.

Jaffe, D.B., Johnston, D., Lasser-Ross, N., Lisman, J.E., Miyakawa, H., and Ross, W.N. (1992). The spread of Na^{+} spikes determines the pattern of dendritic Ca^{2+} entry into hippocampal neurons. Nature *357*, 244–246.

Jares-Erijman, E.A., and Jovin, T.M. (2003). FRET imaging. Nat. Biotechnol. *21*, 1387–1395.

Ji, N., Milkie, D.E., and Betzig, E. (2010). Adaptive optics via pupil segmentation for high-resolution imaging in biological tissues. Nat. Methods *7*, 141–147.

Jia, H., Rochefort, N.L., Chen, X., and Konnerth, A. (2010). Dendritic organization of sensory input to cortical neurons in vivo. Nature *464*, 1307–1312.

Jia, H., Rochefort, N.L., Chen, X., and Konnerth, A. (2011). In vivo two-photon imaging of sensory-evoked dendritic calcium signals in cortical neurons. Nat. Protoc. *6*, 28–35.

Johnson, I.D., and Spence, M.T.Z. (2010). Molecular Probes Handbook, A guide to fluorescecent probes and labeling technologies, 11th Edition (Eugene, OR, USA: Molecular Probes).

Jonas, P., Racca, C., Sakmann, B., Seeburg, P.H., and Monyer, H. (1994). Differences in Ca^{2+} permeability of AMPA-type glutamate receptor channels in neocortical neurons caused by differential GluR-B subunit expression. Neuron *12*, 1281–1289.

Judkewitz, B., Rizzi, M., Kitamura, K., and Häusser, M. (2009). Targeted single-cell electroporation of mammalian neurons in vivo. Nat. Protoc. *4*, 862–869.

Jung, J.C., Mehta, A.D., Aksay, E., Stepnoski, R., and Schnitzer, M.J. (2004). In vivo mammalian brain imaging using one- and two-photon fluorescence microendoscopy. J. Neurophysiol. *92*, 3121–3133.

Kano, M., Garaschuk, O., Verkhratsky, A., and Konnerth, A. (1995). Ryanodine receptor-mediated intracellular calcium release in rat cerebellar Purkinje neurones. J. Physiol. *487*, 1–16.

Kerr, J.N., de Kock, C.P., Greenberg, D.S., Bruno, R.M., Sakmann, B., and Helmchen, F. (2007). Spatial organization of neuronal population responses in layer 2/3 of rat barrel cortex. J. Neurosci. *27*, 13316–13328.

Kerr, J.N., Greenberg, D., and Helmchen, F. (2005). Imaging input and output of neocortical networks in vivo. Proc. Natl. Acad. Sci. USA *102*, 14063–14068.

Kirkby, P.A., Srinivas Nadella, K.M., and Silver, R.A. (2010). A compact Acousto-Optic Lens for 2D and 3D femtosecond based 2-photon microscopy. Opt. Express *18*, 13721–13745.

Kitamura, K., Judkewitz, B., Kano, M., Denk, W., and Häusser, M. (2008). Targeted patch-clamp recordings and single-cell electroporation of unlabeled neurons in vivo. Nat. Methods *5*, 61–67.

Kobat, D., Durst, M.E., Nishimura, N., Wong, A.W., Schaffer, C.B., and Xu, C. (2009). Deep tissue multiphoton microscopy using longer wavelength excitation. Opt. Express *17*, 13354–13364.

Koester, H.J., and Sakmann, B. (1998). Calcium dynamics in single spines during coincident pre- and postsynaptic activity depend on relative timing of back-propagating action potentials and subthreshold excitatory postsynaptic potentials. Proc. Natl. Acad. Sci. USA *95*, 9596–9601.

Koester, H.J., and Sakmann, B. (2000). Calcium dynamics associated with action potentials in single nerve terminals of pyramidal cells in layer 2/3 of the young rat neocortex. J. Physiol. *529*, 625–646.

Koh, D.S., Burnashev, N., and Jonas, P. (1995). Block of native Ca(2+)-permeable AMPA receptors in rat brain by intracellular polyamines generates double rectification. J. Physiol. *486*, 305–312.

Komiyama, T., Sato, T.R., O'Connor, D.H., Zhang, Y.X., Huber, D., Hooks, B.M., Gabitto, M., and Svoboda, K. (2010). Learning-related fine-scale specificity imaged in motor cortex circuits of behaving mice. Nature *464*, 1182–1186.

Konnerth, A., Dreessen, J., and Augustine, G.J. (1992). Brief dendritic calcium signals initiate long-lasting synaptic depression in cerebellar Purkinje cells. Proc. Natl. Acad. Sci. USA *89*, 7051–7055.

Kotlikoff, M.I. (2007). Genetically encoded Ca^{2+} indicators: using genetics and molecular design to understand complex physiology. J. Physiol. *578*, 55–67.

Kovalchuk, Y., Eilers, J., Lisman, J., and Konnerth, A. (2000). NMDA receptor-mediated subthreshold Ca(2+) signals in spines of hippocampal neurons. J. Neurosci. *20*, 1791–1799.

Kozloski, J., Hamzei-Sichani, F., and Yuste, R. (2001). Stereotyped position of local synaptic targets in neocortex. Science *293*, 868–872.

Kreile, A.K., Bonhoeffer, T., and Hübener, M. (2011). Altered visual experience induces instructive changes of orientation preference in mouse visual cortex. J. Neurosci. *31*, 13911–13920.

Kreitzer, A.C., Gee, K.R., Archer, E.A., and Regehr, W.G. (2000). Monitoring presynaptic calcium dynamics in projection fibers by in vivo loading of a novel calcium indicator. Neuron *27*, 25–32.

Kumar, M., Keller, B., Makalou, N., and Sutton, R.E. (2001). Systematic determination of the packaging limit of lentiviral vectors. Hum. Gene Ther. *12*, 1893–1905.

Langevin, L.M., Mattar, P., Scardigli, R., Roussigné, M., Logan, C., Blader, P., and Schuurmans, C. (2007). Validating in utero electroporation for the rapid analysis of gene regulatory elements in the murine telencephalon. Dev. Dyn. *236*, 1273–1286.

Larkum, M.E., Watanabe, S., Nakamura, T., Lasser-Ross, N., and Ross, W.N. (2003). Synaptically activated Ca^{2+} waves in layer 2/3 and layer 5 rat neocortical pyramidal neurons. J. Physiol. *549*, 471–488.

Lasser-Ross, N., Miyakawa, H., Lev-Ram, V., Young, S.R., and Ross, W.N. (1991). High time resolution fluorescence imaging with a CCD camera. J. Neurosci. Methods *36*, 253–261.

LeChasseur, Y., Dufour, S., Lavertu, G., Bories, C., Deschênes, M., Vallée, R., and De Koninck, Y. (2011). A microprobe for parallel optical and electrical recordings from single neurons in vivo. Nat. Methods *8*, 319–325.

Lechleiter, J.D., Lin, D.T., and Sieneart, I. (2002). Multi-photon laser scanning microscopy using an acoustic optical deflector. Biophys. J. *83*, 2292–2299.

Levene, M.J., Dombeck, D.A., Kasischke, K.A., Molloy, R.P., and Webb, W.W. (2004). In vivo multiphoton microscopy of deep brain tissue. J. Neurophysiol. *91*, 1908–1912.

Li, J., Mack, J.A., Souren, M., Yaksi, E., Higashijima, S., Mione, M., Fetcho, J.R., and Friedrich, R.W. (2005). Early development of functional spatial maps in the zebrafish olfactory bulb. J. Neurosci. *25*, 5784–5795.

Li, Y., Van Hooser, S.D., Mazurek, M., White, L.E., and Fitzpatrick, D. (2008). Experience with moving visual stimuli drives the early development of cortical direction selectivity. Nature *456*, 952–956.

Lichtman, J.W., and Conchello, J.A. (2005). Fluorescence microscopy. Nat. Methods *2*, 910–919.

Lilley, C.E., Groutsi, F., Han, Z., Palmer, J.A., Anderson, P.N., Latchman, D.S., and Coffin, R.S. (2001). Multiple immediate-early gene-deficient herpes simplex virus vectors allowing efficient gene delivery to neurons in culture and widespread gene delivery to the central nervous system in vivo. J. Virol. *75*, 4343–4356.

Liu, S.J., and Zukin, R.S. (2007). Ca^{2+}-permeable AMPA receptors in synaptic plasticity and neuronal death. Trends Neurosci. *30*, 126–134.

Liu, S.Q., and Cull-Candy, S.G. (2000). Synaptic activity at calcium-permeable AMPA receptors induces a switch in receptor subtype. Nature *405*, 454–458.

Llano, I., González, J., Caputo, C., Lai, F.A., Blayney, L.M., Tan, Y.P., and Marty, A. (2000). Presynaptic calcium stores underlie large-amplitude miniature IPSCs and spontaneous calcium transients. Nat. Neurosci. *3*, 1256–1265.

Llinás, R., and Nicholson, C. (1975). Calcium role in depolarization-secretion coupling: an aequorin study in squid giant synapse. Proc. Natl. Acad. Sci. USA *72*, 187–190.

Lohmann, C., Finski, A., and Bonhoeffer, T. (2005). Local calcium transients regulate the spontaneous motility of dendritic filopodia. Nat. Neurosci. *8*, 305–312.

Looger, L.L., and Griesbeck, O. (2011). Genetically encoded neural activity indicators. Curr. Opin. Neurobiol., in press. Published online November 19, 2011.

Lu, K.P., and Means, A.R. (1993). Regulation of the cell cycle by calcium and calmodulin. Endocr. Rev. *14*, 40–58.

Luo, L., Callaway, E.M., and Svoboda, K. (2008). Genetic dissection of neural circuits. Neuron *57*, 634–660.

Lüscher, C., and Huber, K.M. (2010). Group 1 mGluR-dependent synaptic long-term depression: mechanisms and implications for circuitry and disease. Neuron *65*, 445–459.

Lütcke, H., Murayama, M., Hahn, T., Margolis, D.J., Astori, S., Zum Alten Borgloh, S.M., Göbel, W., Yang, Y., Tang, W., Kügler, S., et al. (2010). Optical recording of neuronal activity with a genetically-encoded calcium indicator in anesthetized and freely moving mice. Front Neural Circuits *4*, 9.

Lyons, M.R., and West, A.E. (2011). Mechanisms of specificity in neuronal activity-regulated gene transcription. Prog. Neurobiol. *94*, 259–295.

Mahanty, N.K., and Sah, P. (1998). Calcium-permeable AMPA receptors mediate long-term potentiation in interneurons in the amygdala. Nature *394*, 683–687.

Manita, S., and Ross, W.N. (2009). Synaptic activation and membrane potential changes modulate the frequency of spontaneous elementary Ca2+ release events in the dendrites of pyramidal neurons. J. Neurosci. *29*, 7833–7845.

Mank, M., and Griesbeck, O. (2008). Genetically encoded calcium indicators. Chem. Rev. *108*, 1550–1564.

Mank, M., Reiff, D.F., Heim, N., Friedrich, M.W., Borst, A., and Griesbeck, O. (2006). A FRET-based calcium biosensor with fast signal kinetics and high fluorescence change. Biophys. J. *90*, 1790–1796.

Mank, M., Santos, A.F., Direnberger, S., Mrsic-Flogel, T.D., Hofer, S.B., Stein, V., Hendel, T., Reiff, D.F., Levelt, C., Borst, A., et al. (2008). A genetically encoded calcium indicator for chronic in vivo two-photon imaging. Nat. Methods *5*, 805–811.

Mao, B.Q., Hamzei-Sichani, F., Aronov, D., Froemke, R.C., and Yuste, R. (2001). Dynamics of spontaneous activity in neocortical slices. Neuron *32*, 883–898.

Mao, T., O'Connor, D.H., Scheuss, V., Nakai, J., and Svoboda, K. (2008). Characterization and subcellular targeting of GCaMP-type genetically-encoded calcium indicators. PLoS ONE *3*, e1796.

Margrie, T.W., Brecht, M., and Sakmann, B. (2002). In vivo, low-resistance, whole-cell recordings from neurons in the anaesthetized and awake mammalian brain. Pflugers Arch. *444*, 491–498.

Margrie, T.W., Meyer, A.H., Caputi, A., Monyer, H., Hasan, M.T., Schaefer, A.T., Denk, W., and Brecht, M. (2003). Targeted whole-cell recordings in the mammalian brain in vivo. Neuron *39*, 911–918.

Martin, J.R., Rogers, K.L., Chagneau, C., and Brûlet, P. (2007). In vivo bioluminescence imaging of Ca signalling in the brain of Drosophila. PLoS ONE *2*, e275.

Mayer, M.L., Westbrook, G.L., and Guthrie, P.B. (1984). Voltage-dependent block by Mg^{2+} of NMDA responses in spinal cord neurones. Nature *309*, 261–263.

Minderer, M., Liu, W., Sumanovski, L.T., Kügler, S., Helmchen, F., and Margolis, D.J. (2012). Chronic imaging of cortical sensory map dynamics using a genetically encoded calcium indicator. J. Physiol. *590*, 99–107.

Mittmann, W., Wallace, D.J., Czubayko, U., Herb, J.T., Schaefer, A.T., Looger, L.L., Denk, W., and Kerr, J.N. (2011). Two-photon calcium imaging of evoked activity from L5 somatosensory neurons in vivo. Nat. Neurosci. *14*, 1089–1093.

Miyawaki, A., Griesbeck, O., Heim, R., and Tsien, R.Y. (1999). Dynamic and quantitative Ca^{2+} measurements using improved cameleons. Proc. Natl. Acad. Sci. USA *96*, 2135–2140.

Miyawaki, A., Llopis, J., Heim, R., McCaffery, J.M., Adams, J.A., Ikura, M., and Tsien, R.Y. (1997). Fluorescent indicators for Ca^{2+} based on green fluorescent proteins and calmodulin. Nature *388*, 882–887.

Mizrahi, A., Crowley, J.C., Shtoyerman, E., and Katz, L.C. (2004). High-resolution in vivo imaging of hippocampal dendrites and spines. J. Neurosci. *24*, 3147–3151.

Monahan, P.E., and Samulski, R.J. (2000). Adeno-associated virus vectors for gene therapy: more pros than cons? Mol. Med. Today *6*, 433–440.

Mrsic-Flogel, T.D., Hofer, S.B., Ohki, K., Reid, R.C., Bonhoeffer, T., and Hübener, M. (2007). Homeostatic regulation of eye-specific responses in visual cortex during ocular dominance plasticity. Neuron *54*, 961–972.

Murayama, M., and Larkum, M.E. (2009). In vivo dendritic calcium imaging with a fiberoptic periscope system. Nat. Protoc. *4*, 1551–1559.

Murayama, M., Pérez-Garci, E., Lüscher, H.R., and Larkum, M.E. (2007). Fiberoptic system for recording dendritic calcium signals in layer 5 neocortical pyramidal cells in freely moving rats. J. Neurophysiol. *98*, 1791–1805.

Murayama, M., Pérez-Garci, E., Nevian, T., Bock, T., Senn, W., and Larkum, M.E. (2009). Dendritic encoding of sensory stimuli controlled by deep cortical interneurons. Nature *457*, 1137–1141.

Nagai, T., Sawano, A., Park, E.S., and Miyawaki, A. (2001). Circularly permuted green fluorescent proteins engineered to sense Ca2+. Proc. Natl. Acad. Sci. USA *98*, 3197–3202.

Nagai, T., Yamada, S., Tominaga, T., Ichikawa, M., and Miyawaki, A. (2004). Expanded dynamic range of fluorescent indicators for $Ca^{(2+)}$ by circularly permuted yellow fluorescent proteins. Proc. Natl. Acad. Sci. USA *101*, 10554–10559.

Nagayama, S., Enerva, A., Fletcher, M.L., Masurkar, A.V., Igarashi, K.M., Mori, K., and Chen, W.R. (2010). Differential axonal projection of mitral and tufted cells in the mouse main olfactory system. Front Neural Circuits *4*, 120.

Nagayama, S., Zeng, S., Xiong, W., Fletcher, M.L., Masurkar, A.V., Davis, D.J., Pieribone, V.A., and Chen, W.R. (2007). In vivo simultaneous tracing and $Ca^{(2+)}$ imaging of local neuronal circuits. Neuron *53*, 789–803.

Nakai, J., Ohkura, M., and Imoto, K. (2001). A high signal-to-noise $Ca^{(2+)}$ probe composed of a single green fluorescent protein. Nat. Biotechnol. *19*, 137–141.

Nakamura, T., Barbara, J.G., Nakamura, K., and Ross, W.N. (1999). Synergistic release of Ca^{2+} from IP_3-sensitive stores evoked by synaptic activation of mGluRs paired with backpropagating action potentials. Neuron *24*, 727–737.

Nathanson, J.L., Jappelli, R., Scheeff, E.D., Manning, G., Obata, K., Brenner, S., and Callaway, E.M. (2009a). Short Promoters in Viral Vectors Drive Selective Expression in Mammalian Inhibitory Neurons, but do not Restrict Activity to Specific Inhibitory Cell-Types. Front Neural Circuits *3*, 19.

Nathanson, J.L., Yanagawa, Y., Obata, K., and Callaway, E.M. (2009b). Preferential labeling of inhibitory and excitatory cortical neurons by endogenous tropism of adeno-associated virus and lentivirus vectors. Neuroscience *161*, 441–450.

Neher, E. (1995). The use of fura-2 for estimating Ca buffers and Ca fluxes. Neuropharmacology *34*, 1423–1442.

Neher, E., and Augustine, G.J. (1992). Calcium gradients and buffers in bovine chromaffin cells. J. Physiol. *450*, 273–301.

Neher, E., and Sakaba, T. (2008). Multiple roles of calcium ions in the regulation of neurotransmitter release. Neuron *59*, 861–872.

Nevian, T., and Helmchen, F. (2007). Calcium indicator loading of neurons using single-cell electroporation. Pflugers Arch. *454*, 675–688.

Nevian, T., and Sakmann, B. (2006). Spine Ca^{2+} signaling in spike-timing-dependent plasticity. J. Neurosci. *26*, 11001–11013.

Nguyen, Q.T., Callamaras, N., Hsieh, C., and Parker, I. (2001). Construction of a two-photon microscope for video-rate $Ca^{(2+)}$ imaging. Cell Calcium *30*, 383–393.

Nimmerjahn, A., Kirchhoff, F., Kerr, J.N., and Helmchen, F. (2004). Sulforhodamine 101 as a specific marker of astroglia in the neocortex in vivo. Nat. Methods *1*, 31–37.

Niswender, C.M., and Conn, P.J. (2010). Metabotropic glutamate receptors: physiology, pharmacology, and disease. Annu. Rev. Pharmacol. Toxicol. *50*, 295–322.

Nowak, L., Bregestovski, P., Ascher, P., Herbet, A., and Prochiantz, A. (1984). Magnesium gates glutamate-activated channels in mouse central neurones. Nature *307*, 462–465.

O'Donovan, M.J., Bonnot, A., Wenner, P., and Mentis, G.Z. (2005). Calcium imaging of network function in the developing spinal cord. Cell Calcium *37*, 443–450.

Oheim, M., Beaurepaire, E., Chaigneau, E., Mertz, J., and Charpak, S. (2001). Two-photon microscopy in brain tissue: parameters influencing the imaging depth. J. Neurosci. Methods *111*, 29–37.

Ohki, K., Chung, S., Ch'ng, Y.H., Kara, P., and Reid, R.C. (2005). Functional imaging with cellular resolution reveals precise micro-architecture in visual cortex. Nature *433*, 597–603.

Ohki, K., Chung, S., Kara, P., Hübener, M., Bonhoeffer, T., and Reid, R.C. (2006). Highly ordered arrangement of single neurons in orientation pinwheels. Nature *442*, 925–928.

Ohmiya, Y., and Hirano, T. (1996). Shining the light: the mechanism of the bioluminescence reaction of calcium-binding photoproteins. Chem. Biol. *3*, 337–347.

Oka, Y., Katada, S., Omura, M., Suwa, M., Yoshihara, Y., and Touhara, K. (2006). Odorant receptor map in the mouse olfactory bulb: in vivo sensitivity and specificity of receptor-defined glomeruli. Neuron *52*, 857–869.

Oliver, A.E., Baker, G.A., Fugate, R.D., Tablin, F., and Crowe, J.H. (2000). Effects of temperature on calcium-sensitive fluorescent probes. Biophys. J. *78*, 2116–2126.

Orrenius, S., Zhivotovsky, B., and Nicotera, P. (2003). Regulation of cell death: the calcium-apoptosis link. Nat. Rev. Mol. Cell Biol. *4*, 552–565.

Osakada, F., Mori, T., Cetin, A.H., Marshel, J.H., Virgen, B., and Callaway, E.M. (2011). New rabies virus variants for monitoring and manipulating activity and gene expression in defined neural circuits. Neuron *71*, 617–631.

Otsu, Y., Bormuth, V., Wong, J., Mathieu, B., Dugué, G.P., Feltz, A., and Dieudonné, S. (2008). Optical monitoring of neuronal activity at high frame rate with a digital random-access multiphoton (RAMP) microscope. J. Neurosci. Methods *173*, 259–270.

Palmer, A.E., Giacomello, M., Kortemme, T., Hires, S.A., Lev-Ram, V., Baker, D., and Tsien, R.Y. (2006). Ca^{2+} indicators based on computationally redesigned calmodulin-peptide pairs. Chem. Biol. *13*, 521–530.

Paredes, R.M., Etzler, J.C., Watts, L.T., Zheng, W., and Lechleiter, J.D. (2008). Chemical calcium indicators. Methods *46*, 143–151.

Plant, T.D., Schirra, C., Katz, E., Uchitel, O.D., and Konnerth, A. (1998). Single-cell RT-PCR and functional characterization of Ca^{2+} channels in motoneurons of the rat facial nucleus. J. Neurosci. *18*, 9573–9584.

Pologruto, T.A., Yasuda, R., and Svoboda, K. (2004). Monitoring neural activity and [Ca^{2+}] with genetically encoded Ca^{2+} indicators. J. Neurosci. *24*, 9572–9579.

Pozzan, T., Arslan, P., Tsien, R.Y., and Rink, T.J. (1982). Anti-immunoglobulin, cytoplasmic free calcium, and capping in B lymphocytes. J. Cell Biol. *94*, 335–340.

Ramsey, I.S., Delling, M., and Clapham, D.E. (2006). An introduction to TRP channels. Annu. Rev. Physiol. *68*, 619–647.

Ravin, R., Spira, M.E., Parnas, H., and Parnas, I. (1997). Simultaneous measurement of intracellular Ca^{2+} and asynchronous transmitter release from the same crayfish bouton. J. Physiol. *501*, 251–262.

Raymond, C.R., and Redman, S.J. (2006). Spatial segregation of neuronal calcium signals encodes different forms of LTP in rat hippocampus. J. Physiol. *570*, 97–111.

Regehr, W.G., and Tank, D.W. (1991a). The maintenance of LTP at hippocampal mossy fiber synapses is independent of sustained presynaptic calcium. Neuron *7*, 451–459.

Regehr, W.G., and Tank, D.W. (1991b). Selective fura-2 loading of presynaptic terminals and nerve cell processes by local perfusion in mammalian brain slice. J. Neurosci. Methods *37*, 111–119.

Regehr, W.G., and Tank, D.W. (1994). Dendritic calcium dynamics. Curr. Opin. Neurobiol. *4*, 373–382.

Reid, C.A., Fabian-Fine, R., and Fine, A. (2001). Postsynaptic calcium transients evoked by activation of individual hippocampal mossy fiber synapses. J. Neurosci. *21*, 2206–2214.

Rizzuto, R., and Pozzan, T. (2006). Microdomains of intracellular Ca^{2+}: molecular determinants and functional consequences. Physiol. Rev. *86*, 369–408.

Rizzuto, R., Simpson, A.W., Brini, M., and Pozzan, T. (1992). Rapid changes of mitochondrial Ca^{2+} revealed by specifically targeted recombinant aequorin. Nature *358*, 325–327.

Rochefort, N.L., Garaschuk, O., Milos, R.I., Narushima, M., Marandi, N., Pichler, B., Kovalchuk, Y., and Konnerth, A. (2009). Sparsification of neuronal activity in the visual cortex at eye-opening. Proc. Natl. Acad. Sci. USA *106*, 15049–15054.

Rochefort, N.L., Jia, H., and Konnerth, A. (2008). Calcium imaging in the living brain: prospects for molecular medicine. Trends Mol. Med. *14*, 389–399.

Rochefort, N.L., Narushima, M., Grienberger, C., Marandi, N., Hill, D.N., and Konnerth, A. (2011). Development of direction selectivity in mouse cortical neurons. Neuron *71*, 425–432.

Rogers, K.L., Stinnakre, J., Agulhon, C., Jublot, D., Shorte, S.L., Kremer, E.J., and Brûlet, P. (2005). Visualization of local Ca^{2+} dynamics with genetically encoded bioluminescent reporters. Eur. J. Neurosci. *21*, 597–610.

Rogers, M., and Dani, J.A. (1995). Comparison of quantitative calcium flux through NMDA, ATP, and ACh receptor channels. Biophys. J. *68*, 501–506.

Ross, W.N., and Werman, R. (1987). Mapping calcium transients in the dendrites of Purkinje cells from the guinea-pig cerebellum in vitro. J. Physiol. *389*, 319–336.

Rothschild, G., Nelken, I., and Mizrahi, A. (2010). Functional organization and population dynamics in the mouse primary auditory cortex. Nat. Neurosci. *13*, 353–360.

Rueckel, M., Mack-Bucher, J.A., and Denk, W. (2006). Adaptive wavefront correction in two-photon microscopy using coherence-gated wavefront sensing. Proc. Natl. Acad. Sci. USA *103*, 17137–17142.

Runyan, C.A., Schummers, J., Van Wart, A., Kuhlman, S.J., Wilson, N.R., Huang, Z.J., and Sur, M. (2010). Response features of parvalbumin-expressing interneurons suggest precise roles for subtypes of inhibition in visual cortex. Neuron *67*, 847–857.

Rusakov, D.A., Wuerz, A., and Kullmann, D.M. (2004). Heterogeneity and specificity of presynaptic Ca^{2+} current modulation by mGluRs at individual hippocampal synapses. Cereb. Cortex *14*, 748–758.

Sabatini, B.L., Oertner, T.G., and Svoboda, K. (2002). The life cycle of $Ca^{(2+)}$ ions in dendritic spines. Neuron *33*, 439–452.

Sasaki, T., Takahashi, N., Matsuki, N., and Ikegaya, Y. (2008). Fast and accurate detection of action potentials from somatic calcium fluctuations. J. Neurophysiol. *100*, 1668–1676.

Sato, T.R., Gray, N.W., Mainen, Z.F., and Svoboda, K. (2007). The functional microarchitecture of the mouse barrel cortex. PLoS Biol. *5*, e189.

Sawinski, J., Wallace, D.J., Greenberg, D.S., Grossmann, S., Denk, W., and Kerr, J.N. (2009). Visually evoked activity in cortical cells imaged in freely moving animals. Proc. Natl. Acad. Sci. USA *106*, 19557–19562.

Schneggenburger, R., Zhou, Z., Konnerth, A., and Neher, E. (1993). Fractional contribution of calcium to the cation current through glutamate receptor channels. Neuron *11*, 133–143.

Schwaller, B. (2010). Cytosolic Ca^{2+} buffers. Cold Spring Harb Perspect Biol *2*, a004051.

Seelig, J.D., Chiappe, M.E., Lott, G.K., Dutta, A., Osborne, J.E., Reiser, M.B., and Jayaraman, V. (2010). Two-photon calcium imaging from head-fixed Drosophila during optomotor walking behavior. Nat. Methods *7*, 535–540.

Segal, M. (1995). Fast imaging of [Ca]i reveals presence of voltage-gated calcium channels in dendritic spines of cultured hippocampal neurons. J. Neurophysiol. *74*, 484–488.

Sherman, L., Ye, J.Y., Albert, O., and Norris, T.B. (2002). Adaptive correction of depth-induced aberrations in multiphoton scanning microscopy using a deformable mirror. J. Microsc. *206*, 65–71.

Shevtsova, Z., Malik, J.M., Michel, U., Bähr, M., and Kügler, S. (2005). Promoters and serotypes: targeting of adeno-associated virus vectors for gene transfer in the rat central nervous system in vitro and in vivo. Exp. Physiol. *90*, 53–59.

Shigetomi, E., Kracun, S., Sofroniew, M.V., and Khakh, B.S. (2010). A genetically targeted optical sensor to monitor calcium signals in astrocyte processes. Nat. Neurosci. *13*, 759–766.

Shimogori, T., and Ogawa, M. (2008). Gene application with in utero electroporation in mouse embryonic brain. Dev. Growth Differ. *50*, 499–506.

Shimomura, O. (1997). Membrane permeability of coelenterazine analogues measured with fish eggs. Biochem. J. *326*, 297–298.

Shimomura, O., Johnson, F.H., and Saiga, Y. (1962). Extraction, purification and properties of aequorin, a bioluminescent protein from the luminous hydromedusan, Aequorea. J. Cell. Comp. Physiol. *59*, 223–239.

Shimomura, O., Kishi, Y., and Inouye, S. (1993). The relative rate of aequorin regeneration from apoaequorin and coelenterazine analogues. Biochem. J. *296*, 549–551.

Skeberdis, V.A., Chevaleyre, V., Lau, C.G., Goldberg, J.H., Pettit, D.L., Suadicani, S.O., Lin, Y., Bennett, M.V., Yuste, R., Castillo, P.E., and Zukin, R.S. (2006). Protein kinase A regulates calcium permeability of NMDA receptors. Nat. Neurosci. *9*, 501–510.

Smith, S.J., and Augustine, G.J. (1988). Calcium ions, active zones and synaptic transmitter release. Trends Neurosci. *11*, 458–464.

Smith, S.J., Buchanan, J., Osses, L.R., Charlton, M.P., and Augustine, G.J. (1993). The spatial distribution of calcium signals in squid presynaptic terminals. J. Physiol. *472*, 573–593.

Smith, S.L., and Häusser, M. (2010). Parallel processing of visual space by neighboring neurons in mouse visual cortex. Nat. Neurosci. *13*, 1144–1149.

Sobczyk, A., Scheuss, V., and Svoboda, K. (2005). NMDA receptor subunit-dependent [Ca^{2+}] signaling in individual hippocampal dendritic spines. J. Neurosci. *25*, 6037–6046.

Sobczyk, A., and Svoboda, K. (2007). Activity-dependent plasticity of the NMDA-receptor fractional Ca^{2+} current. Neuron *53*, 17–24.

Sohya, K., Kameyama, K., Yanagawa, Y., Obata, K., and Tsumoto, T. (2007). GABAergic neurons are less selective to stimulus orientation than excitatory neurons in layer II/III of visual cortex, as revealed by in vivo functional Ca^{2+} imaging in transgenic mice. J. Neurosci. *27*, 2145–2149.

Soudais, C., Skander, N., and Kremer, E.J. (2004). Long-term in vivo transduction of neurons throughout the rat CNS using novel helper-dependent CAV-2 vectors. FASEB J. *18*, 391–393.

Spruston, N., Schiller, Y., Stuart, G., and Sakmann, B. (1995). Activity-dependent action potential invasion and calcium influx into hippocampal CA1 dendrites. Science *268*, 297–300.

Stephens, D.J., and Allan, V.J. (2003). Light microscopy techniques for live cell imaging. Science *300*, 82–86.

Stinnakre, J., and Tauc, L. (1973). Calcium influx in active Aplysia neurones detected by injected aequorin. Nat. New Biol. *242*, 113–115.

Stosiek, C., Garaschuk, O., Holthoff, K., and Konnerth, A. (2003). In vivo two-photon calcium imaging of neuronal networks. Proc. Natl. Acad. Sci. USA *100*, 7319–7324.

Sullivan, M.R., Nimmerjahn, A., Sarkisov, D.V., Helmchen, F., and Wang, S.S. (2005). In vivo calcium imaging of circuit activity in cerebellar cortex. J. Neurophysiol. *94*, 1636–1644.

Sumbre, G., Muto, A., Baier, H., and Poo, M.M. (2008). Entrained rhythmic activities of neuronal ensembles as perceptual memory of time interval. Nature *456*, 102–106.

Svoboda, K., Denk, W., Kleinfeld, D., and Tank, D.W. (1997). In vivo dendritic calcium dynamics in neocortical pyramidal neurons. Nature *385*, 161–165.

Svoboda, K., Helmchen, F., Denk, W., and Tank, D.W. (1999). Spread of dendritic excitation in layer 2/3 pyramidal neurons in rat barrel cortex in vivo. Nat. Neurosci. *2*, 65–73.

Svoboda, K., and Yasuda, R. (2006). Principles of two-photon excitation microscopy and its applications to neuroscience. Neuron *50*, 823–839.

Swandulla, D., Hans, M., Zipser, K., and Augustine, G.J. (1991). Role of residual calcium in synaptic depression and posttetanic potentiation: fast and slow calcium signaling in nerve terminals. Neuron *7*, 915–926.

Tabata, H., and Nakajima, K. (2001). Efficient in utero gene transfer system to the developing mouse brain using electroporation: visualization of neuronal migration in the developing cortex. Neuroscience *103*, 865–872.

Takahara, Y., Matsuki, N., and Ikegaya, Y. (2011). Nipkow confocal imaging from deep brain tissues. J. Integr. Neurosci. *10*, 121–129.

Takahashi, N., Kitamura, K., Matsuo, N., Mayford, M., Kano, M., Matsuki, N., and Ikegaya, Y. (2012). Locally synchronized synaptic inputs. Science *335*, 353–356.

Takano, T., Tian, G.F., Peng, W., Lou, N., Libionka, W., Han, X., and Nedergaard, M. (2006). Astrocyte-mediated control of cerebral blood flow. Nat. Neurosci. *9*, 260–267.

Takechi, H., Eilers, J., and Konnerth, A. (1998). A new class of synaptic response involving calcium release in dendritic spines. Nature *396*, 757–760.

Tamamaki, N., Yanagawa, Y., Tomioka, R., Miyazaki, J., Obata, K., and Kaneko, T. (2003). Green fluorescent protein expression and colocalization with calretinin, parvalbumin, and somatostatin in the GAD67-GFP knock-in mouse. J. Comp. Neurol. *467*, 60–79.

Tao, H.W., Zhang, L.I., Engert, F., and Poo, M. (2001). Emergence of input specificity of ltp during development of retinotectal connections in vivo. Neuron *31*, 569–580.

Theer, P., Hasan, M.T., and Denk, W. (2003). Two-photon imaging to a depth of 1000 microm in living brains by use of a Ti:Al2O3 regenerative amplifier. Opt. Lett. *28*, 1022–1024.

Tian, L., Hires, S.A., Mao, T., Huber, D., Chiappe, M.E., Chalasani, S.H., Petreanu, L., Akerboom, J., McKinney, S.A., Schreiter, E.R., et al. (2009). Imaging neural activity in worms, flies and mice with improved GCaMP calcium indicators. Nat. Methods *6*, 875–881.

Tóth, K., and McBain, C.J. (1998). Afferent-specific innervation of two distinct AMPA receptor subtypes on single hippocampal interneurons. Nat. Neurosci. *1*, 572–578.

Trevelyan, A.J., Sussillo, D., Watson, B.O., and Yuste, R. (2006). Modular propagation of epileptiform activity: evidence for an inhibitory veto in neocortex. J. Neurosci. *26*, 12447–12455.

Tsai, P.S., Friedman, B., Ifarraguerri, A.I., Thompson, B.D., Lev-Ram, V., Schaffer, C.B., Xiong, Q., Tsien, R.Y., Squier, J.A., and Kleinfeld, D. (2003). All-optical histology using ultrashort laser pulses. Neuron *39*, 27–41.

Tsien, R.Y. (1980). New calcium indicators and buffers with high selectivity against magnesium and protons: design, synthesis, and properties of prototype structures. Biochemistry *19*, 2396–2404.

Tsien, R.Y. (1981). A non-disruptive technique for loading calcium buffers and indicators into cells. Nature *290*, 527–528.

Tsien, R.Y. (1989). Fluorescent probes of cell signaling. Annu. Rev. Neurosci. *12*, 227–253.

Tsien, R.W., and Tsien, R.Y. (1990). Calcium channels, stores, and oscillations. Annu. Rev. Cell Biol. *6*, 715–760.

Tsien, R.Y., Pozzan, T., and Rink, T.J. (1982). Calcium homeostasis in intact lymphocytes: cytoplasmic free calcium monitored with a new, intracellularly trapped fluorescent indicator. J. Cell Biol. *94*, 325–334.

Tsien, R.Y., Rink, T.J., and Poenie, M. (1985). Measurement of cytosolic free Ca^{2+} in individual small cells using fluorescence microscopy with dual excitation wavelengths. Cell Calcium *6*, 145–157.

Usowicz, M.M., Sugimori, M., Cherksey, B., and Llinás, R. (1992). P-type calcium channels in the somata and dendrites of adult cerebellar Purkinje cells. Neuron *9*, 1185–1199.

Varga, Z., Jia, H., Sakmann, B., and Konnerth, A. (2011). Dendritic coding of multiple sensory inputs in single cortical neurons in vivo. Proc. Natl. Acad. Sci. USA *108*, 15420–15425.

Vogelstein, J.T., Packer, A.M., Machado, T.A., Sippy, T., Babadi, B., Yuste, R., and Paninski, L. (2010). Fast nonnegative deconvolution for spike train inference from population calcium imaging. J. Neurophysiol. *104*, 3691–3704.

Vogelstein, J.T., Watson, B.O., Packer, A.M., Yuste, R., Jedynak, B., and Paninski, L. (2009). Spike inference from calcium imaging using sequential Monte Carlo methods. Biophys. J. *97*, 636–655.

Wachowiak, M., and Cohen, L.B. (2001). Representation of odorants by receptor neuron input to the mouse olfactory bulb. Neuron *32*, 723–735.

Wachowiak, M., Cohen, L.B., and Zochowski, M.R. (2002). Distributed and concentration-invariant spatial representations of odorants by receptor neuron input to the turtle olfactory bulb. J. Neurophysiol. *87*, 1035–1045.

Wachowiak, M., Denk, W., and Friedrich, R.W. (2004). Functional organization of sensory input to the olfactory bulb glomerulus analyzed by two-photon calcium imaging. Proc. Natl. Acad. Sci. USA *101*, 9097–9102.

Wallace, D.J., Meyer zum Alten Borgloh, S., Astori, S., Yang, Y., Bausen, M., Kügler, S., Palmer, A.E., Tsien, R.Y., Sprengel, R., Kerr, J.N., et al. (2008). Single-spike detection in vitro and in vivo with a genetic Ca^{2+} sensor. Nat. Methods *5*, 797–804.

Wang, J.W., Wong, A.M., Flores, J., Vosshall, L.B., and Axel, R. (2003). Two-photon calcium imaging reveals an odor-evoked map of activity in the fly brain. Cell *112*, 271–282.

Wang, S.S., Denk, W., and Häusser, M. (2000). Coincidence detection in single dendritic spines mediated by calcium release. Nat. Neurosci. *3*, 1266–1273.

Wang, X., Lou, N., Xu, Q., Tian, G.F., Peng, W.G., Han, X., Kang, J., Takano, T., and Nedergaard, M. (2006). Astrocytic Ca^{2+} signaling evoked by sensory stimulation in vivo. Nat. Neurosci. *9*, 816–823.

Waters, J., and Helmchen, F. (2004). Boosting of action potential backpropagation by neocortical network activity in vivo. J. Neurosci. *24*, 11127–11136.

Waters, J., Larkum, M., Sakmann, B., and Helmchen, F. (2003). Supralinear Ca^{2+} influx into dendritic tufts of layer 2/3 neocortical pyramidal neurons in vitro and in vivo. J. Neurosci. *23*, 8558–8567.

Waters, J., Schaefer, A., and Sakmann, B. (2005). Backpropagating action potentials in neurones: measurement, mechanisms and potential functions. Prog. Biophys. Mol. Biol. *87*, 145–170.

Wettschureck, N., and Offermanns, S. (2005). Mammalian G proteins and their cell type specific functions. Physiol. Rev. *85*, 1159–1204.

Wilson, T. (2010). Spinning-disk microscopy systems. Cold Spring Harb Protoc *2010*, pdb.top88.

Wilt, B.A., Burns, L.D., Wei Ho, E.T., Ghosh, K.K., Mukamel, E.A., and Schnitzer, M.J. (2009). Advances in light microscopy for neuroscience. Annu. Rev. Neurosci. *32*, 435–506.

Winship, I.R., and Murphy, T.H. (2008). In vivo calcium imaging reveals functional rewiring of single somatosensory neurons after stroke. J. Neurosci. *28*, 6592–6606.

Wirth, D., Gama-Norton, L., Riemer, P., Sandhu, U., Schucht, R., and Hauser, H. (2007). Road to precision: recombinase-based targeting technologies for genome engineering. Curr. Opin. Biotechnol. *18*, 411–419.

Witten, I.B., Steinberg, E.E., Lee, S.Y., Davidson, T.J., Zalocusky, K.A., Brodsky, M., Yizhar, O., Cho, S.L., Gong, S., Ramakrishnan, C., et al. (2011). Recombinase-driver rat lines: tools, techniques, and optogenetic application to dopamine-mediated reinforcement. Neuron *72*, 721–733.

Wokosin, D.L., Loughrey, C.M., and Smith, G.L. (2004). Characterization of a range of fura dyes with two-photon excitation. Biophys. J. *86*, 1726–1738.

Xu, C., Zipfel, W., Shear, J.B., Williams, R.M., and Webb, W.W. (1996). Multiphoton fluorescence excitation: new spectral windows for biological nonlinear microscopy. Proc. Natl. Acad. Sci. USA *93*, 10763–10768.

Xu, X., Soutto, M., Xie, Q., Servick, S., Subramanian, C., von Arnim, A.G., and Johnson, C.H. (2007). Imaging protein interactions with bioluminescence resonance energy transfer (BRET) in plant and mammalian cells and tissues. Proc. Natl. Acad. Sci. USA *104*, 10264–10269.

Yaksi, E., and Friedrich, R.W. (2006). Reconstruction of firing rate changes across neuronal populations by temporally deconvolved Ca2+ imaging. Nat. Methods *3*, 377–383.

Yaksi, E., von Saint Paul, F., Niessing, J., Bundschuh, S.T., and Friedrich, R.W. (2009). Transformation of odor representations in target areas of the olfactory bulb. Nat. Neurosci. *12*, 474–482.

Yamada, Y., Michikawa, T., Hashimoto, M., Horikawa, K., Nagai, T., Miyawaki, A., Häusser, M., and Mikoshiba, K. (2011). Quantitative comparison of genetically encoded ca indicators in cortical pyramidal cells and cerebellar purkinje cells. Front Cell Neurosci *5*, 18.

Yang, G., Pan, F., Parkhurst, C.N., Grutzendler, J., and Gan, W.B. (2010). Thinned-skull cranial window technique for long-term imaging of the cortex in live mice. Nat. Protoc. *5*, 201–208.

Yasuda, R., Sabatini, B.L., and Svoboda, K. (2003). Plasticity of calcium channels in dendritic spines. Nat. Neurosci. *6*, 948–955.

Yizhar, O., Fenno, L.E., Davidson, T.J., Mogri, M., and Deisseroth, K. (2011). Optogenetics in neural systems. Neuron *71*, 9–34.

Yu, D., Baird, G.S., Tsien, R.Y., and Davis, R.L. (2003). Detection of calcium transients in Drosophila mushroom body neurons with camgaroo reporters. J. Neurosci. *23*, 64–72.

Yuste, R., and Denk, W. (1995). Dendritic spines as basic functional units of neuronal integration. Nature *375*, 682–684.

Yuste, R., and Katz, L.C. (1991). Control of postsynaptic Ca2+ influx in developing neocortex by excitatory and inhibitory neurotransmitters. Neuron *6*, 333–344.

Yuste, R., Majewska, A., Cash, S.S., and Denk, W. (1999). Mechanisms of calcium influx into hippocampal spines: heterogeneity among spines, coincidence detection by NMDA receptors, and optical quantal analysis. J. Neurosci. *19*, 1976–1987.

Yuste, R., Peinado, A., and Katz, L.C. (1992). Neuronal domains in developing neocortex. Science *257*, 665–669.

Zhang, F., Aravanis, A.M., Adamantidis, A., de Lecea, L., and Deisseroth, K. (2007). Circuit-breakers: optical technologies for probing neural signals and systems. Nat. Rev. Neurosci. *8*, 577–581.

Zhao, Y., Araki, S., Wu, J., Teramoto, T., Chang, Y.F., Nakano, M., Abdelfattah, A.S., Fujiwara, M., Ishihara, T., Nagai, T., and Campbell, R.E. (2011). An expanded palette of genetically encoded Ca^{2+} indicators. Science *333*, 1888–1891.

Zucker, R.S. (1999). Calcium- and activity-dependent synaptic plasticity. Curr. Opin. Neurobiol. *9*, 305–313.

Project II – Development of direction selectivity in mouse cortical neurons

Published in **Neuron**, 2011, 71(3): 425-432

Neuron
Report

Development of Direction Selectivity in Mouse Cortical Neurons

Nathalie L. Rochefort,[1,2] Madoka Narushima,[1,2,3] Christine Grienberger,[1] Nima Marandi,[1] Daniel N. Hill,[1] and Arthur Konnerth[1,*]
[1]Institute of Neuroscience and Center for Integrated Protein Science, Technical University Munich, Biedersteinerstrasse 29, 80802 Munich, Germany
[2]These authors contributed equally to this work
[3]Present address: Department of Physiology, Tokyo Women's Medical University, Kawada-cho 8-1, Shinjuku-ku, 162-8666 Tokyo, Japan
*Correspondence: arthur.konnerth@lrz.tum.de
DOI 10.1016/j.neuron.2011.06.013

SUMMARY

Previous studies of the ferret visual cortex indicate that the development of direction selectivity requires visual experience. Here, we used two-photon calcium imaging to study the development of direction selectivity in layer 2/3 neurons of the mouse visual cortex in vivo. Surprisingly, just after eye opening nearly all orientation-selective neurons were also direction selective. During later development, the number of neurons responding to drifting gratings increased in parallel with the fraction of neurons that were orientation, but not direction, selective. Our experiments demonstrate that direction selectivity develops normally in dark-reared mice, indicating that the early development of direction selectivity is independent of visual experience. Furthermore, remarkable functional similarities exist between the development of direction selectivity in cortical neurons and the previously reported development of direction selectivity in the mouse retina. Together, these findings provide strong evidence that the development of orientation and direction selectivity in the mouse brain is distinctly different from that in ferrets.

INTRODUCTION

Throughout the visual system of vertebrates, neurons are tuned to respond to different features of a visual scene, such as the position, orientation, or direction of motion of a given object. In the mammalian primary visual cortex, most neurons respond selectively to a preferred orientation of visual stimuli. Some of these neurons are also direction selective, in that they are significantly more activated by a preferred direction of stimulus motion than by any other direction (Hubel, 1959; Hubel and Wiesel, 1959). Since the first recordings of visual responses in the cat primary visual cortex (Hubel, 1959; Hubel and Wiesel, 1959), numerous studies have focused on the mechanisms underlying the development of selective properties of visual cortical neurons. These studies were mostly performed in carnivores, such as cats and ferrets, and in primates. In these species, orientation and direction preferences are elaborated with a high degree of selectivity only at the cortical level along the retino-geniculo-cortical pathway (see review in White and Fitzpatrick, 2007) and neurons with a similar orientation or direction preference are clustered into radial columns (Hubel and Wiesel, 1962, 1968; Blasdel and Salama, 1986; Bonhoeffer and Grinvald, 1991; Bosking et al., 1997). It has been shown that orientation and direction selectivity are established by different mechanisms. While the initial establishment of orientation selectivity in cortical neurons is independent of visual experience (see review in White and Fitzpatrick, 2007), several lines of evidence indicate that the emergence of direction selectivity strictly requires visual experience. Thus, direction-preference maps are absent at eye opening and do not develop in ferrets that are reared in darkness (Li et al., 2006). Moreover, visual experience with moving stimuli just after eye opening drives the emergence of direction-selective responses in the ferret visual cortex (Li et al., 2008). However, the connectivity and the mechanisms that are necessary for the emergence of direction selectivity remain unclear.

In recent years, rodents and especially mice are becoming an attractive model for the investigation of such mechanisms in vivo. Various transgenic mice lines have been used to study visual system development (Fagiolini et al., 2003; Cang et al., 2005), plasticity (Fagiolini et al., 2004; Syken et al., 2006; Wang et al., 2010), and function of specific cell types in the visual cortex (Sohya et al., 2007; Kerlin et al., 2010; Runyan et al., 2010). It is important to remember that unlike in ferrets, cats, and primates, neurons in the primary visual cortex of rodents are not organized into orientation columns. Instead, orientation-selective neurons are distributed in a mixed "salt-and-pepper" manner throughout the primary visual cortex (Ohki et al., 2005; Van Hooser et al., 2005). Nevertheless, highly tuned orientation- and direction-selective neurons have been shown to be abundant in the mouse visual cortex (Dräger, 1975; Métin et al., 1988; Sohya et al., 2007; Niell and Stryker, 2008; Wang et al., 2010). While the emergence of orientation selectivity has been investigated in the rodent visual cortex (Fagiolini et al., 1994, 2003), the development of direction selectivity has so far received less attention, except in recent studies that investigated the emergence of direction selectivity at the level of the mouse retina.

In mice, retinal ganglion cells exhibit strong direction selectivity (Elstrott et al., 2008; Yonehara et al., 2009). Remarkably, this strong direction selectivity is already present at eye opening (Elstrott et al., 2008; Chen et al., 2009; Yonehara et al., 2009).

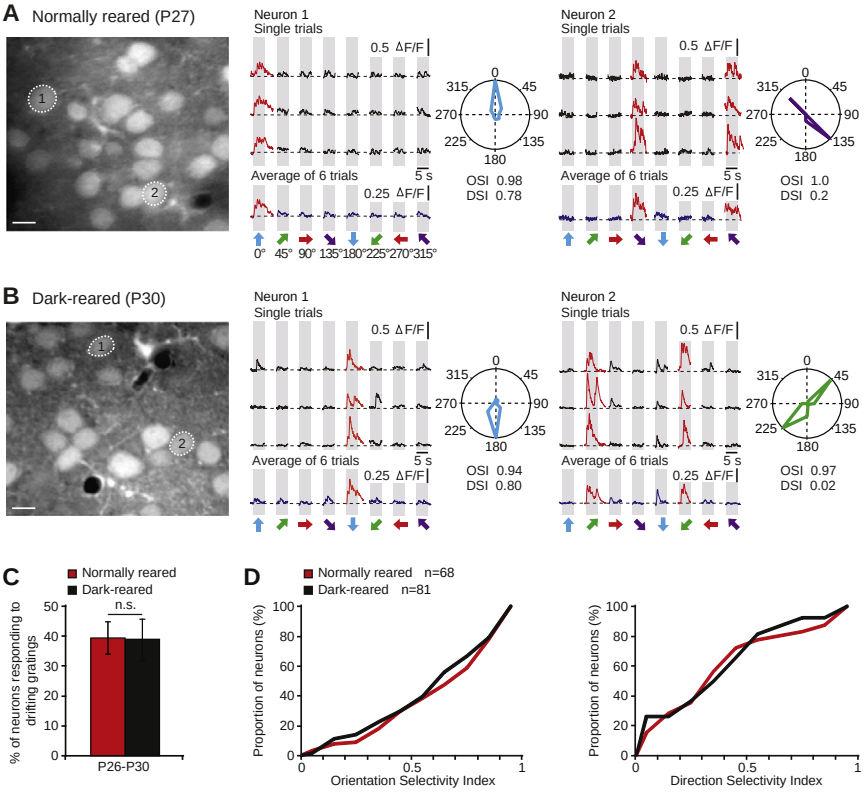

Figure 1. Orientation-Selective and Direction-Selective Neurons in Normally Reared and Dark-Reared Juvenile Mice

(A and B) In vivo two-photon images of layer 2/3 neurons in the visual cortex of normally reared (A) and dark-reared (B) juvenile mice (P27 and P30, respectively) are shown in the left panels. Calcium transients evoked by visual stimulation of orientation-selective neurons indicated in left panels are shown in the middle and right panels. Gray regions indicate periods of visual stimulation with drifting gratings (0.03 cpd, 1 Hz) schematized by oriented arrows on the bottom of each panel. Three single trials are represented with black lines and the average of six trials is shown in blue. Neuron 1 responded selectively to a horizontal drifting grating moving in the upward direction (red calcium transients). The right panels are polar plots showing the neuron's response function to oriented drifting gratings. The responses to each of the eight directions tested were normalized with respect to the maximal response. The response function was constructed by connecting lines between the eight values. OSI, orientation-selectivity index; DSI, direction-selectivity index. Scale bars = 10 μm. (C) Percentage of neurons responding to drifting gratings (0.03 cpd) in normally reared (red) and dark-reared (black) juvenile mice (P26–P30) (n.s., not significantly different, Mann-Whitney test, $p = 0.767$; n = 174 and 220 neurons, respectively). Error bars indicate SEM. (D) Cumulative distributions of OSI and DSI from all responsive neurons of normally reared (red) and dark-reared (black) juvenile mice. No significant difference was found between the two groups (Mann-Whitney test, OSI, $p = 0.50$; DSI, $p = 0.15$).

Moreover, robust directional responses have been detected in dark-reared mice and in mice lacking cholinergic retinal waves (Elstrott et al., 2008; Chen et al., 2009), indicating that visual experience and patterned activity are not required for the development of direction selectivity in the mouse retina. At present, it is unknown how the early presence of direction selectivity in the retina is related to the motion sensitivity of cortical neurons and when and how direction selectivity emerges in the mouse visual cortex. In this study, we investigated the development of orientation and direction selectivity in the mouse primary visual cortex by using in vivo two-photon calcium imaging (Stosiek et al., 2003; Rochefort et al., 2009). We characterized the responses of layer 2/3 neurons to oriented drifting gratings with single-cell resolution at different developmental stages, from eye opening until adulthood, in normally reared mice as well as in mice reared in darkness for a month.

RESULTS

Orientation- and Direction-Selective Neurons in the Visual Cortex of Dark-Reared Mice

We first compared neuronal calcium signals evoked by drifting gratings in the monocular region of the primary visual cortex of normally reared and dark-reared juvenile mice (P26–P30). For this purpose, we presented drifting gratings to the contralateral eye while performing two-photon calcium imaging recordings of layer 2/3 neurons stained with the fluorescent calcium indicator dye OGB1-AM (Rochefort et al., 2009). Figure 1A illustrates such recordings obtained in a normally reared juvenile mouse (P27). In the field of view (left panel of Figure 1A), neuron 1 displayed large calcium transients during the presentation of a specific orientation and direction of the drifting gratings (middle panel, direction of 0°, red calcium transients), but no significant responses for all the other directions. A quantitative analysis of the stimulus-evoked responses showed that the neuron had an orientation-selectivity index (OSI) of 0.98 and a direction-selectivity index (DSI) of 0.78. Thus, this neuron was defined as a highly tuned orientation- and direction-selective neuron (Niell and Stryker, 2008). In the same field of view, neuron 2 displayed large calcium transients for one orientation of the drifting gratings, but not for a specific direction of motion (right panel, responses for both directions of 135° and 315°). Thus, this neuron was identified as a highly tuned orientation-selective, but not direction-selective, neuron (OSI, 1.0; DSI, 0.2). Surprisingly, both orientation- and direction-selective neurons were also found in the visual cortex of dark-reared mice. Figure 1B illustrates an example of a direction-selective (middle panel) and of an orientation-selective neuron (right panel) in a juvenile dark-reared mouse (P30). An analysis of all recorded neurons in normally reared and dark-reared mice showed that the percentage of

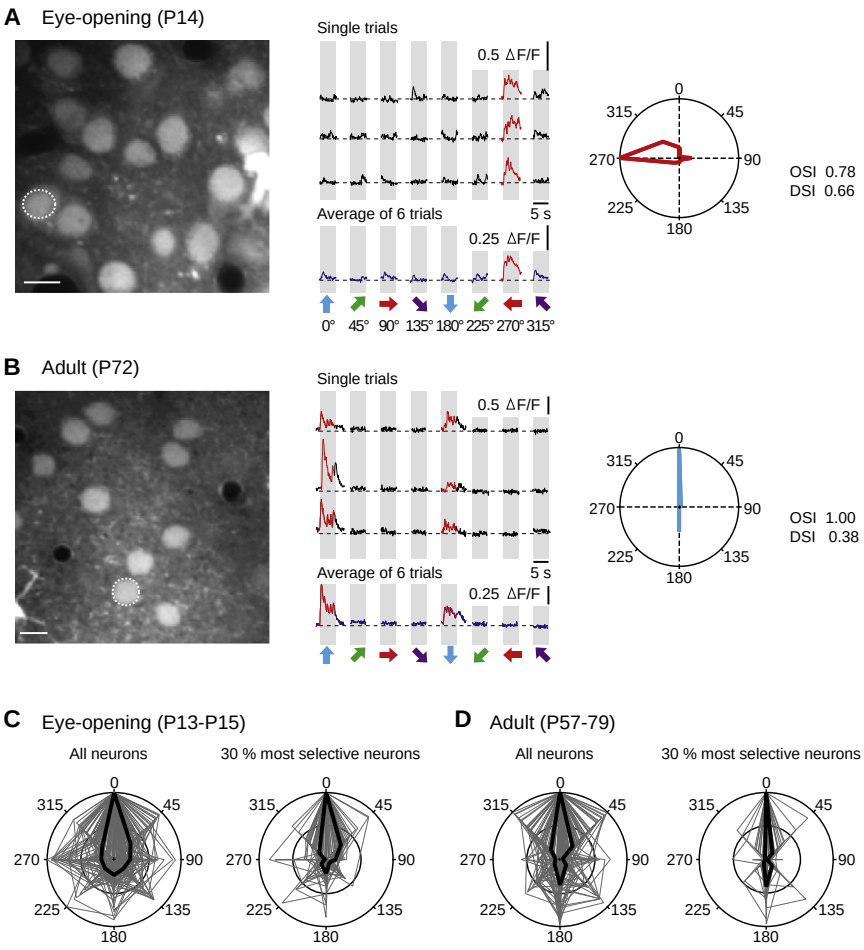

Figure 2. Direction-Selective Neurons Are Present Just after Eye Opening

(A and B) In vivo two-photon images of layer 2/3 neurons in the visual cortex of normally reared mice at eye opening (P14) and in adulthood (P72) are shown in the right panels. Calcium transients evoked by drifting gratings (0.03 cpd) in the neurons indicated in the left panels are shown in the middle panels. The same conventions are used as in Figure 1. The right panels are polar plots showing the neuron's response function to oriented drifting gratings. Scale bars = 10 μm. (C and D) Overlay of polar plots obtained from the visually evoked activity in all neurons (left panels, n = 167 and 81 neurons, respectively) and in the 30% most selective neurons (right panels) in normally reared mice just after eye opening (P13–P15) and in adulthood (P57–P79). Polar plots were normalized by the maximal response and rotated to place the preferred direction at 0°. Black lines indicate median tuning function.

neurons responding to drifting gratings was not significantly different in the two groups (Figure 1C). Furthermore, the tuning level of the responsive neurons was also remarkably similar (Figure 1D and Figure S1, available online). The quantitative estimation of orientation and direction tuning showed no significant differences between the cumulative distributions of both OSIs and DSIs (Mann-Whitney test: OSI, p = 0.50; DSI, p = 0.15) (Figure 1D). In addition, we explored whether the visual stimulation itself modified the level of orientation and direction selectivity in dark-reared mice. We found that both OSIs and DSIs were not significantly different between the first and last trials of visual stimulation (Figure S2). Thus, we conclude that both orientation and direction selectivity develop without visual experience during the first postnatal month in the mouse visual cortex.

Orientation- and Direction-Selective Neurons at Eye Opening

It has been recently shown that the earliest light-evoked responses are detected in the mouse retina at P10 (Tian and Copenhagen, 2003; Chen et al., 2009), ~2–3 days before the eyes open. We found that just before eye opening (P10–P12), neurons of the mouse visual cortex were spontaneously active, but no activity could be evoked by drifting gratings presented either through closed eyelids or after the gentle opening of the eyelids with forceps (Figures S3A and S3B). Only strong luminance changes, consisting either of light flashes or of a sudden transition between a black and a gray screen (Figure S3C), could elicit a response from layer 2/3 neurons. It is important to note the remarkably dense response pattern, with more than 80% of neurons activated in the field of view (Figure S3C, left panel, red neurons; Figure S3D). A similarly dense activity pattern was also observed when the eyelids were gently opened with forceps in these mice (Figure S3C). These results indicate that, at early stages of development, activity patterns are dense not only spontaneously (Rochefort et al., 2009), but also in response to a sensory stimulus. By contrast, in adult mice (P57–P79), the activity pattern becomes much sparser, with only 23% of the recorded neurons responding to such changes in luminance (Figure S3D).

The earliest responses evoked by drifting gratings were detected just after eye opening, i.e., on the day of eye opening or 1 day later (Figure 2A). Nearly half of these responsive neurons were orientation selective (OSI > 0.5) (Figures 2A, 2C, and 4D). We overlaid the polar plots obtained from all responsive neurons recorded just after eye opening (Figure 2C). The median tuning function (Figure 2C, black line) shows that the early responsive neurons were selective not only for the orientation of the drifting gratings but also for their direction of motion. Remarkably, nearly all (93%) of the orientation-selective neurons were also direction selective (OSI > 0.5 and DSI > 0.5) (Figures 2A, 2C, and 4D). Thus, in the mouse visual cortex, the earliest neurons tuned for the orientation of the stimulus appear just after eye opening and are strongly tuned for the direction of stimulus motion.

Interestingly, we noticed that at early stages after eye opening, most direction-selective neurons had a directional preference

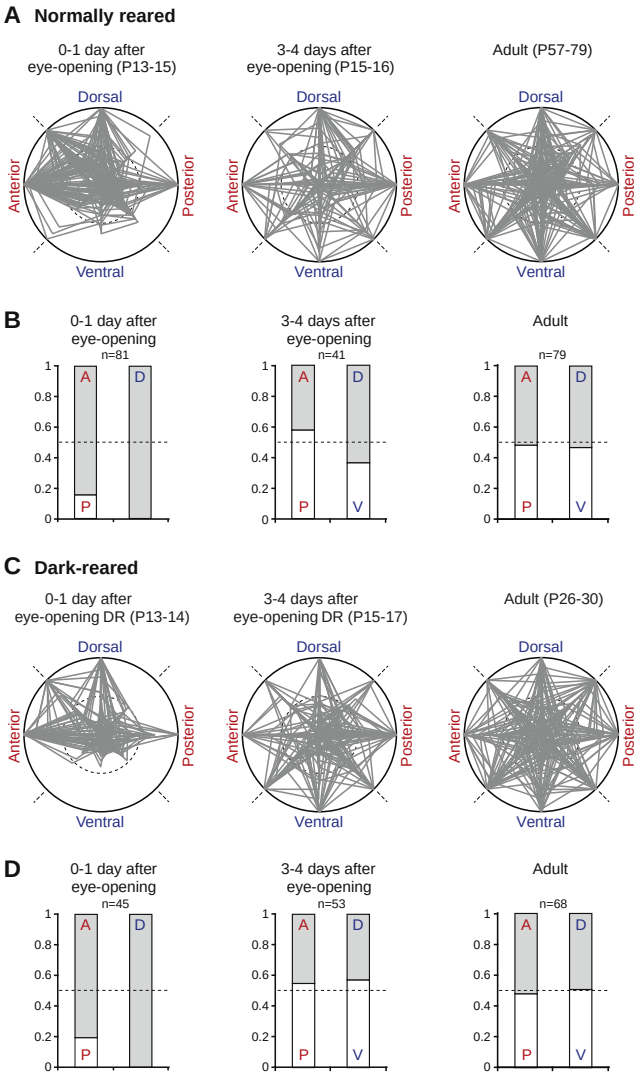

Figure 3. Preference for Anterodorsal Directions at Eye Opening

(A) Overlay of polar plots obtained from the responses evoked by drifting gratings (0.03 cpd) in all selective neurons (OSI > 0.5) of normally reared mice at different postnatal ages from eye opening (P13–P15) to adulthood (P57–P79). Polar plots were normalized by the maximal response. (B) The symmetry of preferred directions along a given axis (anterior-posterior or dorsal-ventral) was tested by calculating the fraction of neurons with a preference for a given direction (e.g., anterior [A]) along the axis versus the fraction of neurons with a preference for the opposite direction (e.g., posterior [P]). A perfectly symmetric axis would have 50% of neurons preferring either opposite direction (dashed lines). For the four postnatal ages, the light gray and white bars show for each axis the fraction of neurons with a preference for the anterior (A) versus posterior (P) direction and for the dorsal (D) versus ventral (V) direction, respectively. (C and D) Same conventions as in (A) and (B) for polar plots obtained for all selective neurons (OSI > 0.5) in dark-reared mice at three different postnatal ages from eye opening (P13–P15) to adulthood (P30).

for gratings moving toward either the anterior (270°, Figure 2A) or the dorsal direction (0°). In order to compare the distribution of preferred directions in young and adult mice, we overlapped the polar plots obtained from all orientation-selective neurons recorded at different ages: just after eye opening (0–1 day), 3–4 days after eye opening, and in 2-month-old adult mice (Figure 3A). Just after eye opening, the direction-selective neurons displayed a clear preference for the anterior direction along the anterior-posterior axis as well as a preference for the dorsal direction along the ventral-dorsal axis (Figures 3A and 3B). Not a single neuron was found with a preference for the ventral direction (Figure 3A). In order to quantify this bias, we counted the number of neurons with a preference for a given direction along each axis (anterior-posterior and ventral-dorsal). The representation of opposite directions was strongly biased along both axes, with anterior and dorsal directions being significantly overrepresented (Figure 3B). This distribution of direction preferences did not depend on the preferred spatial frequency of the drifting gratings (Figure S4). A few days later (3–4 days after eye opening), this asymmetric organization disappeared (Figures 3A and 3B). As in 2-month-old adult mice, the distributions along the anterior-posterior and ventral-dorsal axes were roughly symmetric in that the number of neurons that prefer a given direction of motion was roughly the same along both axes (Figures 3A and 3B). It is noteworthy that the oblique orientations were strongly underrepresented just after eye opening (especially 45°, 135°, and 225°) and this bias disappeared 3–4 days after eye opening.

We found that the bias in the distribution of direction preferences was similarly present in the visual cortex of dark-reared animals just after eye opening. As in normally reared animals, this bias disappeared 3–4 days after eye opening (Figures 3C and 3D). At the three ages tested (0–1 day, 3–4 days after eye opening, and young adult, P26–P30), no differences were noticed in the direction preference of visual cortical neurons of normally reared and dark-reared mice. These results indicate that the developmental change of the direction-preference distribution is a highly robust intrinsic process that does not depend on visual experience.

Developmental Changes in Orientation and Direction Selectivity

The above-mentioned developmental increase in the responsiveness to all directions of stimulus motion was paralleled by a steep increase in the overall number of motion-sensing visual cortex neurons. Thus, the proportion of neurons responding to drifting gratings (0.03 cpd) increased significantly between the day of eye opening and just 2–3 days later (from 12% to 33%, n = 1216 neurons in 20 mice and n = 201 neurons in 7 mice, respectively, Mann-Whitney test, $p < 0.001$) (Figure 4A). This proportion increased further during the next 2 months, eventually reaching a value of 42.5% (n = 174 neurons in 7 mice). This proportion of neurons responding to drifting gratings in layer 2/3 of the visual cortex of adult mice is similar to what has been described in other studies by using two-photon imaging in mouse (Zariwala et al., 2011) and rat visual cortex (Ohki et al., 2005). In addition, we tested five other spatial frequencies of drifting gratings (0.01, 0.015, 0.02, 0.04, and 0.08 cpd) in two age groups (0–1 day after eye opening and at 2 months old). Taking into account the responses to all spatial frequencies tested, we found an increase of 12% in the proportion of neurons responding to drifting gratings in both age groups (Figure S5A). We thus reached a value of 55% of neurons responding to drifting gratings in adult mice, which is very close to what was found in a previous study testing a larger set of spatial frequencies (Kerlin et al., 2010).

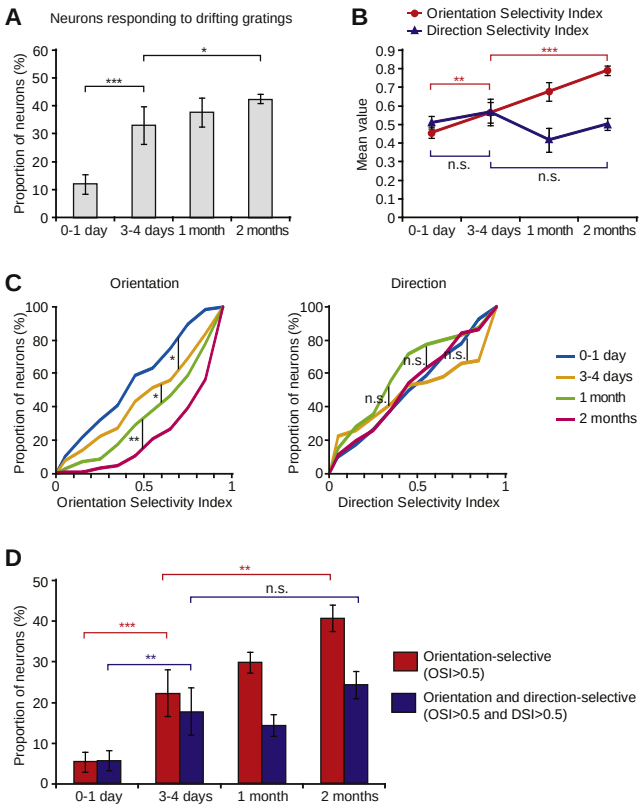

Figure 4. Proportion of Responsive Neurons and Population Tuning Develops during the First Two Postnatal Months

(A) Percentage of neurons responding to drifting gratings (0.03 cpd) in normally reared mice at four different ages from eye opening (0–1 day after eye opening, P13–P15) to adulthood (P57–P79) (Mann-Whitney test, *p < 0.05, ***p < 0.001, n = 1216, 201, 174, and 174 neurons from 20, 7, 10, and 7 mice, respectively). Error bars indicate SEM. (B) Mean OSI (red) and DSI (blue) in all neurons responding to drifting gratings (0.03 cpd) in normally reared mice. The results showed a significant increase of the mean OSI during the first 2 postnatal months (Mann-Whitney test, OSI, **p < 0.01, ***p < 0.001). In contrast, no significant difference (n.s., Mann-Whitney test, p = 0.62, 0–1 and 3–4 days after eye opening; p = 0.56, 3–4 days and 2 months) was found between mean DSIs. Error bars indicate SEM (n = 167, 62, 68, and 81 neurons, respectively). (C) Cumulative distributions of OSI and DSI from all neurons responding to drifting gratings (0.03 cpd) recorded in normally reared mice of four different ages. The results show a significant increase of OSI during the first 2 postnatal months (Mann-Whitney test, OSI, *p < 0.05, **p < 0.01). In contrast, no significant difference was found between DSI at different ages (n = 167, 62, 68, and 81 neurons, respectively). (D) Percentage of orientation-selective neurons (OSI > 0.5, red) and of direction-selective neurons (OSI > 0.5 and DSI > 0.5, blue) among all neurons recorded in normally reared mice at four different ages, during the presentation of drifting gratings (0.03 cpd) (Mann-Whitney test, **p < 0.01, ***p < 0.001; n.s., p = 0.14). Error bars indicate SEM.

During the first 2 postnatal months, not only did the proportion of neurons responding to drifting gratings increase, but also the proportion of orientation-selective neurons increased among the responsive neurons. Figure 4B compares the development of orientation and direction selectivity during this period. The mean OSI values indicate a significant increase of the orientation tuning between the day of eye opening, 3–4 days after eye opening, and 2 months later (Mann-Whitney test, p < 0.05) (Figure 4B; see also Figure 2). In addition, the tuning width of the orientation-selective responses decreases slightly during development from a mean value of 32° at eye opening to 27° in 2-month-old adults (Figure S6). The values found in adult mice (mean, 27°; median, 26°) are similar to those previously described for orientation-selective neurons in the adult mouse visual cortex (Niell and Stryker, 2008; Wang et al., 2010). Notably, already in the youngest age group (0–1 day after eye opening), a significant proportion (35%) of the orientation-selective neurons had a narrow tuning width (<30°) (Figure S6A). Whereas orientation tuning increased during development, the mean DSI values (Figure 4B and Figure S7) showed no significant change in the direction tuning between the day of eye opening, 3–4 days later, and in adults. In line with these results, the cumulative distributions of OSIs and DSIs clearly showed a significant increase of orientation but not of direction selectivity during the first 2 postnatal months (Figure 4C). These tuning properties did not depend on the preferred spatial frequency of the drifting gratings (Figure S5B).

Thus, just after eye opening, among orientation-selective neurons (5% of all recorded neurons with gratings of 0.03 cpd) nearly all were highly tuned for the direction of stimulus motion (Figure 4D and Figure S8). At 3–4 days after eye opening, the proportion of neurons responding to drifting gratings increased and the vast majority of the orientation-selective neurons were still strongly direction selective (17.5% of all cortical neurons with gratings of 0.03 cpd, Figure 4D and Figure S8). At this early stage, most of the orientation-selective neurons did not respond at all to the opposite direction of movement of the preferred orientation (Figure 2A and Figures S7A and S7B) and only 4% of all cortical neurons were strictly orientation selective (responding to both directions of movement). This was followed by a 4-fold increase in the proportion of strictly orientation-selective neurons, whereas the proportion of direction-selective ones remained stable (Figure 4D). As a consequence, at the age of 2 postnatal months, only half of the orientation-tuned neurons were also direction selective (Figure 4D and Figure S8). The tuning properties of these neurons were largely similar to those reported by previous studies in normally reared adult mice (Niell and Stryker, 2008; Wang et al., 2010). Altogether, these results establish that the early development of direction selectivity is distinctly different from that of orientation selectivity in the mouse visual cortex.

DISCUSSION

In this study, we obtained unexpected insights into the development of direction selectivity in neurons of the mouse visual cortex. Neurons selective for the orientation of drifting gratings were detected just after eye opening and nearly all were also highly tuned for the direction of stimulus motion. Furthermore, we found a marked preference of these cortical neurons for anterodorsal directions. During later development, the number of neurons responding to drifting gratings increased in parallel with the fraction of neurons that were orientation selective but not direction selective. This developmental increase was similar in normally reared and dark-reared mice. Together, these findings indicate that the early development of orientation and direction selectivity depends on intrinsic factors of mouse visual cortical neurons, without a detectable contribution from visual experience.

Different Development of Orientation Selectivity and Direction Selectivity in Mice and Ferrets

Before eye opening, cortical neurons can respond to visual stimuli through closed eyelids. For example, in ferrets, the firing of visual cortex neurons is modulated by drifting gratings presented through closed eyelids (Krug et al., 2001). These results, however, contrast with those obtained in the present study in mice, where drifting grating stimuli were ineffective before eye opening. In our hands, only strong luminance changes could evoke cortical activity before eye opening and this activity was characterized by simultaneous calcium transients in the majority of layer 2/3 neurons. This dense activity is reminiscent of the spontaneous activity pattern recorded before eye opening (Rochefort et al., 2009). An important feature of the spontaneous activity is that it undergoes a transition from dense to sparse just after eye opening (Rochefort et al., 2009). Our present results indicate that such a transition from a dense activity to a stimulus-specific one also occurs around eye opening for stimulus-evoked neuronal responses. Interestingly, a recent study provides additional support for major functional changes in the rat visual cortex during the period just preceding eye opening (Colonnese et al., 2010). It has been suggested that this switch prepares the developing cortex for patterned vision (Colonnese et al., 2010).

Neurons responding to drifting gratings were first observed in the mouse visual cortex soon after eye opening. At this early stage (0–1 day and 3–4 days after eye opening), nearly all orientation-selective neurons are also direction selective. Then the fraction of neurons that are orientation, but not direction, selective gradually increases during the first 2 postnatal months. These results are in contrast to those obtained in the ferret visual cortex, where the developmental sequence is characterized by the presence of orientation-selective neurons at eye opening that subsequently acquire direction selectivity and achieve functional maturity around 2 weeks after eye opening (Li et al., 2006; White and Fitzpatrick, 2007). Thus, from different states at eye opening, the mouse and ferret visual systems undergo converging developmental processes, such that in adults of both species, nearly half of the orientation-selective neurons are also direction selective. The origin of the orientation-selective neurons that are lacking direction selectivity in the mouse visual cortex is unknown. This fraction of neurons appears around 3-4 days after eye opening and increases during the following 2 months (Figure 4D; red area in Figure S8). Future studies need to establish whether these purely orientation-selective neurons evolve from direction-selective ones or whether they constitute a separate class that emerges de novo at about 3-4 days after eye opening.

Importantly, in ferrets, dark rearing prevents the formation of direction-selective maps. This indicates a crucial role of visual experience for this developmental process (Li et al., 2006). In the mouse visual cortex, our data show that dark rearing has no detectable influence on the development of direction selectivity (Figure 1 and Figure S9). It should be noted that we focused our study primarily on the early development of orientation selectivity and direction selectivity and not on the effect of long-term visual deprivation. It has previously been shown that in the absence of visual input, orientation selectivity normally appears during the first postnatal month (Iwai et al., 2003; Wang et al., 2010), but then degrades after prolonged lack of visual experience in rodents (Benevento et al., 1992; Fagiolini et al., 1994, 2003; Iwai et al., 2003) and cats (Frégnac and Imbert, 1978; Crair et al., 1998).

Distinctive Features of the Mouse Visual System

In mice, direction selectivity is already present at the level of the retina (Elstrott and Feller, 2009). On-Off direction-selective ganglion cells have been detected in mouse retina at the time of eye opening (P14) (Elstrott et al., 2008; Chen et al., 2009). It was shown that at this developmental stage these direction-selective ganglion cells exhibit a strong preference for motion toward either the temporal or the ventral pole of the retina, which in visual coordinates corresponds to anterior and dorsal motion direction (Elstrott et al., 2008). Similar results were obtained in the retina of dark-reared mice of the same age (Elstrott et al., 2008). In adult retinas, the anteroposterior asymmetry disappears and the ventro-dorsal one is strongly reduced (Elstrott et al., 2008). Interestingly, our present results demonstrate a strikingly similar developmental pattern of direction selectivity in the upper layer visual cortical neurons. Thus, as in the retina, direction selectivity was detected at eye opening and emerges independently of visual experience. Furthermore, direction-selective neurons recorded just after eye opening in both the cortex and the retina have a similar preference for the dorsal and anterior directions of motion. This preference disappeared in the cortical neurons of adult mice.

One possible conclusion from these results is that in the mouse visual system direction selectivity emerges in the retina and is relayed to the visual cortex. This notion finds support in the previous observations that On-Off direction-selective retinal ganglion cells project both to the LGN and to the superior colliculus in specific laminae (Huberman et al., 2009). In line with this anatomical evidence, direction-selective neurons were recorded in the rat superior colliculus around eye opening (P13) and, as in the mouse visual cortex, the proportion of direction-selective neurons was found to remain stable from P15 to adulthood (Fortin et al., 1999). By contrast, the relay of direction-selective information through the rodent LGN is less clear. While the receptive fields of neurons in the mouse LGN were described as center-surround with exclusively ON-center or OFF-center responses (Grubb and Thompson, 2003), direction-selective cells in mouse or rat LGN are not yet described. However, it remains unclear whether LGN neurons that receive direct projections from direction-selective retinal ganglion cells were ever studied specifically. Another possibility is that LGN-receptive fields are more broadly tuned and that direction selectivity is generated again at the cortical level. It is noteworthy that the directional tuning of the cortical neurons recorded in this study is more narrow than the directional tuning of the mouse retinal ganglion cells (Elstrott et al., 2008). This result indicates that in mice the direction selectivity is refined along the retino-geniculo-cortical pathway. It is unclear whether such a possible refinement is found only in mice. Interestingly, there is some evidence for direction bias in the retinal ganglion cells of cats (Levick and Thibos, 1980; Shou et al., 1995) as well as in the cat and primate LGN (Vidyasagar and Urbas, 1982; Thompson et al., 1994; Xu et al., 2002). However, detailed studies in the retina and LGN of these species are needed for solving this issue.

Taken together, there is accumulating evidence that the anatomical difference between the primary visual cortices of higher mammals (ferrets, cats, or primates) and rodents, i.e., columnar organization versus salt-and-pepper structure, is paralleled by functional differences during development. These differences include the amount of visual experience before eye opening (through eyelids), the developmental time course of the maturation of orientation selectivity and direction selectivity, and the relative contributions of visual experience versus intrinsic factors. However, despite these differences during development, the mature visual cortex of mice preserves many fundamental properties of visual circuit function (Ohki et al., 2005; Niell and Stryker, 2008). A detailed comparison and evaluation of these differences may be critical for a better understanding of visual information processing in the mammalian visual system.

EXPERIMENTAL PROCEDURES

Animals and Surgery

All experimental procedures were performed in accordance with institutional animal welfare guidelines and were approved by the government of Bavaria, Germany. C57BL/6 mice were either reared in 12 hr/12 hr light/dark cycles (P10–P12, n = 5; P13–P15, n = 20; P15–P16, n = 7; P26–P30, n = 10; P57–P79, n = 7) or born and reared in complete darkness (P13–P15, n = 12; P15–P17, n = 10; P26–P30, n = 9). The day of birth (P0) was accurately ascertained as was the day of eye opening. For this, the eyes were checked four times per day (at 8 am, 1 pm, 6 pm, and 8 pm) beginning at the age of P10 and the eyes were considered opened as soon as we observed the initial break in the membrane sealing the eyelids. Strips of Ilford-FP4 plus 125 film were attached to the wall of the dark-rearing room and then developed to confirm that the films (and the mice) had not been exposed to light.

Animals were prepared for in vivo two-photon calcium imaging as described previously (Stosiek et al., 2003; see Supplemental Information). Ophthalmic ointment (Bepanthen, Bayer) was applied to both eyes to prevent dehydration during surgery. After surgery, the level of anesthetic was decreased to 0.8% isoflurane for recordings (breathing rate: 110–130 breaths/min). For dark-reared animals, the surgery was done under red light and the eyes were covered with an opaque eye cream and a black cone. The cone and the cream were removed just before (around 2–3 min) starting the recordings.

High-Speed Two-Photon Ca^{2+} Imaging

In vivo calcium imaging was performed by using a custom-built two-photon microscope based on a Ti:Sapphire pulsing laser (model: Chameleon; repetition rate: 80 MHz; pulse width: 140 fs; Coherent) and resonant galvo/mirror (8 kHz; GSI Group Inc.) system (Sanderson and Parker, 2003). The scanner was mounted on an upright microscope (BX51WI, Olympus, Tokyo, Japan) equipped with a water-immersion objective (60 ×, 1.0 NA, Nikon, Japan or 40 ×/0.8, Nikon, Japan). Emitted photons were detected by photomultiplier tubes (H7422-40; Hamamatsu). Full-frame images at 480 × 400 pixels resolution were acquired at 30 Hz by custom-programmed software written in LabVIEW™ (version 8.2; National Instruments). At each focal plane, we imaged spontaneous activity for at least 4 min and visually evoked activity for 6 to 10 trials.

Visual Stimulation

Visual stimuli were generated in Matlab™ (release 2007b; Mathworks Inc.) by using the Psychophysics Toolbox (http://psychtoolbox.org/wikka.php?wakka = HomePage). Visual stimuli were projected onto a screen placed 30 cm from the contralateral eye, covering 80° x 67° of the visual field. Each trial of visual stimulation started with a gray screen (mean luminance) for 5 s, followed by a stationary square-wave grating for 5 s and the corresponding drifting grating for 5 s (0.03 cpd, 1 Hz, 8 directions, contrast 98%, mean luminance 19.1 cd/m^2). At each focal plane, evoked activity was imaged during 6–10 trials. See Supplemental Information for more details.

Data Analysis

Image analysis was performed offline in two steps. First, the software ImageJ (http://rsb.info.nih.gov/ij/) was used to draw regions of interest (ROIs) around cell bodies and around a large area of cell-free neuropil. In the next step, custom-made routines written in Igor Pro (Wavemetrics, Lake Oswego, OR) were used for the detection of wave-associated calcium transients in individual neurons. Calcium signals were expressed as relative fluorescence changes ($\Delta f/f$) corresponding to the mean fluorescence from all pixels within specified ROIs. For each ROI, a transient was accepted as a signal when its amplitude was greater than three times the standard deviation of the noise band. After the automatic analysis, all traces were carefully inspected. Neurons were defined as responsive to moving gratings when their activity during the presentation of at least one of the eight directions was significantly higher than their activity during the interstimuli period (ANOVA test). The activity was evaluated by the integral of the calcium transients. An OSI (e.g., Niell and Stryker, 2008) was calculated in order to quantify the tuning level of the neurons with regard to the orientation of the drifting grating. The OSI was defined as $(R_{pref} - R_{ortho})/(R_{pref} + R_{ortho})$, where R_{pref}, the response in the preferred orientation, was the response with the largest magnitude. R_{pref} was determined as the mean of the integrals of the calcium transients for the two corresponding opposite directions. R_{ortho} was similarly calculated as the response evoked by the orthogonal orientation. With this index, perfect orientation selectivity would give OSI = 1, an equal response to all orientations would have OSI = 0, and 3:1 selectivity corresponds to OSI = 0.5. Highly and poorly tuned neurons were defined as neurons with an OSI > 0.5 and OSI < 0.5, respectively. Similarly, a DSI was defined as $(R_{pref} - R_{opp})/(R_{pref} + R_{opp})$, where R_{opp} is the response in the direction opposite to the preferred direction.

Statistical Analysis

The following values were compared between normally reared and dark-reared mice and between different age groups, by using a Mann-Whitney test with a two-tailed level of significance set at $\alpha = 0.05$ (SPSS 16.0 software): percentage of neurons responding to drifting gratings, cumulative distributions of OSI and DSI, OSI and DSI mean values.

SUPPLEMENTAL INFORMATION

Supplemental Information includes Supplemental Experimental Procedures and nine figures and can be found with this article online at doi:10.1016/j.neuron.2011.06.013.

ACKNOWLEDGMENTS

We thank Jia Lou for excellent technical assistance. This study was supported by grants of the Deutsche Forschungsgemeinschaft to A.K. and by the Friedrich Schiedel Foundation. A.K. is a Carl von Linde Senior Fellow of the Institute for Advanced Study of the Technische Universität München. N.L.R. was supported by the DFG (IRTG 1373). M.N. was supported by the Japan Society for the Promotion of Science Postdoctoral Fellowships for Research Abroad.

Accepted: June 8, 2011
Published: August 10, 2011

REFERENCES

Benevento, L.A., Bakkum, B.W., Port, J.D., and Cohen, R.S. (1992). The effects of dark-rearing on the electrophysiology of the rat visual cortex. Brain Res. *572*, 198–207.

Blasdel, G.G., and Salama, G. (1986). Voltage-sensitive dyes reveal a modular organization in monkey striate cortex. Nature *321*, 579–585.

Bonhoeffer, T., and Grinvald, A. (1991). Iso-orientation domains in cat visual cortex are arranged in pinwheel-like patterns. Nature *353*, 429–431.

Bosking, W.H., Zhang, Y., Schofield, B., and Fitzpatrick, D. (1997). Orientation selectivity and the arrangement of horizontal connections in tree shrew striate cortex. J. Neurosci. *17*, 2112–2127.

Cang, J., Rentería, R.C., Kaneko, M., Liu, X., Copenhagen, D.R., and Stryker, M.P. (2005). Development of precise maps in visual cortex requires patterned spontaneous activity in the retina. Neuron *48*, 797–809.

Chen, M., Weng, S., Deng, Q., Xu, Z., and He, S. (2009). Physiological properties of direction-selective ganglion cells in early postnatal and adult mouse retina. J. Physiol. *587*, 819–828.

Colonnese, M.T., Kaminska, A., Minlebaev, M., Milh, M., Bloem, B., Lescure, S., Moriette, G., Chiron, C., Ben-Ari, Y., and Khazipov, R. (2010). A conserved switch in sensory processing prepares developing neocortex for vision. Neuron *67*, 480–498.

Crair, M.C., Gillespie, D.C., and Stryker, M.P. (1998). The role of visual experience in the development of columns in cat visual cortex. Science *279*, 566–570.

Dräger, U.C. (1975). Receptive fields of single cells and topography in mouse visual cortex. J. Comp. Neurol. *160*, 269–290.

Elstrott, J., and Feller, M.B. (2009). Vision and the establishment of direction-selectivity: a tale of two circuits. Curr. Opin. Neurobiol. *19*, 293–297.

Elstrott, J., Anishchenko, A., Greschner, M., Sher, A., Litke, A.M., Chichilnisky, E.J., and Feller, M.B. (2008). Direction selectivity in the retina is established independent of visual experience and cholinergic retinal waves. Neuron *58*, 499–506.

Fagiolini, M., Pizzorusso, T., Berardi, N., Domenici, L., and Maffei, L. (1994). Functional postnatal development of the rat primary visual cortex and the role of visual experience: dark rearing and monocular deprivation. Vision Res. *34*, 709–720.

Fagiolini, M., Katagiri, H., Miyamoto, H., Mori, H., Grant, S.G., Mishina, M., and Hensch, T.K. (2003). Separable features of visual cortical plasticity revealed by N-methyl-D-aspartate receptor 2A signaling. Proc. Natl. Acad. Sci. USA *100*, 2854–2859.

Fagiolini, M., Fritschy, J.M., Löw, K., Möhler, H., Rudolph, U., and Hensch, T.K. (2004). Specific GABAA circuits for visual cortical plasticity. Science *303*, 1681–1683.

Fortin, S., Chabli, A., Dumont, I., Shumikhina, S., Itaya, S.K., and Molotchnikoff, S. (1999). Maturation of visual receptive field properties in the rat superior colliculus. Brain Res. Dev. Brain Res. *112*, 55–64.

Frégnac, Y., and Imbert, M. (1978). Early development of visual cortical cells in normal and dark-reared kittens: relationship between orientation selectivity and ocular dominance. J. Physiol. *278*, 27–44.

Grubb, M.S., and Thompson, I.D. (2003). Quantitative characterization of visual response properties in the mouse dorsal lateral geniculate nucleus. J. Neurophysiol. *90*, 3594–3607.

Hubel, D.H. (1959). Single unit activity in striate cortex of unrestrained cats. J. Physiol. *147*, 226–238.

Hubel, D.H., and Wiesel, T.N. (1959). Receptive fields of single neurones in the cat's striate cortex. J. Physiol. *148*, 574–591.

Hubel, D.H., and Wiesel, T.N. (1962). Receptive fields, binocular interaction and functional architecture in the cat's visual cortex. J. Physiol. *160*, 106–154.

Hubel, D.H., and Wiesel, T.N. (1968). Receptive fields and functional architecture of monkey striate cortex. J. Physiol. *195*, 215–243.

Huberman, A.D., Wei, W., Elstrott, J., Stafford, B.K., Feller, M.B., and Barres, B.A. (2009). Genetic identification of an On-Off direction-selective retinal ganglion cell subtype reveals a layer-specific subcortical map of posterior motion. Neuron *62*, 327–334.

Iwai, Y., Fagiolini, M., Obata, K., and Hensch, T.K. (2003). Rapid critical period induction by tonic inhibition in visual cortex. J. Neurosci. *23*, 6695–6702.

Kerlin, A.M., Andermann, M.L., Berezovskii, V.K., and Reid, R.C. (2010). Broadly tuned response properties of diverse inhibitory neuron subtypes in mouse visual cortex. Neuron *67*, 858–871.

Krug, K., Akerman, C.J., and Thompson, I.D. (2001). Responses of neurons in neonatal cortex and thalamus to patterned visual stimulation through the naturally closed lids. J. Neurophysiol. *85*, 1436–1443.

Levick, W.R., and Thibos, L.N. (1980). Orientation bias of cat retinal ganglion cells. Nature *286*, 389–390.

Li, Y., Fitzpatrick, D., and White, L.E. (2006). The development of direction selectivity in ferret visual cortex requires early visual experience. Nat. Neurosci. *9*, 676–681.

Li, Y., Van Hooser, S.D., Mazurek, M., White, L.E., and Fitzpatrick, D. (2008). Experience with moving visual stimuli drives the early development of cortical direction selectivity. Nature *456*, 952–956.

Métin, C., Godement, P., and Imbert, M. (1988). The primary visual cortex in the mouse: receptive field properties and functional organization. Exp. Brain Res. *69*, 594–612.

Niell, C.M., and Stryker, M.P. (2008). Highly selective receptive fields in mouse visual cortex. J. Neurosci. *28*, 7520–7536.

Ohki, K., Chung, S., Ch'ng, Y.H., Kara, P., and Reid, R.C. (2005). Functional imaging with cellular resolution reveals precise micro-architecture in visual cortex. Nature *433*, 597–603.

Rochefort, N.L., Garaschuk, O., Milos, R.I., Narushima, M., Marandi, N., Pichler, B., Kovalchuk, Y., and Konnerth, A. (2009). Sparsification of neuronal activity in the visual cortex at eye-opening. Proc. Natl. Acad. Sci. USA *106*, 15049–15054.

Runyan, C.A., Schummers, J., Van Wart, A., Kuhlman, S.J., Wilson, N.R., Huang, Z.J., and Sur, M. (2010). Response features of parvalbumin-expressing interneurons suggest precise roles for subtypes of inhibition in visual cortex. Neuron *67*, 847–857.

Sanderson, M.J., and Parker, I. (2003). Video-rate confocal microscopy. Methods Enzymol. *360*, 447–481.

Shou, T., Leventhal, A.G., Thompson, K.G., and Zhou, Y. (1995). Direction biases of X and Y type retinal ganglion cells in the cat. J. Neurophysiol. *73*, 1414–1421.

Sohya, K., Kameyama, K., Yanagawa, Y., Obata, K., and Tsumoto, T. (2007). GABAergic neurons are less selective to stimulus orientation than excitatory neurons in layer II/III of visual cortex, as revealed by in vivo functional Ca^{2+} imaging in transgenic mice. J. Neurosci. *27*, 2145–2149.

Stosiek, C., Garaschuk, O., Holthoff, K., and Konnerth, A. (2003). In vivo two-photon calcium imaging of neuronal networks. Proc. Natl. Acad. Sci. USA *100*, 7319–7324.

Syken, J., Grandpre, T., Kanold, P.O., and Shatz, C.J. (2006). PirB restricts ocular-dominance plasticity in visual cortex. Science *313*, 1795–1800.

Thompson, K.G., Zhou, Y., and Leventhal, A.G. (1994). Direction-sensitive X and Y cells within the A laminae of the cat's LGNd. Vis. Neurosci. *11*, 927–938.

Tian, N., and Copenhagen, D.R. (2003). Visual stimulation is required for refinement of ON and OFF pathways in postnatal retina. Neuron *39*, 85–96.

Van Hooser, S.D., Heimel, J.A., Chung, S., Nelson, S.B., and Toth, L.J. (2005). Orientation selectivity without orientation maps in visual cortex of a highly visual mammal. J. Neurosci. *25*, 19–28.

Vidyasagar, T.R., and Urbas, J.V. (1982). Orientation sensitivity of cat LGN neurones with and without inputs from visual cortical areas 17 and 18. Exp. Brain Res. *46*, 157–169.

Wang, B.S., Sarnaik, R., and Cang, J. (2010). Critical period plasticity matches binocular orientation preference in the visual cortex. Neuron *65*, 246–256.

White, L.E., and Fitzpatrick, D. (2007). Vision and cortical map development. Neuron *56*, 327–338.

Xu, X., Ichida, J., Shostak, Y., Bonds, A.B., and Casagrande, V.A. (2002). Are primate lateral geniculate nucleus (LGN) cells really sensitive to orientation or direction? Vis. Neurosci. *19*, 97–108.

Yonehara, K., Ishikane, H., Sakuta, H., Shintani, T., Nakamura-Yonehara, K., Kamiji, N.L., Usui, S., and Noda, M. (2009). Identification of retinal ganglion cells and their projections involved in central transmission of information about upward and downward image motion. PLoS ONE *4*, e4320.

Zariwala, H.A., Madisen, L., Ahrens, K.F., Bernard, A., Lein, E.S., Jones, A.R., and Zeng, H. (2011). Visual tuning properties of genetically identified layer 2/3 neuronal types in the primary visual cortex of cre-transgenic mice. Front Syst Neurosci *4*, 162.

Neuron, Volume *71*

Supplemental Information

Development of Direction Selectivity

in Mouse Cortical Neurons

Nathalie L. Rochefort, Madoka Narushima, Christine Grienberger, Nima Marandi, Daniel N. Hill, and Arthur Konnerth

SUPPLEMENTAL EXPERIMENTAL PROCEDURES

Animals and Surgery

Animals were prepared for in vivo two-photon calcium imaging as described previously (Stosiek et al., 2003). Briefly, the mice were placed onto a warming plate (38°C) and anesthetized by inhalation of 1.5% isoflurane (Curamed, Karlsruhe, Germany) in pure O_2. After removing the skin, a custom-made recording chamber (Garaschuk *et al.*, 2006b) was then glued to the skull with cyanoacrylic glue (UHU, Buhl-Baden, Germany). The mouse was then transferred into the set-up, placed onto a warming plate (38° C) and continuously supplied with 0.8-1% isoflurane in pure O_2 (breathing rate 110-130 per minute). The position of the primary visual cortex was located according to brain atlas coordinates (Bregma -3 to -4.5 mm, 2-3 mm lateral to the midline (Paxinos and Franklin, 2001)). In younger animals, the position of the primary visual cortex (0-1 mm anterior to the lambda suture, 1.5-3 mm lateral to the midline) was identified according to the Golgi atlas of the postnatal mouse brain (Valverde, 1998). In all experiments the location of the imaged neurons was confirmed post-hoc by imaging of the stained brain area. A small craniotomy (~0.8×0.6 mm) was performed above the monocular region of primary visual cortex using a thin (30G) injection needle. The recording chamber was perfused with warm (37° C) artificial cerebrospinal fluid containing (in mM): 125 NaCl, 4.5 KCl, 26 $NaHCO_3$, 1.25 NaH_2PO_4, 2 $CaCl_2$, 1 $MgCl_2$, 20 glucose, pH 7.4, when bubbled with 95% O_2 and 5% CO_2. The neurons were stained in vivo with the fluorescent calcium indicator dye Oregon Green BAPTA-1 (OGB-1) following the protocol described in detail in (Stosiek et al., 2003).

Visual Stimulation

For the purpose of the present study, we imaged the activity of many neurons simultaneously, so we optimized the stimulus parameters for a population of neurons rather than for individual neurons. In line with previous studies, we chose a set of spatio-temporal frequencies for the drifting gratings (0.03 cpd, 1 Hz) that were effective for the activation of mouse visual cortex neurons (Ohki et al., 2005; Sohya et al., 2007). For adult mice, these parameters were very close to the mean values obtained from

electrophysiological recordings in layer 2/3 of the mouse visual cortex (Niell and Stryker, 2008; Gao *et al.*, 2010). We tested five other spatial frequencies (0.01, 0.015, 0.02, 0.04, 0.08 cpd) in two age groups of normally-reared animals (0-1 day after eye opening and 2 months). For these experiments, each trial of visual stimulation started with a gray screen lasting for 2 s, followed by a stationary square-wave grating lasting for 3 s, and then the corresponding drifting grating that was presented for 2 s. Before eye-opening, no activity could be evoked by drifting gratings with spatio-temporal frequencies of 0.03 cpd, 1 Hz and 0.015 cpd, 1 Hz. We thus tested for responses to strong luminance changes by using a full field uniform black screen (luminance 0.5 cd/m^2) for 5 s followed by a full field uniform gray screen (19.1 cd/m^2) for 5 s. At each focal plane, evoked activity was imaged over 6 to 10 trials.

Data Analysis

Astrocytes were excluded from the analysis based on their brighter appearance after staining with OGB1-AM (Kerr et al., 2005) and their specific morphology with clearly visible processes. In an initial set of experiments, we verified that at all stages of development astrocytes are clearly identified by their brighter appearance after staining with OGB1-AM by using co-staining with sulforhodamine 101 (Nimmerjahn *et al.*, 2004; Garaschuk *et al.*, 2006).

Polar plots were used to show a neuron's response function to oriented drifting gratings. The responses to each of the 8 tested directions were normalized with respect to the maximal response. Then, the function was constructed by connecting lines between the 8 values. The orientation tuning curves were fit as the sum of two Gaussians and a baseline offset (Niell and Stryker, 2008). The Gaussians were constrained to have equal widths with means separated by π. A tuning width was then calculated as the half-width at half-maximum of the fitted peak relative to baseline.

Supplementary figure 1

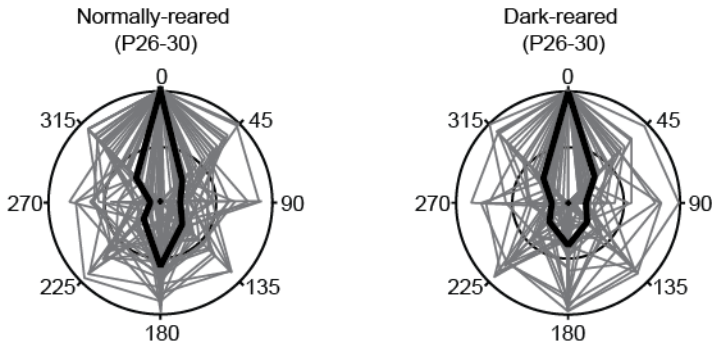

Figure S1, Related to Figure 1. Orientation and Direction-Selective Neurons in Normally Reared and Dark-Reared Juvenile Mice

Overlay of polar plots obtained from the visually-evoked activity in all neurons imaged in normally-reared and dark-reared juvenile mice (n=68 and 81 neurons, respectively). Polar plots were normalized by the maximal response and rotated to place the preferred direction at 0°. Black lines indicate median tuning function.

Supplementary figure 2

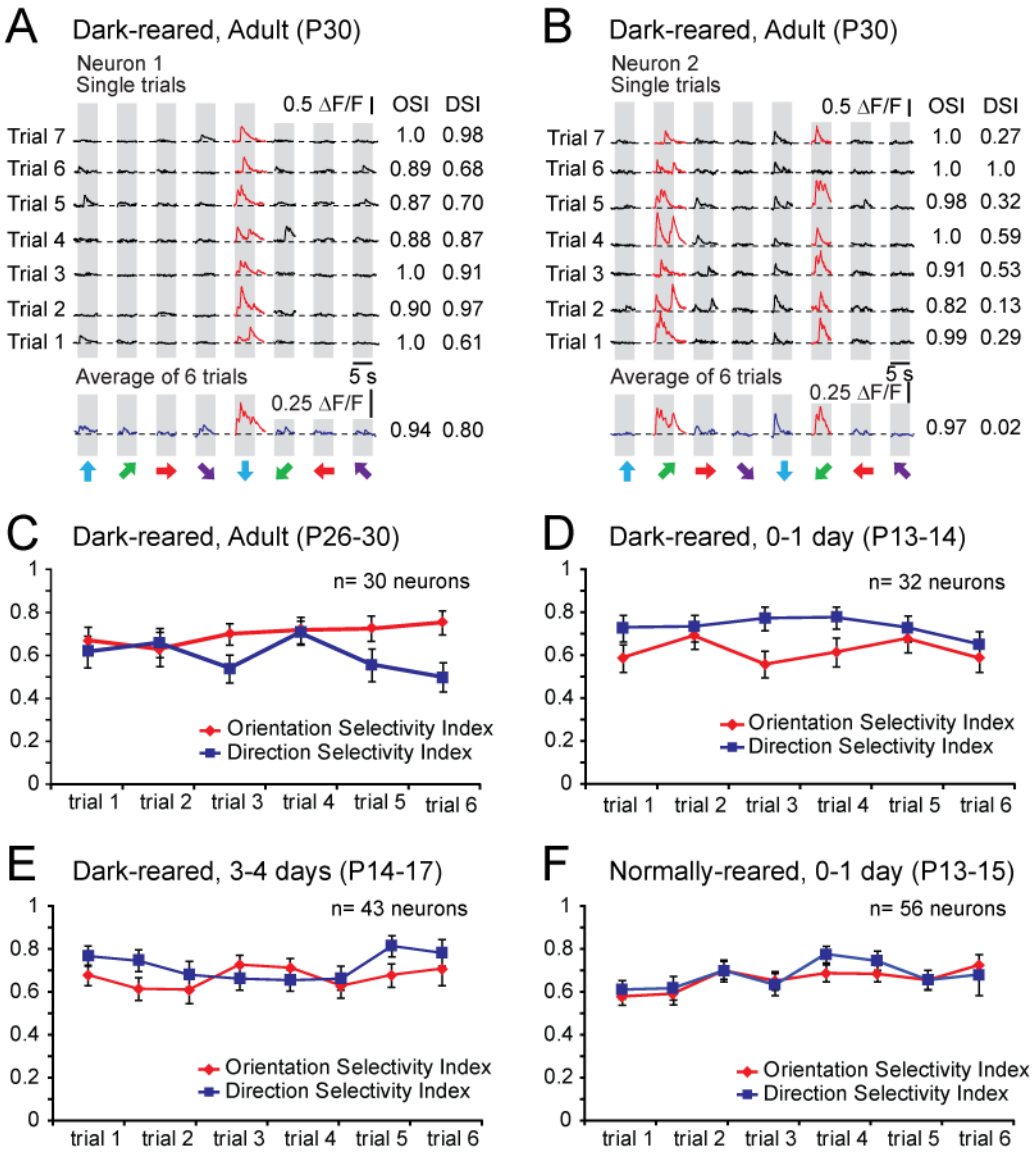

Figure S2, Related to Figure 1. Orientation and Direction Selectivity of Layer 2/3 Neurons in Dark-Reared Mice (P26-30) in Consecutive Trials of Visual Stimulation

(A and B) Calcium transients evoked by visual stimulation in the two orientation-selective neurons indicated in the left panel of Figure 1B. Grey regions indicate periods of visual stimulation with drifting gratings (0.03 cpd) schematized by oriented arrows on the bottom of each panel. The six consecutive single trials (from trial 1 to trial 6) are represented with black lines and the average of 6 trials is shown in blue.

(C–F) Orientation and direction-selectivity indices calculated from the responses recorded in single trials. The indices were calculated for each trial in which a response was observed during the presentation of the preferred orientation. The indices calculated for the 6 consecutive trials did not differ significantly between the first and the last trials.

Supplementary figure 3

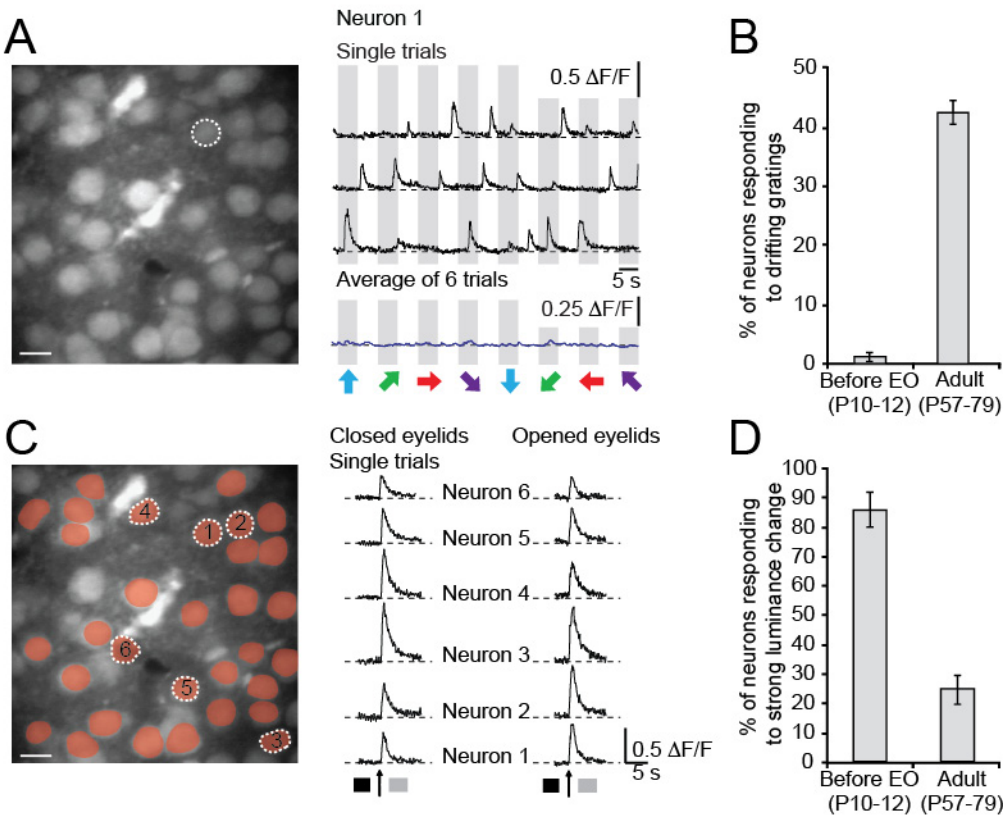

Figure S3, Related to Figure 2. Light-Evoked Responses before Eye-Opening

(A) Left panel, In vivo two-photon image of layer 2/3 neurons in the visual cortex of a P12 mouse, before natural eye-opening. Right panel, calcium transients recorded during visual stimulation with drifting gratings (0.03 cpd) in the neuron indicated in the left panel, after the gentle opening of the eyelids with forceps. Same conventions as in Figure 1.
(B) Percentage of neurons responding to drifting gratings in young mice before natural eye-opening (opened eyelids) and in adult mice (Mann-Whitney test, $p<0.0001$). Error bars indicate SEM (n=187 and 174 neurons, respectively).
(C) Left panel, in vivo two-photon image of the same region shown in panel a. The visual stimulus consisted of a transition between a black and grey screen (increasing luminance). Neurons activated by this visual stimulation are shown in red. Right panel, calcium transients evoked by visual stimulation in the six neurons indicated in the left panel. Evoked calcium transients were observed through closed eyelids (left column) as well as after the gentle opening of the eyelids with forceps (right column).
(D) Percentage of neurons responding to the strong luminance change (full field black/grey screen flicker), in young mice before natural eye-opening (opened eyelids) and in adult mice (Mann-Whitney test, $p<0.0001$). In adult mice, 42.5 % of the neurons responded to drifting gratings, 8.3 % responded both to drifting gratings and full field black/grey screen flicker, 14.6 % responded only to full field black/grey screen and 44.4 % responded neither to drifting gratings nor to full field black/grey flicker. Error bars indicate SEM (n=187 and 174 neurons, respectively). Scale bars, 10 µm.

Supplementary figure 4

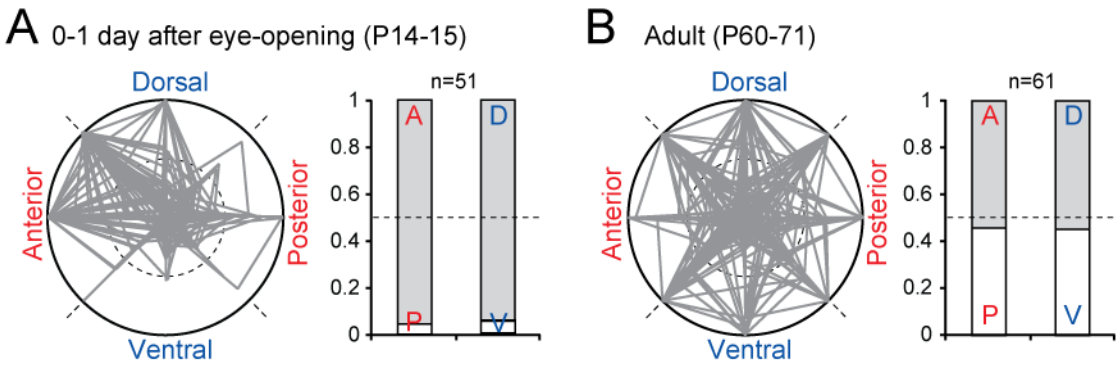

Figure S4, Related to Figure 3. Preference for Antero-Dorsal Directions at Eye-Opening Does Not Depend on the Preferred Spatial Frequency of the Drifting Gratings

(A and B) *Left panels*, overlap of all polar plots obtained from the visually-evoked responses in all selective neurons (OSI>0.5) that did not respond to drifting gratings of 0.03 cpd but responded to another spatial frequency tested. We recorded visual responses during the presentation of drifting gratings of 6 different spatial frequencies (0.01, 0.015, 0.02, 0.03, 0.04, 0.08 cpd). The orientation-selective neurons that did not respond to drifting gratings of 0.03 cpd but that responded to at least one other spatial frequency are plotted here. For each neuron, the polar plot was constructed from the responses to the spatial frequency that gave peak response at the preferred orientation. Polar plots were normalized by the maximal response. Comparison with the polar plots obtained from the orientation-selective neurons that responded to drifting gratings of 0.03 cpd (Figures 3A and 3B) indicates that the preference for antero-dorsal directions at eye-opening does not depend on the preferred spatial frequency of the drifting gratings. *Right panels*, same legend as Figure 3B.

Supplementary figure 5

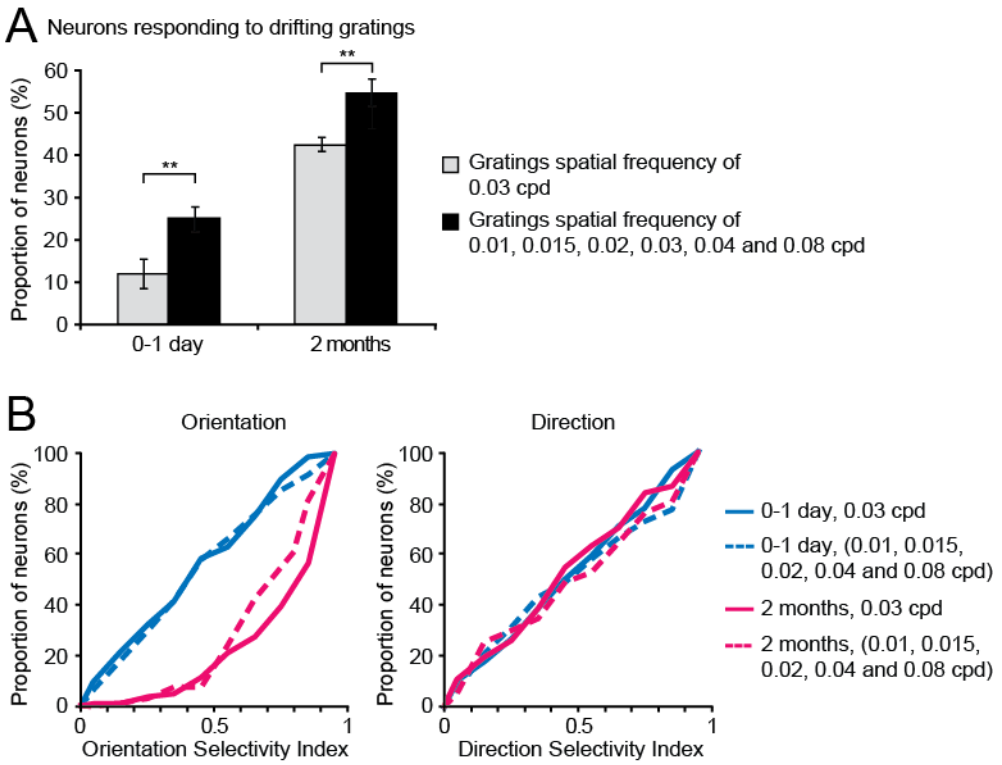

Figure S5, Related to Figure 4. Orientation And Direction Tuning Properties Do Not Depend on the Preferred Spatial Frequency of the Drifting Gratings

(A) Percentage of neurons responding to drifting gratings in young (0-1 day after eye-opening, P13-P15) and adult (P57-79) normally-reared mice (Mann-Whitney test, **p<0.01). Grey bars indicate the proportion of neurons responding to drifting gratings with a spatial frequency of 0.03 cpd (n=1216, 174 neurons, respectively). Black bars indicate the proportion of neurons that responded to drifting gratings of at least one spatial frequency among the six tested (0.01, 0.015, 0.02, 0.03, 0.04, 0.08 cpd) (n=899, 283 neurons, respectively). Error bars indicate SEM.
(B) Cumulative distributions of orientation (OSI) and direction (DSI) selectivity indices from neurons recorded in normally-reared mice at 0-1 day after eye-opening (P13-P15) and in adults (2 months, P57-79). Continuous lines show the OSI and DSI distribution of all neurons that responded to drifting gratings of 0.03 cpd (n=167, 81 neurons for 0-1 day and 2 months, respectively). Dashed lines show the distribution of OSI and DSI from all neurons that did not respond to 0.03 cpd drifting gratings but responded to at least one other spatial frequency tested (0.01, 0.015, 0.02, 0.04, 0.08 cpd) (n=132, 66 neurons, respectively). The results showed no significant difference between both groups at the two ages tested (Mann-Whitney test).

Supplementary figure 6

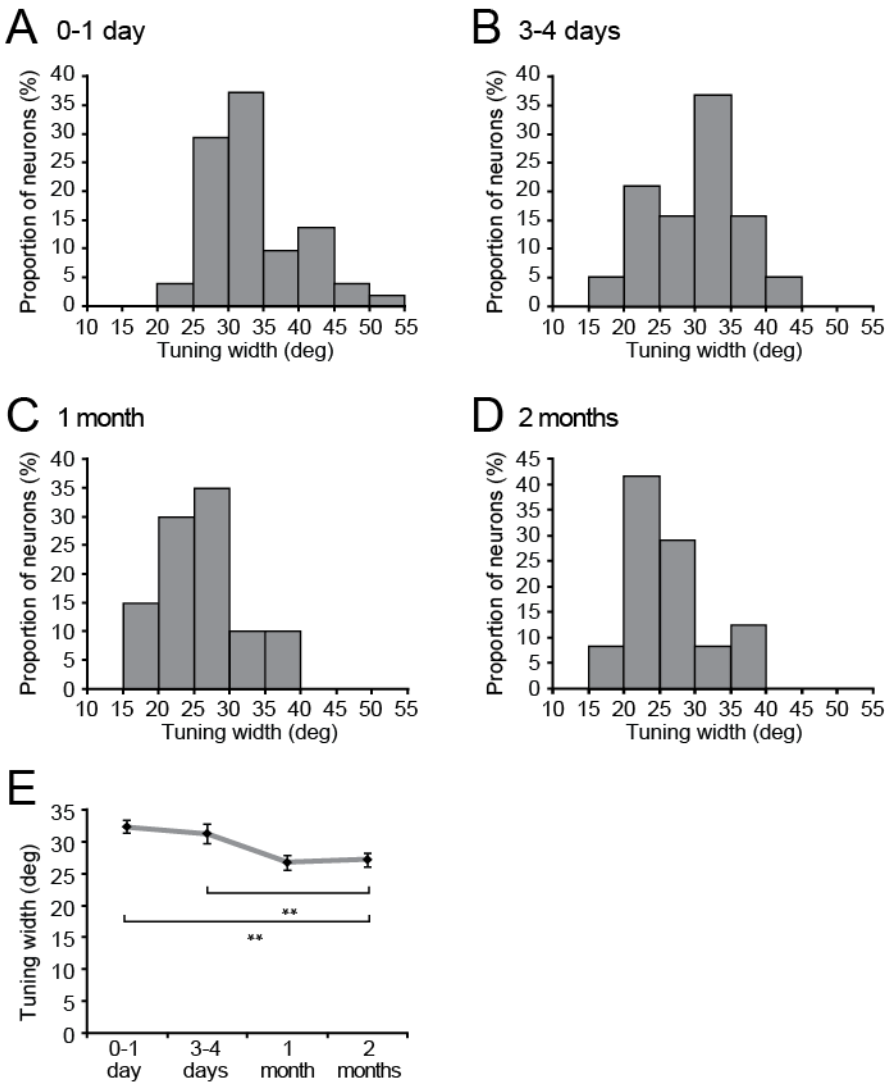

Figure S6, Related to Figure 4. Tuning Widths of the Orientation-Selective Neuronal Responses during the First Two Postnatal Months

(A–D) Histograms of the distribution of tuning widths (half-width at half-maximum) for the orientation-selective neurons recorded at four different ages from eye-opening (0-1 day after eye-opening, P13-P15) to adulthood (2 months, P57-79) in normally-reared mice.
(E) Mean tuning width for orientation-selective neurons recorded in the four age groups (Mann-Whitney test, **$p<0.01$, n=81, 41, 49 and 79 neurons, respectively). Error bars indicate SEM.

Supplementary figure 7

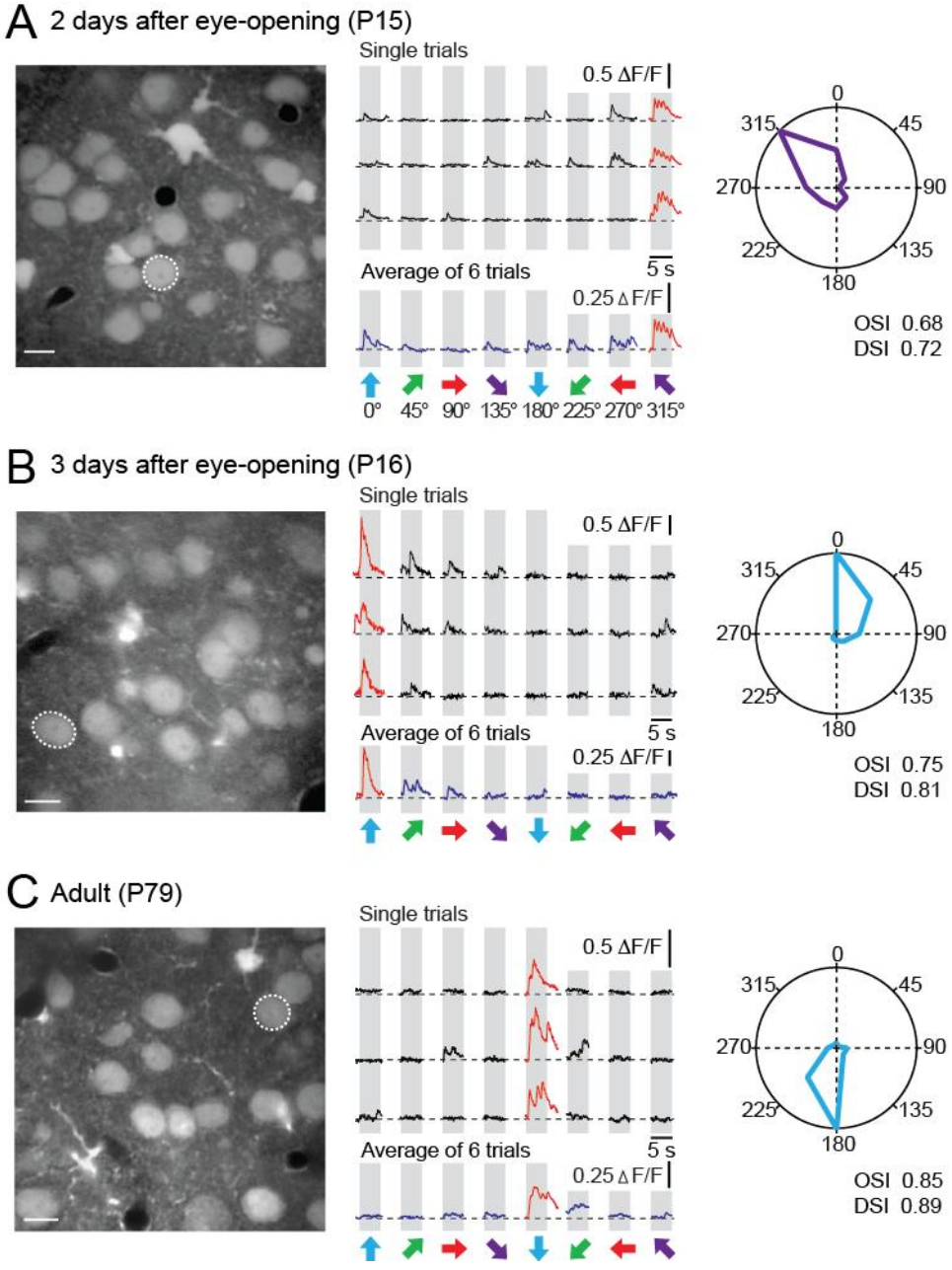

Figure S7, Related to Figure 4. Direction-Selective Neurons at Different Ages after Eye-Opening

(A–C) Left panels, in vivo two-photon image of layer 2/3 neurons in the visual cortex of normally-reared mice at two days (A) and three days (B) after eye-opening and at adulthood (C). Middle panels, calcium transients evoked by drifting gratings (0.03 cpd) in direction-selective neurons indicated in left panels. Same conventions as in Figure 1. Right panels, polar plots showing the neuron's response function to oriented drifting gratings. OSI, orientation selectivity index; DSI, direction selectivity index. Scale bars, 10 μm.

Supplementary figure 8

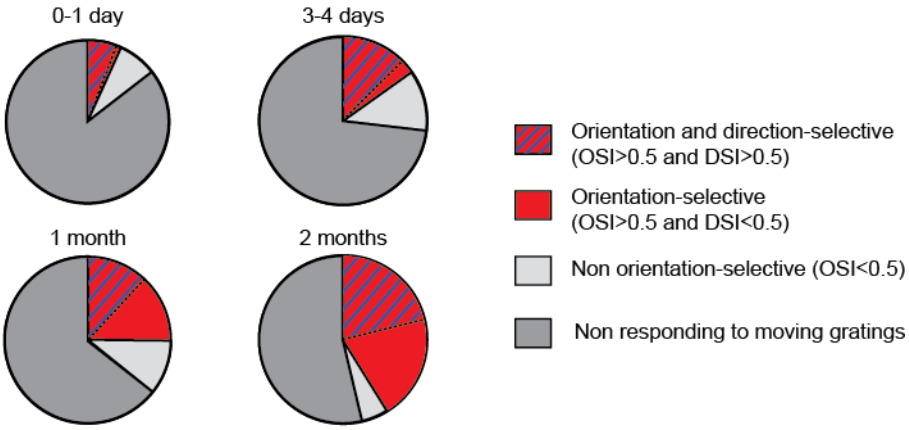

Figure S8, Related to Figure 4. Development of Orientation and Direction Selectivity during the First Two Postnatal Months, in Normally Reared Mice (Gratings, 0.03 cpd)

Pie charts showing the relative proportions of neurons that are both orientation and direction-selective (blue stripes, OSI>0.5 and DSI>0.5), only orientation-selective but not direction-selective (red, OSI>0.5 and DSI<0.5), non orientation-selective but responding to drifting gratings (light grey) and not responding to drifting gratings (dark grey). Note the increase of orientation tuned neurons (red) in adult mice. Just after eye-opening (0-1 day and 3-4 days after eye opening), nearly all the orientation-selective neurons were also direction-selective, whereas at 2 months only half of the orientation tuned neurons were also direction-selective.

Supplementary figure 9

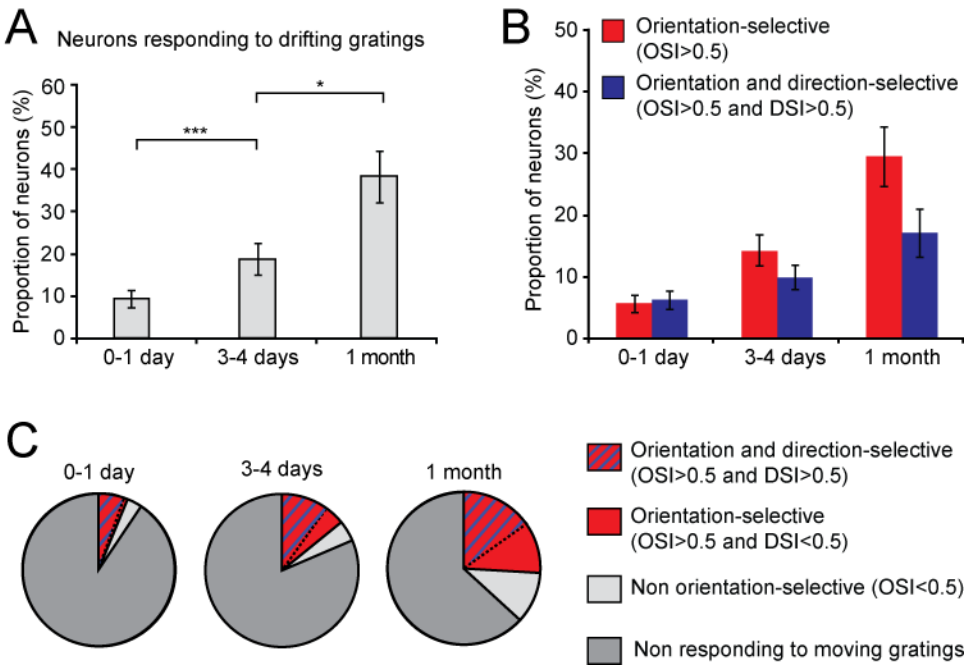

Figure S9, Related to Figure 4. Proportion of Responsive Neurons and Population Tuning Development during the First Postnatal Month, in Dark-Reared Mice

(A) Percentages of neurons responding to drifting gratings (0.03 cpd) in dark-reared mice at three different ages from eye-opening (0-1 day after eye-opening, P13-P14) to one postnatal month (P26-30) (Mann-Whitney test, *p<0.05, ***p<0.001, n=799, 506 and 220 neurons, respectively). Error bars indicate SEM.
(B) Percentages of orientation-selective neurons (OSI>0.5, red) and of direction-selective neurons (OSI>0.5 and DSI>0.5, blue) among all neurons recorded in dark-reared mice at three different ages, during the presentation of drifting gratings (0.03 cpd). Error bars indicate SEM.
(C) Pie charts showing the relative proportions of neurons that are both orientation and direction-selective (blue stripes, OSI>0.5 and DSI>0.5), only orientation-selective but not direction-selective (red, OSI>0.5 and DSI<0.5), non orientation-selective but responding to drifting gratings (light grey) and not responding to drifting gratings (dark grey).

Project III – Staged decline of neuronal function *in vivo* in an animal model of Alzheimer's disease

Published in **Nature Communications**, 2012, 3: 774

nature COMMUNICATIONS

OPEN

ARTICLE

Received 24 Jan 2012 | Accepted 12 Mar 2012 | Published 10 Apr 2012

DOI: 10.1038/ncomms1783

Staged decline of neuronal function *in vivo* in an animal model of Alzheimer's disease

Christine Grienberger[1,*], Nathalie L. Rochefort[1,*], Helmuth Adelsberger[1], Horst A. Henning[1], Daniel N. Hill[1], Julia Reichwald[2], Matthias Staufenbiel[2] & Arthur Konnerth[1]

The accumulation of amyloid-β in the brain is an essential feature of Alzheimer's disease. However, the impact of amyloid-β-accumulation on neuronal dysfunction on the single cell level *in vivo* is poorly understood. Here we investigate the progression of amyloid-β load in relation to neuronal dysfunction in the visual system of the APP23×PS45 mouse model of Alzheimer's disease. Using *in vivo* two-photon calcium imaging in the visual cortex, we demonstrate that a progressive deterioration of neuronal tuning for the orientation of visual stimuli occurs in parallel with the age-dependent increase of the amyloid-β load. Importantly, we find this deterioration only in neurons that are hyperactive during spontaneous activity. This impairment of visual cortical circuit function also correlates with pronounced deficits in visual-pattern discrimination. Together, our results identify distinct stages of decline in sensory cortical performance *in vivo* as a function of the increased amyloid-β-load.

[1] Institute of Neuroscience and Center for Integrated Protein Science, Technical University Munich, Biedersteinerstr. 29, 80802 Munich, Germany. [2] Novartis Institutes for Biomedical Research, 4002 Basel, Switzerland. *These authors contributed equally to this work. Correspondence and requests for materials should be addressed to A.K. (email: arthur.konnerth@lrz.tu-muenchen.de).

While learning and memory defects are key symptoms of Alzheimer's disease (AD)[1], patients progressively exhibit complex cognitive impairments[2], and even deficits in central sensory processing, particularly at advanced stages of their disease. Thus, different sensory modalities can be affected[3–5] including information processing in the visual system[6–9]. The amyloid-β (Aβ)-peptide has been identified as a key molecule in the pathogenesis of AD. It accumulates in various forms in AD brains, including soluble oligomeric entities and insoluble Aβ-plaques[10]. The presence of Aβ-plaques is a defining criterion for the diagnosis of AD[1]. *In vitro* studies have suggested different mechanisms of action for Aβ, including changes in ion-channel properties[11–13], impairments of synaptic transmission and synaptic plasticity of individual neurons exposed to Aβ[14–18]. In addition, morphological studies have revealed abnormal geometries of dendrites and axons in post-mortem human brains of AD patients[19] as well as neuritic dystrophies and a loss of dendritic spines in brains of AD mouse models[12,20–22]. These structural changes suggest that the accumulation of Aβ could lead to an impairment of neuronal signal integration and affect neuronal circuit function[19,22].

Effects of Aβ on the network level have also recently been investigated *in vivo* in different mouse models of AD[23]. Recordings of electrically evoked activity showed that synaptic integration is disrupted in the Aβ-plaques-containing cortex[22]. In addition, generalized spontaneous aberrant excitatory activity was recorded by electroencephalography in the cortex and the hippocampus of another AD mouse model[24]. Furthermore, local field potential recordings of oscillatory activity in the olfactory bulb and the piriform cortex revealed abnormal spontaneous and odour-related activity in the Tg2576 mouse model of AD[25]. Using two-photon calcium imaging, a recent study of the spontaneous ongoing activity in the frontal cortex identified two fractions of neurons with impaired activity[26]. In addition to a pronounced silencing of activity in a fraction of neurons, a separate fraction of neurons was found to be hyperactive in the Aβ-containing cortex. It remains an open question, however, how Aβ impacts the functionality of individual cortical neurons *in vivo* and how this is associated with a behavioural phenotype. Here we used the visual system of the APP23×PS45 mice as a cortical circuit model to investigate the relation between Aβ-load, neuronal circuit function and behavioural performance. The visual cortex is in many ways a well-suited model system for such a study, as neuronal networks underlying spontaneous and sensory-evoked activity can be examined *in vivo*. Thus, in the visual cortex, the functionality of a neuron within the cortical circuit can be directly evaluated in an anaesthetized animal by using specific visual stimuli. For example, one functional property of the visual neurons that can be directly assessed is their orientation selectivity, that is, their capacity to respond more significantly to one principal orientation of a visual stimulus than any other. To study neuronal network activity in the visual cortex *in vivo*, powerful experimental techniques are readily implemented in mouse models. In recent years, two-photon calcium imaging of cortical circuits allowed the simultaneous recording of the activity of multiple neurons *in vivo,* with single-cell resolution[27–30]. Furthermore, two-photon microscopy is increasingly used for the imaging of Aβ-related pathologies[20,21,31].

In the present study, we used *in vivo* two-photon calcium imaging to investigate the network effects of Aβ at the level of single cortical neurons in the APP23×PS45 transgenic mouse model of AD[32,33]. We imaged *in vivo* both the spontaneous and stimulus-evoked activity of neurons in the primary visual cortex of transgenic mice at different stages of the disease as well as of wild-type (WT) control mice. We also determined the Aβ-load, including both soluble Aβ and insoluble Aβ-plaques, of the visual cortex and the visual performance of the transgenic mice at different ages. Our results provide experimental evidence for the relation between cortical Aβ-load and functional impairments of neuronal circuits at the single cell level *in vivo*.

Results

Impaired tuning of visual cortex neurons in APP23×PS45 mice. We assessed the functional properties of the visual cortex neurons by determining their orientation selectivity, that is, their capacity to respond better to one principal orientation of a visual stimulus than any other. The analysis of the neuronal tuning properties by *in vivo* two-photon calcium imaging allows the simultaneous analysis of the activity of many neurons in defined cortical layers[29,34]. These analyses rely on the recording of calcium transients in the neuronal cell bodies. It has been shown that these calcium transients directly reflect action potential firing (for example, refs 27, 29, 35). Here we examined neuronal calcium signals evoked by drifting grating stimulation in the primary visual cortex of aged (8–10 months) WT and APP23×PS45 mice. Drifting gratings were presented to the contralateral eye, while performing two-photon calcium imaging of neurons in the monocular region of the primary visual cortex after staining the tissue with the fluorescent calcium indicator dye OGB1-AM (Fig. 1a)[27]. Figure 1b illustrates an experiment that was performed in an 8-month-old WT mouse. In the field of view, we identified a neuron that showed large calcium transients for a specific orientation of the drifting gratings (directions of 135 and 315°), but no significant responses for all the other directions. A quantitative analysis of the stimulus-evoked responses showed that the neuron had an orientation selectivity index (OSI) of 0.96 and a direction selectivity index (DSI) of 0.41 (see also polar plot in Fig. 1c). Thus, this neuron was defined as a highly tuned orientation-selective neuron[36]. On the whole, neurons from aged WT mice were found to be as highly tuned for orientation (Fig. 1d) as those in younger rodents[30].

Next, we used the same approach to analyse aged APP23×PS45 mice (Fig. 2). A remarkable feature of the visual cortex of these 8–10-month-old transgenic mice was the presence of Aβ-plaques (Fig. 2a,b) as well as a high amount of soluble Aβ (see below). We then studied the tuning properties of neurons in such Aβ-containing visual cortices. While some neurons had normal tuning properties, there was an increased incidence of neurons that were remarkably poorly tuned. For example, Fig. 2b illustrates the results obtained from such a neuron that happened to be located near an Aβ-plaque. Unlike the typical highly tuned neurons of WT mice, this neuron produced large calcium transients in response to several directions of the drifting grating stimulation. This relatively low level of tuning was reflected by the values for OSI (0.56) and DSI (0.22) (see also, polar plot in Fig. 2c). A systematic analysis of the OSI and DSI in all recorded responsive neurons established the significantly reduced tuning performance of visual cortex neurons in aged APP23×PS45 mice (Fig. 2d,e, Mann–Whitney test, OSI $P < 0.001$, DSI $P < 0.05$).

Age-related increase in Aβ-load and impaired neuronal function. To determine the relation between Aβ-load and cortical dysfunction, we examined three extra age groups at earlier stages of the disease (1.5–2, 3–3.25 and 4–4.5-month-old animals, Fig. 3). Figure 3a shows that plaques were absent at the age of 2 months, were sparse and present only in deeper layers in the cortex of 3-month-old mice, spread out also to upper cortical layers at the age of 4 months and, finally, were abundant and widely distributed in 9-month-old mice. A quantification of the age-dependent increase in plaque density, in the primary visual cortex, is provided in Fig. 3b. Although a similar development of plaques was observed in the lateral geniculate nucleus, no plaques were found in the retina throughout all ages tested in APP23×PS45 mice (Supplementary Fig. S1). In addition, in the primary visual cortex, we found that the level of soluble Aβ paralleled the age-dependent increase in plaque density, although significant levels were already detected in the two youngest age

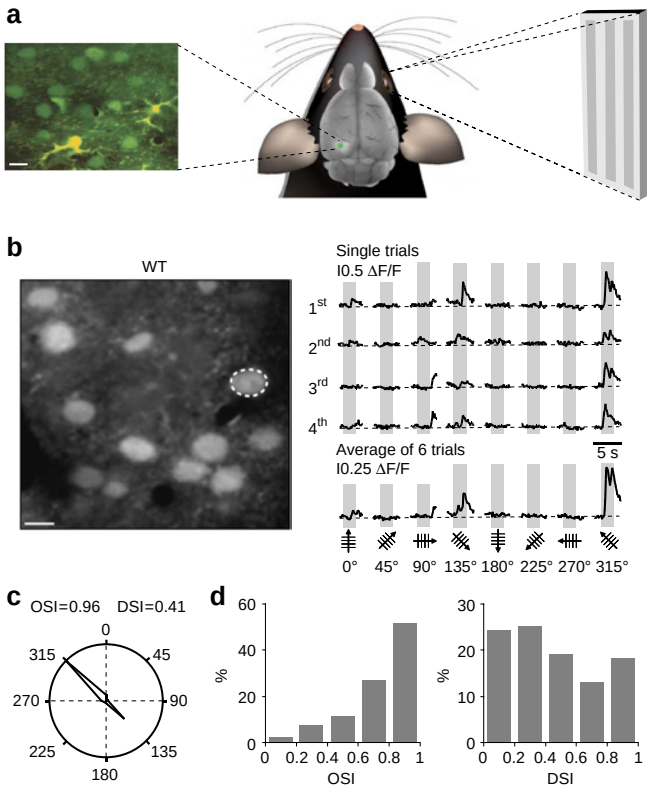

Figure 1 | Orientation and direction tuning of visual cortex neurons in 8–10 month-old WT mice. (**a**) Experimental arrangement for *in vivo* two-photon calcium imaging of stimulation-evoked neuronal activity. Left panel, *in vivo* two-photon image of cortical layer 2/3 of the primary visual cortex stained *in vivo* with the fluorescent calcium indicator dye Oregon Green BAPTA-1 (green) and the glial marker Sulforhodamine 101 (yellow). Right panel, visual stimuli (drifting gratings) were projected on a screen placed 30 cm away from the contralateral eye of the mouse. (**b**) Left panel, *in vivo* two-photon image of layer 2/3 neurons in the visual cortex of a WT mouse (8-months). Right panel, stimulus-evoked calcium transients recorded from the orientation selective neuron indicated in the left panel by a white dotted circle. Grey regions indicate periods of visual stimulation with drifting gratings schematized by oriented arrows on the bottom of each panel. Four single trials are represented on top and the average of six trials is shown below. Scale bar, 10 μm. (**c**) Polar plot showing the neuron's response function to oriented drifting gratings. The responses to each of the eight directions tested were normalized with respect to the maximal response. Then, the function was constructed by connecting the eight values. (**d**) Distribution of the orientation (OSI) and direction (DSI) selectivity indices of all responsive neurons ($n = 131$ neurons) recorded in the visual cortices of 13 WT mice.

groups (Fig. 3c). We then determined the tuning levels of visual cortex neurons in the four different age groups (Fig. 3d,e). Interestingly, the two earliest age groups studied, virtually lacking plaques, did not have measurable impairments in orientation selectivity (Fig. 3d, e). No significant difference was found between 1.5–2-month-old WT and APP23×PS45 mice (Fig. 3d; Mann–Whitney test, $P = 0.61$) as well as between 1.5–2-month-old and 3–3.25-month-old APP23×PS45 mice (Fig. 3d; Mann–Whitney test, $P = 0.63$). At the two later stages (4–4.5 and 8–10month), orientation tuning gradually decreased, as indicated by the upward shift of the cumulative distribution curves (Fig. 3d) and the relative changes of highly and broadly tuned neurons, respectively (Fig. 3e). Thus, during the first three months, neuronal orientation tuning was found to be normal and Aβ-plaques almost absent while soluble Aβ-levels were moderately increased. After the age of 4 months, the increase of Aβ-load, including both Aβ-plaques and soluble Aβ, was associated with the progressive impairment of orientation tuning of visual cortex neurons. To exclude the possibility that the PS45 mutation had an effect on neuronal tuning properties, we performed experiments in PS45 mice of 8–10 months of age. We found no significant difference in OSI or DSI between WT and PS45 mice (Supplementary Fig. S2; Mann–Whitney test, OSI $P = 0.60$, DSI $P = 0.23$), indicating that the PS45 mutation alone is not sufficient for causing the neuronal deficits observed in APP23×PS45 mice.

We next investigated the visual performance of the APP23×PS45 mice and found that the aged (8- to 10-month-old) transgenic mice showed specific deficits in a visual pattern discrimination test[37,38]. (Supplementary Methods; Supplementary Fig. S3). Although the aged APP23×PS45 could discriminate drifting gratings of two orientations separated by 45°, they were not able to discriminate gratings that were just 22.5° apart, as indicated by the fact that their performance never exceeded the chance level (Supplementary Fig. S3d, middle panel). It is important to note that young (3-month-old) APP23×PS45 mice, with only few plaques and relatively low levels of soluble Aβ present in their visual cortex (Fig. 3b,c), did not show such deficits in visual discrimination (Supplementary Fig. S4). As a control, we performed an extra behavioural test to evaluate optomotor responses[39] (Supplementary Fig. S5). It is known that optokinetic eye movements are largely driven by subcortical visual pathways[40,41]. We found that both aged WT and transgenic animals (8–10 months) had similar optomotor responses during the presentation of gratings (Supplementary Fig. S5), indicating that the deficits observed in the visual discrimination task in the transgenic animals is not due to an alteration of retina function or of those subcortical pathways that are involved in optokinetic eye movements. In conclusion, the staged decline of neuronal function in the visual cortex of APP23×PS45 mice was associated with a decline in visual discrimination performance.

Visually evoked versus spontaneous neuronal activity. How does the impaired neuronal signalling in response to visual stimuli relate to the spontaneous activity? To address this question, we first performed a frequency analysis of the spontaneous activity in both WT and APP23×PS45 mice (Fig. 4a,b; Supplementary Fig. S6). We found that a substantial fraction of the neurons in the visual cortex of APP23×PS45 mice had activity patterns that were distinctly different from those encountered in the WT mice: some of the neurons displaying an increased activity (for example, Neuron 2, Fig. 4b), while others being hypoactive or even silent (for example, Neuron 3, Fig. 4b). In line with previous results obtained in the frontal cortex[26], the neurons were classified based on their frequency of spontaneous calcium transients as 'normal' (frequency range: 0.25–4 transients per min), hypoactive (<0.25 transients per min) and hyperactive neurons (>4 transients per min) (Supplementary Fig. S6a,b). The analysis of the spontaneous activity clearly demonstrates that, in APP23×PS45 mice, the proportion of 'normal' neurons was substantially reduced, whereas the fraction of hypo- and hyperactive neurons was significantly larger (Fig. 4c, Mann–Whitney test, hypoactive $P < 0.05$, 'normal' $P < 0.001$ and hyperactive neurons $P < 0.001$). We determined the distribution of neurons as a function of their distance to the nearest plaque. The results show that there is a trend for hyperactive neurons to be more abundant near plaques (Supplementary Fig. S7c), although less pronounced than what had been reported for the frontal cortex[26]. Furthermore, in line with previous work, using a double transgenic model of AD[42], we found an increase in the fraction of active astrocytes in the aged APP23×PS45 mice (Supplementary Fig. S8b). Notably, in parallel to the changes in Aβ-load and in neuronal orientation tuning (Fig. 3), we found an age-dependent increase of both hypo- and hyper-active neurons (and a corresponding decrease in 'normal' neurons) (Fig. 4d-f).

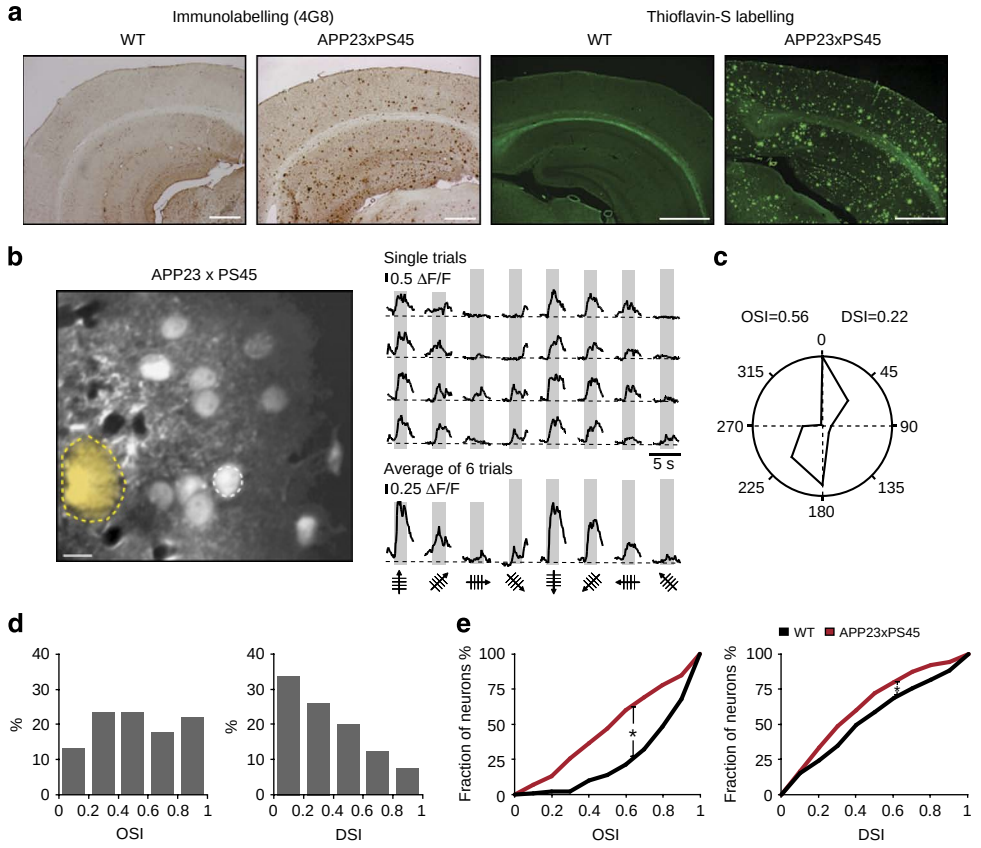

Figure 2 | Impaired orientation/direction tuning of visual cortex neurons in 8–10-month-old APP23×PS45 mice. (**a**) Amyloid-β-deposition in APP23×PS45 mice. Micrographs of coronal brain slices of visual cortices stained with the 4G8 antibody (**a**) and Thioflavin-S (**b**). The slices were obtained from a wild-type (WT, left panels) and an APP23×PS45 mouse (right panels) of the same age (9-months). Scale bars, 500 μm. (**b**) Left panel, *in vivo* two-photon image of layer 2/3 neurons in the visual cortex of an APP23×PS45 mouse (8-months). The broken yellow line delineates a Thioflavin-S-positive plaque observed in the imaged focal plane. Right panel, stimulus-evoked calcium transients recorded from the neuron indicated by a white-dotted circle in the left panel. Grey regions indicate periods of visual stimulation with drifting gratings schematized by oriented arrows on the bottom of each panel. Single trials are represented on top and, the average of six trials is shown below. Scale bar, 10 μm. (**c**) Polar plot showing the neuron's response function to oriented drifting gratings. The responses to each of the eight directions tested were normalized with respect to the maximal response. Then, the function was constructed by connecting the eight values. (**d**) Distribution of the orientation (OSI) and direction (DSI) selectivity indices of all responsive neurons ($n = 145$ neurons) recorded in the visual cortices of 15 APP23×PS45 mice. (**e**) Cumulative distributions of the orientation (OSI) and direction (DSI) selectivity indices determined for all responsive neurons recorded in WT (black) and APP23×PS45 (red) mice. Overall the visual cortex neurons of APP23×PS45 mice have significantly lower orientation and direction selectivities compared with WT ones (Mann–Whitney test, OSI, $^*P < 0.001$; DSI, $^*P < 0.05$).

These results made us wonder whether the impaired tuning is a general feature of all neurons in APP23×PS45 mice, or whether impaired tuning is a particular problem of the hypo- or hyper-active neurons.

To deal with this question, we initially determined the activity status ('normal', hypo- or hyper-active) of the neurons in the field of view by recording their spontaneous activity during at least 4 min, and we then imaged their activity evoked by drifting gratings of different orientations. We first focused on the neurons that had a 'normal' frequency of their spontaneous activity. Fig. 5a illustrates the results obtained from such a 'normal' neuron. We found that this neuron responded specifically to one orientation of drifting gratings, but not to all the other directions. For this neuron, we calculated an OSI of 0.99 and a DSI of 0.47, values that were strikingly similar to highly tuned neurons in WT mice (Fig. 5b; see also Fig 1c). The overlaid polar plots of large numbers of 'normal' neurons of both genotypes (WT, $n = 107$ and APP23×PS45, $n = 67$ neurons) and the calculated median tuning functions revealed a high degree of similarity (Fig. 5c). Accordingly, the cumulative distributions of OSIs and DSIs did not show any significant difference in the two genotypes (Fig. 5d, Mann–Whitney test, OSI, $P = 0.39$; DSI, $P = 0.92$). Furthermore, the amplitudes of spontaneous and visually evoked calcium transients were also similar in both genotypes (Supplementary Fig. S9b). These results strongly indicate that, in APP23×PS45 mice, the fraction of neurons, with a 'normal' spontaneous activity, has tuning properties, for both orientation and direction, which are indistinguishable from those found in WT mice.

In contrast to the 'normal' neurons, the fraction of hypoactive neurons, which included both the totally silent neurons and the neurons with a very low frequency of spontaneous activity (< 0.25 transients per min), were characterized by a total absence of visually evoked responses (Fig. 5e). A similar complete absence of visually evoked responses was observed in all hypoactive neurons tested ($n = 90$ neurons in 15 mice) in APP23×PS45 mice. It is interesting to note that, in WT animals, 20% of the hypoactive neurons (11 out of 55 neurons tested in 13 mice) did respond normally to visual stimulation with drifting gratings and, in fact, had tuning properties for orientation and direction that were similar to those obtained for 'normal' neurons (Mann–Whitney test, OSI, $P = 0.67$; DSI $P = 0.17$). These observations suggest that there is a difference between

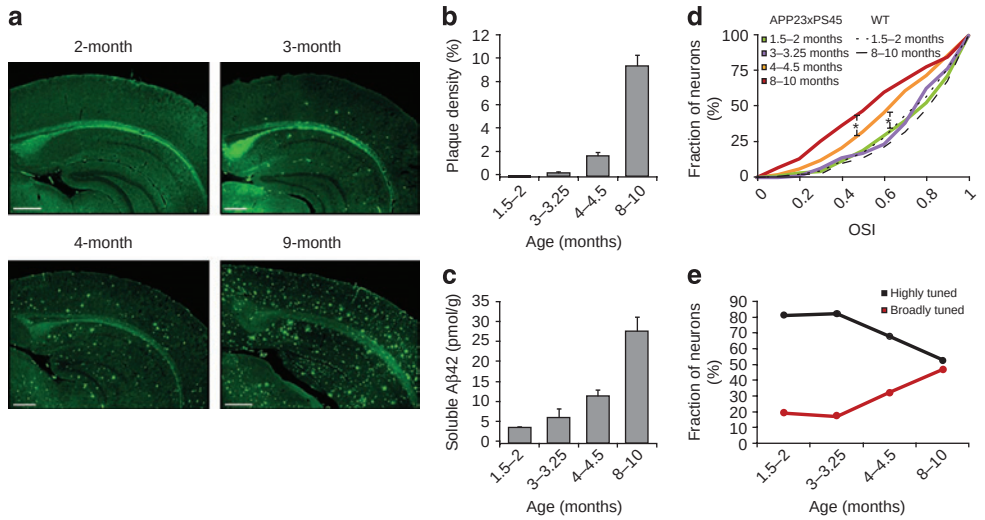

Figure 3 | Age dependence of amyloid-β-load and orientation tuning in the visual cortex of APP23×PS45 mice. (**a**) Amyloid-β-deposition in the visual cortex of APP23×PS45 mice. Micrographs of coronal brain slices of visual cortices stained with Thioflavin-S. The slices were obtained from 2-, 3-, 4- and 9-month-old APP23×PS45 mice. Scale bars, 500 μm. (**b**) Plaque density in the visual cortex of APP23×PS45 mice, determined in the four different age groups (1.5–2-, 3–3.25-, 4–4.5- and 8–10-month-old, $n = 5$, 4, 5 and 6 mice, respectively). (**c**) Concentration of soluble Aβ42 in the forebrain of APP23×PS45 mice ($n = 5$, 5, 6 and 5 mice, respectively). (**d**) Cumulative distributions of the OSIs determined for all responsive neurons recorded in APP23×PS45 mice at the different age groups ($n = 95$, 94, 149 and 145 neurons in 7, 6, 8 and 15 mice, respectively) as well as in 1.5–2-month-old and 8–10-month-old WT mice ($n = 132$ and 131 neurons in 7 and 13 mice, respectively). Functional impairments were observed only from the age of 4–4.5-months (Mann–Whitney test, APP23×PS45, 2-4-months, $^*P < 0.005$; 4–8-months, $^*P < 0.005$). (**e**) Proportion of highly (OSI>0.5) and broadly (OSI < 0.5) tuned neurons in the visual cortex of APP23×PS45 mice (same neurons as in **d**).

hypoactive neurons of WT and APP23×PS45 mice. One possibility is that hypoactive neurons in the visual cortex of APP23×PS45 mice are unable to fire, because they have impaired membrane properties. Alternatively, they can still fire action potentials, but they are silenced by inhibitory inputs. To address this issue, we applied the $GABA_A$ receptor antagonist gabazine and found that spontaneous activity could be restored with this treatment (Supplementary Fig. S7a,b). However, except for random calcium transients during single-trial recordings, no clear and reliable visually evoked responses were resolved in the disinhibited neurons (Fig. 5f). Thus, hypoactive neurons preserve some functional intrinsic properties, but seem to lack the mechanisms responsible for the detection of sensory-evoked signals.

Impaired tuning of hyperactive neurons of APP23×PS45 mice. In a next attempt to identify the poorly tuned neurons that are frequently encountered in the diseased cortex, we focused on the hyperactive neurons. Fig. 6a shows the stimulus-evoked responses of a hyperactive neuron. This neuron was poorly tuned and produced large calcium transients in response to several orientations and directions (6/8) of the drifting gratings (Fig. 6b top panel, OSI = 0.38, DSI = 0.07). Similar broad tuning levels were found to be a general property of all the hyperactive neurons in aged APP23×PS45 mice (Fig. 6b, lower panel). This conclusion is strikingly illustrated by the comparison of the cumulative distributions of the OSIs of hyperactive and 'normal' neurons in APP23×PS45 mice, showing the age dependence of hyperactive neurons impairment (Supplementary Fig. S9a, 4–4.5 months, Mann–Whitney test, $P < 0.001$; 8–10 months, Mann–Whitney test, OSI, $P < 0.001$).

In view of the impaired tuning of hyperactive neurons, it is interesting to ask whether the frequency of spontaneous activity correlates inversely with the tuning performance over the entire frequency range. In WT mice, there was no evidence for such a correlation and a high OSI was determined for the majority of both normal and hyperactive neurons, as indicated by the scatterplot shown in Fig. 6c. By contrast, the results obtained for APP23×PS45 mice showed that the vast majority of neurons with a low OSI were in the upper-left quadrant of the scatter plot, whereas the neurons with a high OSI were in the lower-right quadrant, corresponding to the 'normal' frequency range (Fig. 6d). A quantitative comparison for the two genotypes underscored this impression by showing that the proportion of 'normal' neurons with high-and-low OSI values was similar (Fig. 6e). Instead, there was a striking contrast between the hyperactive neurons in the two genotypes (Fig. 6f). Whereas the hyperactive neurons of WT mice had mostly a high OSI, the hyperactive neurons of APP23×PS45 mice had mostly low OSI values. This indicates that high spontaneous activity *per se* does not explain the loss in orientation tuning. To verify this conclusion independently, we analysed periods of spontaneous activity by randomly assigning periods of nominal stimulation (see Methods). The results demonstrate that even in conditions of high spontaneous activity, the level of false positive responses is low (Supplementary Fig. S10). Together, these results establish that a major source for the impaired orientation and direction tuning in APP23×PS45 mice is the hyperactive neurons and that this loss of tuning is not due to a simple increase in spontaneous activity, but to qualitative functional changes that are disease specific.

Discussion

In this study, we obtained direct insights into the relation between the age-dependent increase of Aβ-load, specific changes in the function of cortical neurons *in vivo* and behavioural alterations in a mouse model of AD. First, we found that the staged increase of Aβ-load, including both insoluble Aβ-plaques and soluble Aβ, in the visual cortex, was paralleled by reduced orientation and direction tunings of many neurons as well as reduced performance in a visual discrimination test. Second, the spontaneous ongoing activity of a large fraction of neurons was also massively changed in the visual cortex of APP23×PS45 mice, with substantial fractions of hypo- and hyper-active neurons. Third, while hypoactive neurons were entirely unresponsive to visual stimuli, we found that impaired orientation and direction tuning was primarily due to massively impaired

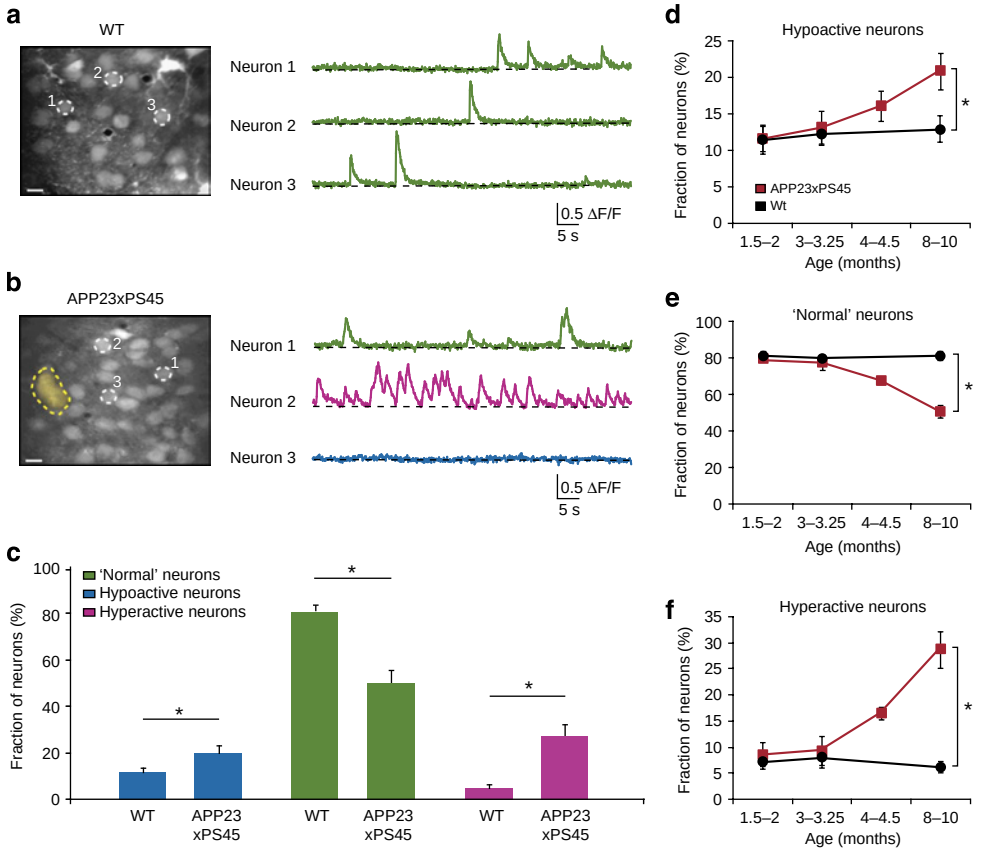

Figure 4 | Age-dependence of spontaneous activity in the visual cortex of WT and APP23×PS45 mice. (**a**,**b**) Spontaneous calcium transients recorded *in vivo* from layer 2/3 neurons of the visual cortex of a WT (**a**) and an APP23×PS45 (**b**) mouse (10- and 9-months, respectively). Left panels, *in vivo* two-photon images (*z*-stack, 0.5 µm step, ±20 µm from the imaged focal plane). The broken yellow line delineates a Thioflavin-S positive plaque. Right panels, spontaneous calcium transients colour-coded according to the activity frequency: green for 'normal' neurons (0.25–4 transients per min), purple for hyperactive neurons (>4 transients per min) and blue for hypoactive neurons (0–0.25 transients per minute). Scale bar, 10 µm. (**c**) Bar graph showing the relative proportion of hypoactive, 'normal' and hyperactive neurons in 8–10-month-old WT and APP23×PS45 mice ($n = 630$ and 806 neurons in 15 and 19 mice, respectively). Error bars indicate s.e.m. (Mann–Whitney test, hypoactive $^*P < 0.05$, 'normal' $^*P < 0.001$ and hyperactive neurons $^*P < 0.001$). (**d**–**f**) Proportion of hypoactive, 'normal' and hyperactive neurons in WT (black; $n = 686$, 411, 630 neurons in 9, 5 and 15 mice, respectively) and APP23×PS45 (red; $n = 634$, 620, 750 and 806 neurons in 10, 9, 10 and 19 APP23×PS45 mice, respectively) mice at four different age groups (1.5–2, 3–3.25, 4–4.5 and 8–10 months). Error bars indicate s.e.m. (Mann–Whitney test, hypoactive $^*P < 0.05$, 'normal' $^*P < 0.001$ and hyperactive neurons $^*P < 0.001$).

performance of the hyperactive neurons. Together, the results establish that there is a parallel progression in the change of Aβ-load, cortical dysfunction and sensory deficits in the APP23×PS45 mouse model of AD.

In vivo two-photon imaging in animal models advanced substantially our understanding of the pathomechanisms that underlie AD[20,21,31,43]. Several studies have analysed the morphological and activity changes of neurons. They revealed neuritic dystrophies and a loss of dendritic spines[20,43], an increased resting calcium level in a subset of dendrites[21], an increase in activity and resting calcium concentration in glial cells[42], as well as an increase in the fraction of hyperactive neurons[26]. In this study, we used *in vivo* two-photon calcium imaging to analyse sensory-evoked neuronal signals in the APP23×PS45 mouse model. We found in this mouse model an age-dependent increase of Aβ in the visual cortex. Furthermore, in the diseased visual cortex of these mice, the orientation and direction tuning of many neurons was substantially lower than in WT mice. It is important to note that in the young transgenic mice, in which Aβ-aggregates were absent, the tuning level of the neurons was not different from that of WT mice of the same age. This is an indication that visual cortex development of APP23×PS45 transgenic mice, during the first postnatal months, is not disrupted.

The overview of the age-related changes illustrated in Table 1 suggests that the decline in visual processing can be associated with distinct stages[6]. In our mouse model of AD, stage I lasts from birth until the age of about 3 months. During this early period, visual discrimination and visual cortex function are normal, while plaques are largely absent and soluble Aβ-levels are moderately increased. The results obtained in 4–4.5-month-old mice revealed an intermediate stage, stage II, in which the plaques were present at substantial higher densities in the visual cortex, soluble Aβ-levels were also higher and orientation/direction tuning of visual cortex neurons showed significant signs of impairment. Finally, the most severe changes were found at the age of 7–8 months, corresponding to stage III. At stage III, all parameters tested, namely, plaque density, soluble Aβ-concentration, orientation tuning and visual discrimination deviated most severely from the control values obtained in WT mice. It is important to note that, while nearly 50% of the neurons in the primary visual cortex were functionally impaired, the transgenic mice were still able to discriminate gratings differing by 45°. This indicates that even a reduced circuit of 'normal' neurons is largely capable of sustaining physiological activities, perhaps with the help of compensatory mechanisms[23,44]. Such reduced circuits may account for the observations in humans that apparently normal

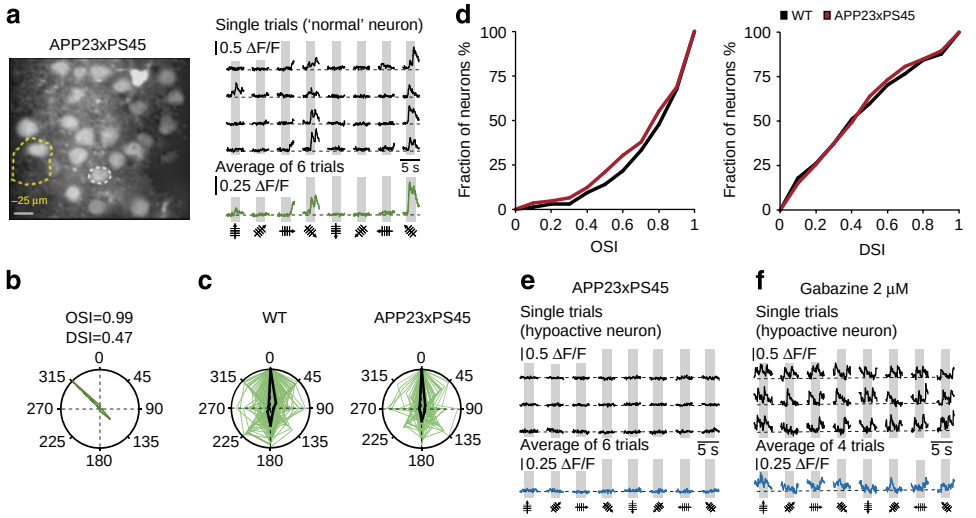

Figure 5 | Response of normal and hypoactive neurons to stimulus orientation and direction. (**a**) Left panel, *in vivo* two-photon image of layer 2/3 neurons in the visual cortex of an APP23×PS45 mouse (8-months). The broken yellow line delineates a Thioflavin-S-positive plaque that was located 25 µm below the imaged focal plane (seen on the *z*-stack). Right panel, calcium transients evoked by visual stimulation in the 'normal' neuron indicated in the left panel by a white-dotted circle. Scale bar, 10 µm. (**b**) Polar plot showing the neuron's response function to oriented drifting gratings. The responses to each of the eight directions tested were normalized with respect to the maximal response. Then, the function was constructed by connecting the eight values. (**c**) Overlap of the polar plots obtained for all responsive 'normal' neurons recorded in 13 WT ($n = 107$ neurons) and 15 APP23×PS45 ($n = 67$ neurons) mice. Polar plots were normalized to a preferred direction of 0° and maximal response. Black lines indicate median tuning function. (**d**) Cumulative distributions of the orientation (OSI) and direction (DSI) selectivity indices determined for all 'normal' neurons recorded in 13 WT (black) and 15 APP23×PS45 (red) mice. 'Normal' neurons were similarly tuned for orientation and direction in both APP23×PS45 and WT mice (Mann–Whitney test, OSI, $P = 0.39$; DSI, $P = 0.92$). (**e**) Calcium imaging of a hypoactive neuron's activity recorded during visual stimulation in the layer 2/3 of an APP23×PS45 mouse (8.5-months). Four single trials are represented with black lines and the average of six trials is shown in blue. (**f**) Calcium transients recorded from the same neuron as in panel **e** after application of gabazine.

cognitive function is largely sustained, despite the presence of substantial neuropathology in their brains[45,46].

The mechanisms underlying the changed neuronal activity in the diseased visual cortex are likely to involve a redistribution of synaptic inhibition[47] and excitation[24], as it has been proposed for the impaired spontaneous activity in the frontal cortex[26]. This is suggested by the observation that similar fractions of hypo- and hyperactive neurons were detected in both cortical regions. Furthermore, application of the $GABA_A$ receptor antagonist gabazine was able to induce neuronal activity in hypoactive neurons, indicating that excessive inhibition is one of the reasons for the impaired network activity.

Interestingly, chronic functional impairments, by traumatic or ischemic lesions of the cortex, share important similarities with those observed in the Aβ-containing cortical regions, which are enriched with hyperactive neurons. For example, it is clinically well established that the cortical area that is adjacent to the traumatically destroyed cortical tissue is a trigger site for post-traumatic epileptic seizures[48]. Furthermore, a strong increase of neuronal excitability has been observed in regions surrounding experimental cortical lesions in the cat visual cortex[49]. This hyperexcitability was shown to cause an increase in both spontaneous and visually evoked activity. The major consequence of the functional reorganization in the cortical region surrounding the lesion was the enlargement of receptive fields that included the lost parts of the visual field representation[50,51]. It was suggested that neurons at the border of a lesion receive subthreshold inputs outside their original receptive field and that these inputs become functional after the lesion[50,51]. Finally, in rodent models of stroke, post-lesion hyperexcitability was shown to develop in the somatosensory cortex over the first week to month after the incident[52,53]. In addition, an expansion of the receptive field size and a loss of specificity in the neuron's response to sensory stimulation were found in the peri-infarct region[52]. *In vivo* two-photon calcium imaging showed that the limb selectivity of individual neurons was altered after the stroke such that neurons that were previously selective for a single contralateral limb processed information from multiple limbs[52]. In analogy to these findings, Aβ-plaques can be interpreted as multiple small cortical lesions, causing hyperexcitability and loss of functional selectivity owing to structural and functional changes in their vicinity. In addition, soluble Aβ may form a synaptotoxic microenvironment for the neurons surrounding the Aβ-plaques[31]. The precise cellular mechanisms underlying the hyperexcitability in AD will need to be established in future studies. Some mechanisms may be similar to those suggested to contribute to the hyperactivity observed after brain injuries that cause post-traumatic epilepsy. They include sprouting of excitatory inputs, loss of GABAergic inhibition and loss of trophic support normally provided by brain-derived neurotrophic factor (for review, see ref. 54).

Methods

Animals and surgery. All experimental procedures were performed in accordance with institutional animal welfare guidelines and were approved by the Government of Bavaria, Germany. APP23×PS45 mice were generated from two already existing transgenic mouse lines as described previously[26]. Briefly, one line, APP23[32], overexpresses human amyloid precursor protein (APP) with the Swedish double mutation at positions 670/671, whereas the other, PS45 (ref. 33) carries a transgene for the human Presenilin 1 bearing the G384A mutation (both lines are driven by a Thy-1 promoter). APP23×PS45 mice were reared in 12/12 h light/dark cycles (P46-P60, $n = 10$; 3–3.25 months, $n = 9$; 4–4.5 months, $n = 10$; 8–10 months, $n = 19$). These mice were compared with WT mice with the same strain background (C57Bl/6) and of similar ages (P55-P60, $n = 9$; 3–3.25 months, $n = 5$; 8–10 months, $n = 15$) and to the PS45 mouse line (8–10 months, $n = 5$). Genotypes were systematically determined by PCR analysis.

Animals were prepared for *in vivo* two-photon calcium imaging, as described previously[29]. Briefly, the mice were placed onto a warming plate (38 °C) and anaesthetized by inhalation of 1.5% isoflurane (Curamed, Karlsruhe, Germany) in pure O_2. After removing the skin, a custom-made recording chamber[55] was then glued to the skull with cyanoacrylic glue (UHU, Buhl-Baden, Germany).

The mouse was then transferred into the set-up, placed onto a warming plate (38 °C), and continuously supplied with 0.8–1% isoflurane in pure O_2 (breathing rate, 110–130 b.p.m.). The position of the primary visual cortex was located according to brain atlas coordinates (Bregma −3 to −4.5, 2–3 mm lateral to the midline)[56]. In all experiments, the correct location of the imaged neurons was confirmed post-hoc by imaging of the stained brain area (for example, Fig. 1a). A small craniotomy (~0.8×0.6 mm) was performed above the monocular region of primary visual cortex using a thin (30-gauge) injection needle. The recording chamber was perfused with warm (37 °C) extracellular perfusion saline containing (in mM):

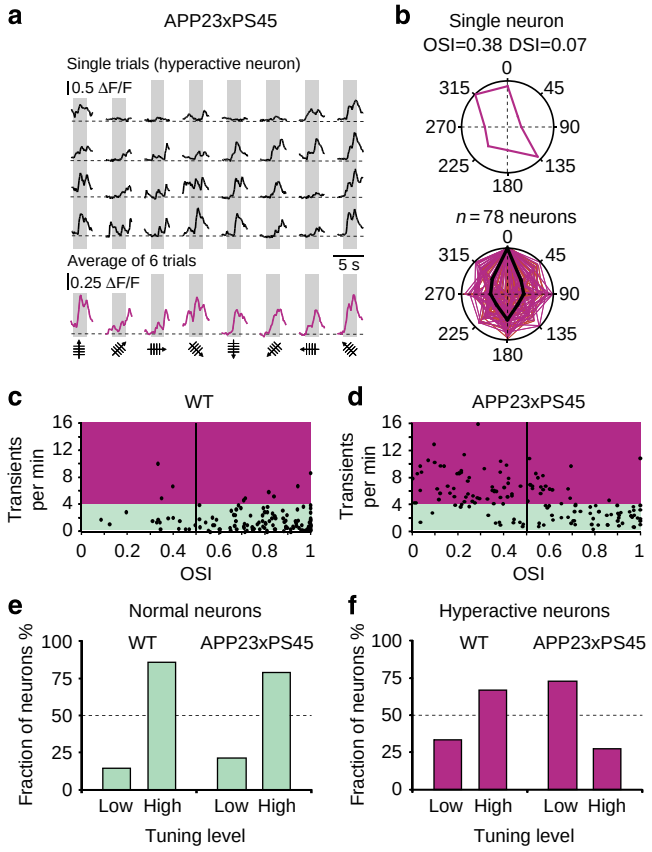

Figure 6 | Response of hyperactive neurons to stimulus orientation and direction. (**a**) Stimulus-evoked calcium transients recorded from a hyperactive neuron in an APP23×PS45 mouse (8-months). (**b**) Top panel, polar plot showing the response function (purple lines) to oriented drifting gratings of the same neuron as in panel **a**. Lower panel, overlap of the polar plots obtained for all responsive hyperactive neurons recorded in 15 APP23×PS45 mice ($n = 78$ neurons). Polar plots were normalized to a preferred direction of 0° and maximal response. Black lines indicate median tuning function. (**c,d**) Scatter plots showing the relation between the OSI and the frequency of spontaneous calcium transients in WT (**c**) and APP23×PS45 (**d**) mice ($n = 131$ and 145 neurons from 13 and 15 mice, respectively). The coloured areas indicate the frequency domains of 'normal' (green) and hyperactive (purple) spontaneous activity. (**e,f**) Comparison of the fractions of 'normal' (**e**) and hyperactive (**f**) neurons with low (OSI < 0.5) and high orientation tuning (OSI>0.5) levels in WT and APP23×PS45 mice (same neurons as in **c,d**).

125 NaCl, 4.5 KCl, 26 $NaHCO_3$, 1.25 NaH_2PO_4, 2 $CaCl_2$, 1 $MgCl_2$, 20 glucose, pH 7.4, when bubbled with 95% O_2 and 5% CO_2. The neurons were stained *in vivo* with the fluorescent calcium indicator dye Oregon Green BAPTA-1 (OGB-1) following the protocol described in detail in ref. 29. Amyloid-β-plaques were stained *in vivo* in a comparable way, by pressure-injecting Thioflavin-S (0.001% (w/v)). Eye cream (Bepanthen, Bayer) was applied on both eyes to prevent dehydration during surgery. After surgery, the anaesthesia level was decreased to 0.8% isoflurane for recordings (breathing rate, 110–130 b.p.m.).

Two-photon calcium imaging. *In vivo* calcium imaging was performed by using a custom-built two-photon microscope based on Ti:Sapphire pulsing laser (model: Chameleon, repetition rate: 80 MHz, pulse width: 140 fs; Coherent) and resonant galvo-mirror (8 kHz; GSI) system[57]. The scanner was mounted on an upright microscope (BX51WI, Olympus, Tokyo, Japan) equipped with a water-immersion objective (×60, 1.0 NA Nikon, Japan or ×40, 0.8″ NA Nikon, Japan). Emitted photons were detected by photomultiplier tubes (H7422-40; Hamamatsu). Full-frame images at 480×400 pixel resolution were acquired at 30 Hz by custom-programmed software based on LabVIEW (version 8.2; National Instruments). At each focal plane, we imaged spontaneous activity (for at least 4 min) as well as visually evoked activity (6 to 10 trials of visual stimulation). For simultaneous visualization of Aβ-plaques and cortical neurons labelled with OGB-1, the emitted fluorescence light was split at 515 nm. To identify the amyloid plaques close to the recorded neurons, the brain region (± about 200 µm, centred on the recorded neurons) was scanned through in the *z* direction (z-stack, 2 µm step), at the end of each experiment.

Drug application. Gabazine (2 µM) was added to the extracellular saline solution perfusing the chamber attached to the mouse's skull ('bath' application).

Visual stimulation. Visual stimuli were generated by Matlab (release 2007b; Mathworks) with the 'Psychtoolbox' add-on package (http://psychtoolbox.org/wikka.php?wakka=HomePage). Visual stimuli were projected on a screen placed 30 cm from the contralateral eye, covering 80°×67° of the visual field. Each trial of visual stimulation started with a grey screen (mean luminance) for 5 s, followed by a stationary square-wave grating for 4 s and the corresponding drifting phase for 2 s (0.03 c.p.d., 1 Hz, 8 directions, contrast 80%, mean luminance 3.7 cd m^{-2}). We used stationary gratings during the inter-stimulus periods to study specifically the responses to moving gratings. When a blank screen is used during the inter-stimulus period instead of stationary gratings, responses to local changes in luminance may occur. At each focal plane, evoked activities were imaged during 6–10 trials. Under our experimental conditions, this visual stimulation protocol evoked visual responses in 95/313 neurons (APP23×PS45, 1.5–2 months), 132/426 neurons (WT, 1.5–2 months), 94/334 neurons (APP23×PS45, 3–3.25 months), 140/464 neurons (APP23×PS45, 4–4.5 months), 145/404 neurons (APP23×PS45, 8–10 months) and in 131/384 neurons (WT, 8–10 months).

Data analysis. The image analysis was performed off-line in two steps. First, the ImageJ software (http://rsb.info.nih.gov/ij/) was used for drawing regions of interest (ROIs) around cell bodies and around a large area of cell-free neuropil. Astrocytes were identified based on their selective staining by sulforhodamine 101 (refs 58,59), brighter appearance after staining with OGB1-AM[35] and their specific morphology with clearly visible processes. The presence of glial processes was assessed by inspecting 3D-stacks (70 µm below and upper the imaged plane) obtained routinely at the end of each experiment. In the next step, custom-made routines of the Igor Pro software (Wavemetrics, Lake Oswego, Oregon, USA) were used for the detection of wave-associated calcium transients in individual neurons. Calcium signals were expressed as relative fluorescence changes (ΔF/F) corresponding to the mean fluorescence from all pixels within specified ROIs. For each ROI, a transient was accepted as a signal, when its peak amplitude was greater than three times the standard deviation of the noise band. After the automatic analysis, all traces were carefully inspected. The analysis of the visually evoked responses was performed by using the average traces of the 6–10 stimulus trials used during the imaging session (see examples in Figs 1,2 1b and 2b). Neurons were defined as responsive to moving gratings when they responded to at least one of the eight directions with a significant change in fluorescence (mean amplitude during the 2 s of stimulus presentation, t-test) compared with the activity during the 2 s preceding the presentation of the stimulus (standing grating). An OSI (for example, ref. 36) was calculated to quantify the tuning level of the neurons with regard to the orientation of the

Table 1 | Staged decline of visual processing in the APP23×PS45 mouse model.

Stage	Age (months)	Plaque density	Concentration of soluble Aβ	Visual discrimination deficit	Impairment of orientation tuning
I	1.5–2	None	Low	None	None
	3–3.25	Low	Low	None	None
II	4–4.5	Intermediate	Intermediate	Not tested	Intermediate
III	8–10	High	High	High	High

drifting grating. The OSI was defined as $(R_{pref} - R_{ortho})/(R_{pref} + R_{ortho})$, where R_{pref}, the mean response in the preferred orientation, was the response with the largest magnitude in the average trace of the 6–10 trials. R_{pref} was determined as the mean of the integrals of the calcium transients for the two corresponding opposite directions. R_{ortho} was similarly calculated as the response evoked by the orthogonal orientation. With this index, perfect orientation selectivity would give OSI = 1; an equal response to all orientations would have OSI = 0, and 3:1 selectivity corresponds to OSI = 0.5. Highly and poorly tuned neurons were defined as neurons with an OSI>0.5 and OSI < 0.5, respectively. Similarly, a DSI was defined as $(R_{pref} - R_{opp})/(R_{pref} + R_{opp})$, where R_{opp} is the response in the direction opposite to the preferred direction. Polar plots show neuron response function to oriented drifting gratings. The mean responses to each of the eight directions tested were normalized with respect to the maximal response. Then, the function was constructed by connecting the eight values.

Statistical analysis. The following values were compared between APP23×PS45 and WT mice using a Mann–Whitney test with a two-tailed level of significance set at $\alpha = 0.05$. (SPSS 16.0 software): fraction of 'normal', hypoactive and hyperactive neurons, cumulative distributions of OSI and DSI, and percentages of good choices in the pattern discrimination task. The last values were also compared with chance level using a nonparametric χ^2 test.

Measurement of plaque load *in situ*. Coronal brain slices were obtained from brains imaged *in vivo*. After fixation with 4% paraformaldehyde, 25 µm-cryosections of the visual cortex were prepared. Sections were washed in PBS, before heat-induced antigen retrieval (90 °C for 5 min) in 0.1 M citric acid buffer. For the detection of Aβ-deposition, two different methods were applied: immunohistological staining with the 4G8 antibody and Thioflavin-S staining. For the first one, we used primary mouse anti-human Aβ-antibody 4G8 (Covance, Princeton, NJ, USA) with a dilution of 1:1,000 and a secondary biotinylated horse anti-mouse IgG antibody (BA2000, Vector Laboratories, Burlingame, CA, USA) diluted 1:200. The slices were further processed using the Vectorstain Elite ABC Kits (Vector). After the reaction with Diaminobenzidine (Roche, Code 17118096), the slices were dehydrated and cover slipped. Thioflavin-S (0.05% (w/v) in 50% ethanol) was applied for 8 min in darkness by bath application. This was followed by two differentiation steps in 80% ethanol for 10 s each, three washes in distilled water and 30-min washout of the residual dye in a concentrated phosphate buffer[60]. Micrographs were taken using a camera (XC10, Olympus, Tokyo, Japan) mounted on an Olympus microscope (MVX10, Olympus, Tokyo, Japan). The images were processed offline using the ImageJ program (http://rsb.info.nih.gov/ij/).

To determine the plaque density, PFA-fixed slices (200-µm thick) were stained by bath application of Thioflavin (0.005% (w/v)) for 20 min. After 20 min, washout of the residual dye images were taken and processed as described above. The plaque density (in per cent) was then calculated as the relative fraction of green pixels.

Determination of amyloid-β. Frozen forebrain hemispheres (excluding hindbrain and olfactory bulb) from the four different age groups (1.5–2, 3–3.25, 4–4.5 and 8–10 months) were weighed and homogenized at 10% (w/v) in Tris-buffered saline (30 mM Tris–HCl pH 7.6, 137 mM sodium chloride, protease inhibitor cocktail cOmplete, Roche Molecular Biochemicals), using Eppendorf micropestles (Vaudaux-Eppendorf, Schönenbuch, Basel, Switzerland). Aliquots for the analysis of soluble Aβ were removed and stored at -80° until analysis. Quantitative determinations of Aβ were done with electrochemoluminescence-linked immunoassays (Human Aβ40 and Aβ42 Ultrasensitive Kits, Meso Scale Discovery, Gaithersburg, MD). Standard curves with synthetic Aβ1–40 (Bachem) and 1–42 (rPeptide) were set up in non-transgenic mouse forebrain extract, prepared identically to the transgenic samples. For analysis of soluble Aβ, 50 µl of each forebrain homogenate were supplemented with 1 volume of Tris-buffered saline and extracted for 15 min at 4 °C. Homogenates were mixed every 5 minutes. The supernatants of a 15-min centrifugation at 100,000*g* were diluted with 9 volumes of blocking solution from the immunoassay kit. 25 µl of each sample were loaded as duplicates on the assay plates and further processed, according to the manufacturer's protocol. For quantification of total Aβ, homogenates were sonicated on ice, supplemented with concentrated formic acid (final concentration 70%) and extracted for 15 min at 4 °C, with occasional mixing. Extracts were neutralized by addition of 19 volumes 1 M Tris and centrifuged at 20,000*g* for 15 min at 4 °C. The supernatants were either diluted with 6.5 volumes (2–3 months-old animals), or with 149 volumes (4–8 months-old animals) of blocking solution from the immunoassay kit. Aβ-concentrations were read from the standard curves using a point-to-point fit with the software Softmax Pro 4.0 (Molecular Devices, Sunnyvale, CA, USA).

References

1. Blennow, K., de Leon, M. J. & Zetterberg, H. Alzheimer's disease. *Lancet* **368,** 387–403 (2006).
2. Nestor, P. J., Scheltens, P. & Hodges, J. R. Advances in the early detection of Alzheimer's disease. *Nat. Med.* **10**(Suppl), S34–S41 (2004).
3. Djordjevic, J., Jones-Gotman, M., De Sousa, K. & Chertkow, H. Olfaction in patients with mild cognitive impairment and Alzheimer's disease. *Neurobiol. Aging* **29,** 693–706 (2008).
4. Mesholam, R. I., Moberg, P. J., Mahr, R. N. & Doty, R. L. Olfaction in neurodegenerative disease: a meta-analysis of olfactory functioning in Alzheimer's and Parkinson's diseases. *Arch. Neurol.* **55,** 84–90 (1998).
5. Devanand, D. P. *et al.* Olfactory deficits in patients with mild cognitive impairment predict Alzheimer's disease at follow-up. *Am. J. Psychiatry* **157,** 1399–1405 (2000).
6. Bublak, P. *et al.* Staged decline of visual processing capacity in mild cognitive impairment and Alzheimer's disease. *Neurobiol. Aging* **32,** 1219–1230 (2011).
7. Cronin-Golomb, A. *et al.* Visual dysfunction in Alzheimer's disease: relation to normal aging. *Ann. Neurol* **29,** 41–52 (1991).
8. Fernandez, R., Kavcic, V. & Duffy, C. J. Neurophysiologic analyses of low- and high-level visual processing in Alzheimer disease. *Neurology* **68,** 2066–2076 (2007).
9. Trick, G. L. & Silverman, S. E. Visual sensitivity to motion: age-related changes and deficits in senile dementia of the Alzheimer type. *Neurology* **41,** 1437–1440 (1991).
10. Glabe, C. G. Structural classification of toxic amyloid oligomers. *J. Biol. Chem.* **283,** 29639–29643 (2008).
11. Hartley, D. M. *et al.* Protofibrillar intermediates of amyloid beta-protein induce acute electrophysiological changes and progressive neurotoxicity in cortical neurons. *J. Neurosci.* **19,** 8876–8884 (1999).
12. Hsieh, H. *et al.* AMPAR removal underlies Abeta-induced synaptic depression and dendritic spine loss. *Neuron* **52,** 831–843 (2006).
13. Shankar, G. M. *et al.* Natural oligomers of the Alzheimer amyloid-beta protein induce reversible synapse loss by modulating an NMDA-type glutamate receptor-dependent signaling pathway. *J. Neurosci.* **27,** 2866–2875 (2007).
14. Kamenetz, F. *et al.* APP processing and synaptic function. *Neuron* **37,** 925–937 (2003).
15. Chapman, P. F. *et al.* Impaired synaptic plasticity and learning in aged amyloid precursor protein transgenic mice. *Nat. Neurosci.* **2,** 271–276 (1999).
16. Wei, W. *et al.* Amyloid beta from axons and dendrites reduces local spine number and plasticity. *Nat. Neurosci.* **13,** 190–196 (2010).
17. Li, S. *et al.* Soluble oligomers of amyloid Beta protein facilitate hippocampal long-term depression by disrupting neuronal glutamate uptake. *Neuron* **62,** 788–801 (2009).
18. Shankar, G. M. *et al.* Amyloid-beta protein dimers isolated directly from Alzheimer's brains impair synaptic plasticity and memory. *Nat. Med.* **14,** 837–842 (2008).
19. Knowles, R. B. *et al.* Plaque-induced neurite abnormalities: implications for disruption of neural networks in Alzheimer's disease. *Proc. Natl Acad. Sci. USA* **96,** 5274–5279 (1999).
20. Meyer-Luehmann, M. *et al.* Rapid appearance and local toxicity of amyloid-beta plaques in a mouse model of Alzheimer's disease. *Nature* **451,** 720–724 (2008).
21. Kuchibhotla, K. V. *et al.* Abeta plaques lead to aberrant regulation of calcium homeostasis *in vivo* resulting in structural and functional disruption of neuronal networks. *Neuron* **59,** 214–225 (2008).
22. Stern, E. A. *et al.* Cortical synaptic integration *in vivo* is disrupted by amyloid-beta plaques. *J. Neurosci.* **24,** 4535–4540 (2004).
23. Palop, J. J. & Mucke, L. Amyloid-beta-induced neuronal dysfunction in Alzheimer's disease: from synapses toward neural networks. *Nat. Neurosci.* **13,** 812–818 (2010).
24. Palop, J. J. *et al.* Aberrant excitatory neuronal activity and compensatory remodeling of inhibitory hippocampal circuits in mouse models of Alzheimer's disease. *Neuron* **55,** 697–711 (2007).
25. Wesson, D. W. *et al.* Sensory network dysfunction, behavioral impairments, and their reversibility in an Alzheimer's beta-amyloidosis mouse model. *J. Neurosci.* **31,** 15962–15971 (2011).
26. Busche, M. A. *et al.* Clusters of hyperactive neurons near amyloid plaques in a mouse model of Alzheimer's disease. *Science* **321,** 1686–1689 (2008).
27. Rochefort, N. L. *et al.* Sparsification of neuronal activity in the visual cortex at eye-opening. *Proc. Natl Acad. Sci. USA* **106,** 15049–15054 (2009).
28. Ohki, K., Chung, S., Ch'ng, Y. H., Kara, P. & Reid, R. C. Functional imaging with cellular resolution reveals precise micro-architecture in visual cortex. *Nature* **433,** 597–603 (2005).
29. Stosiek, C., Garaschuk, O., Holthoff, K. & Konnerth, A. *In vivo* two-photon calcium imaging of neuronal networks. *Proc. Natl Acad. Sci. USA* **100,** 7319–7324 (2003).
30. Rochefort, N. L. *et al.* Development of direction selectivity in mouse cortical neurons. *Neuron* **71,** 425–432 (2011).
31. Koffie, R. M. *et al.* Oligomeric amyloid beta associates with postsynaptic densities and correlates with excitatory synapse loss near senile plaques. *Proc. Natl Acad. Sci. USA* **106,** 4012–4017 (2009).
32. Sturchler-Pierrat, C. *et al.* Two amyloid precursor protein transgenic mouse models with Alzheimer disease-like pathology. *Proc. Natl Acad. Sci. USA* **94,** 13287–13292 (1997).
33. Herzig, M. C. *et al.* Abeta is targeted to the vasculature in a mouse model of hereditary cerebral hemorrhage with amyloidosis. *Nat. Neurosci.* **7,** 954–960 (2004).

34. Rochefort, N. L., Jia, H. & Konnerth, A. Calcium imaging in the living brain: prospects for molecular medicine. *Trends Mol. Med.* **14,** 389–399 (2008).
35. Kerr, J. N., Greenberg, D. & Helmchen, F. Imaging input and output of neocortical networks *in vivo*. *Proc. Natl Acad. Sci. USA* **102,** 14063–14068 (2005).
36. Niell, C. M. & Stryker, M. P. Highly selective receptive fields in mouse visual cortex. *J. Neurosci.* **28,** 7520–7536 (2008).
37. Wong, A. A. & Brown, R. E. Age-related changes in visual acuity, learning and memory in C57BL/6J and DBA/2J mice. *Neurobiol. Aging* **28,** 1577–1593 (2007).
38. Prusky, G. T., West, P. W. & Douglas, R. M. Behavioral assessment of visual acuity in mice and rats. *Vision Res.* **40,** 2201–2209 (2000).
39. Prusky, G. T., Alam, N. M., Beekman, S. & Douglas, R. M. Rapid quantification of adult and developing mouse spatial vision using a virtual optomotor system. *Invest. Ophthalmol. Vis. Sci.* **45,** 4611–4616 (2004).
40. Douglas, R. M. *et al.* Independent visual threshold measurements in the two eyes of freely moving rats and mice using a virtual-reality optokinetic system. *Vis. Neurosci.* **22,** 677–684 (2005).
41. Thaung, C., Arnold, K., Jackson, I. J. & Coffey, P. J. Presence of visual head tracking differentiates normal sighted from retinal degenerate mice. *Neurosci. Lett.* **325,** 21–24 (2002).
42. Kuchibhotla, K. V., Lattarulo, C. R., Hyman, B. T. & Bacskai, B. J. Synchronous hyperactivity and intercellular calcium waves in astrocytes in Alzheimer mice. *Science* **323,** 1211–1215 (2009).
43. Spires, T. L. *et al.* Dendritic spine abnormalities in amyloid precursor protein transgenic mice demonstrated by gene transfer and intravital multiphoton microscopy. *J. Neurosci.* **25,** 7278–7287 (2005).
44. Palop, J. J., Chin, J. & Mucke, L. A network dysfunction perspective on neurodegenerative diseases. *Nature* **443,** 768–773 (2006).
45. Ashe, K. H. & Zahs, K. R. Probing the biology of Alzheimer's disease in mice. *Neuron* **66,** 631–645 (2010).
46. Price, J. L. & Morris, J. C. Tangles and plaques in nondemented aging and 'preclinical' Alzheimer's disease. *Ann. Neurol.* **45,** 358–368 (1999).
47. Garcia-Marin, V. *et al.* Diminished perisomatic GABAergic terminals on cortical neurons adjacent to amyloid plaques. *Front. Neuroanat.* **3,** 28 (2009).
48. Kharatishvili, I. & Pitkanen, A. Posttraumatic epilepsy. *Curr. Opin. Neurol.* **23,** 183–188 (2010).
49. Eysel, U. T. & Schmidt-Kastner, R. Neuronal dysfunction at the border of focal lesions in cat visual cortex. *Neurosci. Lett.* **131,** 45–48 (1991).
50. Eysel, U. T. & Schweigart, G. Increased receptive field size in the surround of chronic lesions in the adult cat visual cortex. *Cereb. Cortex* **9,** 101–109 (1999).
51. Eysel, U. T. *et al.* Reorganization in the visual cortex after retinal and cortical damage. *Restor. Neurol. Neurosci.* **15,** 153–164 (1999).
52. Winship, I. R. & Murphy, T. H. *In vivo* calcium imaging reveals functional rewiring of single somatosensory neurons after stroke. *J. Neurosci.* **28,** 6592–6606 (2008).
53. Murphy, T. H. & Corbett, D. Plasticity during stroke recovery: from synapse to behaviour. *Nat. Rev. Neurosci.* **10,** 861–872 (2009).
54. Prince, D. A. *et al.* Epilepsy following cortical injury: cellular and molecular mechanisms as targets for potential prophylaxis. *Epilepsia* **50**(Suppl 2), 30–40 (2009).
55. Garaschuk, O., Milos, R. I. & Konnerth, A. Targeted bulk-loading of fluorescent indicators for two-photon brain imaging *in vivo*. *Nat. Protoc.* **1,** 380–386 (2006).
56. Paxinos, G. & Franklin, K. B. J. *The Mouse Brain in Stereotaxic Coordinates* **157**: (Academic Press, San Diego, California, 2001).
57. Sanderson, M. J. & Parker, I. Video-rate confocal microscopy. *Methods Enzymol.* **360,** 447–481 (2003).
58. Garaschuk, O. *et al.* Optical monitoring of brain function *in vivo*: from neurons to networks. *Pflügers Arch.* **453,** 385–396 (2006).
59. Nimmerjahn, A., Kirchhoff, F., Kerr, J. N. & Helmchen, F. Sulforhodamine 101 as a specific marker of astroglia in the neocortex *in vivo*. *Nat. Methods* **1,** 31–37 (2004).
60. Sun, A., Nguyen, X. V. & Bing, G. Comparative analysis of an improved thioflavin-s stain, Gallyas silver stain, and immunohistochemistry for neurofibrillary tangle demonstration on the same sections. *J. Histochem. Cytochem.* **50,** 463–472 (2002).

Acknowledgements

We thank Jia Lou for excellent technical assistance and Prof. Thomas Misgeld for scientific discussions. Supported by the DFG, ERAnet and the Friedrich Schiedel Foundation. A.K. is a Carl von Linde Senior Fellow of the Institute for Advanced Study of the TUM. C.G. and N.L.R. were supported by the DFG (IRTG 1373).

Author contributions

A.K., C.G. and N.L.R. designed the experiments. C.G. and N.L.R. carried out the *in vivo* imaging experiments. C.G., N.L.R. and A.K. performed data analysis. H.A. performed the visual discrimination tests. H.A.H. performed the Aβ-plaques staining in brain slices and retinal sections. M.S. provided the transgenic mice. J.R. and M.S. performed the quantification of soluble Aβ. A.K. wrote the manuscript with help from C.G., N.L.R. and M.S.

Additional information

Supplementary Information accompanies this paper at http://www.nature.com/naturecommunications

Competing financial interests: The authors declare no competing financial interests.

Reprints and permission information is available online at http://npg.nature.com/reprintsandpermissions/

How to cite this article: Grienberger, C. *et al.* Staged decline of neuronal function *in vivo* in an animal model of Alzheimer's disease. *Nat. Commun.* 3:774 doi: 10.1038/ncomms1783 (2012).

Supplementary Information

Staged decline of neuronal function *in vivo* in an animal model of Alzheimer's Disease

Christine Grienberger[1]*, Nathalie L. Rochefort[1]*, Helmuth Adelsberger[1], Horst A. Henning[1], Dan N. Hill[1], Julia Reichwald[2], Matthias Staufenbiel[2] and Arthur Konnerth[1]

*These authors contributed equally to this work

[1]Institute of Neuroscience and Center for Integrated Protein Science, Technical University Munich, Biedersteinerstr. 29, 80802 Munich, Germany

[2]Novartis Institutes for Biomedical Research, 4002 Basel, Switzerland.

- **Supplementary Figures S1-10**
- **Supplementary Methods**

Supplementary Figure 1

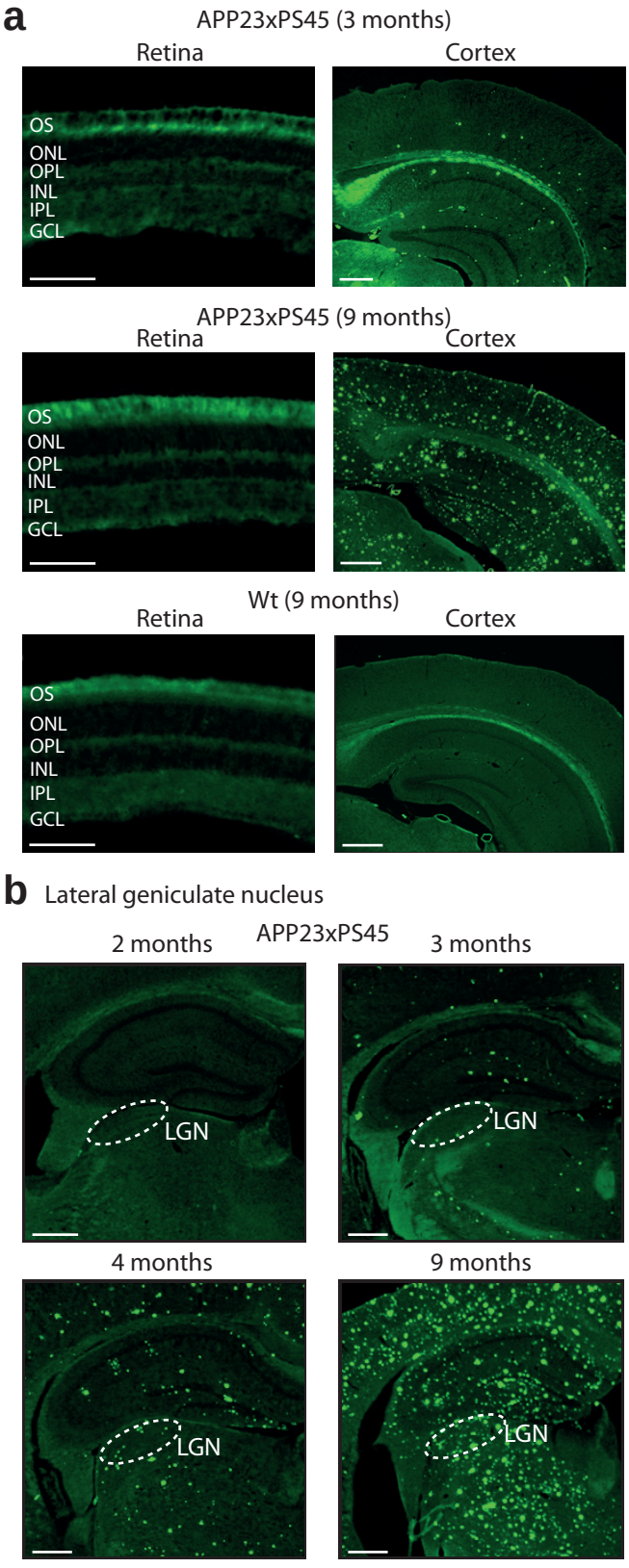

Supplementary Figure 1. (**a**) Absence of amyloid-β plaques in the retina of 3 to 8-10-month-old APP23xPS45 mice. Micrographs of retinal (left panels) and visual cortex sections (right panels) stained with Thioflavin-S. The slices were obtained from a young APP23xPS45 mouse (3 months, upper panels), an aged APP23xPS45 mouse (9 months, middle panels) and an aged Wt mouse (9 months, lower panels), respectively. No plaques were found in the retina throughout all ages tested. The different retina layers are indicated. OS, outer segment of photoreceptors; ONL, outer nuclear layer; OPL, outer plexiform layer; INL, inner nuclear layer; IPL, inner plexiform layer; GCL, ganglion cell layer. (Scale bars, retina 100 µm, cortices 500 µm). (**b**) Development of amyloid-β plaques in the lateral geniculate nucleus (LGN) of APP23xPS45 mice. Micrographs of coronal slices of LGN stained with Thioflavin-S. The slices were obtained from APP23xPS45 mice of 2, 3, 4 and 9 months of age. The white dotted lines indicate the location of the LGN. Scale bars, 500 µm.

Supplementary Figure 2

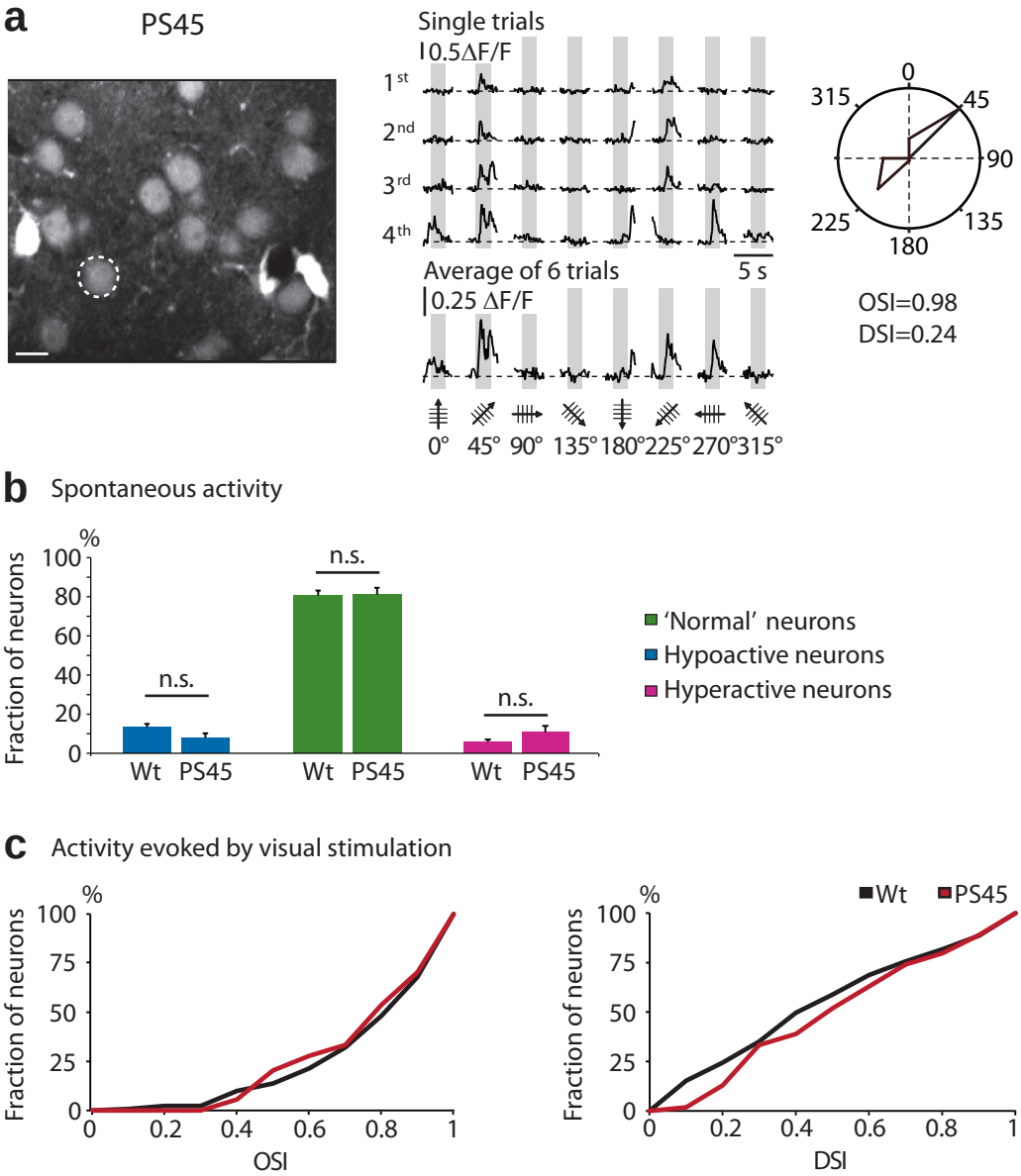

Supplementary Figure 2. Spontaneous activity, orientation and direction tuning of visual cortex neurons in the primary visual cortex of aged PS45 mice (8-10 months). (**a**) *Left panel*, in vivo two-photon image of layer 2/3 neurons in the visual cortex of a PS45 mouse (8 months). *Middle panel*, stimulus-evoked calcium transients recorded from the orientation selective neuron indicated in the left panel by a white dotted circle. Gray regions indicate periods of visual stimulation with drifting gratings schematized by oriented arrows on the bottom of each panel. Four single trials are represented on top and the average of 6 trials is shown below. Scale bar, 10 µm. *Right panel,* polar plot showing the neuron's response function to oriented drifting gratings. OSI, orientation selectivity index; DSI, direction selectivity index. (**b**) Bar graph showing the relative proportion of hypoactive, 'normal' and hyperactive neurons in 8-10-month-old Wt and PS45 mice (n=630 and 345 neurons in 15 and 5 mice, respectively). Error bars indicate SEM. (n.s., no significant difference, Mann-Whitney test; hypoactive, p=0.14; 'normal', p=0.93; hyperactive, p=0.27). (**c**) Cumulative distributions of the orientation (OSI) and direction (DSI) selectivity indices determined for all responsive neurons recorded in Wt (black; n=131 neurons in 13 mice) and PS45 (red; n=54 neurons in 4 mice) mice. No significant difference was found between Wt and PS45 mice (Mann-Whitney test; OSI, p=0.60; DSI, p=0.23).

Supplementary Figure 3

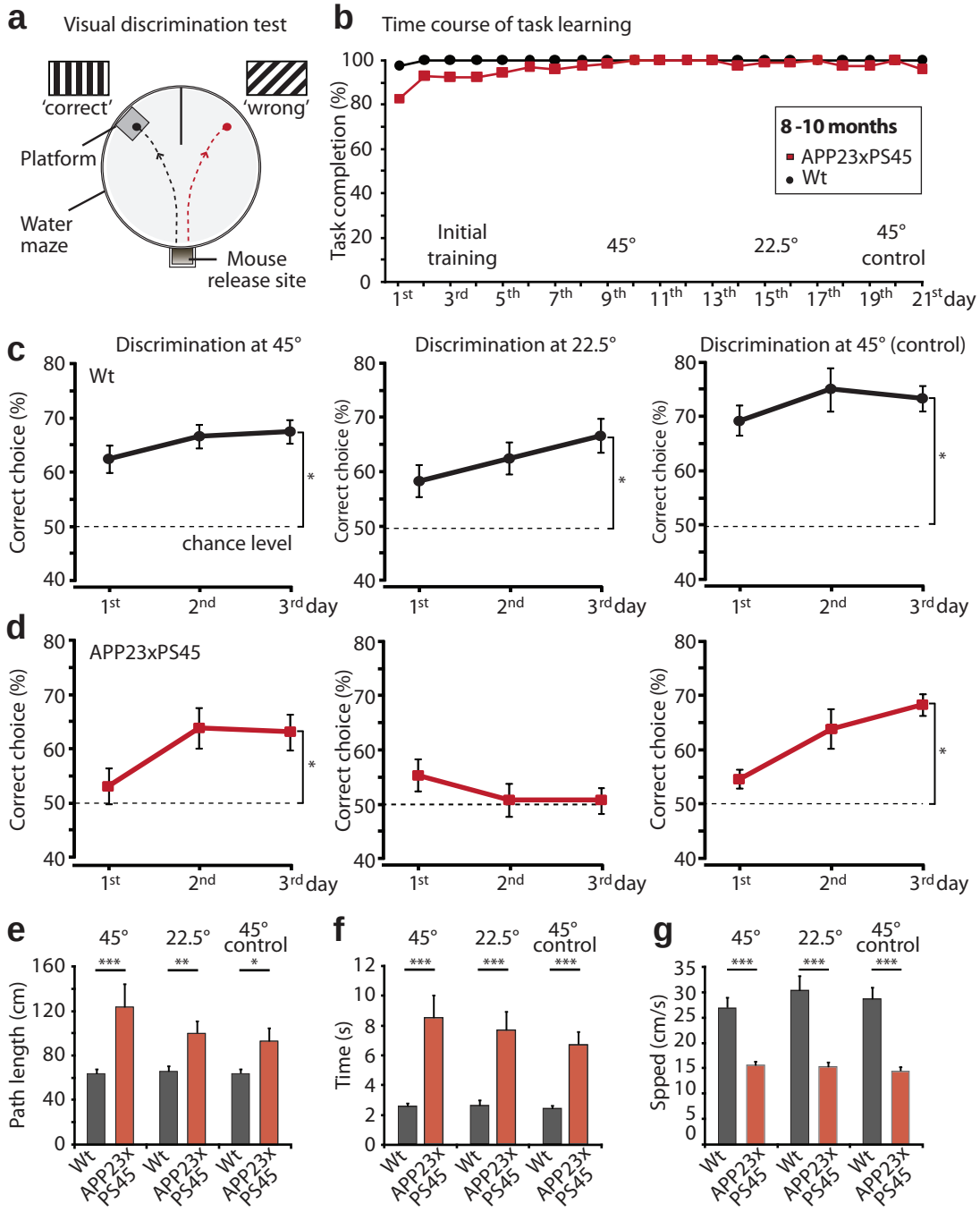

Supplementary Figure 3. Reduced visual discrimination in aged APP23xPS45 mice. (**a**) Schematic illustration of the visual pattern discrimination test. (**b**) Task learning development during the initial training and the testing phases. The task completion rate was estimated by the proportion of trials in which the mice reached either the platform located in front of the correct cue or the position of the platform in front of the wrong cue. (**c-d**) Mean percentages of the correct choices of Wt and APP23xPS45 mice during the visual discrimination test. *Left panels*, visual discrimination test illustrated in panel a (45° angle difference). The 50% chance level is indicated by a dotted line. Asterisks indicate a significant difference from the chance level: Chi-square test, Wt $p<0.001$ (n=12 mice), APP23xPS45 $p<0.005$ (n=13 mice). Error bars indicate SEM. *Middle panels*, the correct visual cue was still a vertically oriented drifting grating whereas the wrong choice was a clockwise 22.5° oriented one. The performance of the APP23xPS45 mice corresponded to the chance level (Chi-square, $p=0.861$), while Wt mice successfully learned the task (*$p<0.001$). *Right panels*, control visual discrimination test (45° angle difference) (Wt *$p<0.001$, APP23xPS45 *$p<0.001$). (**e-g**) Bar graphs showing the path length (e), the time spent to find the platform (f) as well as the swimming speed (g) of APP23xPS45 and Wt mice (8-10 months) during the 3 testing phases of the visual discrimination test. Note that all parameters were constant for both genotypes throughout the entire testing period (*$p<0.021$, **$p<0.005$, ***$p<0.001$).

Supplementary Figure 4

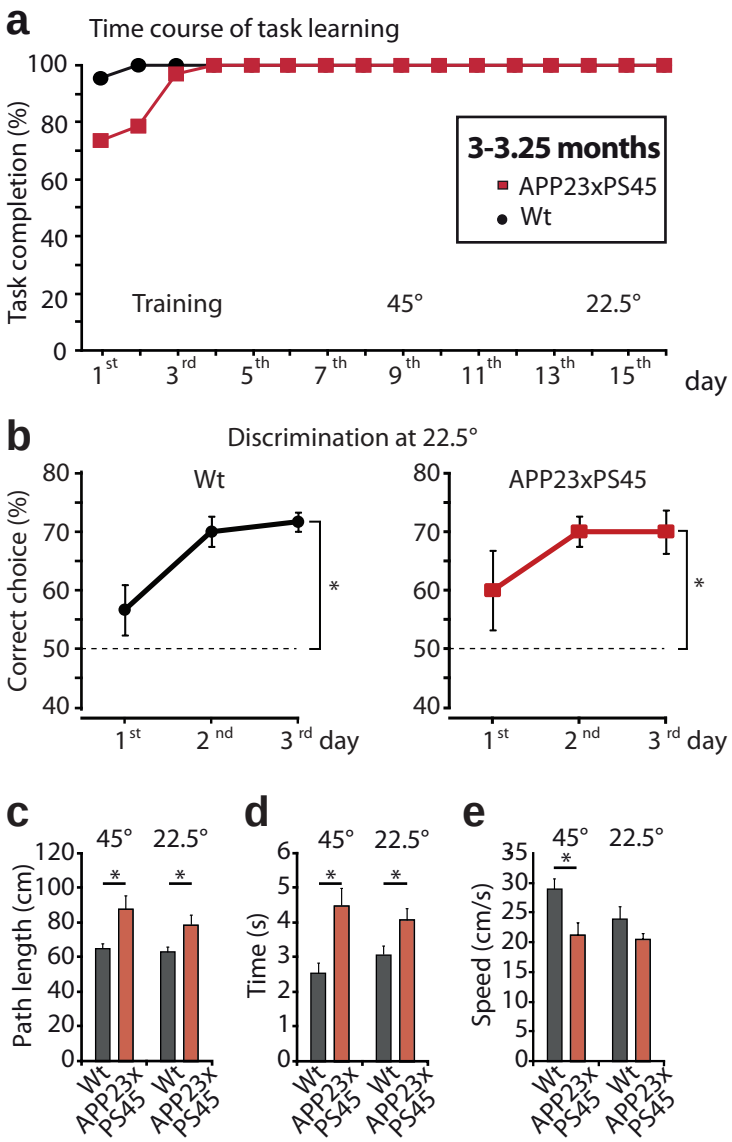

Supplementary Figure 4. Performance of young APP23xPS45 and Wt mice (3-3.25 months) in the visual discrimination test. (**a**) Task learning development during the training and the testing phases. Same legend as Supplementary Fig. 3a. (**b**) Mean percentages of the correct choices of Wt (left panel) and APP23xPS45 (right panel) mice determined for an angle difference of 22.5°. The 50% chance level is indicated by a dotted line. Asterisks indicate significant difference from chance level (Chi-square test; n=6 Wt, $p<0.005$; n=6 APP23xPS45, $p<0.005$). Error bars indicate SEM. (**c-e**) Bar graphs showing the path length (c), the time spent to find the platform (d) as well as the swimming speed (e) of young APP23xPS45 and Wt mice (3-3.25 months) during the two testing phases (orientation difference of 45°, 22.5°) of the visual discrimination test. Note that all parameters were constant for both genotypes throughout the entire visual tests. (Path length: 45° *$p<0.01$, 22.5° *$p<0.05$; Time: 45° *$p<0.001$, 22.5° *$p<0.05$; Swimming speed: 45° *$p<0.005$, 22.5° $p=0.35$).

Supplementary Figure 5

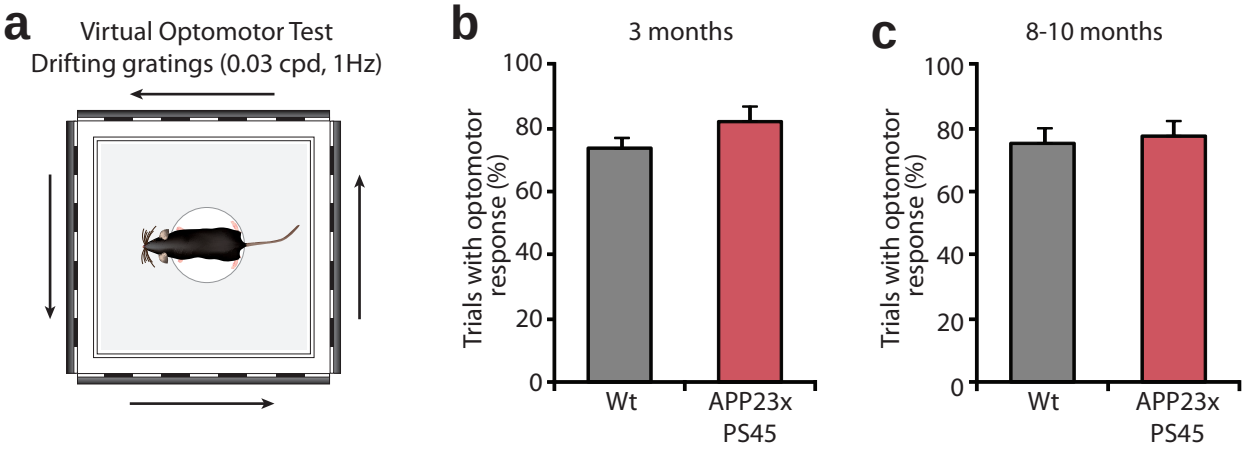

Supplementary Figure 5. Optomotor responses of APP23xPS45 and Wt mice (at 3 months and 8-10 months of age). (**a**) Schematic illustration of the virtual optomotor system. The animal was placed on a platform, unrestrained, in the center of the arena. Rotating stimuli (square-wave vertical gratings, 1 Hz, contrast 80%, 0.03 cpd) were applied on the monitors, where they formed a virtual cylinder around the mouse. The direction of movements changed randomly. Mice responded to the stimuli by rotating their head following the direction of the moving gratings. (**b-c**) Bar graphs showing the percentage of trials with an optomotor response of young (3-3.25 months, panel c) and old (8-10 months, panel d) Wt (black; n=6 and 6 mice, respectively) and APP23xPS45 (red; n=6 and 6 mice, respectively) mice. No significant difference was observed between Wt and transgenic animals. Reliable optomotor responses have been shown to be associated with normal retinal function (Thaung et al., 2002). These results indicate that both Wt and transgenic animals were able to see drifting gratings with the same spatial and temporal frequencies than that used for the visual discrimination test and the in vivo recordings.

Supplementary Figure 6

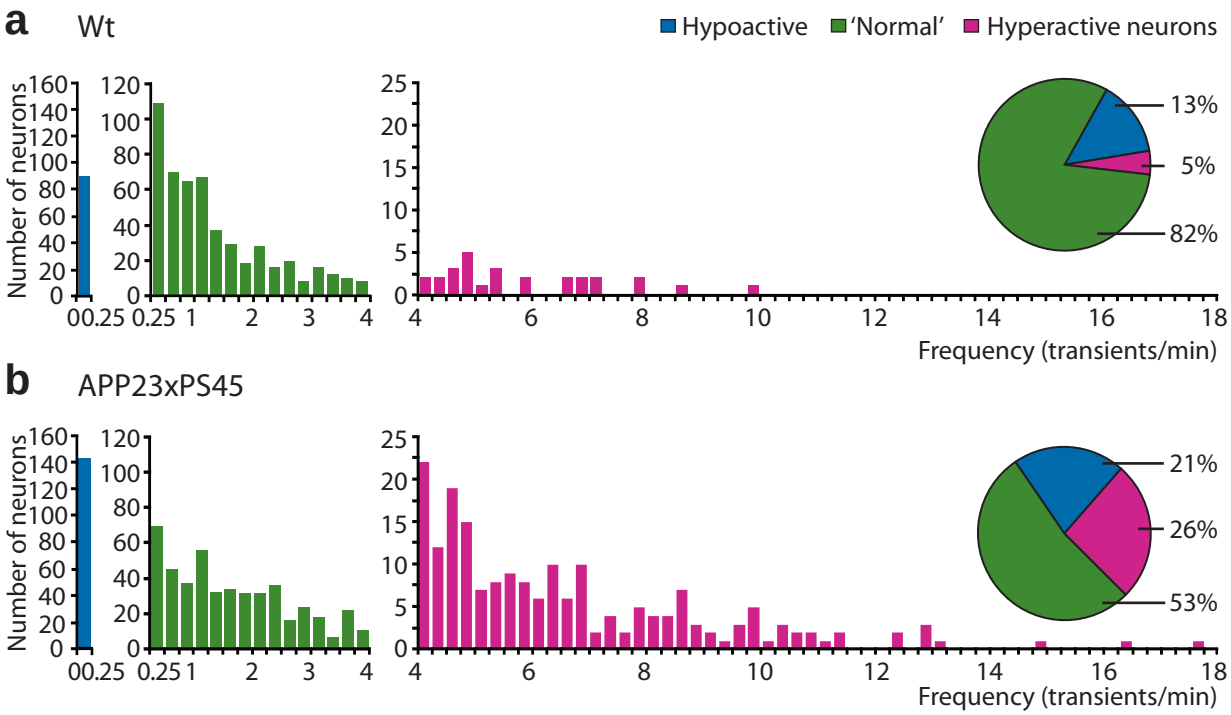

Supplementary Figure 6. (**a-b**) Frequency distribution of calcium transients during spontaneous activity of hypoactive (blue), 'normal' (green) and hyperactive (purple) neurons of APP23xPS45 and Wt mice (n=806 and 630 neurons in 19 and 15 mice, respectively). Spontaneous activity of each neuron was recorded during at least 4 min. Pie charts show fractions of hypoactive, normal and hyperactive neurons in Wt and APP23xPS45 mice.

Supplementary Figure 7

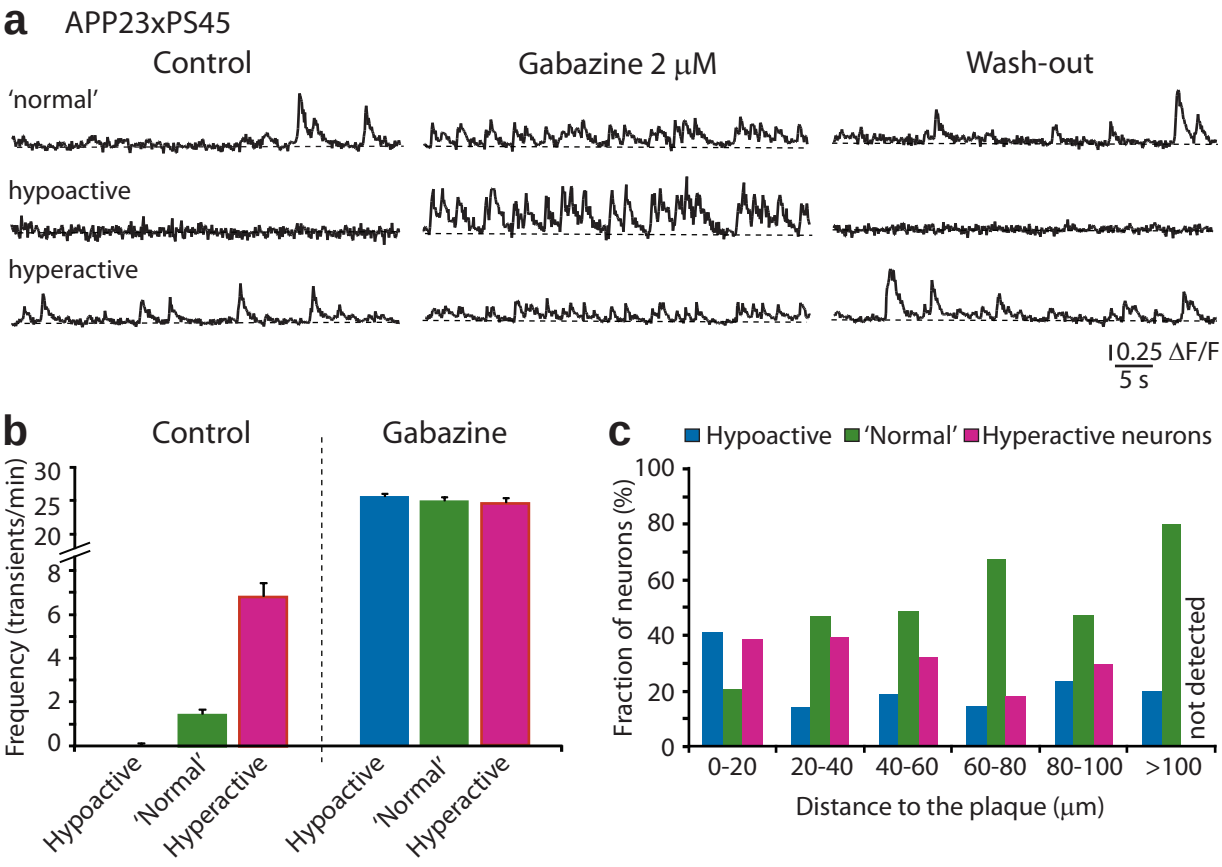

Supplementary Figure 7. (a) Spontaneous calcium transients before, during and after bath application of the $GABA_A$ receptor antagonist gabazine (2 μM) in layer 2/3 'normal', hypoactive and hyperactive neurons in the visual cortex of an APP23xPS45 mouse (8.5 months). (**b**) Summary graph illustrating the effect of gabazine on the frequency of calcium transients (n=6 hypoactive, 12 'normal', and 11 hyperactive neurons). Application of the $GABA_A$ receptor antagonist gabazine increased the frequency of calcium transients in all three types of neurons to the same level of 25 transients/min. However, the relative frequency increase in hyperactive neurons (2.8-fold) was distinctly smaller compared with the frequency increase in 'normal' neurons (17-fold). Error bars indicate SEM. **(c)** Bar graph showing the proportion of silent, normal, and hyperactive neurons at different distances from the border of the nearest plaque (n = 606 neurons in 17 APP23xPS45 mice, 8-10 months).

Supplementary Figure 8

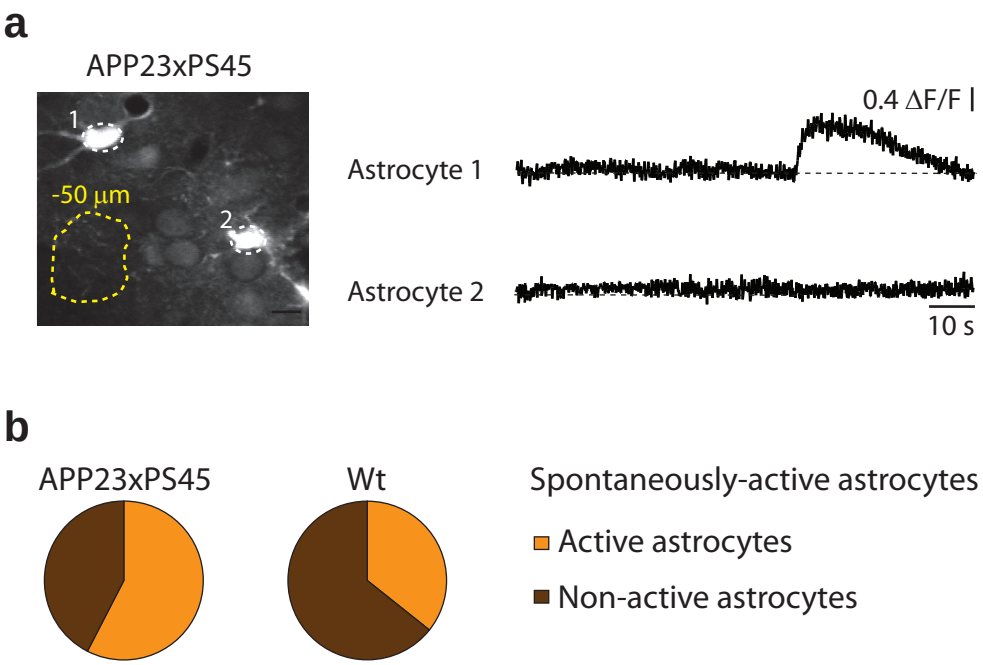

Supplementary Figure 8. Spontaneous activity of astrocytes in the primary visual cortex of aged Wt and APP23xPS45 mice (8-10 months). (**a**) *Left panel*, in vivo two-photon image of layer 2/3 neurons and astrocytes in the visual cortex of an APP23xPS45 mouse (8 months). The broken yellow line delineates a Thioflavin-S plaque observed 50 µm below the imaged focal plane. *Right panel*, spontaneous activity recorded from the astrocytes indicated in the left panel by a white dotted circle. Scale bar, 10 µm. (**b**) Pie charts representing the proportion of spontaneously active astrocytes in aged APP23xPS45 mice (57.5 %, n=66 astrocytes in 17 mice) and Wt mice (35 %, n=42 astrocytes in 14 mice). An astrocyte was considered active when at least one spontaneous calcium transient was recorded during the imaging period of spontaneous activity (at least 4 min).

Supplementary Figure 9

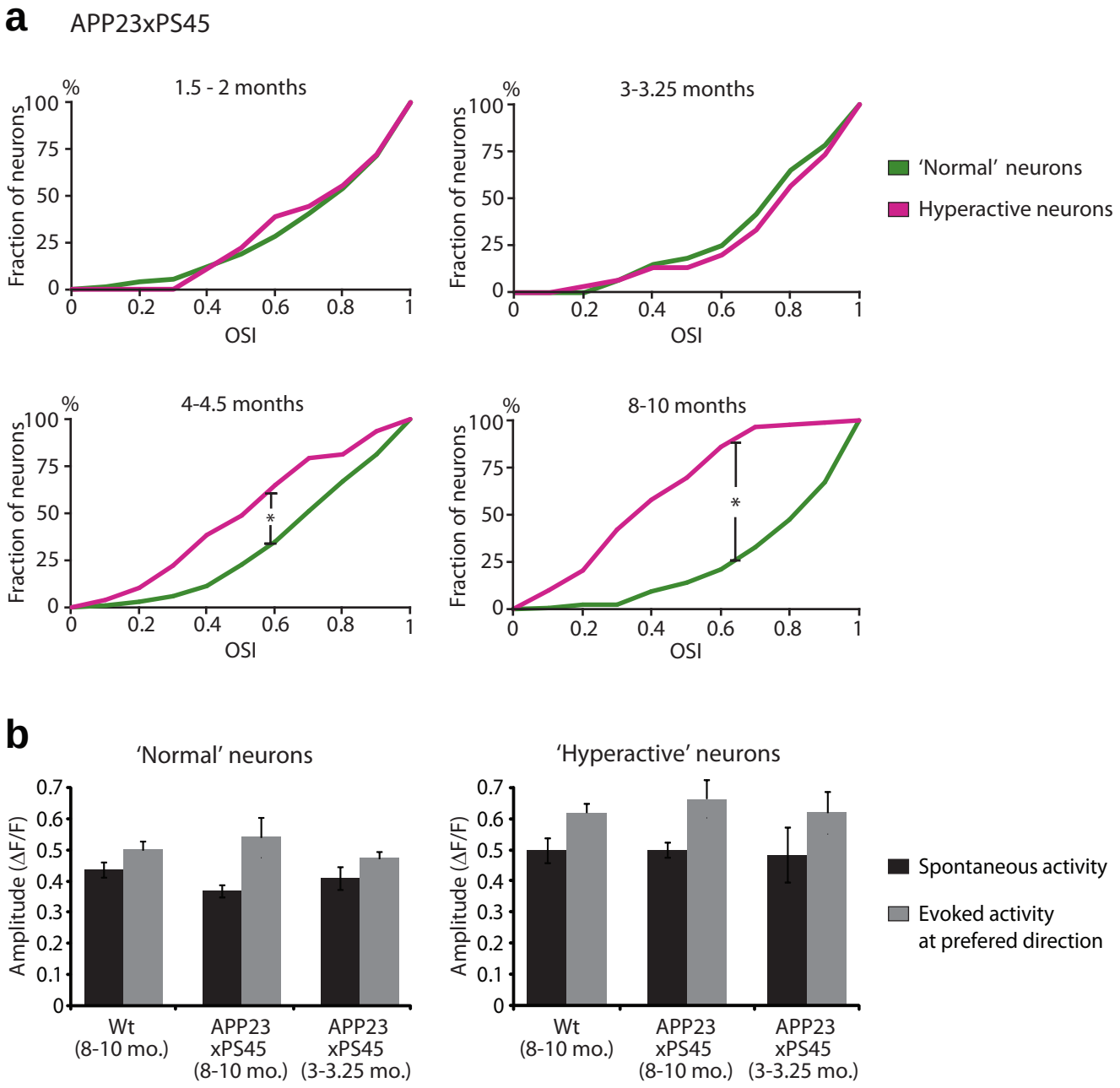

Supplementary Figure 9. (a) Development of functional impairment of hyperactive neurons in the visual cortex of APP23xPS45 mice. Cumulative distributions of orientation selectivity indices (OSI) determined for all responsive 'normal' (green) and hyperactive (purple) neurons recorded in APP23xPS45 mice at the four different ages (1.5-2, 3-3.25, 4-4.5, 8-10 months; n=74, 60, 97, 67 'normal' neurons and n=10, 30, 49, 78 hyperactive neurons in 7, 6, 8, 15 mice, respectively). Note that from the age of 4-4.5 months, hyperactive neurons have lower orientation selectivity compared to 'normal' neurons (Mann-Whitney test, 4-4.5 months *p<0.001; 8-10 months *p<0.001). **(b)** Peak amplitude of the spontaneous and evoked transients in Wt (8-10 months), APP23xPS45 (8-10 months) and young APP23xPS45 (3-3.25 months) mice. The peak amplitude of evoked activity was measured at the prefered direction. The response amplitude of normal and hyperactive neurons did not vary significantly between aged Wt and aged transgenic mice as well as between young (3 months) and aged (8-10 months) transgenic animals.

Supplementary Figure 10

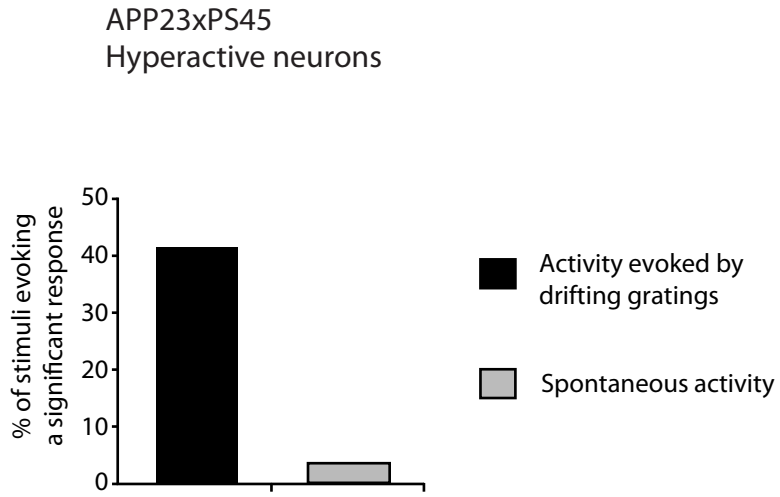

Supplementary Figure 10. Impact of high spontaneous activity on the detection of responses to drifting gratings, in aged APP23xPS45 mice. ***Black bar***, percentage of significant responses to drifting gratings. Neuronal calcium responses evoked by drifting gratings were detected if their mean amplitude during the period of stimulation (2 s) was significantly above (t-test) the activity level during the preceding period (2 s). Using this analysis, hyperactive neurons in APP23xPS45 mice responded significantly to an average of 41.7 % of all drifting gratings. Thus, an hyperactive neuron was responding on average to 3.3 directions among the 8 directions of drifting gratings. ***Grey bar***, same analysis applied to recordings of spontaneous activity in the same neurons, after randomly assigning periods of nominal stimulation. A direction was randomly assigned to 8 epochs (2 seconds each) of the spontaneous activity trials. Then, an average of 6 trials was calculated. Finally, a t-test was performed between each of these epochs and the 2 seconds preceding them (equivalent to the standing grating periods in the evoked trials). Using this analysis, significant responses were detected in only 3.7 % of all stiumuli epochs. Thus, for a given hyperactive neuron only a relatively minor fraction (< 9%) of false positive responses was detected in these conditions. The fact that hyperactive neurons in APP23xPS45 respond to many directions and have a low orientation tuning is thus not due to a simple increase in high spontaneous activity.

Supplementary Methods

Behavioral test, visual pattern discrimination task. The discrimination task was based on the same procedure described in a previous study[62,63]. In a circular water maze (diameter 80 cm, height 32 cm) filled with opaque water (23°C), animals had to locate a platform (10 x 10 cm) that was stable and kept invisible (about 5 mm submerged) in front of a specific visual cue (a grating with specific orientation) (see Supplementary Figure S3a). Visual stimuli were displayed on two identical computer monitors (1280 x 1024 pixels) that were placed along the maze on each side of a 25 cm long divider. Animals had to choose between two different visual cues. The platform was always placed below the correct visual cue computer screen (correct choice). Visual cues consisted of square-wave gratings (1 Hz, contrast 80%, 0.03 cpd as seen from the edge of the platform) and a mean luminance gray screen. Three groups of 8-month-old animals were tested independently (group 1: Wt n=6, APP23xPS45 n=5; group 2: Wt n=3, APP23xPS45 n=5; group 3: Wt n=3, APP23xPS45 n=3). In addition, one group of 3-month-old animals was tested (APP23xPS45 n=6, Wt n=6) with the same protocol.

The test consisted of four phases, the training phase and the three consecutive testing phases. For the first phase (training), the two visual cues were a gray screen (wrong stimulus) and a vertically oriented drifting grating (0°, correct stimulus). For the second phase, visual cues consisted of two drifting gratings of different orientations: a vertically oriented drifting grating (0°, correct stimulus) and a clockwise 45° oriented one (45°, wrong stimulus). For the third phase, the angle difference between both visual cues was reduced to 22.5° (0°, correct stimulus; 22.5°, wrong stimulus). Finally the fourth phase was identical to the second one (0°, wrong stimulus; 45°, correct stimulus). The understanding of the task was assessed during six initial training days (days 1-6). Then, phases 2 (6 days), 3 (6 days) and 4 (3 days) were added. Each day included 10 trials separated by 1-3 min inter-trial intervals. The position of the correct stimulus (left or right side of the divider) was changed pseudo-randomly. Mice were released into the maze from a box with a sliding door (see Supplementary Figure S3a). The percentage of correct choices was used to assess pattern discrimination performance. A correct choice was scored when the mouse touched the hidden platform. An incorrect choice was recorded when the mouse either reached the putative platform position on the wrong side (below the wrong stimulus) or failed to reach any platform position (correct or putative) within 30 s (error of omission). In case of an incorrect choice or an error of omission, animals were placed by the investigator onto the platform. All mice remained on this platform for about 5 s before being returned to their home cage. We verified that the mice were capable of completing the task by determining the proportion of trials in which the mice reached either the platform located in front of the correct cue ('correct' choice) or the position of the platform in front of the wrong cue ('wrong choice'). At the end of the training phase, both Wt and APP23xPS45 mice reached a task completion rate higher than 96% and a level of correct choices significantly above the chance level (Chi-square test, Wt, $p<0.001$, APP23xPS45, $p<0.001$).

During the testing phases 2 and 3 the percentage of correct choices did not significantly change after the third day of testing, for both Wt and transgenic mice groups (Mann-Whitney test; 45° Wt p=0.132;APP23xPS45 p=0.866; 22.5° Wt p=0.254, APP23xPS45 p=0.675). Thus, we show in Supplementary Figure S3c-d, only the results of the first three days. All trials were video-taped with a digital camera (Sony, DCR-HC96E) mounted above the water maze for off-line analysis. Tracking of the swimming routes in the water

maze was performed with a custom-written software (LabView, National Instruments). We quantified the path length, the time spent to find the platform as well as the swimming speed. All these parameters were constant throughout the entire visual tests for both genotypes.

Measure of optomotor responses. The virtual optomotor system consisted of a square array of computer monitors placed at the four sides of a mirror with a side-length of 40 cm. The animal was placed on a platform, unrestrained, in the center of the arena. A camera (Sony, DCR-HC96E) was mounted above the animal in order to video-tape all trials. Rotating stimuli (square-wave vertical gratings, 1 Hz, contrast 80%, 0.03 cpd) were applied on the monitors, where they formed a virtual cylinder around the mouse[64]. Each session consisted of 20 trials, one trial lasting 15 sec. During the trials vertical drifting gratings were presented. The direction of movements changed randomly. The breaks between the trials also varied randomly between 8 and 30 sec. Mice responded to the stimuli by rotating their head following the direction of the moving gratings. Prior to testing the mice were adapted to the environment and arena by placing them on the platform for five minutes on three consecutive days. A session started by placing the animal on the platform while presenting resting gratings and left there for an adaptation period of five minutes. Only trials in which the mice showed no spontaneous movements were included in the evaluation. Sessions were repeated until at least 10 trials could be included into the evaluation. A positive trial was defined as a movement of the head into the same direction as the gratings. No head movements or head movements into the opposite direction were defined as negative trials. If, during the course of testing an animal slipped or jumped off the platform, it was simply returned to the platform and testing was resumed. Experimenters were blind to the genotype of the animals. The results are shown in Supplementary Figure S5. Both Wt and transgenic animals had reliable optomotor responses during the presentation of gratings with the same spatial and temporal frequencies than that used for the visual discrimination test and the *in vivo* recordings. These results indicate that both Wt and transgenic animals were able to see drifting gratings with such spatial and temporal frequencies.

Supplementary References

61. Thaung, C., Arnold, K., Jackson, I.J. & Coffey, P.J. Presence of visual head tracking differentiates normal sighted from retinal degenerate mice. *Neurosci Lett* **325**, 21-4 (2002).
62. Wong, A.A. & Brown, R.E. Age-related changes in visual acuity, learning and memory in C57BL/6J and DBA/2J mice. *Neurobiol Aging* **28**, 1577-93 (2007).
63. Prusky, G.T., West, P.W. & Douglas, R.M. Behavioral assessment of visual acuity in mice and rats. *Vision Res* **40**, 2201-9 (2000).
64. Prusky, G.T., Alam, N.M., Beekman, S. & Douglas, R.M. Rapid quantification of adult and developing mouse spatial vision using a virtual optomotor system. *Invest Ophthalmol Vis Sci* **45**, 4611-6 (2004).